



National Library
of Canada

Bibliothèque nationale
du Canada

Canadian Theses Service

Service des thèses canadiennes

Ottawa, Canada
K1A 0N4

NOTICE

The quality of this microform is heavily dependent upon the quality of the original thesis submitted for microfilming. Every effort has been made to ensure the highest quality of reproduction possible.

If pages are missing, contact the university which granted the degree.

Some pages may have indistinct print especially if the original pages were typed with a poor typewriter ribbon or if the university sent us an inferior photocopy.

Reproduction in full or in part of this microform is governed by the Canadian Copyright Act, R.S.C. 1970, c. C-30, and subsequent amendments.

AVIS

La qualité de cette microforme dépend grandement de la qualité de la thèse soumise au microfilmage. Nous avons tout fait pour assurer une qualité supérieure de reproduction.

S'il manque des pages, veuillez communiquer avec l'université qui a conféré le grade.

La qualité d'impression de certaines pages peut laisser à désirer, surtout si les pages originales ont été dactylographiées à l'aide d'un ruban usé ou si l'université nous a fait parvenir une photocopie de qualité inférieure.

La reproduction, même partielle, de cette microforme est soumise à la Loi canadienne sur le droit d'auteur, SRC 1970, c. C-30, et ses amendements subséquents.

UNIVERSITY OF ALBERTA

THE STABILITY AND INTERFACIAL PHENOMENA OF
A SALT WEDGE FLOW

BY

NOBORU YONEMITSU

A THESIS

SUBMITTED TO THE FACULTY OF GRADUATE STUDIES AND RESEARCH
IN PARTIAL FULFILLMENT OF THE REQUIREMENTS FOR THE DEGREE
OF DOCTOR OF PHILOSOPHY

in

WATER RESOURCES

DEPARTMENT OF CIVIL ENGINEERING

EDMONTON, ALBERTA

FALL, 1991



National Library
of Canada

Bibliothèque nationale
du Canada

Canadian Theses Service Service des thèses canadiennes

Ottawa, Canada
K1A 0N4

The author has granted an irrevocable non-exclusive licence allowing the National Library of Canada to reproduce, loan, distribute or sell copies of his/her thesis by any means and in any form or format, making this thesis available to interested persons.

The author retains ownership of the copyright in his/her thesis. Neither the thesis nor substantial extracts from it may be printed or otherwise reproduced without his/her permission.

L'auteur a accordé une licence irrévocable et non exclusive permettant à la Bibliothèque nationale du Canada de reproduire, prêter, distribuer ou vendre des copies de sa thèse de quelque manière et sous quelque forme que ce soit pour mettre des exemplaires de cette thèse à la disposition des personnes intéressées.

L'auteur conserve la propriété du droit d'auteur qui protège sa thèse. Ni la thèse ni des extraits substantiels de celle-ci ne doivent être imprimés ou autrement reproduits sans son autorisation.

ISBN 0-315-69929-9

Canada

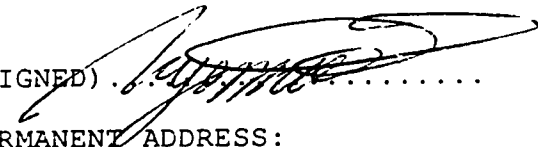
UNIVERSITY OF ALBERTA

RELEASE FORM

NAME OF AUTHOR NOBORU YONEMITSU
TITLE OF THESIS THE STABILITY AND INTERFACIAL WAVE
PHENOMENA OF A SALT WEDGE FLOW
DEGREE FOR WHICH THESIS WAS PRESENTED DOCTOR OF PHILOSOPHY
YEAR THIS DEGREE GRANTED FALL, 1991

Permission is hereby granted to THE UNIVERSITY OF ALBERTA LIBRARY to reproduce single copies of this thesis and to lend or sell such copies for private, scholarly or scientific research purposes only.

The author reserves other publication rights, and neither the thesis nor extensive extracts from it may be printed or otherwise reproduced without the author's written permission.

(SIGNED) .....
PERMANENT ADDRESS:

Northwest Hydraulic Consultants Ltd.
4823 - 99th Street.....
Edmonton, Alberta, T6E 4Y1

DATED *13 Sept* 1991

THE UNIVERSITY OF BRITISH COLUMBIA



Department of Civil Engineering
2324 Main Mall
Vancouver, B.C. Canada V6T 1Z4
Tel: (604) 822-2637
Fax: (604) 822-6901

August 20, 1991

Noboru Yonemitsu
Northwest Hydraulic Consultants
4823 - 99th Street
Edmonton, Alberta
T6E 4Y1

Dear Nobo:

It is with pleasure that I authorize you to use the stability diagrams from
Figs. ~~2 & 3~~ of my paper on "The Stability of a Sheared Density Interface".
PAGES 43 + 44

I have enclosed the signed forms accepting your Ph.D. thesis. Congratulations on a job very well done. Please call me if you're thinking of visiting Vancouver.

Yours sincerely,

Greg Lawrence
Assistant Professor

:kl
Encl.

UNIVERSITY OF ALBERTA

FACULTY OF GRADUATE STUDIES AND RESEARCH

The undersigned certify that they have read, and recommend to the Faculty of Graduate Studies and Research for acceptance, a thesis entitled THE STABILITY AND INTERFACIAL WAVE PHENOMENA OF A SHARP WEDGE FLOW submitted by NOBORU YONEMITSU in partial fulfillment of the requirements for the degree of DOCTOR OF PHILOSOPHY.

M. Rajaratnam
.....
Supervisor

J. Swater
.....
Co-supervisor

H.C. Cheng
.....

R. Stoff
.....

Lawrence
.....

Date *6 Sept 91*
.....

ABSTRACT

The salt wedge is a commonly observed water system in estuaries with relatively small tidal ranges. It is formed by sea water intrusion into the river and often has a very distinctive two layered stratification.

Because of its physical, chemical, biological and economic importance, extensive investigations have been performed on the salt wedge in order to specify both over-all flow properties and mixing phenomena through its density interface. However, particularly in the reproduction of this flow system by laboratory experiments, models show significant complications and the present hydrodynamic stability theories can not interpret the interfacial mixing properties correctly.

In this study, some typical flow configurations in salt wedge flow, especially secondary flow structures, are considered. Based on previous observations, four hydrodynamic stability models are developed to investigate interface stability. Each designed to investigate the effects of the rigid boundary, boundary velocity, viscosity, and displacement of the velocity profile inflection point with respect to the density interface. The results provide qualitative explanations for the observed three-dimensional structures of interfacial phenomena and waves.

Precise experiments have been performed to produce a complete data set (i.e. information such as wedge shape,

velocity and density profiles, wave length and phase velocity, interfacial displacement and the lower layer thickness) in order to verify the theoretical model predictions. Agreement between these experiments and the theoretical results is very good, although the predicted phase velocity of SVB waves is always underestimated.

This work is concluded with a discussion of the possibility of three-dimensional primary instability in a salt wedge flow.

ACKNOWLEDGEMENTS

The author would like to express his sincere appreciation to Dr. N. Rajaratnam and Dr. G. Swaters for their guidance and helpful supervision.

Special thanks are due to Dr. P. Steffler, Mr. S. Lovell and his staff in the Hydraulics Laboratory of the University of Alberta for the technical assistance throughout the experimental phase of the investigation.

Acknowledge is also due to the Alberta Government for the Minister of Advanced Education Scholarship awarded to the author for the period 1986-1988, and the financial assistance provided by the Natural Science and Engineering Council of Canada during 1990.

Acknowledge are also expressed to Mr. D. Tovell, Mr. C.R. Neill and Dr. M. Finlayson for their suggestions and encouragement throughout the preparation and typing of the manuscript.

TABLE OF CONTENTS

INTRODUCTION.....	1
PART ONE: REVIEW OF THE PRESENT KNOWLEDGE.....	7
1.1 INTRODUCTION.....	7
1.2 REVIEW OF EXPERIMENTAL INVESTIGATIONS.....	9
1.2.1 Introduction.....	9
1.2.2 Salt Wedge Experiments.....	9
1.2.3 Interfacial Waves and Instabilities.....	16
1.3 MATHEMATICAL MODELS OF INTERFACIAL WAVES.....	23
1.3.1 Introduction.....	23
1.3.2 Hydrodynamic Stability.....	24
1.3.3 Viscosity Effects on Stability.....	27
1.3.4 Rigid Boundary Effects.....	29
1.3.5 Density Interface Displacement Effects.....	31
1.3.6 Three-Dimensional Instabilities.....	32
1.4 CONCLUSIONS.....	45
PART TWO: THEORETICAL ANALYSIS (INVISCID MODELS).....	47
2.1 INTRODUCTION.....	47
2.2 GOVERNING EQUATIONS.....	48
2.2.1 Basic Assumptions and Governing Equations...48	
2.2.2 Taylor-Goldstein Equation.....	50
2.2.3 Boundary and Matching Conditions.....	54
2.2.4 Perturbation Quantities in the Flow.....	61

2.3	MODEL I: THICKNESS EFFECTS.....	65
2.3.1	Formulation.....	65
2.3.2	Solutions.....	71
2.4	MODEL II: EFFECTS OF VARIATIONS OF BOUNDARY VELOCITY..	98
2.4.1	Formulation.....	98
2.4.2	Solutions.....	107
2.5	DISCUSSION.....	132
2.6	CONCLUSIONS.....	137
PART THREE:	NUMERICAL ANALYSIS (VISCOUS MODELS).....	139
3.1	INTRODUCTION.....	139
3.2	GOVERNING EQUATIONS.....	141
3.2.1	Basic Assumptions and Governing Equations..	141
3.2.2	Orr-Sommerfeld Equation.....	142
3.3	BOUNDARY CONDITIONS.....	147
3.4	CALCULATION METHOD OF EIGENVALUES.....	150
3.4.1	Eigen Equation.....	150
3.4.2	Parasitic Growth Problems and Orthonormalization.....	153
3.4.3	Determination of Eigenvalues.....	157
3.4.4	Perturbation Quantities in the Flow.....	159
3.5	MODEL III: THICKNESS EFFECTS.....	161
3.5.1	Formulation.....	161
3.5.2	Solutions.....	161

3.6	MODEL IV: DENSITY INTERFACE SHIFTING EFFECTS.....	186
3.6.1	Formulation.....	186
3.6.2	Solutions.....	186
3.7	DISCUSSION.....	192
3.8	CONCLUSIONS.....	195
PART FOUR:	EXPERIMENTAL STUDY.....	197
4.1	INTRODUCTION.....	197
4.2	FACILITIES AND PROCEDURES.....	198
4.2.1	Flume.....	198
4.2.2	Laser Doppler Anaemometer.....	201
4.2.3	Wave Detector.....	207
4.2.4	Conductivity-Salinity Meter.....	210
4.3	EXPERIMENTAL RESULTS.....	213
4.4	DISCUSSION.....	240
4.5	CONCLUSIONS.....	253
PART FIVE:	GENERAL CONCLUSIONS.....	254
5.1	CONCLUSIONS.....	254
5.2	DISCUSSION AND SUGGESTIONS.....	259
BIBLIOGRAPHY.....		262
APPENDIX A	RELATIONSHIP BETWEEN REYNOLDS STRESS AND PHASE CHANGE OF PERTURBATION VELOCITY \tilde{w}	268
APPENDIX B	COMPUTER PROGRAMS.....	272
APPENDIX C	DETERMINATION OF WAVE LENGTH λ AND PHASE	

VELOCITY C_R305

LIST OF FIGURES

Figure 1	Schematics of the (arrested) salt wedge and its typical velocity and density profiles.....	2
Figure 2	Classification of typical interfacial phenomena and waves.....	3
Figure 3	Three-dimensional flow structure of salt wedge flow due to the secondary flow in channel.....	4
Figure 1.1	Schematics of the structure of salt wedge showing the three major hydrodynamic regions and their typical velocity profiles.....	13
Figure 1.2	SVA wave trains.....	14
Figure 1.3	Schematics of wave phenomena on the salt wedge.....	15
Figure 1.4	Schematics of experimental flume and process of mixing described by Keulegan (1949).....	20
Figure 1.5	Adopted schematics of stratified flow experiment of Browand and Winant (1973).....	21
Figure 1.6	Velocity distribution of upper layer fluid in the lateral direction (channel dimension of cross section is 50X10 cm, visualized about 1 cm above the density interface by dye injection method).....	22

Figure 1.7	Velocity and density profiles of Kelvin-Helmholtz models.....	34
Figure 1.8	K-H instability in atmosphere (courtesy of M. Jasek).....	34
Figure 1.9	Velocity and density profiles and the stability boundaries (Adopted from Holmboe (1962)).....	35
Figure 1.10	The velocity and density distributions of Hazel's model (1972).....	36
Figure 1.11	The modified stability diagram obtained by Hazel (1972). $U=\tanh(z)$, $\log(\rho_0/\rho)=\text{stanh}(Rz)/R$ with $R=5.0$ case.....	37
Figure 1.12	Adopted stability diagrams calculated by Maslowe and Thompson (1971). (a) Stability curve for temporally varying waves. ($Ri_0=0.15$ case) (b) Neutral boundaries (i.e. $C_I=0.0$) for various Richardson numbers.....	38
Figure 1.13	Velocity and density profiles and the stability boundaries (Adopted from Nishida & Yoshida (1984, 1987)).....	39
Figure 1.14	Velocity and density profiles and the stability boundaries (Adopted from Lalas & Einaudi (1976)).....	40
Figure 1.15	Velocity and density profiles and the stability diagram $R=5.0$ $Pr=7.5$ $Re=50$ $J_0=0.15$ $\alpha=0.7$ case (Adopted	

	from Hino, Nadaoka & Hung (1984)).....	41
Figure 1.10	Mean velocity and density profiles as measures and as predicted by the numerical model examined by Lawrence et al. (1989).....	42
Figure 1.17	Density interface displacement effects (Adopted from Lawrence et al.(1989)) (a) $d=0.0$ case (b) $d=0.25$ case (c) $d=0.5$ case (d) $d=1.0$ case.....	43
Figure 2.1	Boundary conditions.....	55
Figure 2.2	Velocity and density profiles of model I (a) $Z_R > 1.0$ (b) $Z_R < 1.0$	66
Figure 2.3	Dispersion relationship v.s. lower layer thickness Z_R . $Ri=2.0$ cases (a) $Z_R = \text{inf.}$ (b) $Z_R = 3.0$ (c) $Z_R = 2.0$ (d) $Z_R = 1.5$ (e) $Z_R = 1.3$ (f) $Z_R = 1.2$ (g) $Z_R = 1.1$ (h) $Z_R = 1.05$	74
Figure 2.4	Dispersion relationship for $Z_R = \text{inf.}$ SVA and SVB solutions.....	82
Figure 2.5	Dispersion relationship for $Z_R = 3.0$ SVA and SVB solutions.....	83
Figure 2.6	Dispersion relationship for $Z_R = 2.0$ SVA and SVB solutions.....	84
Figure 2.7	Dispersion relationship for $Z_R = 1.2$ SVA and SVB solutions.....	85
Figure 2.8	Neutral boundaries v.s. lower layer thickness Z_R . (a) SVA solutions	

	(b) SVB solutions.....87
Figure 2.9	The perturbation quantities. $Ri=0.2$ $a=0.8$ $c=(-0.389, 0.162)$ unbounded case (a) velocity fluctuation \tilde{w} (b) velocity fluctuation \tilde{u} (c) Reynolds stress τ (d) Displacement η89
Figure 2.10	The perturbation quantities. $Ri=0.2$ $a=0.8$ $c=(0.388, 0.161)$ unbounded case (a) velocity fluctuation \tilde{w} (b) velocity fluctuation \tilde{u} (c) Reynolds stress τ (d) Displacement η91
Figure 2.11	The perturbation quantities. $Ri=0.2$ $a=0.8$ $c=(-0.388, 0.161)$ unbounded case (a) velocity fluctuation \tilde{w} (b) velocity fluctuation \tilde{u} (c) Reynolds stress τ (d) Displacement η93
Figure 2.12	The perturbation quantities. $Ri=0.2$ $a=0.8$ $c=(-0.459, 0.0)$ $Z_R=1.68$ case (a) velocity fluctuation \tilde{w} (b) velocity fluctuation \tilde{u} (c) Reynolds stress τ (d) Displacement η95
Figure 2.13	Stream line of SVA and SVB solutions (on the system moving with C_R).....97
Figure 2.14	Velocity and density distribution of Model II.....99
Figure 2.15	Neutral boundaries v.s. velocity at wall $Z_R=4.0$ cases (a) $U_w=-1.0$

	(b) $U_w = -0.5$ (c) $U_w = 0.0$ (d) $U_w = 0.5$	
	(e) $U_w = 1.0$	105
Figure 2.16	Neutral boundaries. $U_w = -0.5$ cases	
	(a) $Z_R = 4.0$ (b) $Z_R = 3.0$ (c) $Z_R = 2.0$	
	(d) $Z_R = 1.5$ (e) $Z_R = 1.3$ (f) $Z_R = 1.2$	
	(g) $Z_R = 1.1$ (h) $Z_R = 1.05$	107
Figure 2.17	Neutral boundaries. $U_w = 0.0$ cases	
	(a) $Z_R = 4.0$ (b) $Z_R = 3.0$ (c) $Z_R = 2.0$	
	(d) $Z_R = 1.5$ (e) $Z_R = 1.3$ (f) $Z_R = 1.2$	
	(g) $Z_R = 1.1$	111
Figure 2.18	Neutral boundaries. $U_w = 0.5$ cases	
	(a) $Z_R = 4.0$ (b) $Z_R = 3.0$ (c) $Z_R = 2.0$	
	(d) $Z_R = 1.5$ (e) $Z_R = 1.3$ (f) $Z_R = 1.2$	
	(g) $Z_R = 1.1$ (h) $Z_R = 1.05$	114
Figure 2.19	Neutral boundaries on $\alpha - \alpha_{CR}$ plane.	
	$Z_R = 4.0$ cases (a) $U_w = -1.0$ (b) $U_w = -0.5$	
	(c) $U_w = 0.0$ (d) $U_w = 0.5$ (e) $U_w = 1.0$	118
Figure 2.20	Neutral boundaries on $\alpha - \alpha_{CR}$ plane.	
	$U_w = -0.5$ cases (a) $Z_R = 4.0$ (b) $Z_R = 3.0$	
	(c) $Z_R = 2.0$ (d) $Z_R = 1.5$ (e) $Z_R = 1.3$	
	(f) $Z_R = 1.2$ (g) $Z_R = 1.1$ (h) $Z_R = 1.05$	120
Figure 2.21	Dispersion relationship for $Z_R = 3.0$	
	$U_w = 1.0$. (a) SVA solutions (b) SVB	
	solutions.....	124
Figure 2.22	Dispersion relationship for $Z_R = 1.05$	
	$U_w = -0.5$. (a) SVA solutions (b) SVB	
	solutions.....	126

Figure 2.23	The perturbation quantities. $Ri=0.3$ $\alpha=0.1$ $c=(0.108, 0.034)$ $Z_R=3.0$ $U_w=0.5$ case. (a) velocity fluctuation \tilde{w} (b) velocity fluctuation \tilde{u} (c) Reynolds stress τ (d) Displacement η128
Figure 2.24	The perturbation quantities. $Ri=0.4$ $\alpha=0.4$ $c=(0.517, 0.121)$ $Z_R=3.0$ $U_w=0.5$ case. (a) velocity fluctuation \tilde{w} (b) velocity fluctuation \tilde{u} (c) Reynolds stress τ (d) Displacement η130
Figure 2.25	Dispersion relationship of homogeneous case ($Ri=0.0$).....136
Figure 3.1	Determination of eigenvalues.....158
Figure 3.2	Velocity and density distribution of Model III.....164
Figure 3.3	Dispersion relationship for $Z_R=\text{inf.}$ case.....165
Figure 3.4	Dispersion relationship for $Z_R=3.0$ case.....166
Figure 3.5	Dispersion relationship for $Z_R=2.0$ case.....167
Figure 3.6	Neutral boundaries of $Z_R=1.5$ case.....168
Figure 3.7	Neutral boundaries of $Z_R=1.3$ case.....169
Figure 3.8	Neutral boundaries of $Z_R=1.2$ case.....170
Figure 3.9	Neutral boundaries of $Z_R=1.1$ case.....171
Figure 3.10	Neutral boundaries of $Z_R=1.0$ case.....172
Figure 3.11	Neutral boundaries of $Z_R=0.7$ case.....173

Figure 3.12	Relationship between lower layer thickness Z_R and phase velocity, growth rate.....174
Figure 3.13	The perturbation quantities of the flow. $\alpha=0.8$ $Ri=0.4$ $C_R=0.432$ $\alpha C_i=0.084$ $Z_R=3.0$ case (a) velocity fluctuation w' (b) velocity fluctuation u' (c) Reynolds stress τ (d) Displacement η (e) Turbulence energy ϵ175
Figure 3.14	The perturbation quantities of the flow. $\alpha=0.8$ $Ri=0.4$ $C_R=0.432$ $\alpha C_i=0.084$ $Z_R=2.0$ case (a) velocity fluctuation w' (b) velocity fluctuation u' (c) Reynolds stress τ (d) Displacement η (e) Turbulence energy ϵ177
Figure 3.15	The perturbation quantities of the flow. $\alpha=0.8$ $Ri=0.4$ $C_R=0.393$ $\alpha C_i=0.056$ $Z_R=1.0$ case (a) velocity fluctuation w' (b) velocity fluctuation u' (c) Reynolds stress τ (d) Displacement η (e) Turbulence energy ϵ179

Figure 3.16	<p>The perturbation quantities of the flow. $\alpha=0.8$ $Ri=0.4$ $C_R=0.371$ $\alpha C_i=0.011$ $Z_R=0.5$ case</p> <p>(a) velocity fluctuation w' (b) velocity fluctuation u' (c) Reynolds stress τ (d) Displacement η (e) Turbulence energy ϵ.....181</p>
Figure 3.17	<p>The perturbation quantities of the flow. $\alpha=0.8$ $Ri=0.4$ $C_R=0.370$ $\alpha C_i=-0.0016$ $Z_R=0.45$ case</p> <p>(a) velocity fluctuation w' (b) velocity fluctuation u' (c) Reynolds stress τ (d) Displacement η (e) Turbulence energy ϵ.....183</p>
Figure 3.18	<p>Stream lines of SVA and SVB solutions.....185</p>
Figure 3.19	<p>Velocity and density distribution of Model IV.....188</p>
Figure 3.20	<p>Dispersion relationship for density interface displaced case.....189</p>
Figure 3.21	<p>The perturbation quantities of the flow. $\alpha=0.6$ $Ri=0.4$ $C_R=-0.225$ $\alpha C_i=0.135$ $Z_R=3.0$ case</p> <p>(a) velocity fluctuation w' (b) velocity fluctuation u'</p>

	(c) Reynolds stress τ	
	(d) Displacement η	
	(e) Turbulence energy ϵ	190
Figure 4.1	Schematics of the apparatus.....	199
Figure 4.2	Laser optical set up.....	203
Figure 4.3	Block diagram of Laser Doppler Anemometry system.....	204
Figure 4.4	Block diagram of the wave detector.....	208
Figure 4.5	Wave detector output and processed data. (90.6.9(1) case. $\lambda^*=2.10$ cm, $C_R=3.20$ cm/sec.).....	209
Figure 4.6	Calibration of the conductivity- salinity sensor.....	211
Figure 4.7	Side view of the salt-wedge and wave phenomena.....	220
Figure 4.8	Three-dimensional structure on the salt wedge.....	221
Figure 4.9	Secondary flow structure in the channel (40 cm from mouth, total depth=7.0 cm, salt water depth=2.0 cm, $\rho_2=1.032$ g/cc. case).....	222
Figure 4.10	SVA waves in the flume (quasi- equilibrium region).....	223
Figure 4.11	Definition of the characteristic length and velocity scale.....	224
Figure 4.12	Non-dimensionalized velocity profiles.....	225

Figure 4.13	Conductivity profile as output voltage. (at 80 cm from river mouth and 2.0 cm from left wall).....	226
Figure 4.14	Typical velocity profiles and velocity fluctuations (a) stable case (90-7-16 data, Ri=1.42) (b) SVB case (90-7-31 data, Ri=0.91 C _R =-0.870) (c) SVA case (90-8-02 data, Ri=0.94 C _R =0.260).....	233
Figure 4.15	α -Re relationship.....	234
Figure 4.16	Re-Z _R relationship.....	235
Figure 4.17	α - α C _R relationship.....	236
Figure 4.18	α -Ri relationship.....	237
Figure 4.19	Ri-Z _R relationship.....	238
Figure 4.20	Re-Ri relationship.....	239
Figure 4.21	Non-dimensionalized velocity profile (with non-zero d approximation).....	244
Figure 4.22	Displacement effects on the Richardson number Ri and wave number α	251
Figure 4.23	Displacement d and the lower layer thickness Z _R	252
Figure 4.24	Density difference v.s. characteristic length and velocity scales.....	252
Figure 5.1	Adopted stability diagram of primary three-dimensional instability from Smyth & Peltier (1990). (R=3.0, Pr=9.0 case).....	260

Figure C.1 Wave detector output and processed
data example. (90.6.9(1) case.
 $\lambda^*=2.10$ cm, $C_R=3.20$ cm/sec.).....307

LIST OF TABLES

Table	4.1	LDA system setting.....	206
Table	4.2	Significant details of the experiments	227
Table	4.3	Re-calculated parameters of the experiments.....	245

LIST OF SYMBOLS

A_j	Coefficient of variable ($j=1,2,3,\dots$)
a_j	Coefficient of variable ($j=1,2,3,\dots$)
a_{jk}	Elements of eigen matrix ($j,k=1,2,3,\dots$)
B_j, B_j'	Coefficient of variable ($j=1,2,3,\dots$)
C	Complex phase velocity
C_R	Real part of complex phase velocity
C_I	Imaginary part of complex phase velocity
c.c.	Complex conjugate
D	Total depth of the channel
d	Displacement between density interface and center of shear layer
D_R	Real part of determinant
D_I	Imaginary part of determinant
D_{int}	Depth of the density interface
\hat{e}_1	Unit vector of longitudinal direction
\hat{e}_2	Unit vector of lateral direction
\hat{e}_3	Unit vector of vertical direction
F	Focal length of lens
f	Arbitrary function
f_D	Doppler shift frequency
\mathbf{F}	Body force
g	Gravitational acceleration
g_*	Non-dimensional gravitational acceleration
h	Shear layer thickness ($=2L$)
i	Square root of -1

$Im(f)$	Imaginary part of f
K_j	Modification coefficient for re-orthogonalization ($j=1,2,3,\dots$)
L	Characteristic length scale
\mathbf{M}	Eigen matrix
p	Pressure
P_T	Total pressure
P_H	Hydrostatic pressure
P_W	Pressure due to the wave motion
P_0	Mean Pressure
Pr	Prandtl number
R	Hazei's thickness parameter
Re	Reynolds number
R_j, R_j^*	Coefficient of variable ($j=1,2,3,\dots$)
Ri_c	Critical Richardson number
Ri_L	Local (gradient) Richardson number
Ri_o	Over-all Richardson number
$rms(f)$	Root mean square of quantity f
U	Longitudinal velocity
U_0	Mean longitudinal velocity
U_1	Velocity of upper layer
U_2	Velocity of lower layer
U_w	Velocity on the rigid boundary
\tilde{u}	Deviation of longitudinal velocity from mean
V	Characteristic velocity scale
\mathbf{V}	Velocity vector ($= (u, v, w)$)
V_{int}	Velocity of the density interface

\tilde{v}	Deviation of lateral velocity from mean
\tilde{w}	Deviation of vertical velocity from mean
x	Distance from the mouth
x	Longitudinal co-ordinate
y	Distance from the left wall of the channel
y	Lateral co-ordinate
z	Vertical co-ordinate
α	Wave number of small perturbation
ΔC_R	Calculation step of C_R
ΔC_I	Calculation step of C_I
$\Delta\rho$	Density difference between two layers
δ	Thickness of density transition layer
ϵ	Turbulent kinetic energy
γ	Specific weight
$\tilde{\phi}$	Stream function of perturbation field
η	Interface displacement due to wave motions
λ	Wave length of the interfacial waves
λ_L	Wave length of the laser light
ν	Kinematic viscosity
θ	Argument of complex variables
θ_L	Crossing angle of laser beams
ρ_0	Mean density
ρ_1	Density of upper layer
ρ_2	Density of lower layer
ρ_{AV}	Average density
τ	Reynolds stress averaged over wave length
ω	Complex frequency

ξ Integral variable

f^* In superscript, complex conjugate of f (in part four, it indicates dimensional quantity of f)

' In superscript, ordinary derivative in terms of z

[] "jump" bracket

INTRODUCTION

Understanding of instability phenomena of density stratified flows is very important in a broad range of scientific disciplines including Meteorology, Oceanography and several branches of Engineering. Instability phenomena are considered to be key mechanisms in the transition from laminar to turbulent flow and in various mixing phenomena. Much of the existing knowledge comes from work in Atmospheric and Oceanographic science where experimental verification is extremely difficult.

Investigation of estuarial salt wedges offers promise for improving understanding of the role of instability phenomena in mixing processes. Estuarine salt wedges can, in nature, exhibit relatively stable mixing zones that facilitate experimental and field investigation. Salt wedges in steep estuaries with low tidal range and a constant fresh water discharge exhibit these stable characteristics.

Needless to say, the hydrodynamic elements of such a system are best studied in laboratory experiments. Although laboratory experiments have some disadvantages such as channel size and Reynolds number limitation, they do show significant details of salt wedge hydraulics and are quite adequate for examining the relationship between mixing and interfacial wave phenomena. Many attempts have been made to interpret this phenomenon in terms of a shear instability mechanism; however, they fail to give enough accuracy,

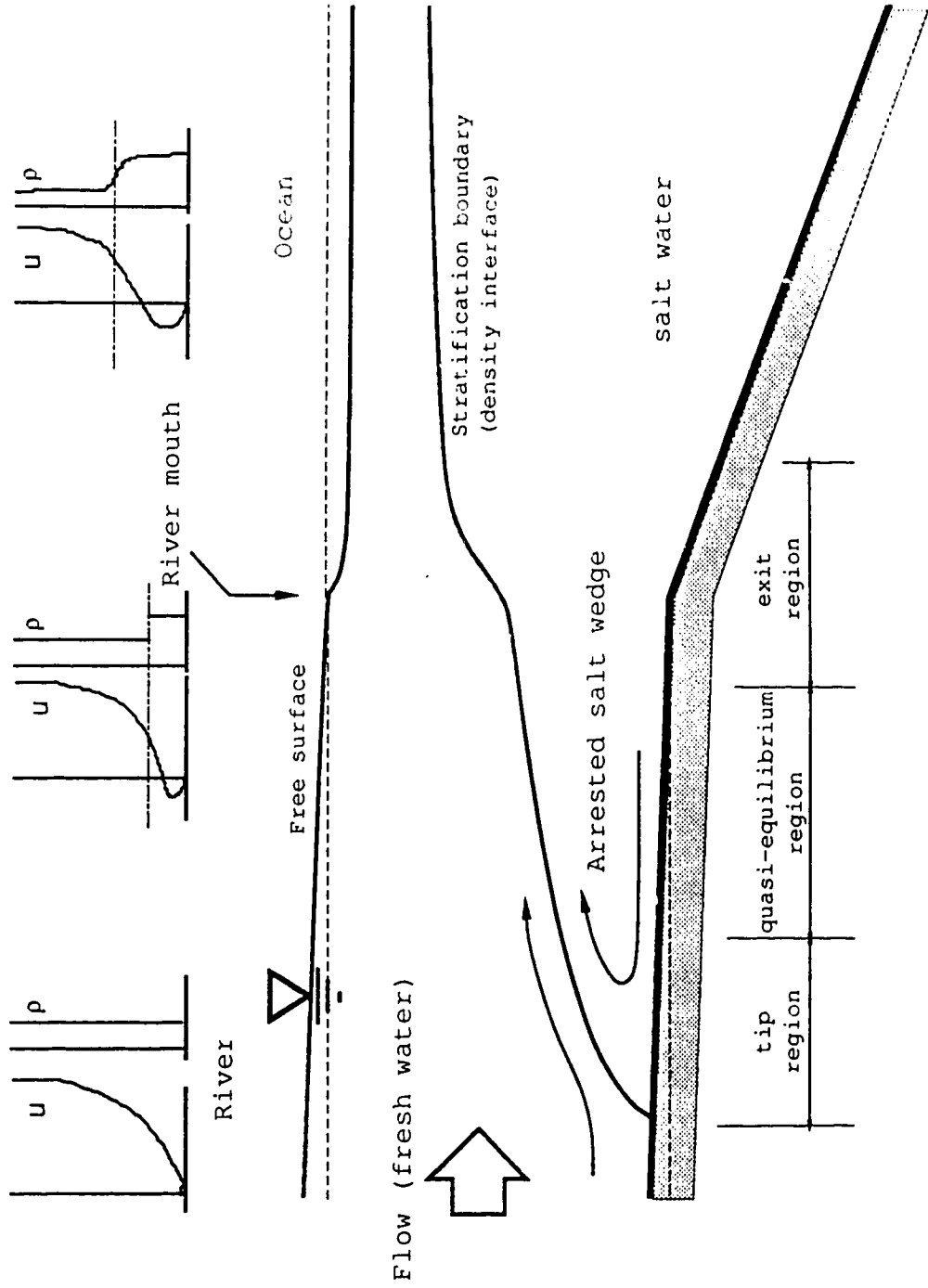
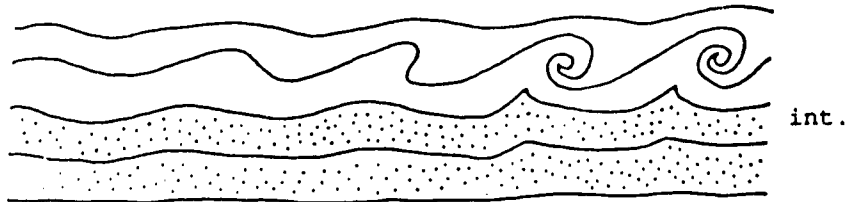
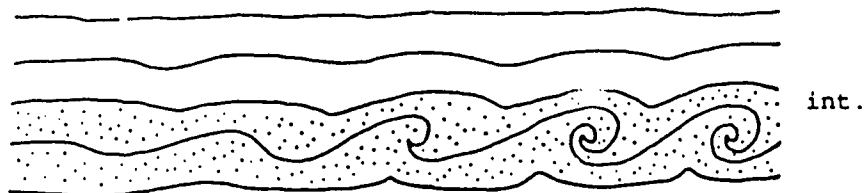


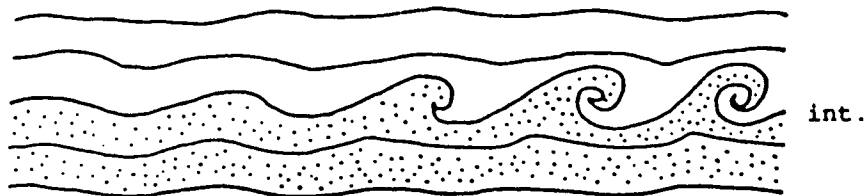
Figure 1. Schematics of the (arrested) salt wedge and its typical velocity and density profiles



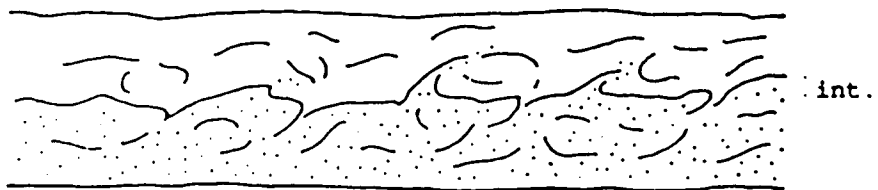
(a) SVA (Spiral Vortex Above the interface) waves.
(Holmboe mode with positive phase velocity $Cr > 0.0$)



(b) SVB (Spiral Vortex Beneath the interface) waves.
(Holmboe mode with negative phase velocity $Cr < 0.0$)



(c) SVC (Spiral Vortex the Center of which coincides
with the interface) waves. (Kelvin-Helmholtz mode)



(d) Breaking and mixing.

Figure 2. Classification of typical interfacial phenomena and waves.

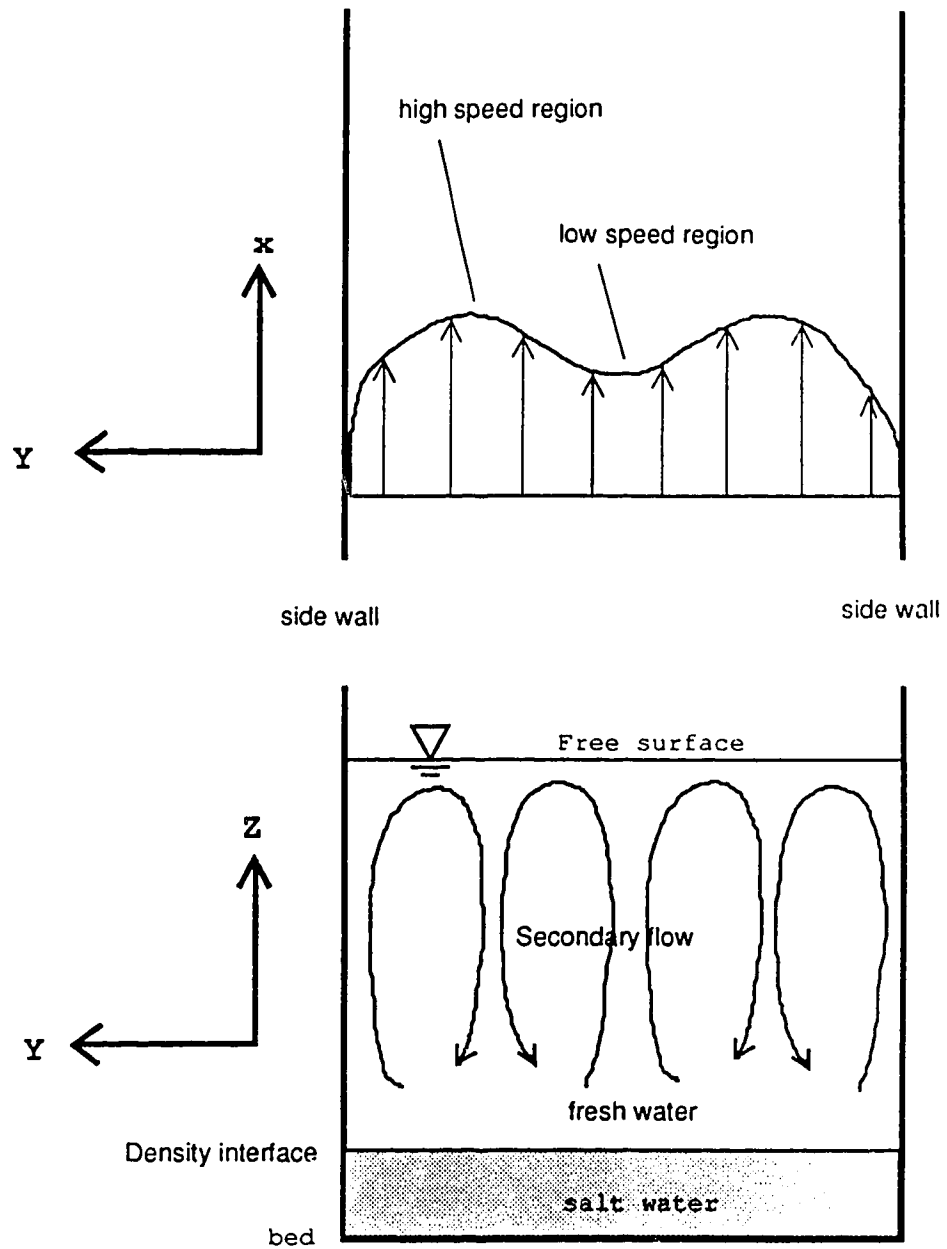


Figure 3. Three dimensional flow structure of salt wedge flow due to the secondary flow in channel.

especially if three-dimensional wave structures exist on the density interface, due mainly to the lack of appropriate models.

From previous knowledge, typical salt wedge flow and its interfacial forms can be summarized as Figure 1 and 2. Velocity and density profiles are often approximated by $\tanh(z)$ and step functions, respectively, which have excellent agreement with experimental observations. Also it was found that secondary flow structures similar as the open channel flows exist on most of the salt wedge flow experiments. This flow structure often creates spanwise velocity distribution which is recognized as high and low speed regions in fresh water layer (Figure 3).

By investigating previous knowledge, relatively weak areas are identified as follows:

Problem (i): Separation of two different type of waves (SVA and SVB) were observed and this phenomenon is called 'one-sidedness'. Present knowledge of stability may explain some stabilizing effects of the rigid boundary conditions, but does not explain the separation of these two waves.

Problem (ii): Previous experiments show that a salt wedge can be divided into three sub-divisions based on their stress distributions. In each region, velocity profiles can be approximated very well by a $\tanh(z)$ function, although the inflection points are often displaced with respect to the density interface. These displacements cause some problems

when applying existing hydrodynamic stability theories to the salt wedge.

Problem (iii): Due to the secondary flow structures in channels, high and low speed regions develop which may cause three-dimensional interfacial wave structure. However, few experimental data are available in the case of salt wedge flow, making it difficult to determine the implications of this phenomenon.

The objective of this study is to obtain a better understanding of the mechanisms of this interfacial wave phenomenon by investigating in an appropriate fashion the hydrodynamic stability of the flow field and then verifying these results by carefully assembled experiments. In this study, experimental and theoretical research will first be reviewed. The subsequent parts of this study will analyse each weak area by using theoretical, numerical and experimental approaches. Theoretical models will employ an inviscid two-dimensional two-layered stratified flow system with appropriate boundary conditions. Numerical study will be applied to two-layer viscous flow with continuous velocity profiles, and detailed experiments will be performed in order to verify these studies.

1. PART ONE: REVIEW OF THE PRESENT KNOWLEDGE

1.1 INTRODUCTION

Experimental and mathematical investigations of salt wedge flow have been performed intensively since World War II because of its high economic and environmental impacts. From a hydrodynamic point of view, this flow is also interesting since it is essentially laminar-turbulent transition flow with density stratification, which is related to various phenomena in the atmosphere and ocean (such as mixing, waves, fluctuations of its properties etc).

However, despite such high demands from engineering, public policy and science, present knowledge is still quite limited due mainly to the complexity of the flow system (for example, tide effects, geometrical limitation of modelling, scale effects, strong non-linearity and time dependence). Until now, two major approaches have been utilized by researchers to understand this flow.

The first approach involves evaluation of the salt wedge using macroscopic parameters to predict overall properties such as entrainment, interfacial friction factor, general wedge shape, total intrusion length, the strength of salt circulation etc. Although relatively good agreements were obtained with this approach, particularly through laboratory experiments, the physics of the salt-wedge is still not so well understood.

Another approach is to pay great attention to the microstructures of the mixing phenomena at or through the density interface in the hope of improving the accuracy of prediction for various applications. However, achievements in this direction are still primitive.

In this study, we will employ this second approach to improve our understanding of mixing phenomena in the salt wedge. The hydrodynamic stability theory and interfacial waves are assumed to be dominant mechanisms of mixing, and applicability of those ideas will be discussed through the experiments.

In this section, we will first briefly review the overall properties of salt wedge experiments and then we will inspect the previous experimental research on the interfacial wave phenomena. Based on this microscopic approach, mathematical and numerical research will be discussed in order to identify relatively weak areas and the associated reasons.

1.2 REVIEW OF EXPERIMENTAL INVESTIGATIONS

1.2.1 Introduction

While any predictive model should be formulated on the basis of the underlying physical principles, the present state of understanding of density-stratified flow is so limited that a good deal of empirical information must be used in model development. Laboratory experiments clearly provide the most comprehensive observational detail, mainly because of their high reproducibility.

In the following subsection, several experimental works on salt wedge flow will be reviewed, paying particular attention to interfacial waves and mixing aspects.

1.2.2 Salt Wedge Experiments

Figure 1.1 summarizes the general overall shape of the salt wedge obtained by experimental observations. Sargent & Jirka (1987) suggested a longitudinal subdivision of the wedge into three regions: the tip region, the quasi-equilibrium region, and the exit region. The tip and exit regions have a highly variable force distribution resulting from adjustments in the internal stress distribution (tip) and vertical accelerations caused by a non-hydrostatic pressure distribution (exit). In practice, it was pointed out that both regions are relatively short (on the order of several water depths) and the quasi-equilibrium region is the

controlling factor for the overall dynamics of the salt wedge.

The density and velocity distributions in the vertical direction are also shown in Figure 1.1. The thickness of the variable density layer is about 1/10 to 1/15 that of the velocity profiles. Therefore, it is commonly accepted that the flow may be vertically divided by the density interface (the 50% point between maximum and minimum density, usually also coincident with the maximum gradient point) into an upper layer and lower layer (the so-called 'two-layer(ed) stratified flow' approximation).

Velocity profiles are often approximated by $\tanh(z)$ or $\text{erf}(z)$ functions due mainly to their mathematical convenience, and acceptable matching with observations. Although there have been several theoretical investigations to determine the velocity distributions based on boundary layer theory, the derived very high order (8th and 9th) polynomial functions do not seem to provide sufficient improvement to justify such a complicated mathematical treatment (see Keulegan 1944). Therefore, the general trend is to approximate the velocity profile using a $\tanh(z)$ function, particularly for upper layer profiles. On the other hand, since the lower layer typically shows reverse flow due to the mass balance in cases of an 'arrested' salt wedge, a second order polynomial function is commonly employed for the velocity approximation, based on width-averaged volume conservation.

In the quasi-equilibrium region, it is generally observed that the inflection point of velocity profiles coincides with its density interface level. By contrast, the tip and exit regions show significant displacement of the velocity inflection points from the density interface due to their stress distributions. This displacement can reach about 20% to 30% of the shear layer thickness; as will be explained later, the conventional hydrodynamic stability theory is not applicable for these cases. Details of the overall flow properties can be found in many papers and articles such as Schijf & Schonfeld (1953), Kaneko (1966), Keulegan (1966), Suga & Takahashi (1976), Grubert (1980), Arita, Jirka & Tamai (1986) and Arita & Jirka (1987). All of these indicate that the dynamics of a salt wedge is strongly related to the interfacial wave phenomena schematically illustrated in Figure 1.2 (which was produced from photographs using visualization technique).

Generally, interfacial waves first form at a distance of about 20 to 30 cm (which is approximately 15 to 20 times longer than shear layer thickness) from the wedge tip and then persist over the main region of the wedge. The predominant waves propagate downstream (see Figure 1.2) and are somewhat irregular in shape with a cusp-like structure as shown in Figure 1.3. (flow pattern (I)). The high vorticity concentrations existing above these interfacial waves can be visualized by injecting dye just above the density interface. As the interfacial wave passes downstream, another type of

1.

wave appears. This wave is generally moving upstream with a very small phase velocity and its shape looks anti-symmetric to other waves with respect to the density interface. These two types of waves eventually interact with each other and induce mixing by ejecting eddies from their crests into both the upper and lower layers (see wave pattern (II)).

Around the exit region, wave amplitudes increase drastically and strong mixing occurs. Waves in this region propagate with almost the same velocity as the density interface velocity, and eventually the interface itself starts rolling up.

Nishida & Yoshida (1984) classified these interfacial phenomena into the four groups shown in Figure 2 in previous section. The flow direction of upper layer is from left to right, and the lower layer flows in the opposite direction. They named the interfacial waves caused by strong vorticity concentration above the interface as "SVA waves"; these have been recognized as fast-propagating predominant waves on the salt wedge by several researchers (each of them given different names, such as wave I by Hino & Hung (1982)). Another commonly observed wave is the SVB wave, due to vorticity concentration below the interface, propagating in the opposite direction to SVA waves (called wave II by Hino & Hung). Although these two waves are identified as Holmboe modes in the Hydrodynamic stability theory, their properties still provoke many questions particularly in a complicated system such as the salt wedge.

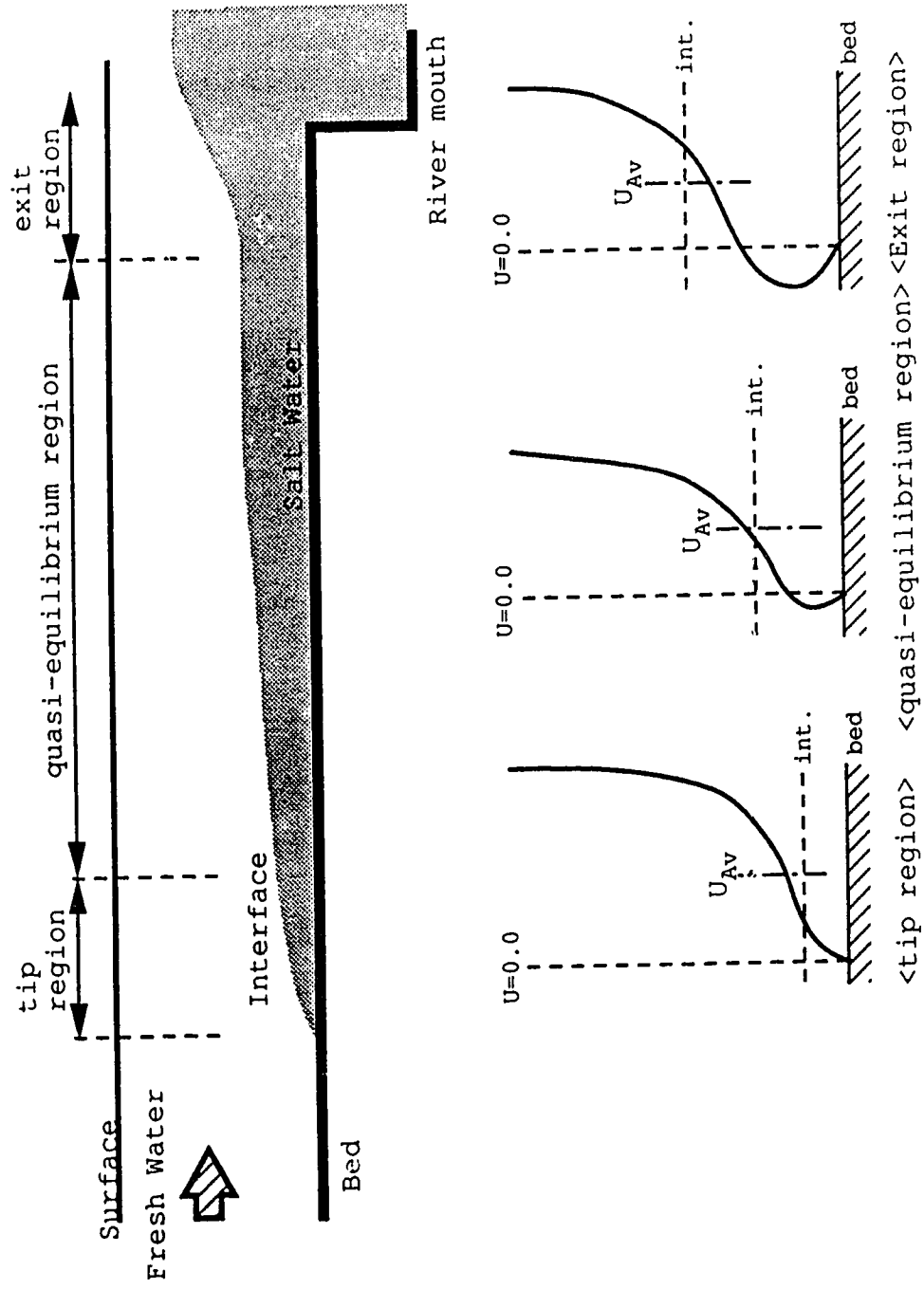


Figure 1.1. Schematic structure of salt wedge with three major hydrodynamic regions and its typical velocity profiles

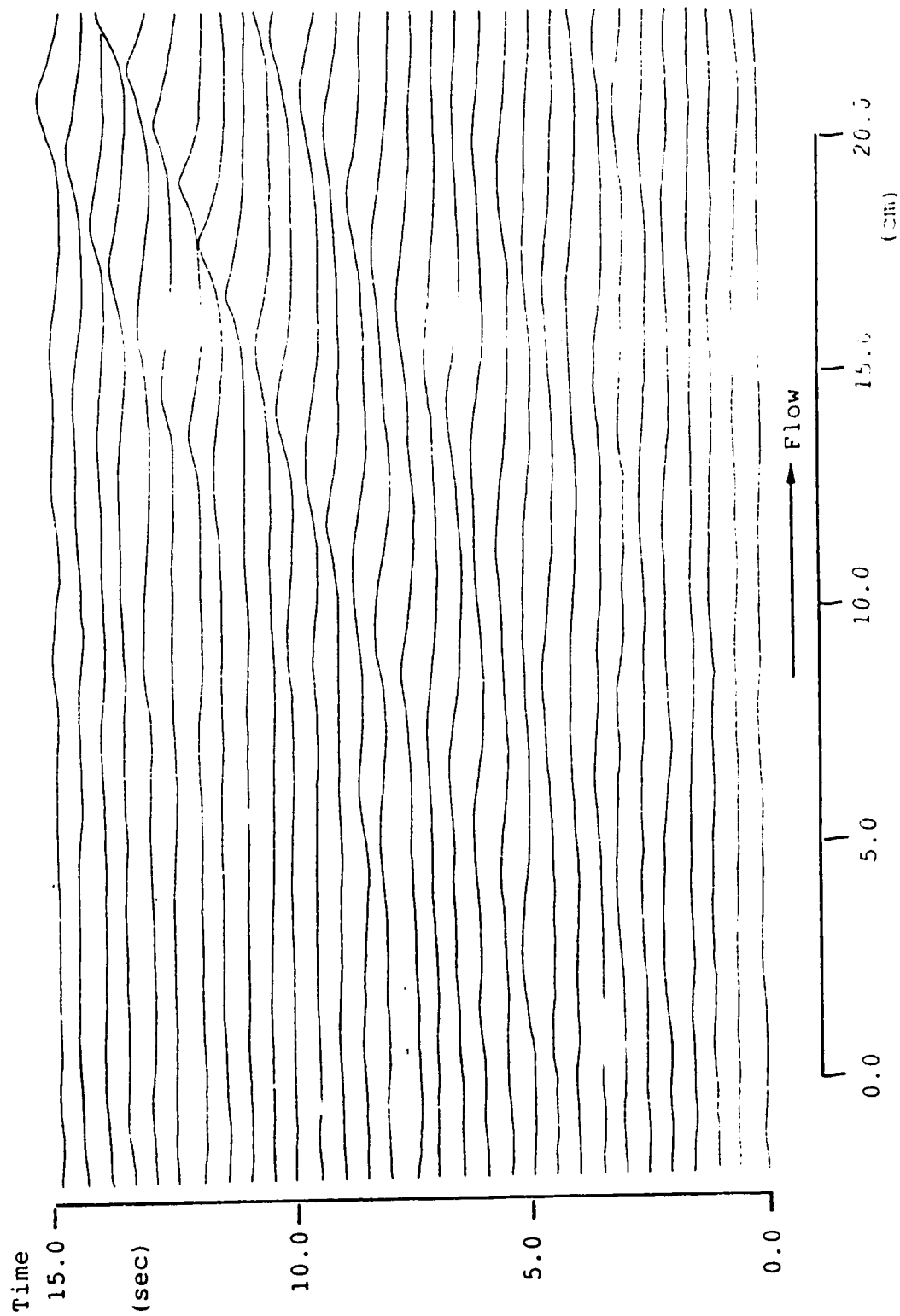


Figure 1.2.SVA wave trains

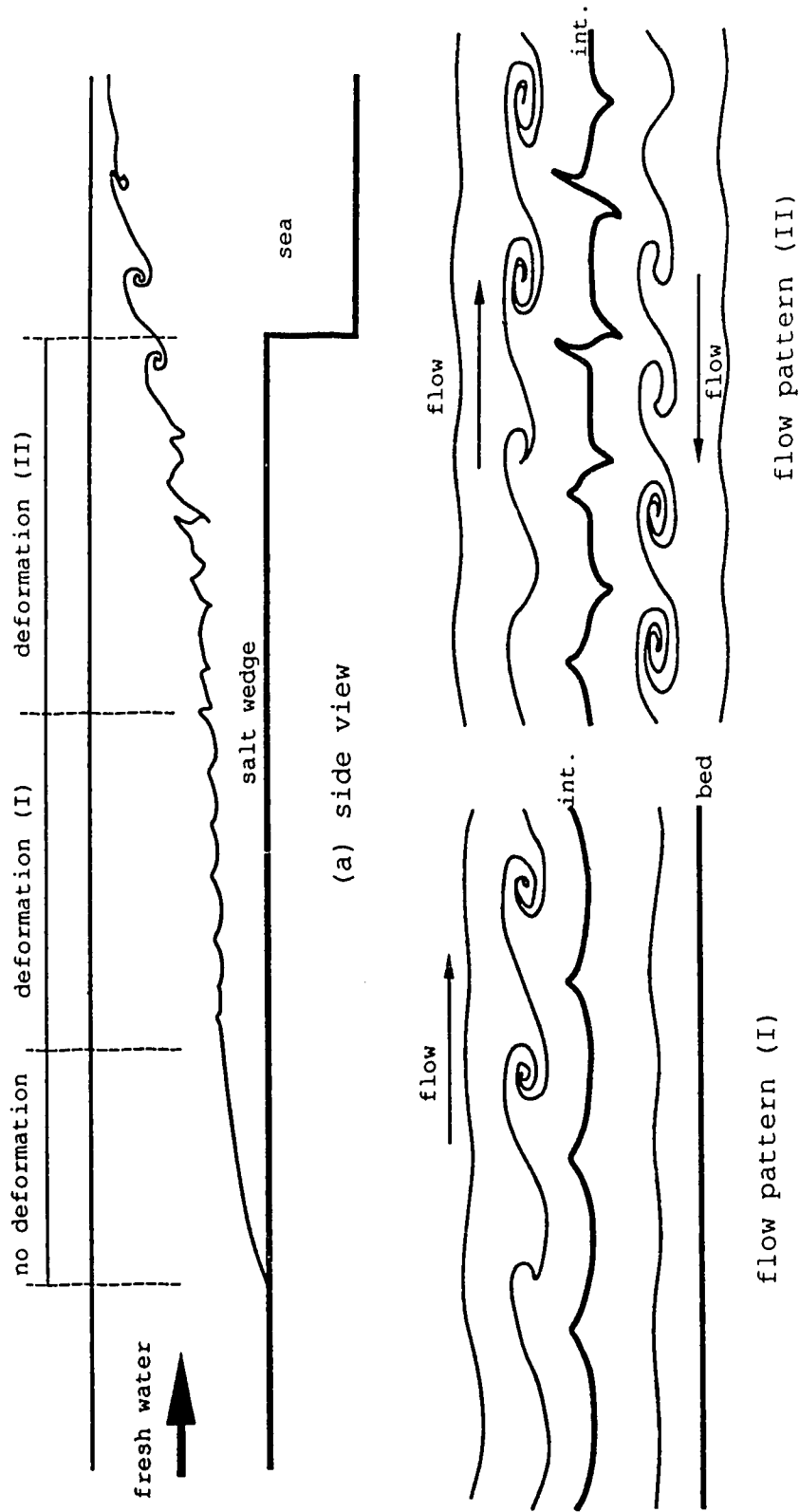


Figure 1.3. Schematics of wave phenomena on the salt wedge

In the exit region, as was mentioned before, a third type of wave is observed, named SVC waves here. These are believed to be caused by a mechanism very similar to the well-known Kelvin-Helmholtz (K-H) instability mechanism. In fact, this type of flow represents the first successful application of stability analysis to actual flow systems in nature.

The fourth pattern is found in more turbulent, well developed flow and often has a smaller density gradient at the density interface level.

This classification is very convenient, especially for salt wedge flow, because of the different names for two Holmboe modes moving in upstream and downstream directions. Therefore, we will follow this Nishida & Yoshida's naming for the rest of this study.

In the next sub-section, experimental work related to these first two Holmboe modes (i.e. SVA and SVB waves) will be reviewed, in order to understand the basic mixing mechanism on the salt wedge.

1.2.3 Interfacial Waves and Instabilities

The earliest experiments which considered stability were performed by Keulegan (1949). His model was designed to investigate the relationship between global (overall) flow properties and the wave mixing phenomena of two layer stratified flow. Figure 1.4 shows schematics of his

apparatus and a sketch of the observed interfacial mixing process. Regardless of discharge variation and initial density differences, the fundamental mixing mechanisms found in these systems were identical: waves always had a sharp crest towards the upper side, and the mechanism of mixing was an ejection of eddies from the crests into the moving current as shown in Figure 1.4. At the time of Keulegan's work, however, this type of instability could not be explained theoretically, making it very difficult to explain this phenomenon. Even with present knowledge of Holmboe instabilities, which provides additional unstable modes in stratified flow, this phenomenon is not clearly understood, since only one type of wave was found in the flow instead of a pair of SVA and SVB waves as predicted by Holmboe (1962). This phenomenon, namely isolation of a single mode, was later found in several experiments, and was called 'one-sidedness' by Maxworthy & Browand (1975).

Although Keulegan's experiments do not provide enough information (such as vertical velocity and density distributions) to evaluate the flow stability using present knowledge, his results clarify the most fundamental mixing mechanism on the salt wedge.

Since the discovery of these additional unstable modes, new experimental data on the Holmboe instability has been quite sparse, despite theoretical and mathematical investigations. This is probably due to the fact that stratification in the atmosphere and ocean has relatively

small density gradients and under such conditions, K-H instability usually has larger growth rates than Holmboe modes. Qualitative investigations and observation of non-linear evolutions of these Holmboe modes was performed experimentally by Browand & Wang (1972), and Browand & Winant (1973). Figure 1.5 shows their experimental set-ups and typical velocity and density profiles. It was found that the overall Richardson number (defined as $Ri = g\Delta\rho h / \rho(\Delta U)^2$ where $\Delta\rho$ and ΔU are density and velocity differences across the shear layer, respectively) varied from 0 to approximately 2.0 as the flow progressed downstream and tended to be stable after a certain distance from the splitter plates. This fact indicates the existence of a critical Richardson number for stability which could not be found using inviscid theory. Although the experiments were intended to investigate mainly strong non-linear evolutions of waves and vortex pairing, which are essential causes of mixing, some aspects are applicable to salt wedges particularly in the region where SVA and SVB waves interact.

Besides the 'one-sidedness' problem, three-dimensional structures of waves and flow are another phenomena still not well understood. Figure 1.6 shows a typical flow pattern observed in a relatively wide open channel (This photograph was taken by Yonemitsu (1986) using dyed thread visualization method): it can be seen that there are high and low speed regions in the lateral directions. The predominant waves (SVA) tend to be highly three-dimensional under this

circumstance, with several wave crest/troughs typically appearing across any wedge section in the high-speed regions of flow. The number of such lateral waves seem to be strongly affected by channel cross-section aspect ratios. There is some research that suggest this three-dimensional structure, particularly in the fresh water layer, is related to the channel secondary flows (Tashiro, Yoshida and Yoneya (1983), Yonemitsu (1986) etc). Visualization indicates that high speed regions tend to have higher shear stress at the interface: therefore, it is understandable that SVA waves are observed more often in these regions. On the other hand, SVB waves always appear in the low speed region where there is stronger back flow and lower interfacial shear stress; a fact which cannot be explained by our present knowledge of stability theory. This fact implies that wave properties may not be predicted accurately using width averaged quantities. Thus, more intensive and precise experiments with consideration of such three-dimensional flow structures must be performed in order to understand the mechanisms of interfacial wave phenomena. In the next sub-section, mathematical treatments of the interfacial wave phenomena will be reviewed.

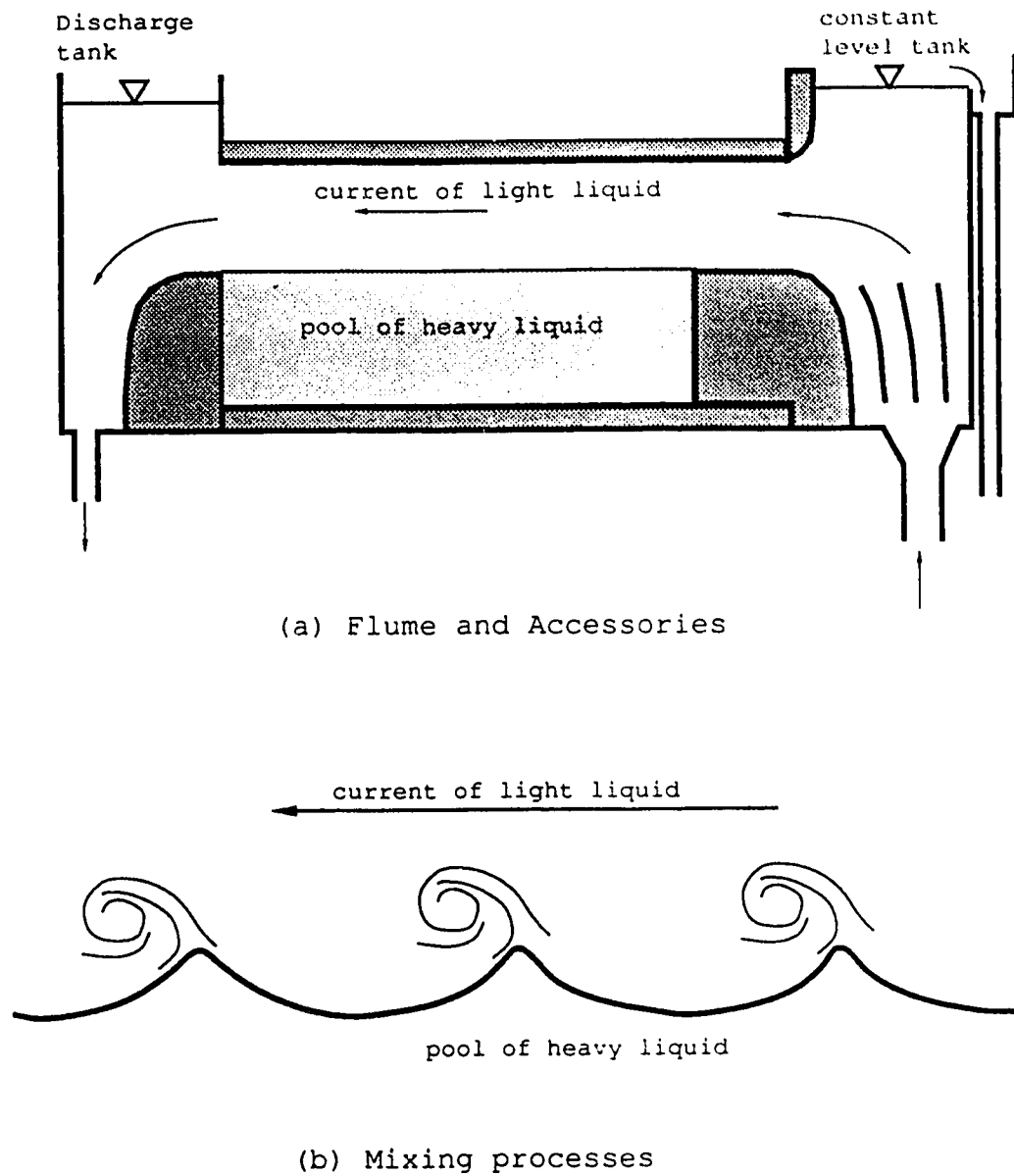
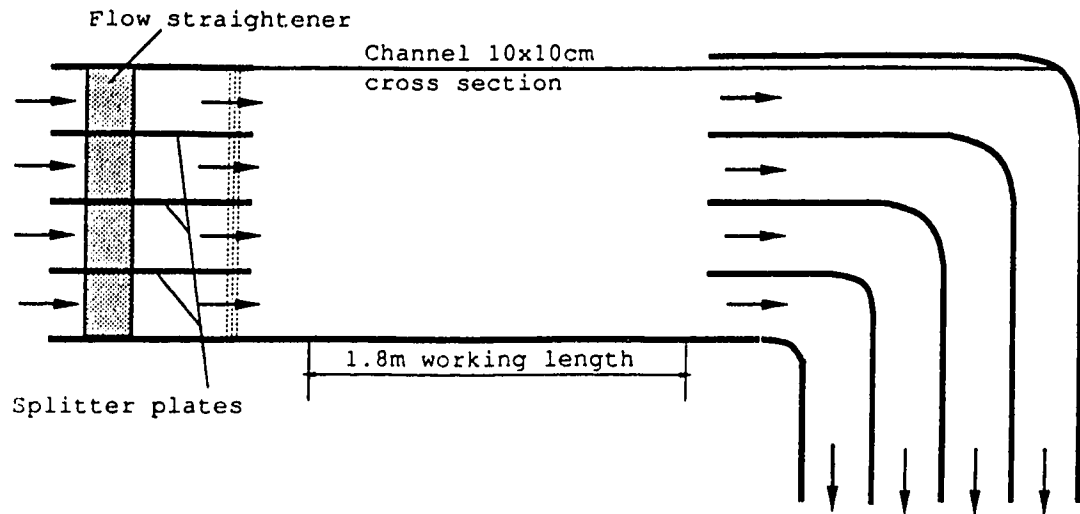
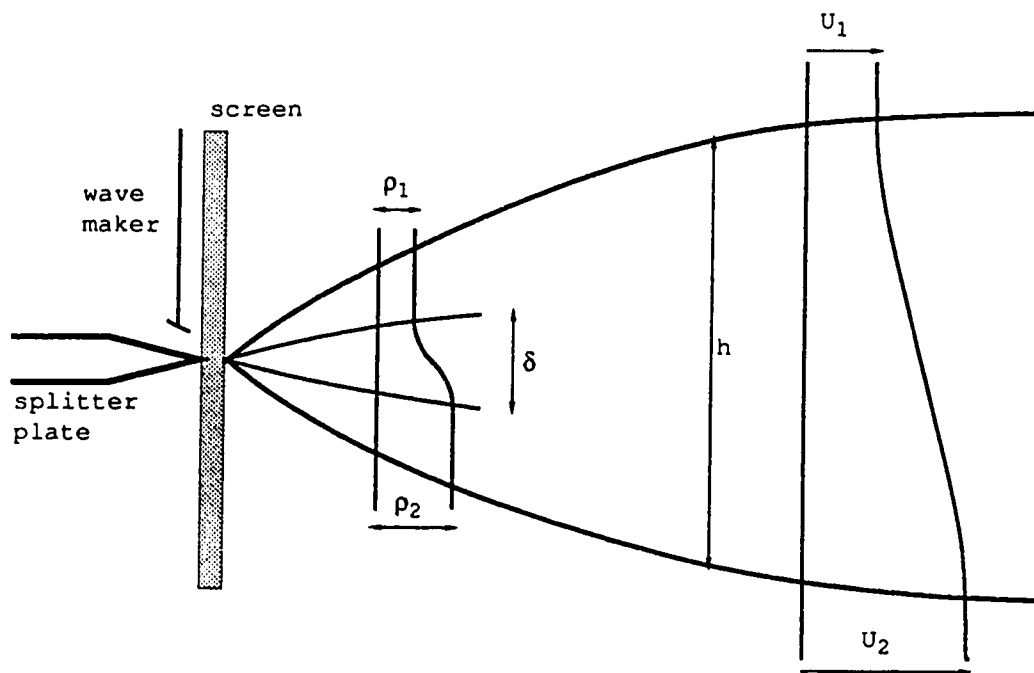


Figure 1.4. Schematics of experimental flume and process of mixing described by Keulegan (1949)



(a) side view of water channel



(b) Density and velocity distributions

Figure 1.5. Adopted schematic of stratified flow experiment of Browand and Winant. (1973)



Figure 1.6. Velocity distribution of upper layer fluid in the lateral direction (channel dimension of cross section is 50x10 cm, visualized about 1cm above the density interface by dye injection method).

1.3 MATHEMATICAL MODELS OF INTERFACIAL WAVES

1.3.1 Introduction

As was mentioned in a previous section, it may be reasonable to treat the arrested salt wedge as two layer stratified flow without mixing at or through the density interface (Schijf & Schonfeld (1953)). This type of treatment is also common in many other areas of fluid dynamics in order to explain a variety of phenomena in the ocean and atmosphere.

Natural bodies of fluid such as the atmosphere, oceans and lakes are characteristically stably stratified. When they are disturbed in any way, internal waves are generated. This wave phenomenon and the generation mechanism have attracted the interests of many researchers since the middle of 19th century. One of the reasons is that this phenomenon is regarded as a primary mechanism of laminar-turbulent flow transition and, therefore, is expected to explain phenomena ranging from temperature fluctuations in the deep ocean to the formation of clouds in the lee of mountains. Because of such a wide variety of applications, intensive research has been performed in the areas of Oceanography, Meteorology and Applied Mathematics. Despite the early research attempts, dramatic progress towards understanding this phenomena has only been accomplished in the last 30 years due mainly to the development of computer and numerical schemes. Examples of books where the mathematical details of the linear stability

theory can be found are Chandrasekhar (1961), Betchov & Criminale (1967), Turner (1973), LeBlond & Mysak (1978), and Drazin & Reid (1981).

In this section, the stability analysis of two-layer and quasi-two-layer systems will be reviewed specifically from the salt wedge application point of view. The review will start with simple two layer inviscid two-dimensional models with piece-wise linear velocity profiles, and then proceed to more complicated systems employing viscosity-diffusivity effects and various boundary conditions. Finally, some of the latest three-dimensional instability theory and its numerical results will also be referred to.

1.3.2 Hydrodynamic Stability

Stability can be defined as the quality of robustness. This idea has been applied widely to mechanical, astronomical and electrical systems which have only a few discrete degrees of freedom. In the study of a continuous medium such as a fluid, however, the number of degrees of freedom is infinite and the question becomes substantially more difficult. In particular, the basic equations take the form of a system of nonlinear partial differential equations. In spite of the additional complications, progress toward an understanding of such system is made with the use of linearized approximations and by appropriately extending the theory developed for discrete systems.

Such a mathematical treatment of stability to explain the waves and mixing mechanism was initiated by Helmholtz (1868) and Kelvin (1871). The velocity and density profiles which they investigated are shown in Figure 1.7. It was found that one unstable wave mode which is $C_R=0.0$ can exist in the system. This wave mode is now called 'Kelvin Helmholtz' (K-H) instability. Although Figure 1.8 shows a typical K-H instability observed in the atmosphere as a cloud formation, field investigations by Woods (1968), Atlas et al. (1970), Gossard et al. (1971), Gossard (1974) and Garrett & Munk (1979) also support the existence of this wave mechanism.

In a two-layer system such as the salt wedge, however, two additional unstable waves which are $C_R \neq 0.0$ with completely different features from K-H instability have been found. These modes are actually dominant waves for the mixing mechanism in the salt wedge; as was mentioned in a previous section, much research has been performed on these waves. Holmboe (1962) found these additional modes by employing a simple two-layer piece-wise linear velocity profile model with so-called 'symmetric wave analysis', and Hazel (1972) obtained details on the structure of these modes through numerical analysis.

Hazel's model utilized continuous velocity and density profiles which were approximated by $\tanh(z)$ functions. The details of these works can be found by reviewing articles by Drazin & Howard (1966), Thorpe (1973), Howard & Maslowe (1973) and Drazin & Reid (1981).

The velocity profiles, density profiles and stability diagrams obtained by Holmboe are shown in Figure 1.9, where α is the wave number, non-dimensionalized by the shear layer thickness d , and Ri_0 is the overall (global) Richardson number defined as follows:

$$Ri_0 = \frac{1}{2} g d \left(\frac{\rho_2 - \rho_1}{\rho_1 + \rho_2} \right) / U^2$$

According to this diagram, it can be seen that unstable modes (called 'over-stability' by Holmboe in order to distinguish these additional dispersive mode from K-H modes, and now these modes are generally called Holmboe modes) are limited to a narrow wave number band which extends to $Ri_0 = \infty$.

The same types of solution were obtained by Hazel numerically using more realistic velocity and density profiles (Figure 1.10 and 1.11). He investigated the flow stability by varying the ratio between shear layer thickness and density transition layer thickness, and helped clarify the relationship between K-H modes and Holmboe modes. To perform a comparison with other two-layer models, it is necessary to modify the solutions, as is shown below, since Hazel's model employed slightly different characteristic scales,

$$\rho_1 = \bar{\rho} \exp \left(- \frac{\sigma}{R} \right), \quad \text{at } y = \infty,$$

$$\rho_2 = \bar{\rho} \exp \left(\frac{\sigma}{R} \right), \quad \text{at } y = -\infty, \text{ and}$$

$$1 - \frac{\rho_1}{\rho_2} = 1 - \gamma = 1 - \exp\left(-\frac{2\sigma}{R}\right)$$

Then,

$$\sigma = -\frac{R}{2} \log \gamma \approx \frac{R}{2} (1 - \gamma), \quad \text{when } 1 - \gamma \ll 1.$$

Therefore,

$$Ri_{Hazel} = \frac{\gamma gh}{v^2} \approx \frac{R \epsilon gh}{2v^2} = \frac{R}{2} Ri_{Holmboe}.$$

Using this conversion, Hazel's solutions give very good agreement with Holmboe's solutions when $R > 5.0$. Although Nishida & Yoshida (1990) pointed out that Hazel's solution for K-H modes disappear asymptotically as R becomes larger (equivalent to the two layer modelling) Hazel's model provides an excellent explanation of the instability mechanism for Holmboe modes. Since it is still not clear just what is the reason for this mismatching between two-layer and continuous density model results, further investigation is required.

1.3.3 Viscosity Effects on Stability

Despite the excellent results of Hazel's calculations, his model could not explain some observed facts such as the presence of a critical value for the overall Richardson number (with regards to instability) and a Reynolds number dependency. Naturally, the next step in stability analysis was to include the viscosity and diffusivity effects into the governing equations (this was particularly necessary for gradually varying stratified flow). Since high Richardson

number flow shows extremely small growth rates in the inviscid models, it is expected that consideration of the viscosity for such systems may decrease growth rates to the point that the flow is stabilized and thus induce the critical Richardson number.

The governing equations were derived by Orr (1906) and Sommerfeld (1908) for the case of viscous flows, and by Koppel (1964) for viscous-diffusive systems. These equations are 4th and 6th order ordinary differential equations respectively, and their mathematical behaviour has been extensively investigated. If the velocity and density profiles such as those of Hazel and Holmboe are used, the solutions become very complicated and the problems must be solved numerically. Maslowe & Thompson (1971) and Miller & Gage (1972) performed this numerical analysis for the 6th order governing equations based on Hazel's velocity and density distributions (see Figure 1.12). It was found that the effects of viscosity on stability was relatively small and the neutral boundaries did not change except for very low Reynolds number flows ($Re < 150$). This result is similar to results obtained by Lessen (1950) and Gotoh (1971) for the homogeneous case. For a salt wedge, the range for Reynolds number is around $50 < Re < 300$ and it may be important to include the viscosity effects to improve the predictions. However, since Hazel's and Holmboe's density distribution produces a relatively thick density transition layer, it is not suitable

to explain the wave phenomena in this type of two layer stratified flow system.

The Orr-Sommerfeld equation (4th order) was employed in the two layer models analyzed by Nishida & Yoshida (1990) since the diffusivity effects are negligibly small for these systems. Figure 1.13 shows the velocity and density profiles and the resulting stability diagrams for different Reynolds numbers. It can be seen clearly that unstable regions are bounded as the Reynolds number Re decreases, and the critical Richardson number Ric is about 1.5. This analysis explains the experimental results very well, particularly in unbounded cases of the two layer system. However, for the analysis of the salt wedge flow, it was found that the phase velocities of Holmboe modes, which have smaller velocities (i.e. SVB), are always underestimated by this calculation. Also, as was mentioned in the previous section, the salt wedge showed subdivisions with different wave formations, and Nishida's results cannot explain the mechanism of this phenomenon. This fact implies that there are other factors determining the stability of a salt wedge besides viscosity.

1.3.4 Rigid Boundary Effects

The other important factor determining the stability of the salt wedge is probably the presence of a rigid boundary. Stability of the flow with such boundaries was first investigated by Howard (1964) on a homogeneous hyperbolic tangential shear layer. It was found that the critical

distance from the inflection point to the rigid boundary (i.e. where the flow becomes stable for all wavelengths) was $Z_{cr}=1.1997$ as non-dimensional length based upon a half length of shear layer thickness. For stratified cases, Hazel (1972) used his model to evaluate the effect of reducing the lower layer thickness. Although the calculations showed some numerical instability problems, the critical values of the lower layer thickness for stability were found to be in the range $1.195 < Z_{cr} < 1.205$.

Both Howard and Hazel employed inviscid models; a treatment followed by Lalas & Einaudi (1976), Einaudi & Lalas (1976), Lindzen & Rosenthal (1976), Davis & Peltier (1977) and Fua & Einaudi (1984) to solve atmospheric boundary layer problems. Although these papers considered models of varying complexity and realism, the main qualitative results of all were identical. For example, the result obtained by Lalas and Einaudi is shown in Figure 1.14. It is clearly seen that the presence of the boundary leads to extra modes of instability. These additional modes have different features from K-H and Holmboe modes and were named 'resonant' modes by Davis & Peltier (1976). The main differences observed were longer wavelengths, lower phase velocity and smaller growth rates than the K-H modes. Besides these facts, these modes propagate in the region between the shear layer and the lower rigid boundary, which is quite similar to the SVB waves. Both Lindzen & Rosenthal (1976) and Davis & Peltier (1976) were able to show that the mechanism responsible for the

existence of resonant instabilities is critical level over-reflection, a phenomena which explains the microscale structures in the atmosphere very well.

However, because of the exponentially varying density profile, this analysis is not applicable to salt wedges. Their definition of the Richardson number is based on density gradient dp/dz , (so-called local or gradient Richardson number Ri_L). In a salt wedge, $Ri_L=0$ except at the density interface where $Ri_L=\infty$. Hino & Hung (1982) introduced this boundary effect into the salt-wedge type flow stability problems by using the realistic velocity and density profiles shown in Figure 1.15. Interestingly, although their calculations show several modes with positive and negative phase velocities, none of them are unstable. Thus, these modes may be due to numerical instabilities.

All these calculations overestimate the stabilizing effects of the rigid boundary, since it was found that salt wedges have SVA waves in the region where $Z_R=0.4$ to 0.5 . A possible explanation of this fact may be that the density interface destabilizes the Holmboe modes. Therefore, in order to evaluate the boundary effects for salt wedge flow, it is necessary to consider two layer viscous models.

1.3.5 Density Interface Displacement Effects

Experiments show that the center of the shear layer tends to be displaced with respect to the density interface especially in the tip and exit regions of the salt wedge.

Lawrence et al. (1991) investigated the stability features of these displaced flow systems by using relatively simple inviscid two-layer models (see Figure 1.16 and 1.17). The results show that additional Holmboe modes appear in the large wave number region near the $Ri_0=0$ axis. These modes have two pairs of complex conjugate roots having positive and negative real parts equal in magnitude. It was also found that new unstable waves, called 'mode I instability', are obtained (providing an extension to K-H instability) which are dispersive. It is interesting that Holmboe modes eventually move closer to the $Ri_0=0$ axis as displacement d increases and disappear at $d=1.0$. This result is understandable since Holmboe modes are induced by the existence of strong stratification in the shear layer and agree with Hazel's analysis qualitatively.

Although this model is quite simple, it indicates that stability properties are strongly influenced by the displacement d . This implies a sensitivity to velocity and, therefore, it will be necessary to develop an appropriate model for the stability analysis of a salt wedge because of its velocity profiles. Such a sensitivity of stability features to background velocity and density profiles may induce three-dimensional wave structures on the density interface, since the flow field is three-dimensional.

1.3.6 Three-Dimensional Instabilities

As was mentioned in section 1.2.3, three-dimensional structures of interfacial waves are another commonly observed problem in salt wedges. Because of the consequences of Squire's theorem (Squire 1933), it is always assumed a priori that an initially one-dimensional flow will pass through a distinct two-dimensional state before being dependent on the third spatial coordinate (lateral direction). Three-dimensional structures are therefore generally considered to be results of secondary non-linear instability after full development of primary two-dimensional instabilities. A typical example of this idea can be seen in a homogeneous fluid analysis such as the numerical analysis of a mixing layer (Metcalfe et al. 1987) etc.

However, in the case of a salt wedge, flow is very laminar and even fully developed interfacial waves have a relatively small non-linearity when compared to homogeneous cases. Therefore, it is natural to consider that three-dimensional wave structures are, somehow, induced by the flow structures caused by channel configurations. Another possibility is the existence of three-dimensional primary instability associated with strong stratification as predicted by Smyth & Peltier (1990). This particular idea will be discussed in part 5.

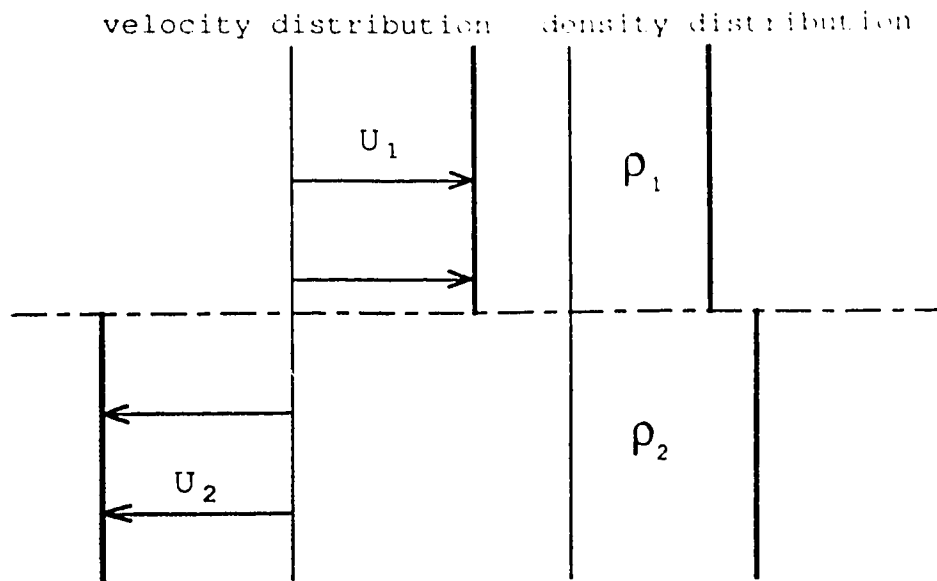


Figure 1.7. Velocity and density profiles of Kelvin Helmholtz models.

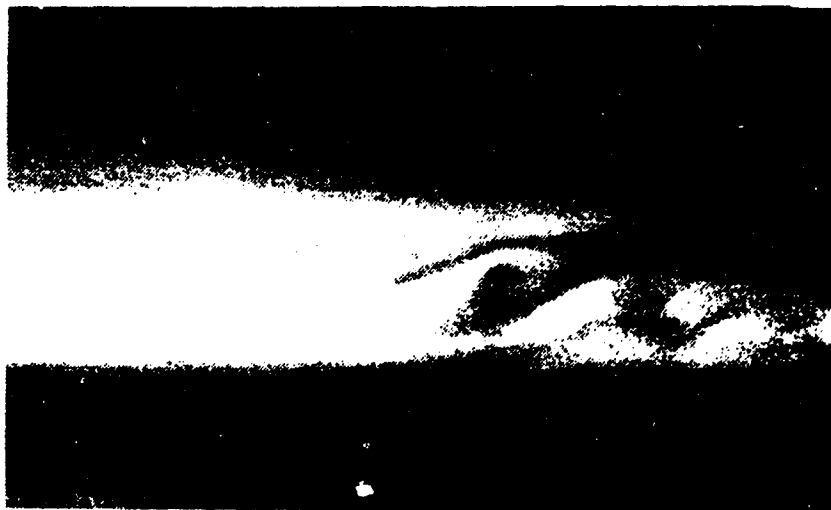
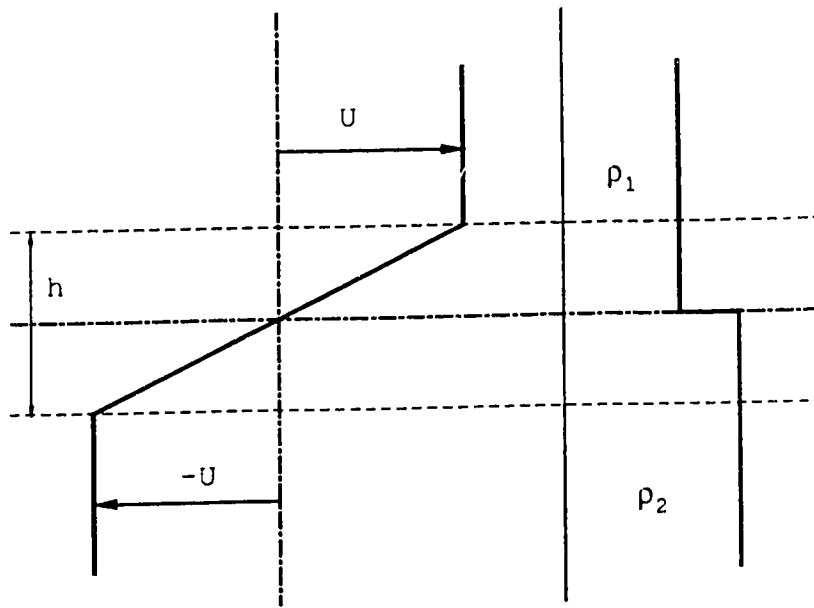
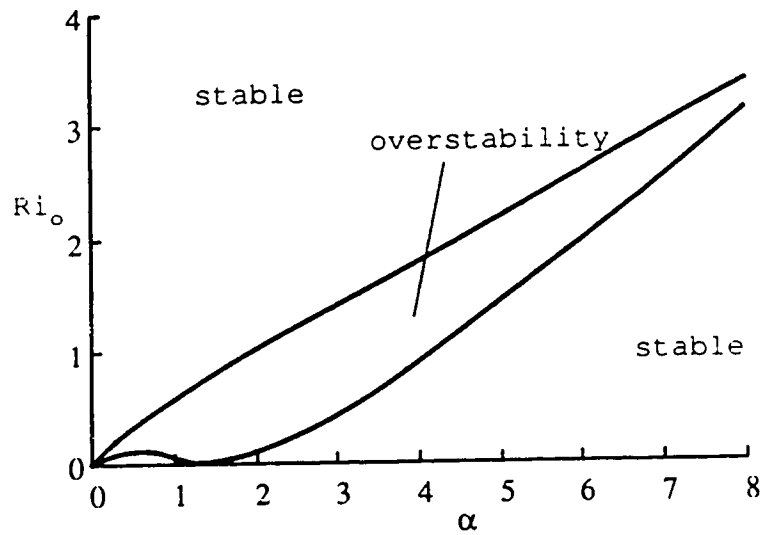


Plate 1.8 K-H instability in atmosphere



(a) Velocity and density profiles



(b) Stability boundaries

Figure 1.9 (a), (b) Velocity and density profiles and the stability boundaries. (Adopted from Holmboe (1962))

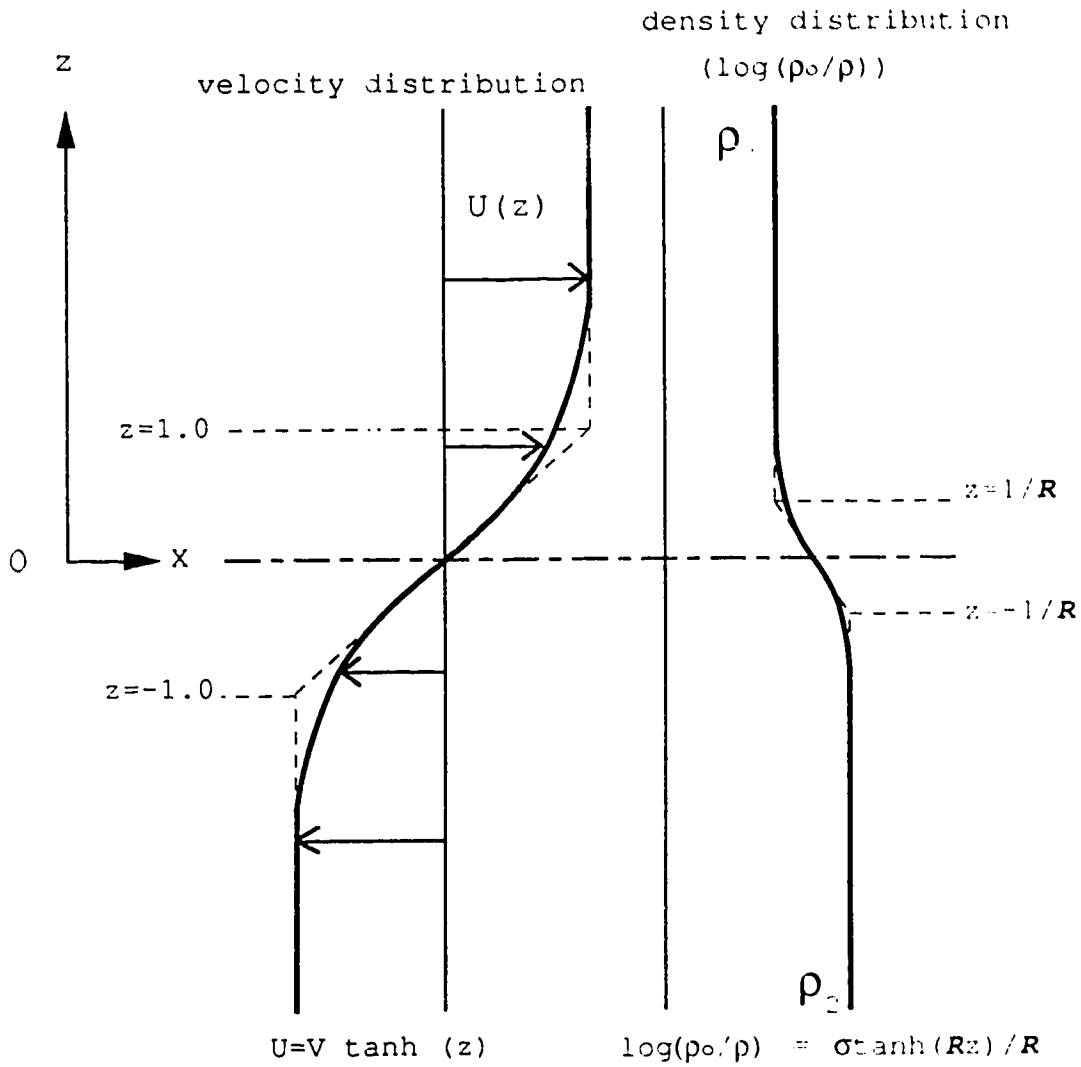


Figure 1.10 The velocity and density distributions of Hazel's model (1972)

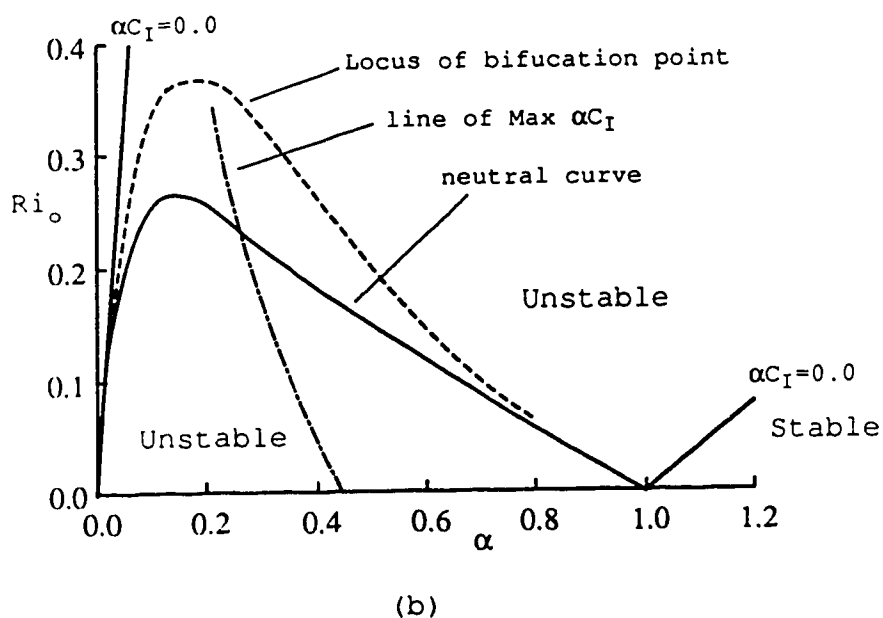
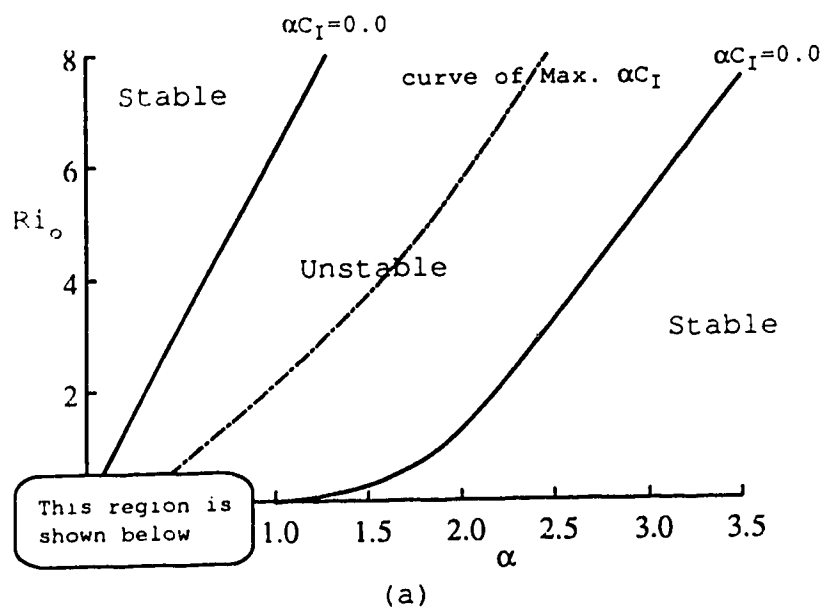
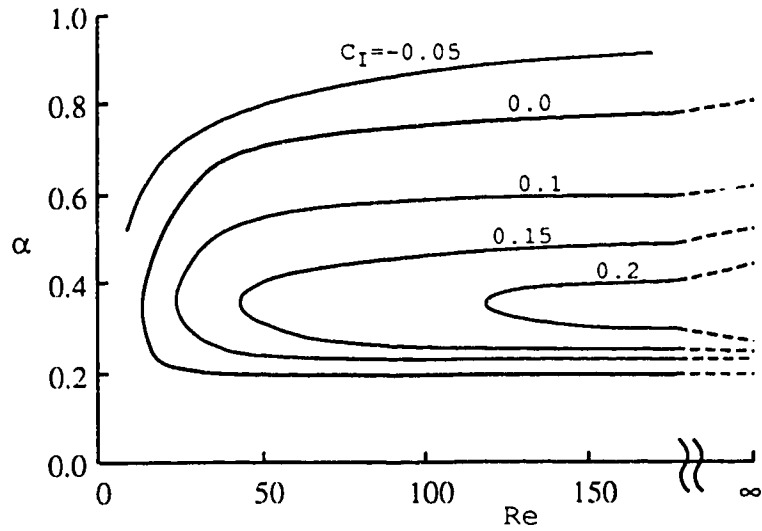
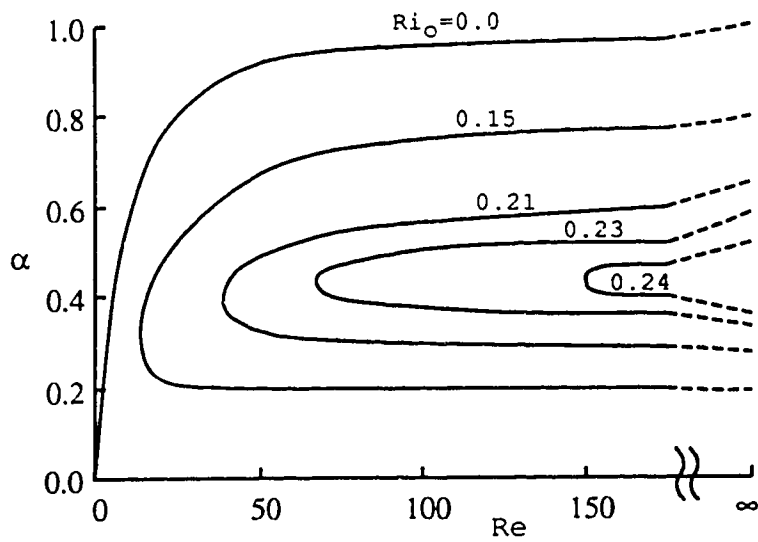


Figure 1.11 (a), (b) The modified stability diagram obtained by Hazel (1972) $U = \tanh(z)$, $\log(\rho_0/\rho) = \sigma \tanh(Rz)/R$ with $R=5.0$ case.

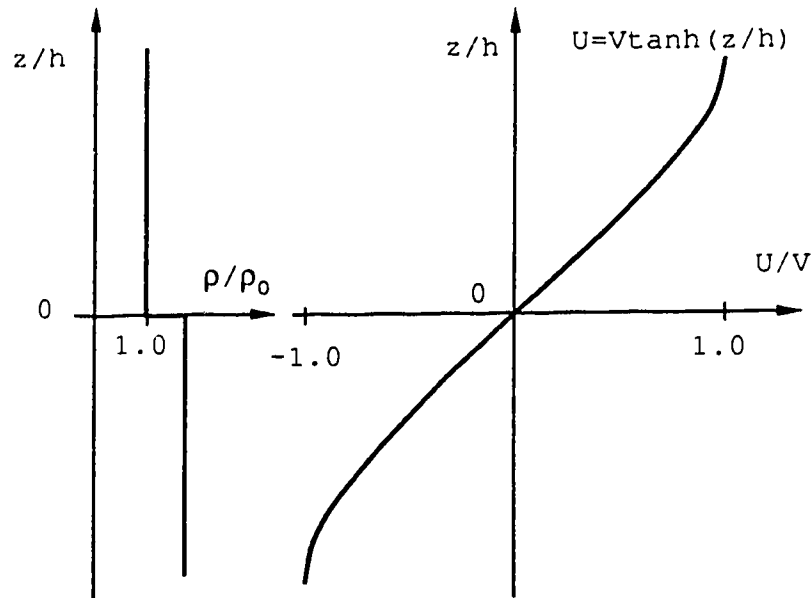


(a) Stability curves for temporally varying waves. ($Ri_0 = 0.15$ case)

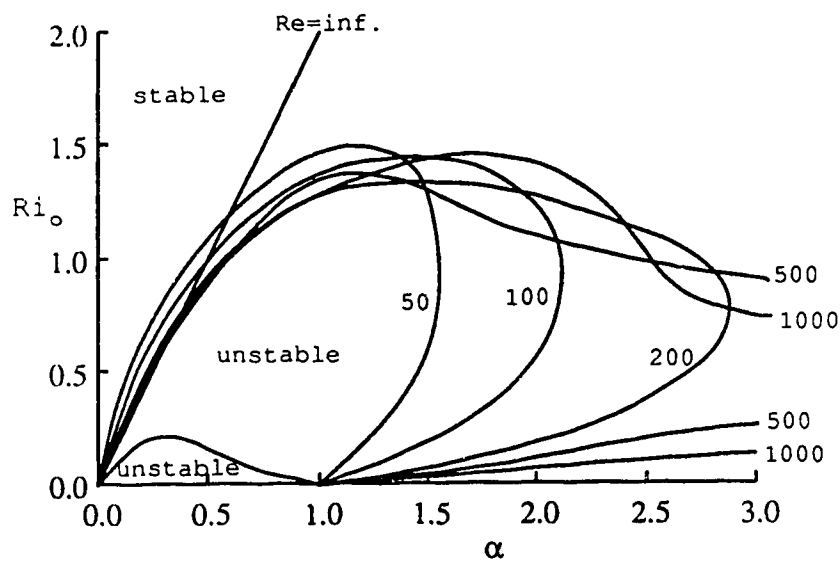


(b) Neutral boundaries (i.e. $C_T = 0.0$) for various Richardson numbers.

Figure 1.12 (a), (b) Adopted stability diagrams calculated by Maslowe and Thompson (1971)

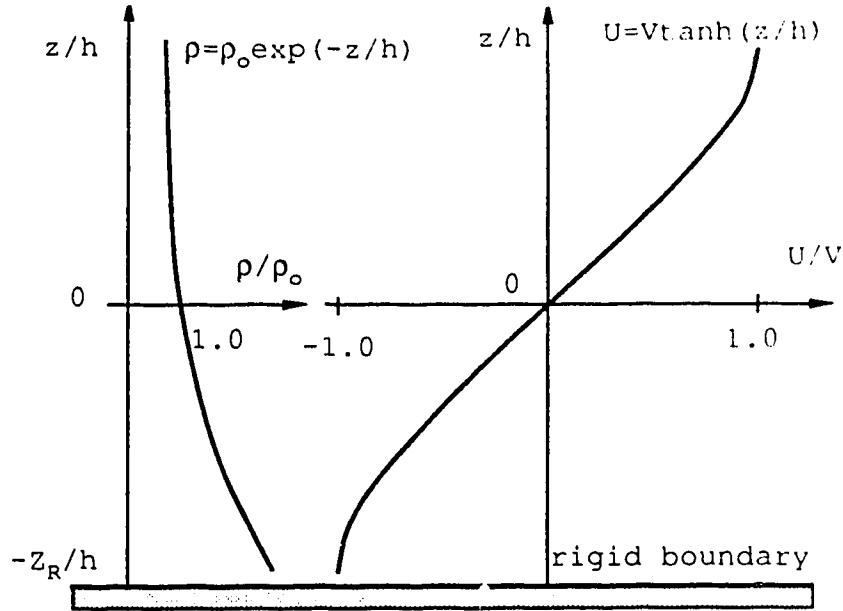


(a) velocity and density profiles

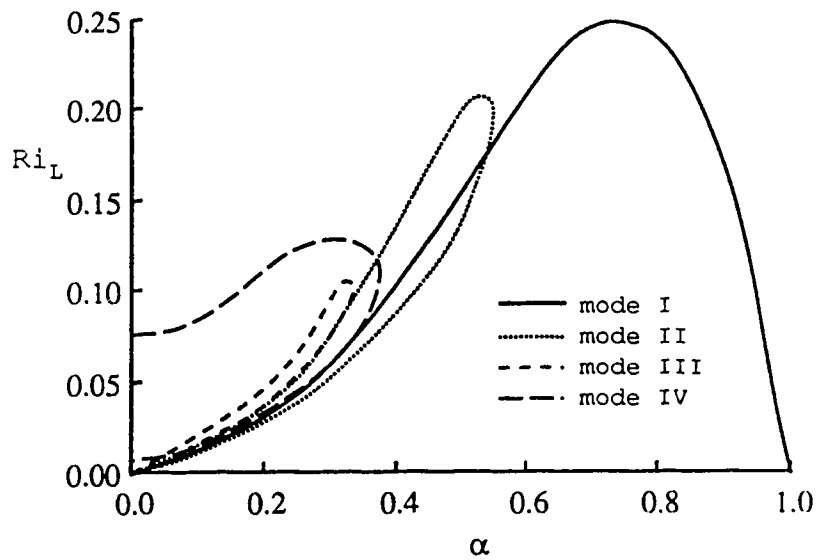


(b) Stability boundaries

Figure 1.13. Velocity and density profiles and the stability boundaries. (Adopted from Nishida and Yoshida (1984, 1987))

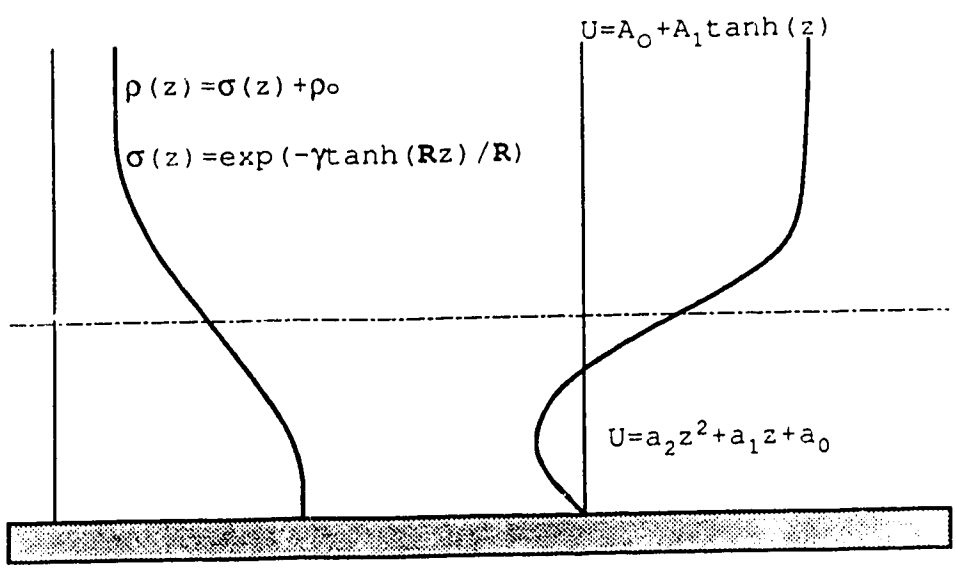


(a) velocity and density profiles

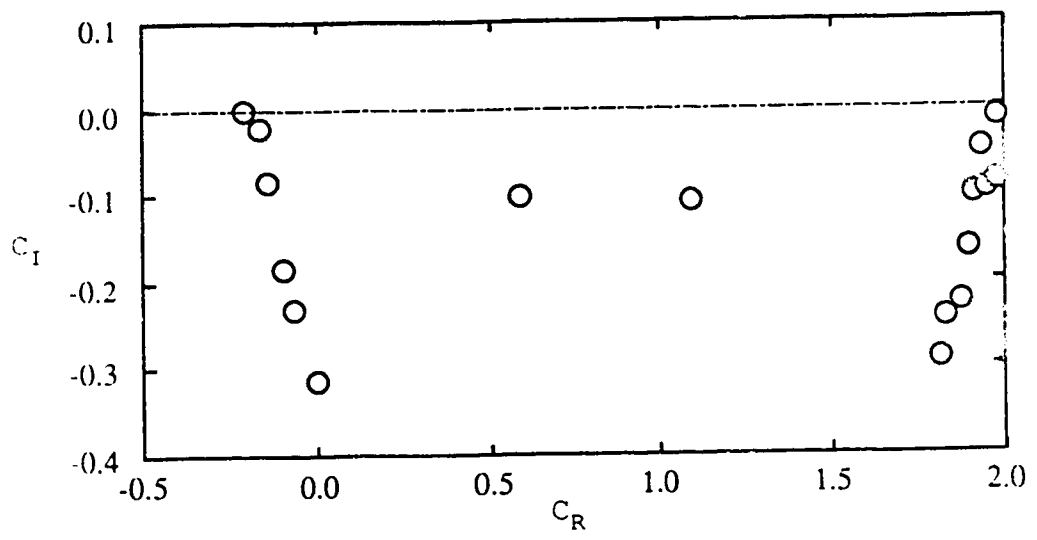


(b) Stability boundaries

Figure 1.14. Velocity and density profiles and the stability boundaries. (Adopted from Lalas and Einaudi (1976))

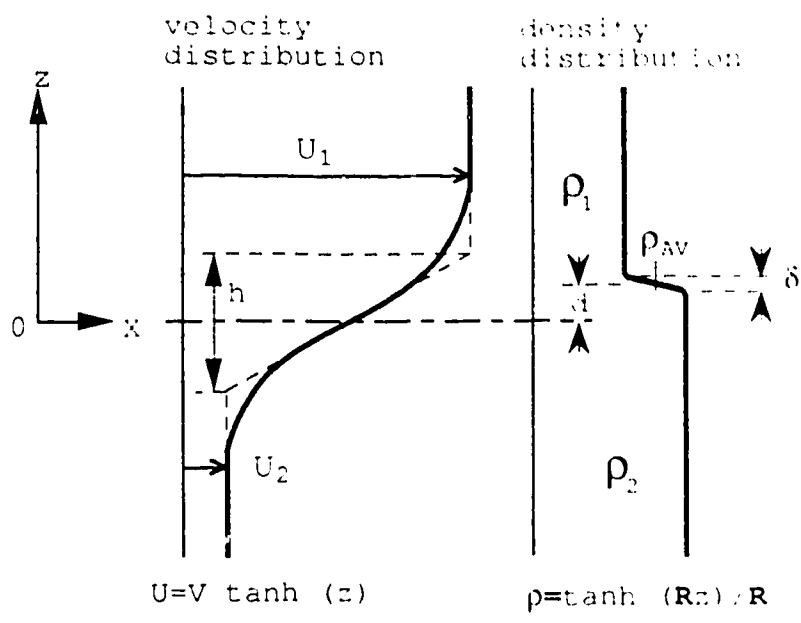


(a) Velocity and density profiles

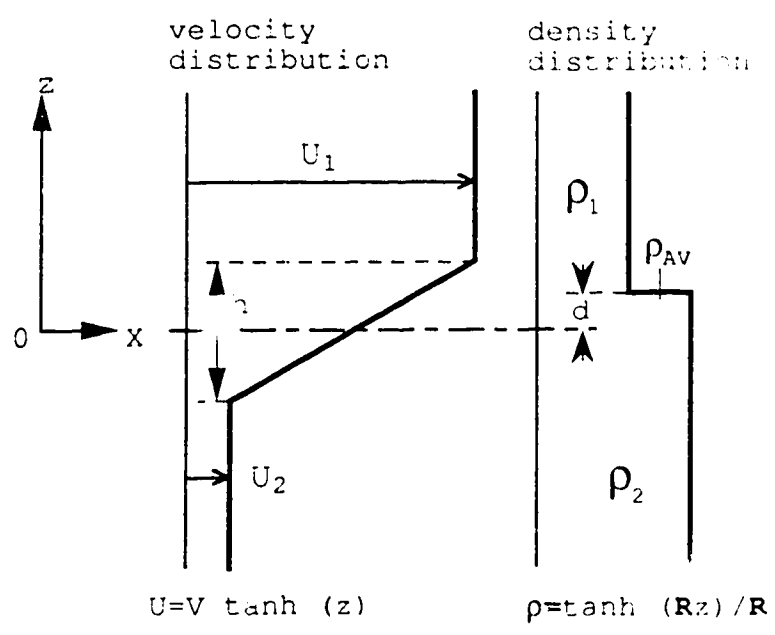


(b) Stability diagram

Figure 1.15. Velocity and density profiles and the stability diagram $R=5.0$ $Pr=7.5$ $Re=50$ $J_0=0.15$ $\alpha=0.7$ case (Adopted from Hino, Nadaoka & Hung (1984))



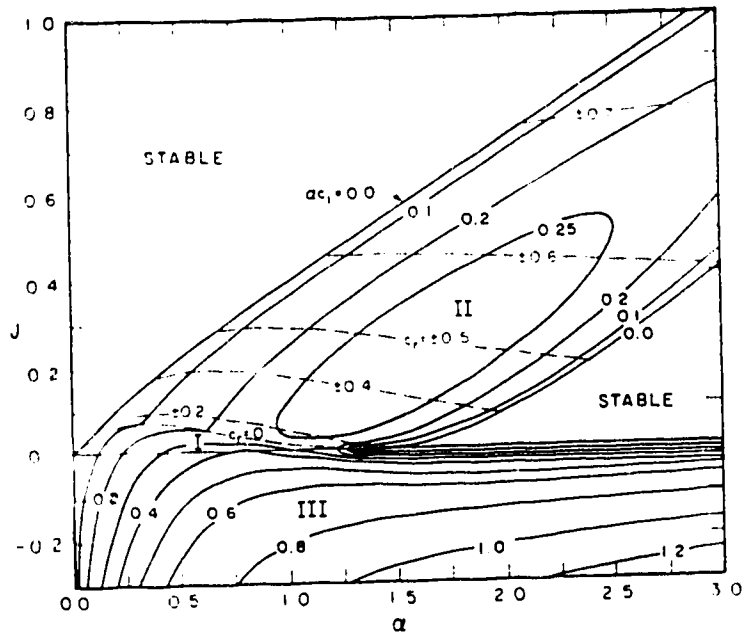
(a) Experimental results



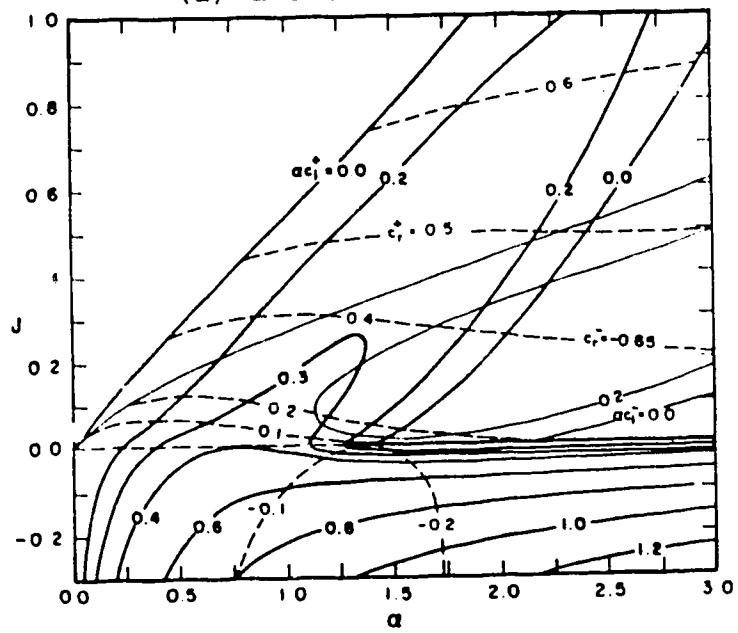
(b) Numerical models

Figure 1.16. Mean velocity and density profiles of measured and numerical model examined by Lawrence, Browand and Redekopp (1991)

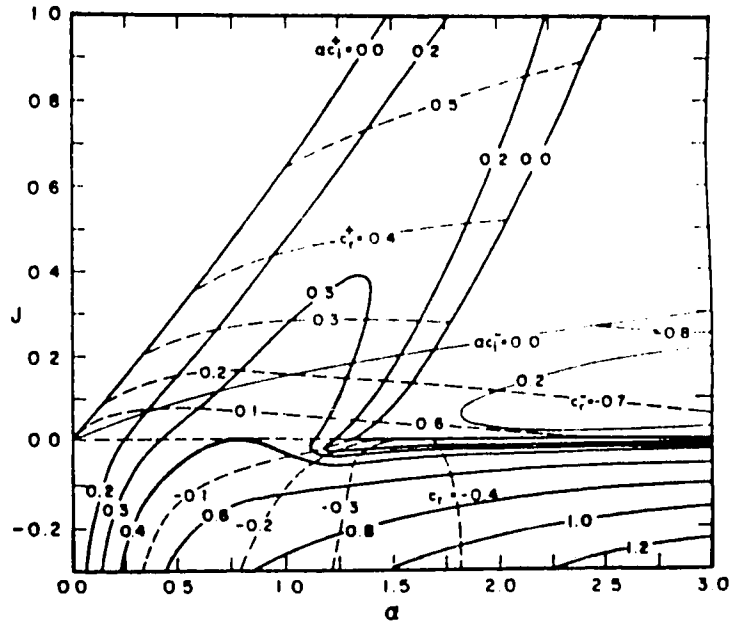
Figure 1.17 (a)-(d) Density interface displacement effects (Adopted from Lawrence et al. (1991))



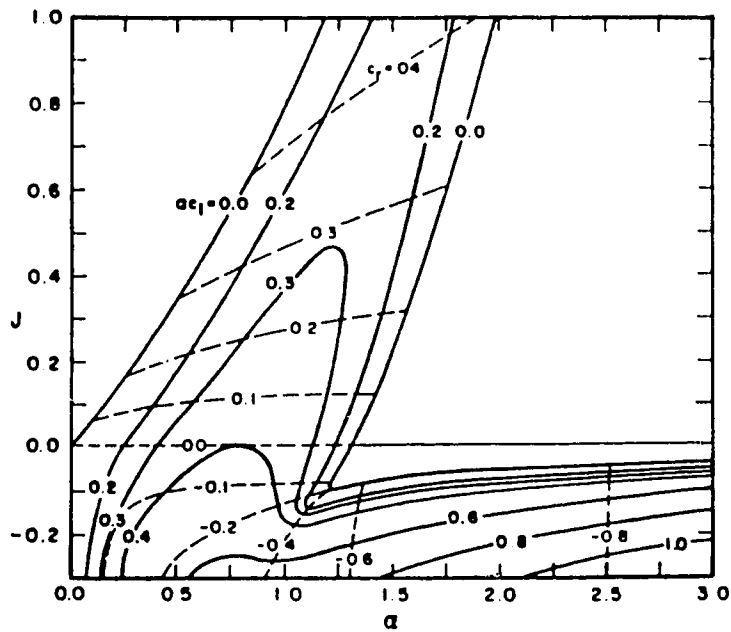
(a) $d=0.0$ case



(b) $d=0.25$ case



(c) $d=0.5$ case



(d) $d=1.0$ case

1.4 CONCLUSION

Based on the forgoing experimental and mathematical review, the following conclusions may be made:

(i) Experiments show that a salt wedge can be separated into three sub-divisions based on their stress distributions: the tip, quasi-equilibrium, and exit regions. In each region, velocity profiles can be approximated by a tanh² function. The inflection points may be significantly displaced with respect to the density interface in the tip and exit regions.

(ii) Due to secondary flow structures in the fresh water layer, high and low speed regions develop. The number of regions is strongly related to the channel aspect ratio.

(iii) Mixing of salt and fresh water in salt wedge flow is dominated by the interfacial wave phenomena. Two wave groups of different phase velocities are observed. These have been named Holmboe modes. For convenience, Holmboe waves with $C_r > 0.0$ will be called SVA waves, those with $C_r < 0.0$ will be called SVB waves.

(iv) SVA waves are predominant through almost the entire range of the salt wedge. In contrast, SVB waves are observed to a limited degree only low speed, relatively low interfacial shear stress regions. There are few mathematical and numerical models applicable to salt wedge flow and no practical explanation exists concerning the localization of these wave modes.

These results indicate that it is necessary to perform further analysis and investigation in the following areas:

(i) Rigid boundary effects on the stability of two-layered stratified flows, both inviscid and viscous cases.

(ii) Effects of velocity inflection point displacement with respect to the density interface for viscous fluids.

(iii) Complete set of wave and flow property measurements with consideration of three-dimensional flow structures in the channel.

In the following sections, these problems will be analysed by performing analytical, numerical and experimental investigations.

2. PART TWO: THEORETICAL ANALYSIS (INVISCID MODELS)

2.1 INTRODUCTION

The waves on a saline wedge with rigid boundaries usually have a very complex three-dimensional structure. In order to understand this problem, many approaches have involved increasing the complexity of velocity and density profiles, at the same time considering non-linear effects on the governing equations. Despite all the efforts, the problem is still not clearly understood. In this section, relatively simple velocity and density distributions will be used to understand the mechanism of the rigid boundary effects on the stability of these systems. The first step in the procedure will be to derive a governing equation by applying infinitesimally small perturbations to the inviscid, incompressible two-dimensional flow. Next, two models will solve this equation for rigid boundary conditions. Model I is designed to evaluate the effects of the lower layer thickness, Z_R , on the stability. Model II will test rigid boundary velocity effects. Both models employ a two-layer density distribution which has a distinctive interface and piece-wise linear velocity profile. These conditions will significantly simplify the analysis and make it easy to understand the physics behind the phenomena.

2.2 GOVERNINIG EQUATIONS

2.2.1 Basic Assumptions and Governing Equations

The Cartesian co-ordinate system is basically the same as was utilized in previous sections and is defined as follows.

1. The X co-ordinate and associated velocity u , U are in the direction of flow parallel to the channel center line. The origin may be established arbitrarily.
2. The Y co-ordinate and velocity v are in the lateral direction of the channel. When two-dimensional (plane) flow is assumed, $\partial/\partial y=0$ and $v=0$.
3. The Z co-ordinate originates at the density interface or the steepest density gradient point and is positive upwards; w is the corresponding velocity.

In this chapter we limit our discussion to two-dimensional incompressible inviscid flow in order to simplify the problem as follows:

- 1) The fluid dynamics is governed by the adiabatic equations. Therefore, the following assumptions may be made:

- i) incompressible flow;

$$\frac{Dp}{Dt} = 0, \quad (2.2.1)$$

where

$$\frac{D}{Dt} = \frac{\partial}{\partial t} + u \frac{\partial}{\partial x} + v \frac{\partial}{\partial y} + w \frac{\partial}{\partial z} \text{ is the}$$

convective derivative.

- ii) no non-conservative processes. (eg. viscosity, diffusivity, etc.)

The continuity equation becomes

$$\nabla \cdot \mathbf{v} = 0 \quad (2.2.2)$$

And the momentum equation becomes

$$\frac{D\mathbf{v}}{Dt} + \frac{1}{\rho} \nabla p + g \hat{\mathbf{e}}_3 = 0 \quad (2.2.3)$$

where $\hat{\mathbf{e}}_3$ is a unit vector of vertical direction.

- 2) Hydrostatic balance between $P_0(z)$ and $\rho_0(z)$ must hold. Thus, in the absence of motion,

$$\mathbf{v} = 0, \quad p = P_0(z), \quad \rho = \rho_0(z) \quad (2.2.4)$$

and P_0 and ρ_0 are exact solutions of the adiabatic equations. Namely,

$$\frac{D\rho_0(z)}{Dt} = 0, \quad \nabla \cdot \mathbf{v} = 0 \quad (2.2.5)$$

$$\therefore \frac{d\rho_0(z)}{dz} = -\rho_0(z) g \quad (2.2.6)$$

- 3) Flow is two-dimensional, which is

$$\frac{\partial}{\partial y} = 0, \quad v = 0 \quad (2.2.7)$$

From conditions 1), 2) and 3), the governing equations become

$$\frac{\partial u}{\partial x} + \frac{\partial w}{\partial z} = 0 \quad (2.2.8)$$

$$\frac{\partial \rho}{\partial t} + u \frac{\partial \rho}{\partial x} + w \frac{\partial \rho}{\partial z} = 0 \quad (2.2.9)$$

$$\rho \left(\frac{\partial u}{\partial t} + u \frac{\partial u}{\partial x} + w \frac{\partial u}{\partial z} \right) + \frac{\partial p}{\partial x} = 0 \quad (2.2.10)$$

$$\rho \left(\frac{\partial w}{\partial t} + u \frac{\partial w}{\partial x} + w \frac{\partial w}{\partial z} \right) + \frac{\partial p}{\partial z} + \rho g = 0 \quad (2.2.11)$$

$$\frac{d\rho_0(z)}{dz} = -\rho_0(z)g \quad (2.2.12)$$

This system of equations will be examined for stability by introducing infinitesimal perturbations on the steady state solutions of the system. The procedure will be described in the next section.

2.2.2 Taylor-Goldstein Equation

We consider steady-state solutions of the form,

$$u = U_0(z) \quad (2.2.13)$$

$$w = 0 \quad (2.2.14)$$

$$\rho = \rho_0(z) \quad (2.2.15)$$

$$p = P_0(z) \quad (2.2.16)$$

where

$$\frac{d\rho_0(z)}{dz} = -\rho_0(z)g \quad (2.2.17)$$

space, the system is called 'unstable'. The governing equations (2.8) to (2.12) obey Squire's theorem (1933), which means that "For every three-dimensional unstable disturbance, there is a more unstable two-dimensional disturbance". It implies that the small perturbations can be written as functions of x, z , and t . Here perturbation quantities are denoted by the tilde superscript.

$$u = U_0(z) + \tilde{u}(x, z, t) , \quad (2.2.18)$$

$$w = 0 + \tilde{w}(x, z, t) , \quad (2.2.19)$$

$$\rho = \rho_0(z) + \tilde{\rho}(x, z, t) , \quad (2.2.20)$$

$$p = p_0(z) + \tilde{p}(x, z, t) . \quad (2.2.21)$$

Substituting these quantities into the adiabatic equation system, the terms containing products of perturbation quantities result from a fluctuation on another fluctuation. If the fluctuation has a frequency ω , the coupled terms will have frequency 0 or 2ω . Therefore they will either modify the nonfluctuating flow or introduce higher harmonics.

Since such difficulties disappear if we assume that the fluctuations and their derivatives have small amplitude, let us linearize the equations by neglecting the quadratic perturbation terms. Then

$$\frac{\partial \tilde{u}}{\partial x} + \frac{\partial \tilde{w}}{\partial z} = 0 , \quad (2.2.22)$$

$$\frac{\partial \tilde{\rho}}{\partial t} + U_0 \frac{\partial \tilde{\rho}}{\partial x} + \tilde{w} \frac{\partial \rho_0}{\partial z} = 0 , \quad (2.2.23)$$

$$\frac{\partial \tilde{u}}{\partial t} + U_0 \frac{\partial \tilde{u}}{\partial x} + \tilde{w} \frac{\partial U_0}{\partial z} + \frac{1}{\rho_0} \frac{\partial \tilde{p}}{\partial x} = 0 \quad (2.2.24)$$

$$\frac{\partial \tilde{w}}{\partial t} + U_0 \frac{\partial \tilde{w}}{\partial x} + \frac{1}{\rho_0} \frac{\partial \tilde{p}}{\partial z} + \frac{\tilde{p}}{\rho_0} \alpha = 0 \quad (2.2.25)$$

The advantage of linearity is that by assuming the solutions of this system are normal mode forms, it is possible to reduce the system of partial differential equations (2.2.22), (2.2.23), (2.2.24), (2.2.25) to ordinary differential equations, facilitating the analysis. Thus, the following forms of solution are assumed:

$$\begin{aligned} \tilde{u} &= (\hat{u}(z) \exp(i\alpha x - i\omega t) + \text{c.c.}) / 2 \\ &= (\hat{u}(z) \exp(i\alpha(x-ct)) + \text{c.c.}) / 2 \end{aligned} \quad (2.2.26)$$

$$\tilde{w} = (\hat{w}(z) \exp(i\alpha(x-ct)) + \text{c.c.}) / 2 \quad (2.2.27)$$

$$\tilde{p} = (\hat{p}(z) \exp(i\alpha(x-ct)) + \text{c.c.}) / 2 \quad (2.2.28)$$

$$\tilde{p} = (\hat{p}(z) \exp(i\alpha(x-ct)) + \text{c.c.}) / 2 \quad (2.2.29)$$

where $c = \frac{\omega}{\alpha}$ is the complex phase velocity and c.c. is the complex conjugate. (2.2.30)

If the complex phase speed is written in the form

$$c = c_R + ic_I \quad (2.2.31)$$

we may rewrite the perturbation quantities as

$$\begin{aligned} \tilde{f} &= (\hat{f}(z) \exp(i\alpha(x - (c_R + ic_I)t)) + \text{c.c.}) / 2 \\ &= (\hat{f}(z) \exp(c_I t) \exp(i\alpha(x - c_R t)) + \text{c.c.}) / 2 \end{aligned} \quad (2.2.32)$$

This relation shows that if the imaginary part of the phase velocity c_I is non-zero, then the perturbation is either growing or decaying with time (i.e. the system is either 'unstable' or 'stable'). If $c_I=0$, then the perturbation

remains with the same amplitude as the initial state, and the system is neutrally stable. Therefore, a complex phase velocity c as a function of the given parameters related to velocity and density profiles, the stability of the flow system can be judged.

Let us substitute (2.2.26) to (2.2.30) into equations (2.2.22) to (2.2.25), then

$$i\alpha \hat{u} + \frac{d\hat{w}}{dz} = 0 \quad , \quad (2.2.33)$$

$$i\alpha (U_0 - c) \hat{p} + \frac{d\rho_0}{dz} \hat{w} = 0 \quad , \quad (2.2.34)$$

$$\rho_0 \left(i\alpha (U_0 - c) \hat{u} + \frac{dU_0}{dz} \hat{w} \right) + i\alpha \hat{p} = 0 \quad , \quad (2.2.35)$$

$$\rho_0 i\alpha (U_0 - c) \hat{w} + \frac{d\hat{p}}{dz} + \hat{p}g = 0 \quad , \quad (2.2.36)$$

Solving this system in terms of \hat{w} produces

$$\left(\rho_0 (U_0 - c) \hat{w}' \right)' - \left(\rho_0 U_0' \hat{w} \right)' - \left\{ \frac{\rho_0' g}{U_0 - c} + \rho_0 \alpha^2 (U_0 - c) \right\} \hat{w} = 0 \quad , \quad (2.2.37)$$

where ' means d/dz .

Equation (2.2.37) is called the Taylor-Goldstein (T-G) equation in honour of its derivation and exploitation by Taylor (1931) and Goldstein (1931). Note that the equation and the boundary conditions, which will be discussed in the

next sub-section, are unchanged when α is replaced by $-\alpha$. Thus, without loss of generality, we can take $\alpha > 0$.

2.2.3 Boundary and Matching Conditions

To simplify the problem, in this section we will consider the very simple flow configuration with constant density and piecewise velocity profiles. In this case, \hat{p} and U_0'' become zero in each layer except for the boundary between layers and the Taylor-Goldstein equation becomes,

$$\frac{d^2 \hat{w}}{dz^2} - \alpha^2 \hat{w} = 0 \quad (2.2.38)$$

The general form of the solution of this equation is well known and is written as

$$\hat{w} = A_1 \exp(\alpha^2 z) + A_2 \exp(-\alpha^2 z) \quad (2.2.39)$$

where A_1 and A_2 are complex coefficients which can be determined by the boundary conditions and matching conditions between layers.

Since the flow is inviscid, there are two types of boundary conditions given as follows:

- 1) Rigid wall boundary: in this case

$$\hat{w} = 0 \quad \text{at } z = z_{\text{wall}} \quad (2.2.40)$$

- 2) Unbounded boundary: Solution has to be 'bounded' at either $z = \infty$ or $z = -\infty$.

The boundaries between each layer are generally deformed by the motion of the fluids (Figure 2.1), and two different matching conditions are required. These are:

1) Kinematic matching condition:

This implies the normal component of the velocity field is continuous across the deformed interface.

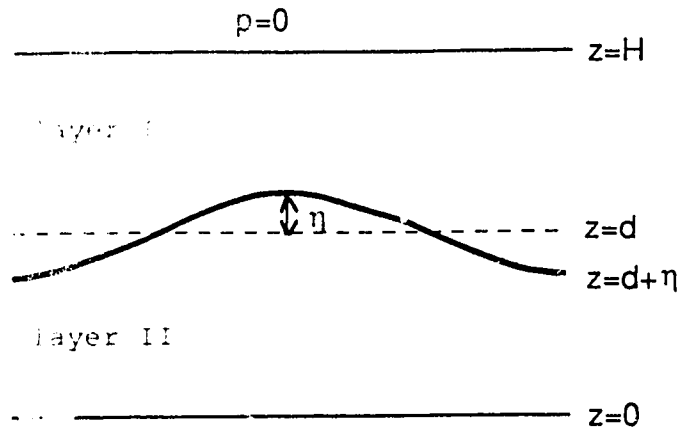


Figure 2.1. Boundary conditions

If we denote that a superscript of + means

$$f^+(d) = \lim_{\epsilon \rightarrow 0} f(d+\epsilon) \quad , \quad (2.2.41)$$

and a superscript of - means

$$f^-(d) = \lim_{\epsilon \rightarrow 0} f(d-\epsilon) \quad . \quad (2.2.42)$$

Then generally, the velocity field due to wave motion

is described as

$$w^+ = \frac{\partial \eta}{\partial t} + u^+ \frac{\partial \eta}{\partial x} \quad , \quad (2.2.43)$$

$$w^- = \frac{\partial \eta}{\partial t} + u^- \frac{\partial \eta}{\partial x} \quad , \quad (2.2.44)$$

at $z = d + \eta$.

However, in this case, it is assumed that wave field is very small (i.e. $\eta \ll d$). Thus,

$$w \approx \tilde{w}^+ , \quad (2.2.45)$$

$$u \approx U_0(z) + \tilde{u} , \quad (2.2.46)$$

and when substituted into (2.2.43) and (2.2.44), Taylor expanding about $z = d$ and neglecting quadratic eddy quantity terms,

$$\tilde{w}^+ = \frac{\partial \eta}{\partial t} + U_0(d^+) \frac{\partial \eta}{\partial x} , \quad (2.2.47)$$

$$\tilde{w}^- = \frac{\partial \eta}{\partial t} + U_0(d^-) \frac{\partial \eta}{\partial x} . \quad (2.2.48)$$

Assuming wave perturbations of the form

$$\begin{aligned} \eta &= (\hat{\eta} \exp(i\alpha x - i\omega t) + \text{c.c.}) / 2 \\ &= (\hat{\eta} \exp(i\alpha(x-ct)) + \text{c.c.}) / 2 , \end{aligned} \quad (2.2.49)$$

then

$$\tilde{w}^+ = (U_0(d^+) - c) \frac{\partial \eta}{\partial x} , \quad (2.2.50)$$

$$\tilde{w}^- = (U_0(d^-) - c) \frac{\partial \eta}{\partial x} , \quad (2.2.51)$$

which is equivalent to

$$\hat{w}^+ = (U_0(d^+) - c) i\alpha \hat{\eta} , \quad (2.2.52)$$

$$\hat{w}^- = (U_0(d^-) - c) i\alpha \hat{\eta} , \quad (2.2.53)$$

implying

$$i\alpha \hat{\eta} = \frac{\hat{w}^+}{(U_0(d^+) - c)} = \frac{\hat{w}^-}{(U_0(d^-) - c)} , \quad (2.2.54)$$

$$\frac{\hat{w}^+}{(U_0(d^+) - c)} - \frac{\hat{w}^-}{(U_0(d^-) - c)} = 0 . \quad (2.2.55)$$

If we define the "jump" bracket [] as

$$[f(z)] = \lim_{\epsilon \rightarrow 0} (f(d+\epsilon) - f(d-\epsilon)), \quad (2.2.56)$$

equation (2.2.) can be re-written as

$$\left[\frac{\widehat{w}}{U - c} \right] = 0 \quad \text{at } z = d, \quad (2.2.57)$$

where [] is the "jump" bracket.

This is the kinematic matching condition.

2) Dynamic matching condition:

This condition states that the pressure must be continuous across the deformed interface.

First, consider the steady state solutions which have no wave-like interfacial deformations. If it is noted that

$$\rho_0(z) = \rho_1(z) \quad \text{in layer I,} \quad (2.2.58)$$

$$\rho_0(z) = \rho_2(z) \quad \text{in layer II,} \quad (2.2.59)$$

$$p_0(z) = p_1(z) \quad \text{in layer I,} \quad (2.2.60)$$

$$p_0(z) = p_2(z) \quad \text{in layer II.} \quad (2.2.61)$$

Then, because of the hydrostatic relationship, in layer I

$$\frac{dp_{1H}}{dz} = - \rho_1(z)g, \quad (2.2.62)$$

$$p_{1H}(z) = 0 \quad \text{at } z=H, \quad (2.2.63)$$

where subscript H indicates hydrostatic pressure.

Likewise, in layer II,

$$\frac{dp_{2H}}{dz} = - \rho_2(z) g \quad (2.2.64)$$

$$\therefore p_{2H} = g \int_1^z \rho_2(\xi) d\xi + \overline{p_{2H}} \quad (2.2.65)$$

where $\overline{p_{2H}}$ is an integration constant.

Since we must have continuity of pressure at $z = d$,
(i.e. $p_{1H}(d) = p_{2H}(d)$)

$$\therefore \overline{p_{2H}} = g \int_1^d \rho_2(\xi) d\xi + g \int_1^d \rho_1(\xi) d\xi \quad (2.2.66)$$

then

$$p_{2H}(z) = g \int_1^z \rho_2(\xi) d\xi + g \int_1^d \rho_1(\xi) d\xi \quad (2.2.67)$$

If we introduce the wave-field as follows:

$$p_{1T} = p_{1H} + p_{1W} \quad (2.2.68)$$

$$p_{2T} = p_{2H} + p_{2W} \quad (2.2.69)$$

where subscripts T and W indicate total and wave-field pressure respectively.

The continuity of the stress field across the deformed interface becomes,

$$p_{1T}(d+\eta) = p_{2T}(d+\eta) \quad (2.2.70)$$

Performing a Taylor expansion of (2.2.70) around d (since $\eta \ll d$) produces,

$$p_{1H}(d) + \frac{dp_{1H}(d)}{dz} \eta + p_{1W}(d) \quad ,$$

$$= p_{1\#}(d) + \frac{dp_{1\#}(d)}{dz} \eta + p_{1w}(d) + O(\eta^2) \quad (2.2.71)$$

Remembering equation (2.2.66), $p_{1\#}(d)$ and $p_{2\#}(d)$ cancel each other. Furthermore, from the hydrostatic relationship, we know

$$\frac{dp_{1\#}(d)}{dz} = -g \rho_1(d^+) \quad (2.2.72)$$

$$\frac{dp_{2\#}(d)}{dz} = -g \rho_2(d^-) \quad (2.2.73)$$

where $d^+ = d + \varepsilon$, $d^- = d - \varepsilon$, $\varepsilon \ll 1$.

Since η is very small, if higher order terms of η are neglected, then

$$-g\eta\rho_1(d^+) + p_{1w}(d^+) = -g\eta\rho_2(d^-) + p_{2w}(d^-) \quad (2.2.74)$$

$$\therefore \{\rho_2(d^-) - \rho_1(d^+)\}g\eta - \{p_{1w} - p_{2w}\} = 0 \quad (2.2.75)$$

$$\therefore \{-g\eta\rho_2 + p_{2w}\} - \{-g\eta\rho_1 + p_{1w}\} = 0 \quad (2.2.76)$$

at $z=d$.

And using the "jump" bracket, (2.2.76) can be written as

$$[-g\eta\rho_0 + p_w] = 0 \quad \text{at } z=d. \quad (2.2.77)$$

Let us take the x-derivative of (2.2.77). Thus,

$$\left[-\rho_0 g \frac{\partial \eta}{\partial x} + \frac{\partial p_w}{\partial x} \right] = 0 \quad \text{at } z=d. \quad (2.2.78)$$

However, from (2.2.50) and (2.2.51),

$$\frac{\partial \eta(d^+)}{\partial x} = \frac{\tilde{w}(d^+)}{(U_0(d^+) - c)} \quad (2.2.79)$$

$$\frac{\partial \eta(d^+)}{\partial x} = \frac{\tilde{w}(d^+)}{(U_0(d^+) - c)}, \quad (2.2.80)$$

so

$$\left[\rho_0 \frac{\partial \eta}{\partial x} \right] = \left[\frac{\rho_0 \tilde{w}}{U_0 - c} \right]. \quad (2.2.81)$$

Also, if the continuity equation (2.2.77),

$$\frac{\partial \tilde{u}}{\partial x} = - \frac{\partial \tilde{w}}{\partial z}, \quad (2.2.82)$$

is substituted into the momentum equation (2.2.84),

$$\frac{\partial \tilde{p}}{\partial x} = - \rho_0 (U_0 - c) \frac{\partial \tilde{u}}{\partial x} - \rho_0 \tilde{w} \frac{\partial U_0}{\partial z}, \quad (2.2.83)$$

then,

$$\frac{\partial \tilde{p}}{\partial x} = \frac{\partial p_w}{\partial x} = \rho_0 (U_0 - c) \frac{\partial \tilde{w}}{\partial z} - \rho_0 \frac{\partial U_0}{\partial z} \tilde{w}. \quad (2.2.84)$$

Therefore, the jump condition at $z=d$ is obtained from (2.2.78), (2.2.81) and (2.2.84) as

$$\left[\rho_0 (U_0 - c) \frac{\partial \tilde{w}}{\partial z} - \rho_0 \frac{\partial U_0}{\partial z} \tilde{w} - \frac{g \rho_0 \tilde{w}}{U_0 - c} \right] = 0, \quad (2.2.85)$$

which is the dynamic matching condition.

The governing equation (2.2.37) and the matching and boundary conditions (2.2.40), (2.2.57) and (2.2.85) construct the eigenvalue problem.

2.2.4 Perturbation Quantities in the Flow

Perturbation quantities in the flow are easily obtained after the system is solved in terms of \hat{w} . From the definitions, (2.2.26) to (2.2.30),

$$\begin{aligned} \tilde{u} &= \left\{ \hat{u}(z) \exp(i\alpha x - i\omega t) + \text{c.c.} \right\} / 2 \\ &= \left\{ \hat{u}(z) \exp(i\alpha(x-ct)) + \text{c.c.} \right\} / 2, \end{aligned} \quad (2.2.87)$$

$$\tilde{w} = \left\{ \hat{w}(z) \exp(i\alpha(x-ct)) + \text{c.c.} \right\} / 2, \quad (2.2.87)$$

$$\tilde{p} = \left\{ \hat{p}(z) \exp(i\alpha(x-ct)) + \text{c.c.} \right\} / 2, \quad (2.2.88)$$

$$\bar{p} = \left\{ \hat{p}(z) \exp(i\alpha(x-ct)) + \text{c.c.} \right\} / 2, \quad (2.2.89)$$

where c.c. means complex conjugate.

And \hat{w} has the form

$$\hat{w}(z) = |\hat{w}| \exp(i\theta). \quad (2.2.90)$$

Based upon this solution, other elements of the perturbation field can be obtained as follows:

From the continuity equation,

$$\frac{\partial \tilde{u}}{\partial x} + \frac{\partial \tilde{w}}{\partial z} = 0, \quad (2.2.91)$$

i.e.

$$i\alpha \tilde{u} + \frac{\partial \tilde{w}}{\partial z} = 0, \quad (2.2.92)$$

then,

$$\begin{aligned} \tilde{u} &= \frac{i}{\alpha} \frac{\partial \tilde{w}}{\partial z} \\ &= \left\{ \frac{i}{\alpha} \frac{d\hat{w}}{dz} \exp(i\alpha(x-ct)) + \text{c.c.} \right\} / 2. \end{aligned} \quad (2.2.93)$$

If the stream function of the perturbation velocity

field is defined as

$$\begin{aligned}\tilde{\phi} &= \hat{\phi}(z) \exp(i\alpha x - i\omega t) \\ &= \hat{\phi}(z) \exp(i\alpha(x - ct))\end{aligned}\quad (2.2.94)$$

then

$$\tilde{w} = -\frac{\partial \tilde{\phi}}{\partial x} = -i\alpha \tilde{\phi}, \quad (2.2.95)$$

so

$$\begin{aligned}\tilde{\phi} &= \frac{i}{\alpha} \tilde{w}, \\ &= \left\{ \frac{i}{\alpha} \hat{w} \exp(i\alpha(x - ct)) + \text{c.c.} \right\} / 2.\end{aligned}\quad (2.2.96)$$

Therefore, from the kinematic matching condition (2.2.57), the interfacial deformation η satisfies

$$\tilde{w} = \frac{\partial \eta}{\partial t} + U_0 \frac{\partial \eta}{\partial x}, \quad (2.2.97)$$

but, by the definition

$$\eta = \hat{\eta} \exp(i\alpha(x - ct)), \quad (2.2.98)$$

then

$$\frac{\partial \eta}{\partial x} = i\alpha \eta, \quad (2.2.99)$$

$$\frac{\partial \eta}{\partial t} = -i\alpha c \eta = -c \frac{\partial \eta}{\partial x}, \quad (2.2.100)$$

then

$$\frac{\partial \eta}{\partial x} = \frac{\tilde{w}}{U_0 - c} = i\alpha \eta, \quad (2.2.101)$$

therefore, the displacement η must be calculated as

$$\eta = -\frac{i}{\alpha} \frac{\tilde{w}}{U_0 - c},$$

$$= \left\{ -\frac{i}{\alpha} \frac{\widehat{w}}{U_0 - c} \exp(i\alpha(x-ct)) + \text{c.c.} \right\} / 2 . \quad (2.2.102)$$

To determine the Reynolds stress τ averaged over the wave length, the following procedure is used.

Since,

$$\tau = \frac{\alpha}{2\pi} \int_0^{2\pi/\alpha} (-\overline{u\widehat{w}}) d\theta , \quad (2.2.103)$$

where θ is the phase $\alpha x - \omega t$,

from (2.2.87) and (2.2.93)

$$\tau = -\frac{\alpha}{2\pi} \int_0^{2\pi/\alpha} \frac{1}{4} \left\{ \frac{i}{\alpha} \frac{d\widehat{w}}{dz} \exp(i\alpha x - i\omega t) - \frac{i}{\alpha} \frac{d\widehat{w}^*}{dz} \exp(i\alpha x - i\omega^* t) \right\} \left\{ \widehat{w} \exp(i\alpha x - i\omega t) + \widehat{w}^* \exp(i\alpha x - i\omega^* t) \right\} d\theta . \quad (2.2.104)$$

Rewritten ω in the form

$$\omega = \omega_R + i\omega_I , \quad (2.2.105)$$

where

$$c = \frac{\omega}{\alpha} = c_R + ic_I ,$$

then,

$$\begin{aligned} \exp(i\alpha x - i\omega t) &= \exp(\omega_I t) \exp(i\alpha x - i\omega_R t) , \\ &= \exp(\omega_I t) \exp(i\theta) , \end{aligned} \quad (2.2.106)$$

and (2.2.104) becomes

$$\tau = -\frac{1}{4} \frac{\alpha}{2\pi} \int_0^{2\pi/\alpha} \left\{ \frac{i}{\alpha} \frac{d\widehat{w}}{dz} \exp(\omega_I t) \exp(i\theta) - \frac{i}{\alpha} \frac{d\widehat{w}^*}{dz} \exp(\omega_I t) \exp(-i\theta) \right\} \left\{ \widehat{w} \exp(\omega_I t) \exp(i\theta) + \widehat{w}^* \exp(\omega_I t) \exp(-i\theta) \right\} d\theta ,$$

$$\begin{aligned}
&= -\frac{1}{4} \frac{\alpha}{2\pi} \int_0^{2\pi/\alpha} i \left\{ \frac{\widehat{w}^*}{\alpha} \frac{d\widehat{w}}{dz} - \frac{\widehat{w}}{\alpha} \frac{d\widehat{w}^*}{dz} \right\} \exp(2\omega_1 t) d\theta \\
&= -\frac{i}{4\alpha} \exp(2\omega_1 t) \left(\widehat{w}^* \frac{d\widehat{w}}{dz} - \widehat{w} \frac{d\widehat{w}^*}{dz} \right) . \tag{2.2.107}
\end{aligned}$$

Therefore, the Reynolds stress averaged over the wave length is

$$\tau = \frac{i}{2\alpha} \exp(2\omega_1 t) \operatorname{Im} \left(\widehat{w}^* \frac{d\widehat{w}}{dz} \right) , \tag{2.2.108}$$

where $\operatorname{Im}(f)$ is imaginary part of f .

2.3 MODEL I: THICKNESS EFFECTS

2.3.1 Formulation

In this section, the effects of a rigid boundary on the flow stability will be examined by using the equations which were derived in the previous section. To simplify the problem, four layers with piecewise linear velocity profiles will be used in this model, which is based on the assumption of Galilean invariance as well as experimental data (see Figure 2.2). In this type of model, the Taylor-Goldstein equation has the form of (2.3.1) since in each layer there is no density stratification and the velocity profile is linear. An advantage of this model is that the eigenvalue equation can be derived analytically from the governing equation. The governing equation is

$$\frac{d^2 \hat{w}}{dz^2} - \alpha^2 \hat{w} = 0 \quad (2.3.1)$$

Note that if \hat{w} is an eigen function with eigenvalue c for some α , then so too is \hat{w}^* with eigenvalue c^* for the same α . Thus, to each unstable mode there is a corresponding stable mode which has a complex conjugate eigenvalue $C_1 < 0$.

Now the general form of solution of (2.3.1) is

$$\hat{w} = A_1 \exp(\alpha z) + A_2 \exp(-\alpha z) \quad (2.3.2)$$

The basic solution procedure is to assume solutions for (2.3.1) in each layer and apply the boundary and matching conditions to determine the unknown coefficients A_1, A_2, \dots .

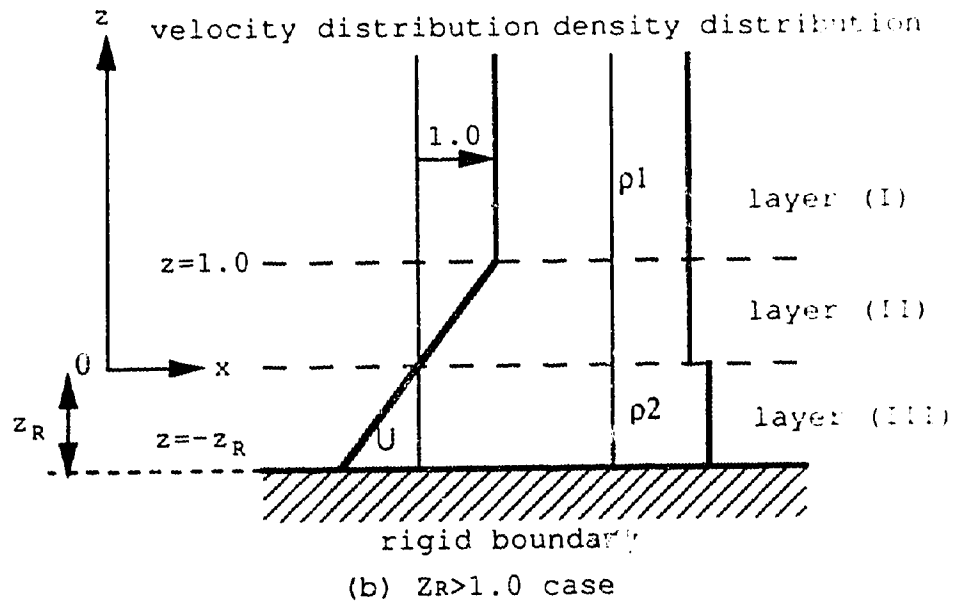
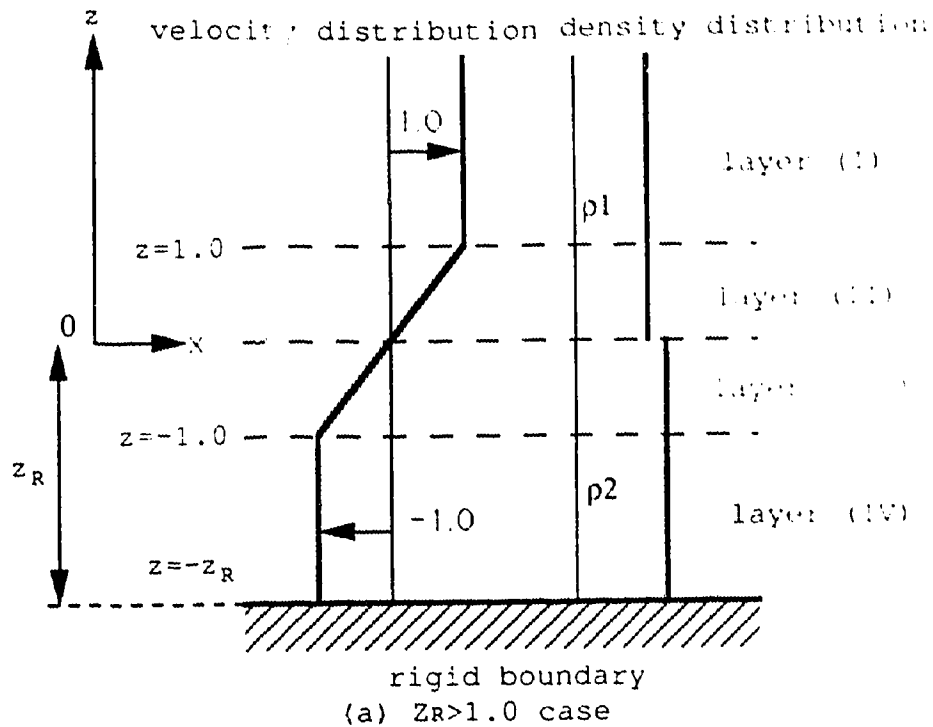


Figure 2.2 (a), (b) Velocity and density profiles of model I

In order to get non-trivial solutions, the eigenvalue equation must be solved, establishing the dispersion relationship for internal waves in this system.

In this model, the formulations are slightly different according to whether the thickness of the lower layer z_R is larger or smaller than half the shear layer thickness: cases (a) and (b). All the quantities in this section are non-dimensionalized by characteristic length and velocity scales L and V . These are chosen as half of shear layer thickness and half of the maximum-minimum velocity difference respectively.

First of all, let us consider model I(a). Although the general solution is written in the form of (2.3.2), the boundary conditions in layers (I) and (IV) require slightly different forms of solution. For layer (I), the boundary condition is that \hat{w} must be 'bounded' at z is infinity, and for layer (IV), the condition is that \hat{w} is zero at $z = -z_R$. Therefore, the solutions for each layer become as follows:

$$\hat{w}_I = A_1 \exp(-\alpha z) , \quad (2.3.3)$$

$$\hat{w}_{II} = A_2 \exp(\alpha z) + A_3 \exp(-\alpha z) , \quad (3.4)$$

$$\hat{w}_{III} = A_4 \exp(\alpha z) + A_5 \exp(-\alpha z) , \quad (5)$$

$$\hat{w}_{IV} = A_6 \sinh(\alpha(z+z_R)) , \quad (6)$$

where A_1, A_2, \dots are coefficients and \hat{w}_I is solution in layer (I).

Applying the kinematic (2.2.40) and dynamic (2.2.57) matching conditions to these solutions, the kinematic matching condition implies

$$A_1 \exp(-\alpha) - A_2 \exp(\alpha) - A_3 \exp(-\alpha) = 0 \text{ at } z=1.0. \quad (2.3.7)$$

And the dynamic matching condition at $z=1.0$ is

$$A_1 \{ \alpha(1-c) \exp(-\alpha) \} + A_2 \{ \alpha(1-c) - 1 \} \exp(\alpha) + A_3 \{ -\alpha(1-c) - 1 \} \exp(-\alpha) = 0, \quad (2.3.8)$$

Thus, at $z=0$

$$A_2 + A_3 - A_4 - A_5 = 0, \quad (2.3.9)$$

$$A_2 \gamma \left\{ \alpha c + 1 - \frac{g_*}{c} \right\} + A_3 \gamma \left\{ -\alpha c + 1 - \frac{g_*}{c} \right\} + A_4 \left\{ -\alpha c - 1 + \frac{g_*}{c} \right\} + A_5 \left\{ \alpha c - 1 + \frac{g_*}{c} \right\} = 0, \quad (2.3.10)$$

And at $z=-1.0$

$$A_4 \exp(-\alpha) + A_5 \exp(\alpha) - A_6 \sinh(\alpha(z_R-1)) = 0, \quad (2.3.11)$$

$$A_4 \gamma \{ \alpha(1+c) + 1 \} \exp(-\alpha) + A_5 \gamma \{ -\alpha(1+c) + 1 \} \exp(\alpha) + A_6 \{ -\alpha(1+c) \cosh(\alpha(z_R-1)) \} = 0, \quad (2.3.12)$$

where

$$\gamma = \frac{\rho_1}{\rho_2}, \quad g_* = \frac{Ri_o}{1-\gamma}, \quad Ri_o = \frac{(1-\gamma)gL}{V^2},$$

which are specific weight, non-dimensional gravitational acceleration and over-all Richardson number.

These conditions may be written in matrix form as

$$\left(\begin{array}{c} \mathbf{M} \end{array} \right) \left(\begin{array}{c} A_1 \\ A_2 \\ A_3 \\ A_4 \\ A_5 \\ A_6 \end{array} \right) = \left(\begin{array}{c} 0 \end{array} \right). \quad (2.3.13)$$

For a non-trivial solution, the $\det \mathbf{M} = 0$ must be satisfied. The determinant of \mathbf{M} can be obtained analytically by using 'Cramer's rule', followed by a sort in terms of the complex phase velocity c . The final form of the dispersion relationship for case(a) is

$$a_4 c^4 + a_3 c^3 + a_2 c^2 + a_1 c + a_0 = 0 , \quad (2.3.14)$$

where

$$\begin{aligned} a_4 &= \gamma B_4 + B_4^\# , \\ a_3 &= \gamma B_3 + B_3^\# , \\ a_2 &= \gamma B_2 + B_2^\# , \\ a_1 &= \gamma B_1 + B_1^\# , \\ a_0 &= \gamma B_0 + B_0^\# , \end{aligned} \quad (2.3.15)$$

$$\begin{aligned} B_4 &= R_1 R_5 , & B_4^\# &= R_1^\# R_5^\# , \\ B_3 &= R_1 R_6 + R_2 R_5 , & B_3^\# &= R_1^\# R_6^\# + R_2^\# R_5^\# , \\ B_2 &= R_2 R_6 + R_3 R_5 , & B_2^\# &= R_2^\# R_6^\# + R_3^\# R_5^\# , \\ B_1 &= R_3 R_6 + R_4 R_5 , & B_1^\# &= R_3^\# R_6^\# + R_4^\# R_5^\# , \\ B_0 &= R_4 R_6 , & B_0^\# &= R_4^\# R_6^\# , \end{aligned} \quad (2.3.16)$$

$$\begin{aligned} R_1 &= 2\alpha^2 , \\ R_2 &= -\alpha(2\alpha+1-\exp(-2\alpha)) , \\ R_3 &= 2\alpha+2\alpha g_*-1+\exp(-2\alpha) , \\ R_4 &= -g_*(2\alpha-1+\exp(-2\alpha)) , \\ R_5 &= \alpha(\alpha \sinh(\alpha z_R - \alpha) + \sinh(\alpha) \cosh(\alpha z_R - \alpha)) , \\ R_6 &= R_5 - \sinh(\alpha) \sinh(\alpha z_R - \alpha) , \end{aligned}$$

$$\begin{aligned}
R_1^{\#} &= \alpha^2 (\cosh(\alpha z_R) \cosh(\alpha z_R - \alpha) + \sinh(\alpha) \sinh(\alpha z_R - \alpha)) , \\
R_2^{\#} &= R_1^{\#} - R_5 - \alpha \cosh(\alpha z_R) \sinh(\alpha z_R - \alpha) , \\
R_3^{\#} &= (1 - g) R_5 - \sinh(\alpha) \sinh(\alpha z_R - \alpha) , \\
R_4^{\#} &= -g (R_5 - \sinh(\alpha) \sinh(\alpha z_R - \alpha)) , \\
R_5^{\#} &= 2\alpha , \\
R_6^{\#} &= -(2\alpha - 1 + \exp(-2\alpha)) .
\end{aligned} \tag{2.3.17}$$

By the same procedure, the dispersion relationship for case (b) can be obtained as follows:

$$a_3 c^3 + a_2 c^2 + a_1 c + a_0 = 0 , \tag{2.3.18}$$

where

$$\begin{aligned}
a_3 &= R_1 R_1^{\#} , \\
a_2 &= R_0 R_2^{\#} + R_1 R_1^{\#} + B_2 , \\
a_1 &= R_0 R_1^{\#} + R_1 R_0^{\#} + B_1 , \\
a_0 &= R_0 R_0^{\#} + B_0 ,
\end{aligned} \tag{2.3.19}$$

$$\begin{aligned}
B_0 &= -(\gamma - 1) g \exp(-2\alpha) \sinh(\alpha z_R) , \\
&= R_{i_0} \exp(-2\alpha) \sinh(\alpha z_R) , \\
B_1 &= (\gamma - 1) \exp(-2\alpha) \sinh(\alpha z_R) , \\
B_2 &= \alpha (\gamma \sinh(\alpha z_R) - \cosh(\alpha z_R)) \exp(-2\alpha) , \\
R_0 &= -2\alpha + 1 , \\
R_1 &= 2\alpha , \\
R_0^{\#} &= (\gamma - 1) g \sinh(\alpha z_R) = -R_{i_0} \sinh(\alpha z_R) , \\
R_1^{\#} &= -(\gamma - 1) \sinh(\alpha z_R) , \\
R_2^{\#} &= \alpha (\cosh(\alpha z_R) + \gamma \sinh(\alpha z_R)) .
\end{aligned} \tag{2.3.20}$$

This dispersion relationship was solved using the IMSL polynomial solver ZRPOLY. A discussion of the results follows.

2.3.2. Solution

The proceeding problems were solved numerically for the parameter ranges $1.0 \leq Z_R \leq \infty$, $0.0 \leq \alpha \leq 3.0$, $0.0 \leq Ri \leq 2.0$. The calculations were performed using the University of Alberta Computing Service's Amdahl 5870 system with IMSL subroutine library and FORTRAN 77 programming language. Figure 2.3 to Figure 2.13 summarize the results obtained. These include the dispersion relationship, neutral boundaries, growth rates on α - Ri plane and some other perturbation quantity profiles. Figure 2.3 illustrates that a lower layer thickness Z_R , does not affect the stability of the flow until it becomes less than 2.0. However, with decreasing Z_R , the growth rate of SVB waves gradually decreases until $Z_R=1.03$, all the SVB waves are stabilized and only SVA waves can exist. As there is no critical value for SVA waves in the range of the calculations, it implies that the wave may be observed in upper layer under this condition. This so-called "one-sidedness" phenomena was studied by Maxworthy and Browand (1975).

The critical value of $Z_R=1.03$ is slightly smaller than calculated by Howard (1964) which was $Z_R=1.1997$ for the homogeneous case. As mentioned in part one, Hazel (1972) calculated this criterion and estimated the value to be in

the range $1.195 < Z_R < 1.205$. Although his calculation showed some problems due to the numerical instabilities with small wave number and Richardson numbers, the criterion had a tendency to converge towards Howard's value as $Ri \rightarrow 0$.

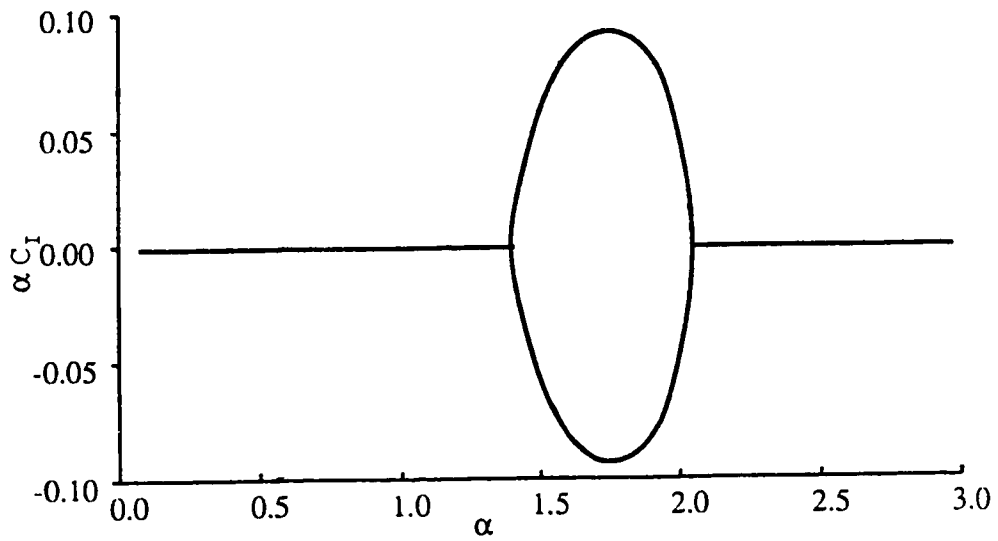
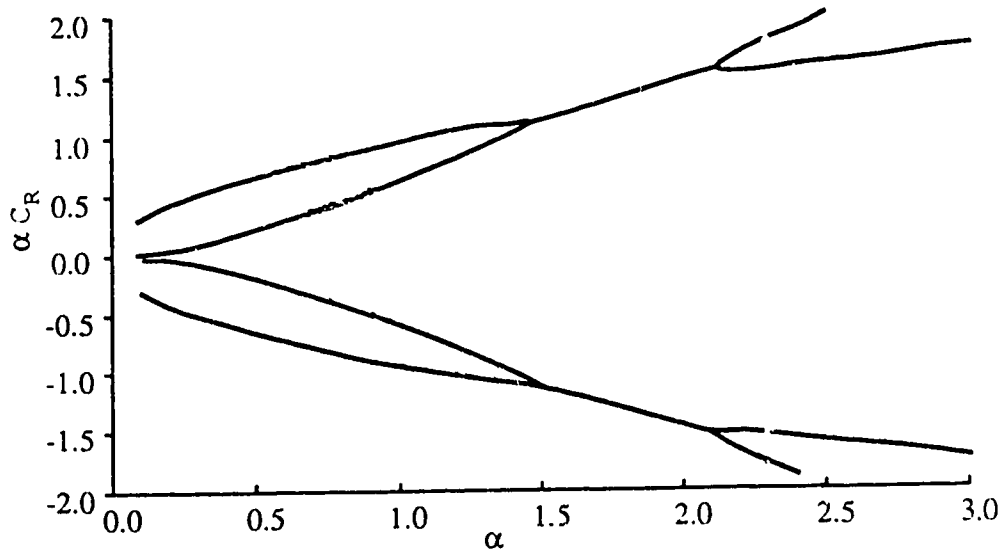
Figure 2.8 shows the neutral boundaries for different values of Z_R and illustrates that both SVA and SVB wave numbers tend to get smaller as Z_R decreases. Furthermore, the internal structure of the stability boundaries is shown in Figures 2.4 to 2.7. It is interesting to note that as $Z_R \rightarrow 1.0$, the waves which have smaller Richardson number are relatively stable compared to the waves for which Ri is about 0.6 to 1.0. This sounds contradictory since a smaller Richardson number usually implies less density difference and greater instability. This problem will be discussed later in section 2.5.

The perturbation quantities (such as \tilde{u} , \tilde{w} , τ , η) are presented in Figures 2.9 to 2.12. By comparing Figure 2.9 to 2.10 (which shows the complex conjugate eigenvalues of 2.9), it is easy to see that \tilde{u} and η are exactly the same, but \tilde{w} has the opposite phase and the Reynolds stress τ is positive for the unstable case and negative for stable case. There is a clear relationship between the Reynolds stress and the phase of \tilde{w} since both of them imply the direction of energy transfer between turbulence and the mean flow. It can be shown that $d\theta/dz > 0$ and $\tau > 0$ are necessary conditions for instability, (see Appendix A), and can easily be seen in Figure 2.12 which is a neutral mode case. These plots also

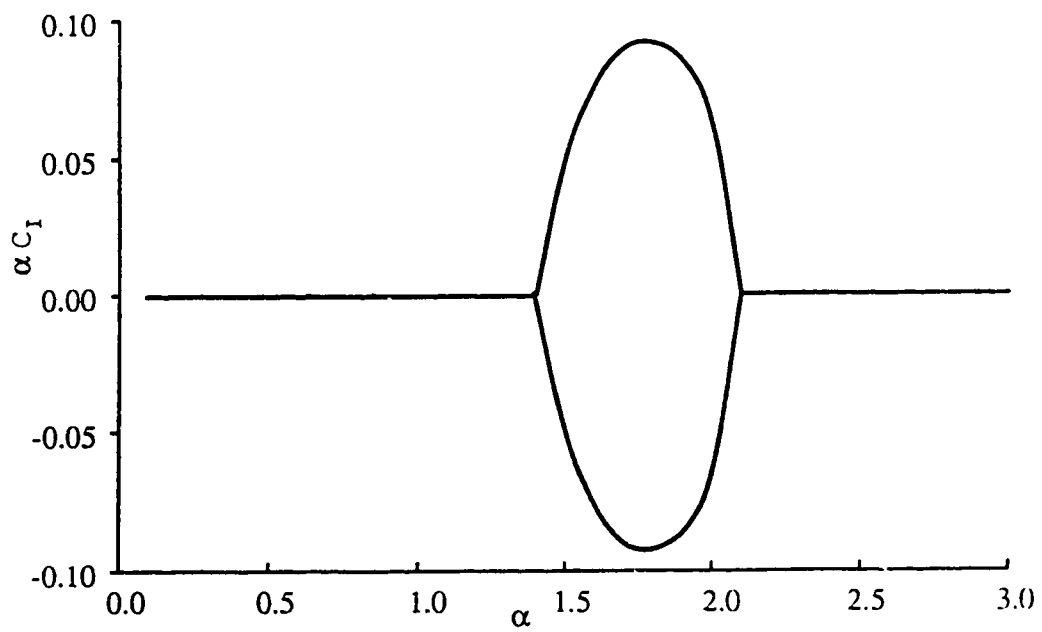
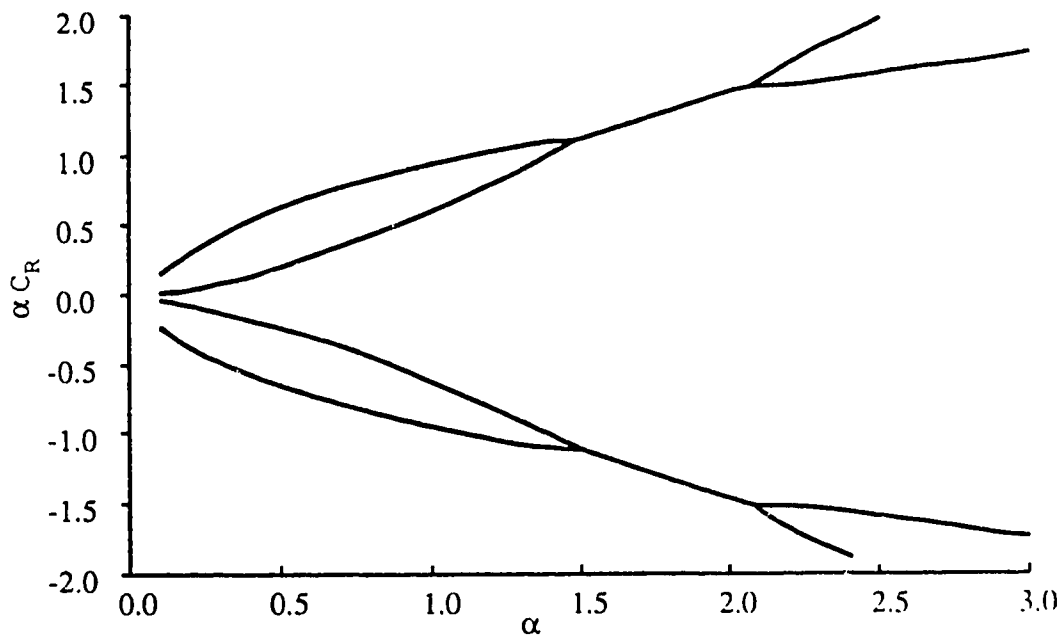
show that the critical level has a maximum displacement η which corresponds to the observations.

Figure 2.13, the streamlines of these waves are plotted and have very good agreement with experiments.

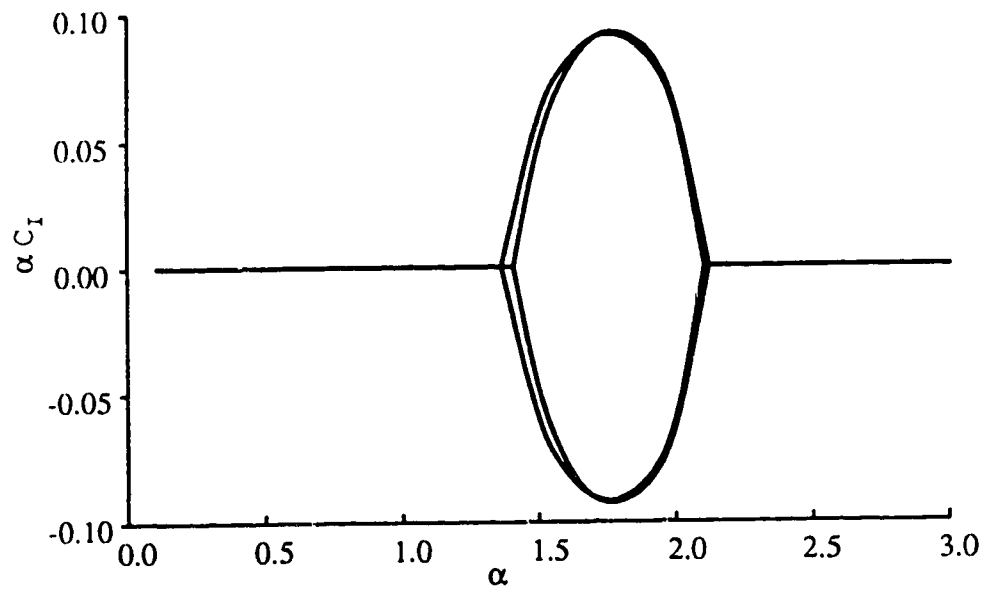
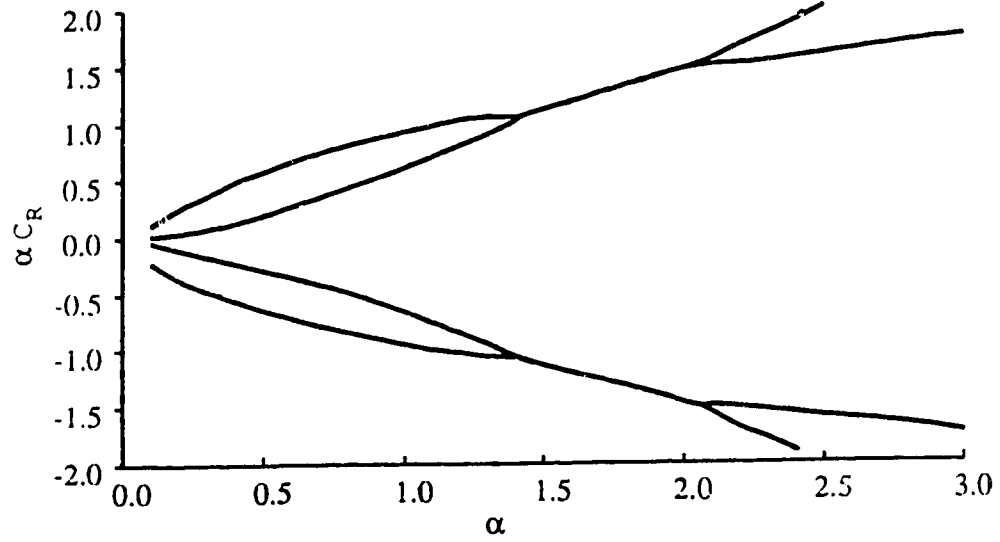
Figure 2.3 (a)-(h). Dispersion relationship V.S. lower layer thickness ZR . $Ri=2.0$ case



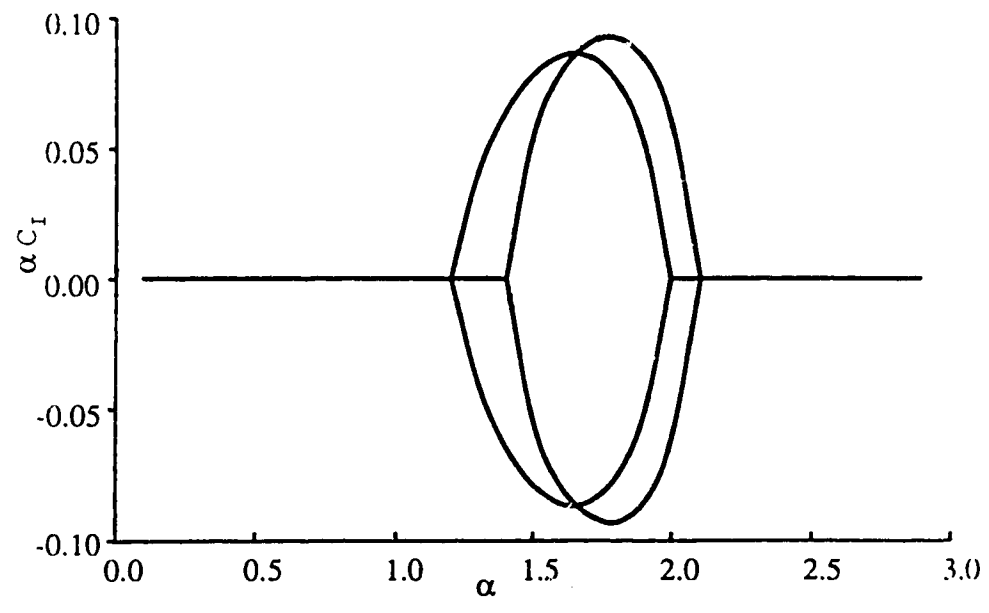
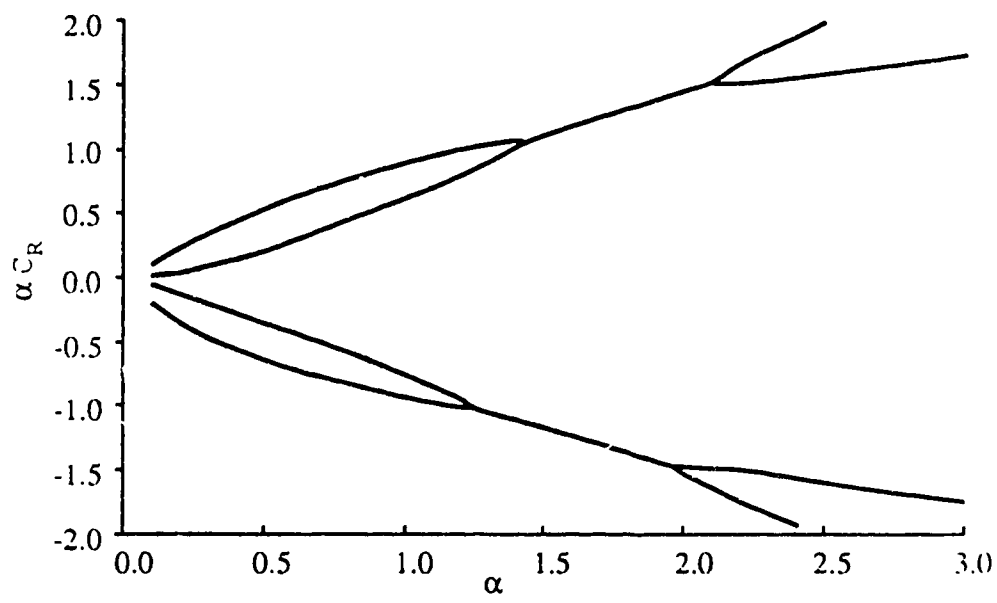
(a) $ZR = \text{inf.}$ case



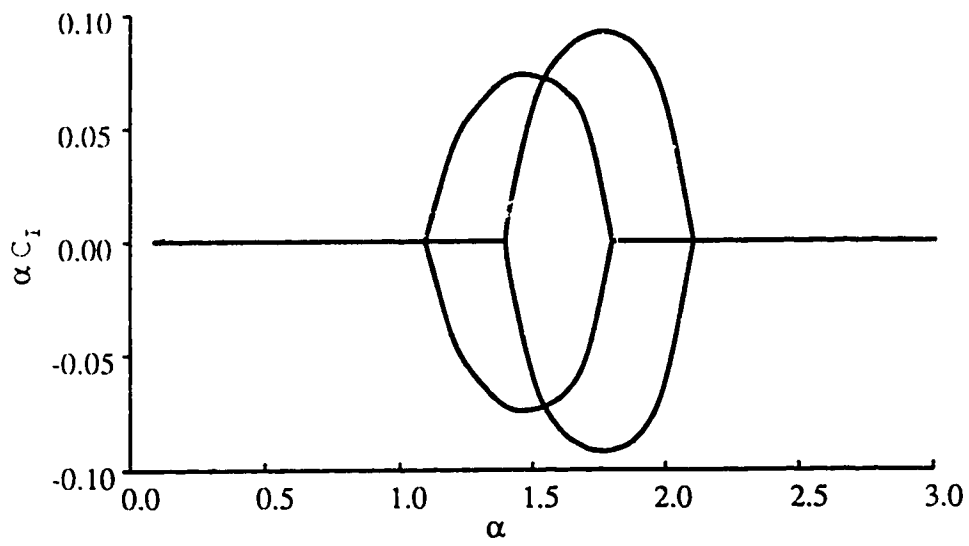
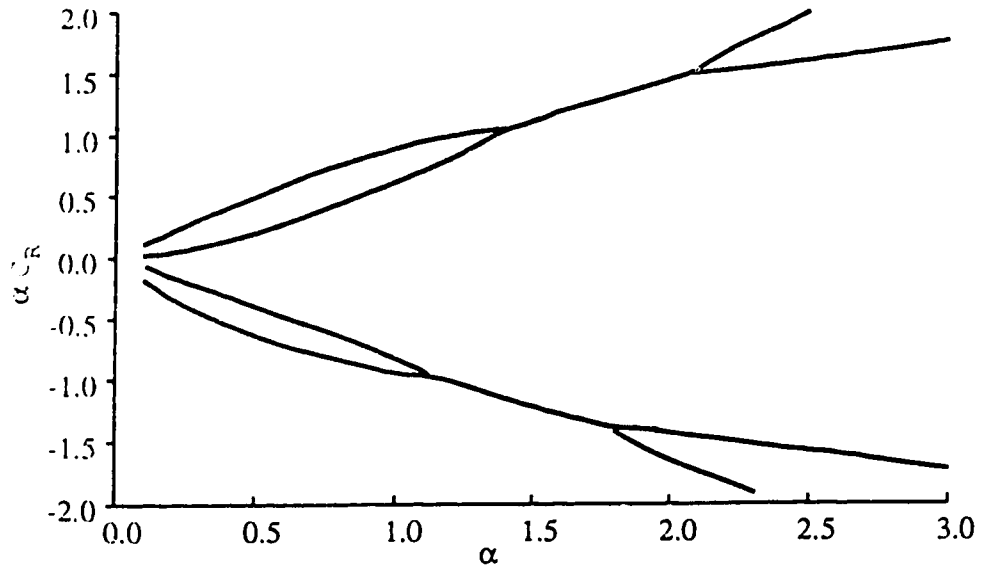
(b) ZR=3.0 case

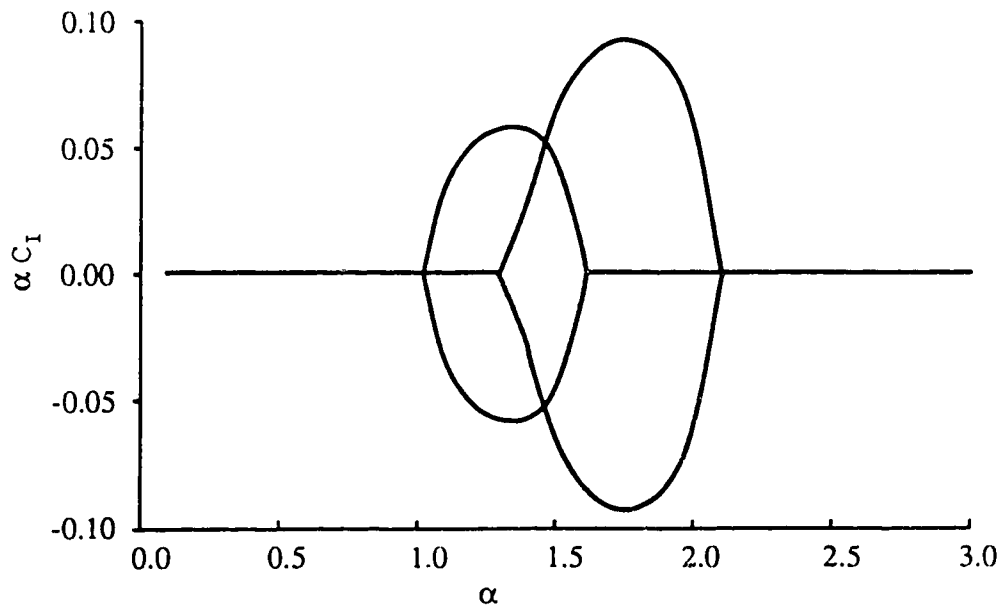
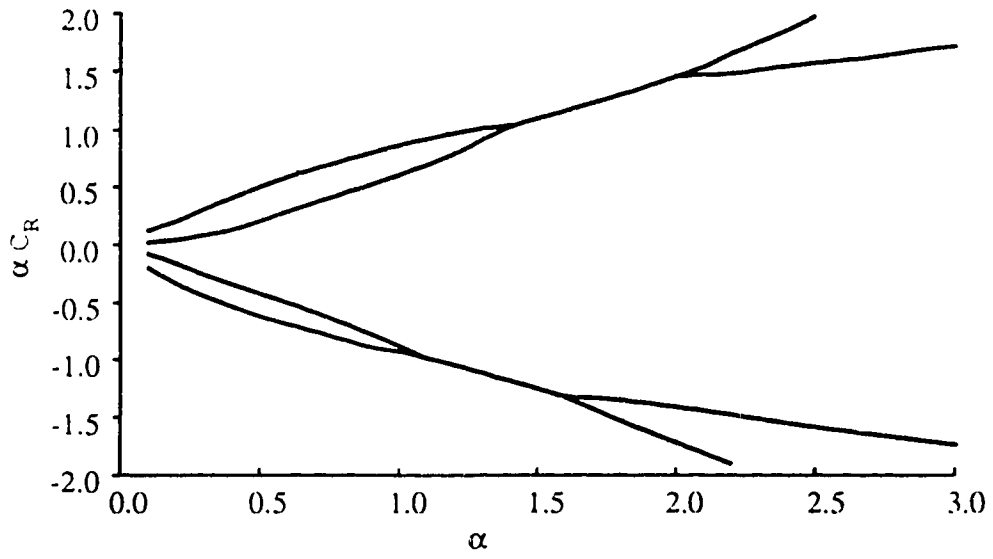


(c) $ZR=2.0$ case

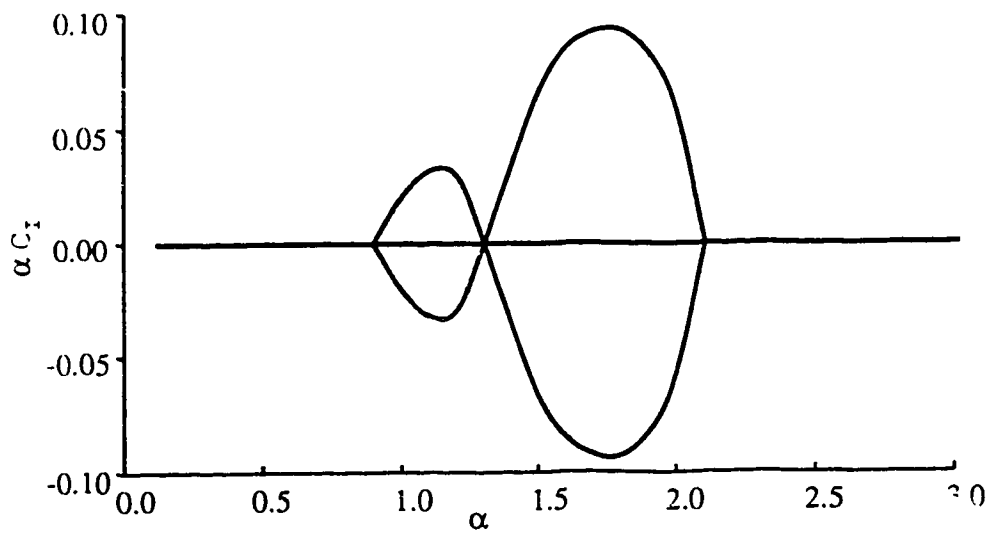
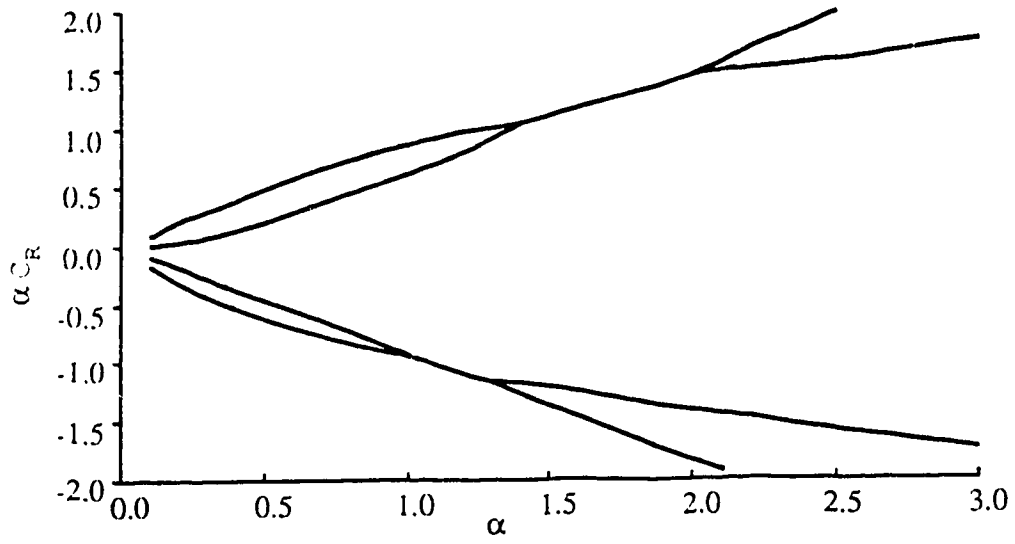


(d) $ZR=1.5$ case

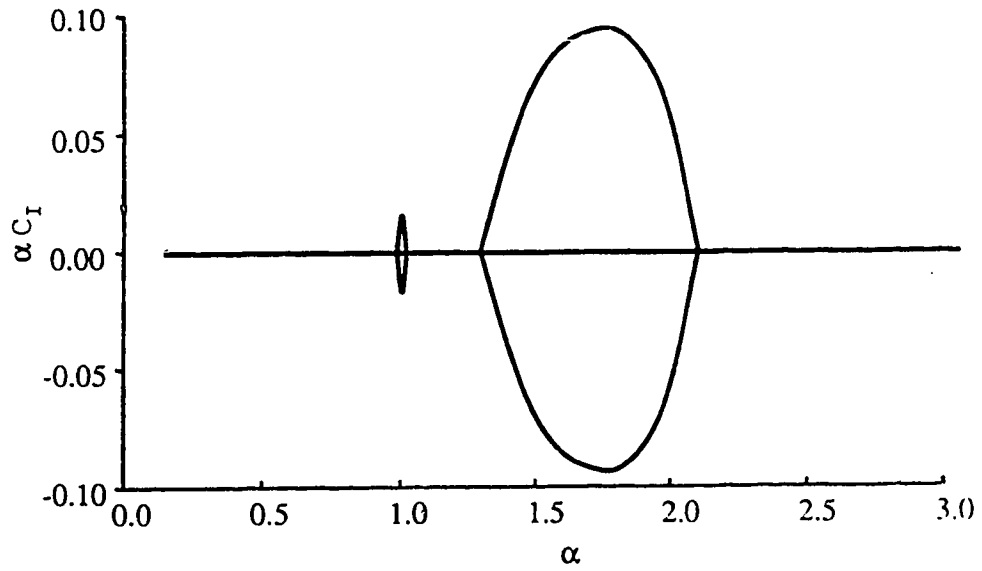
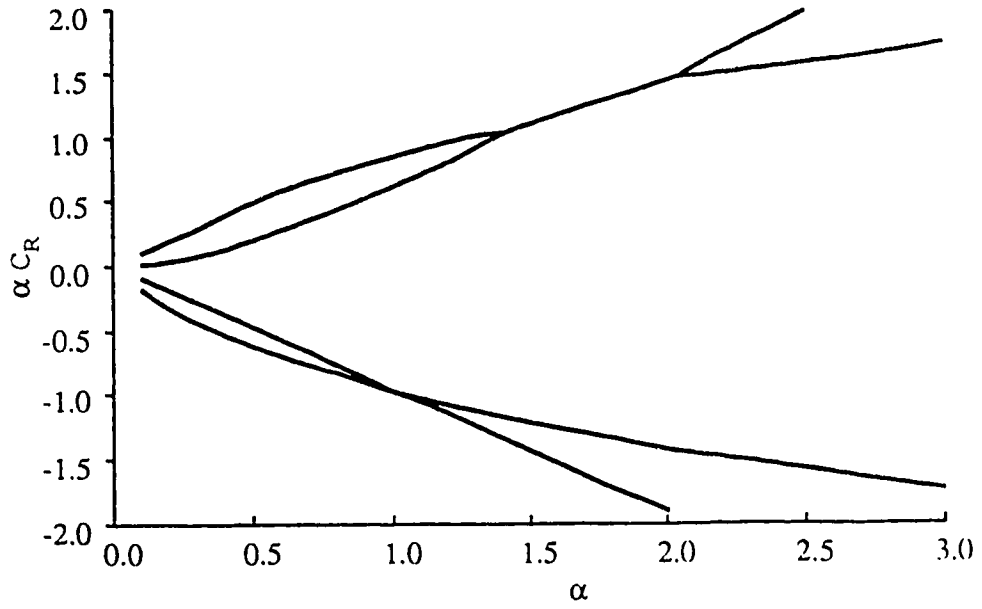
(e) $ZR=1.3$ case



(f) $ZR=1.2$ case



(g) ZR=1.1 case

(h) $ZR=1.05$ case

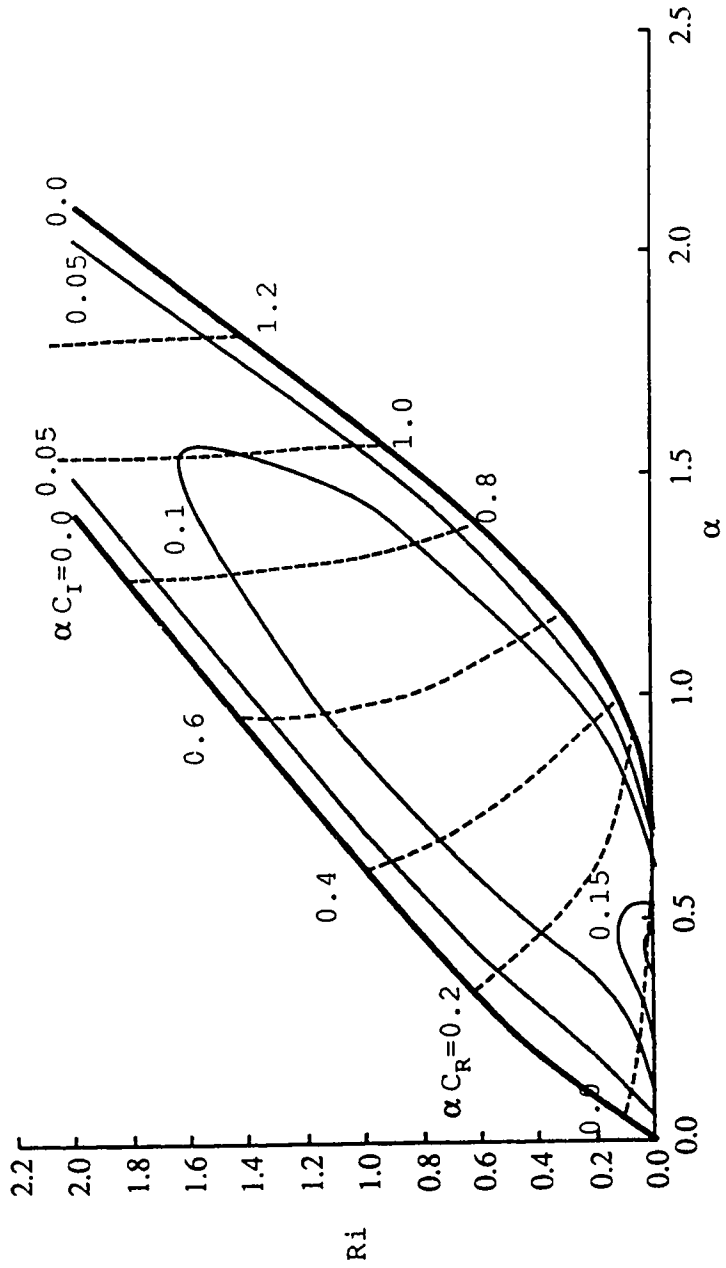


Figure 2.4. Dispersion relationship for $Z_R = \text{inf}$. SVA and SVB solution

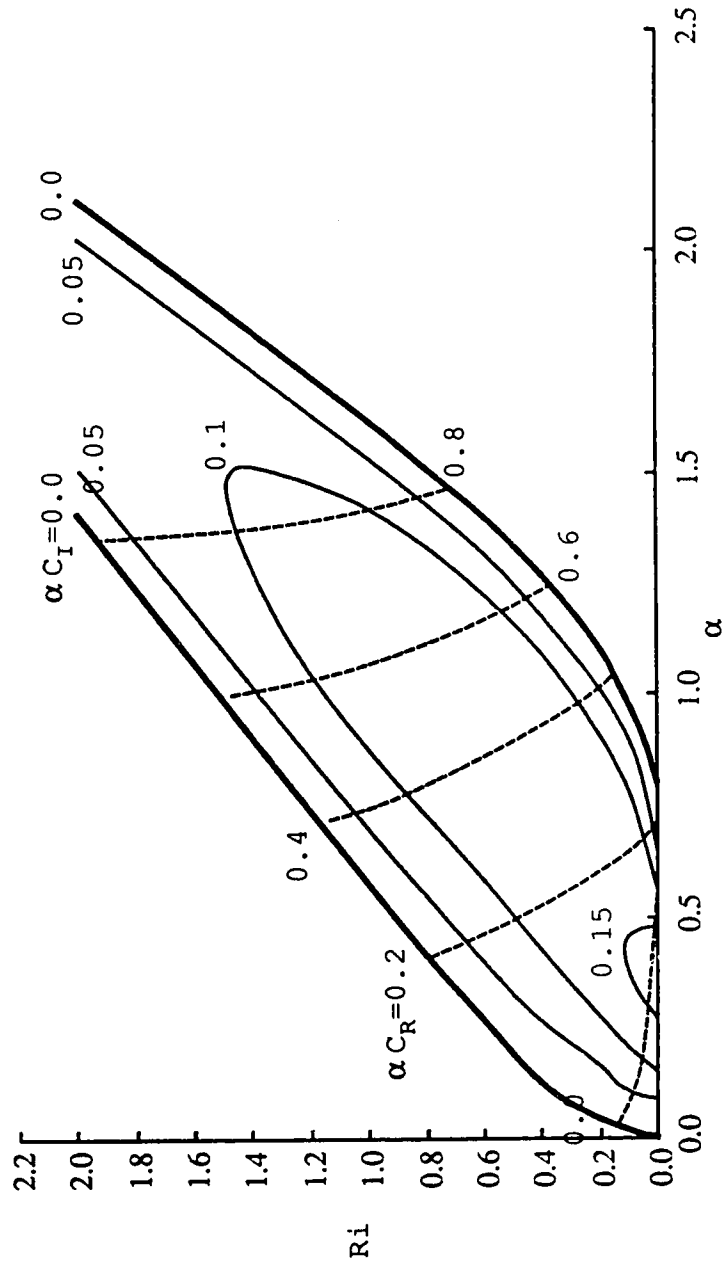


Figure 2.5. Dispersion relationship for $ZR=3.0$ SVA and SVB solution

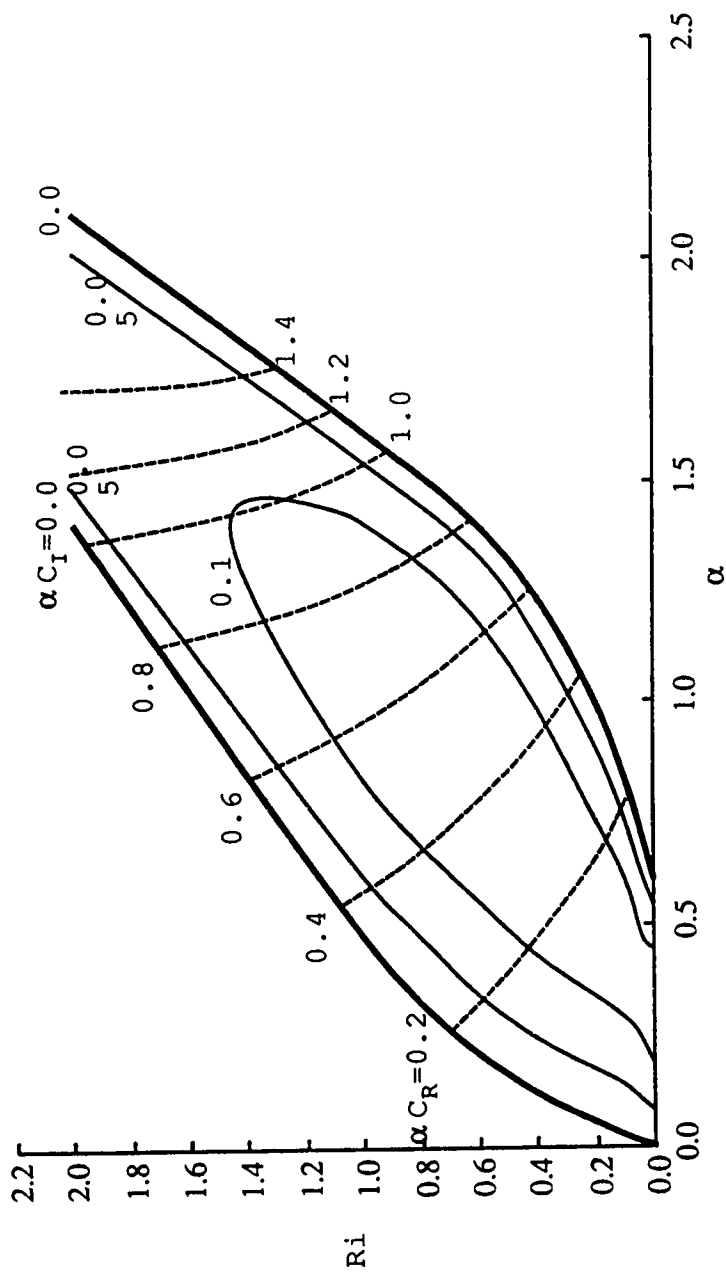
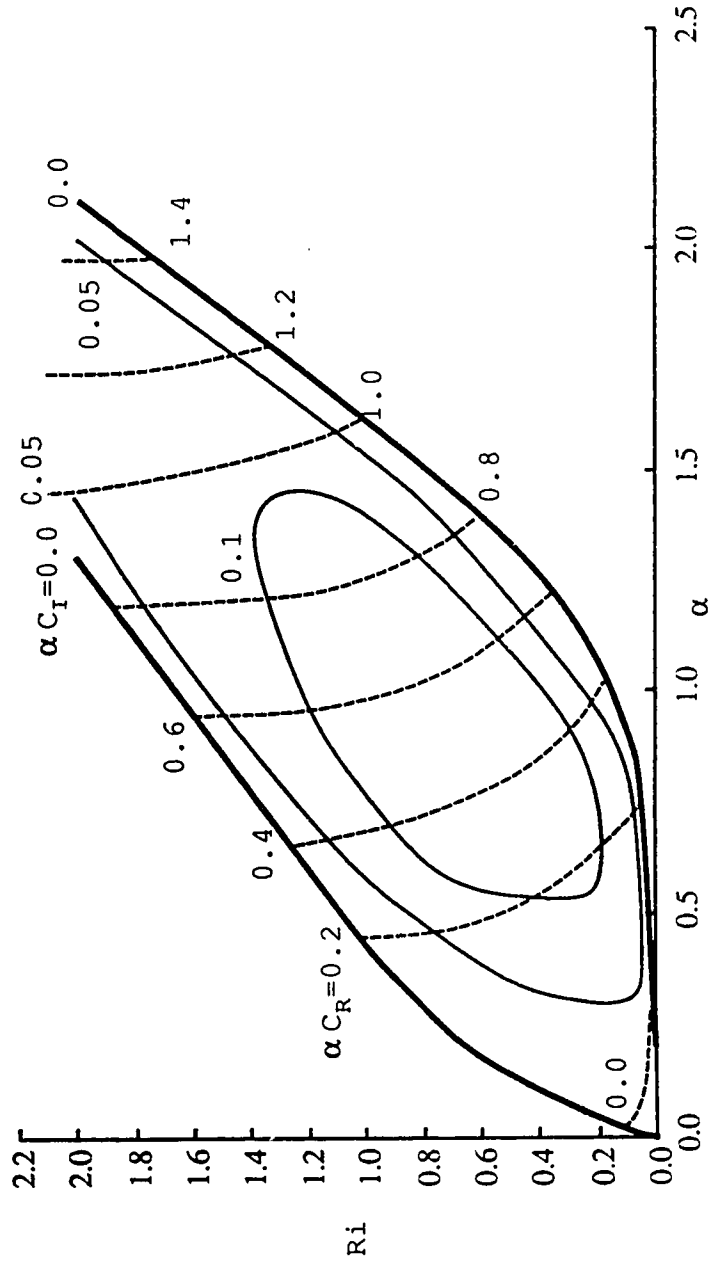
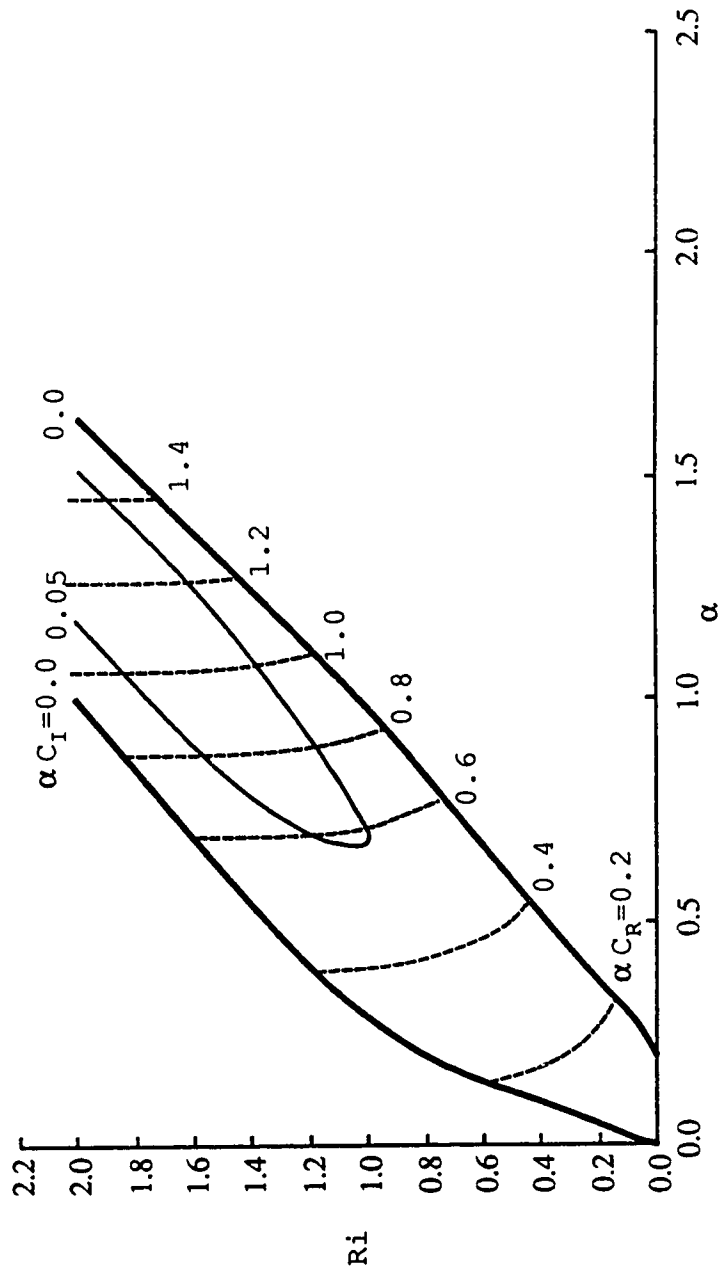


Figure 2.6. Dispersion relationship for $zR=2.0$ SVA and SVB solution

Figure 2.7 (a)-(b). Dispersion relationship for $ZR=1.2$

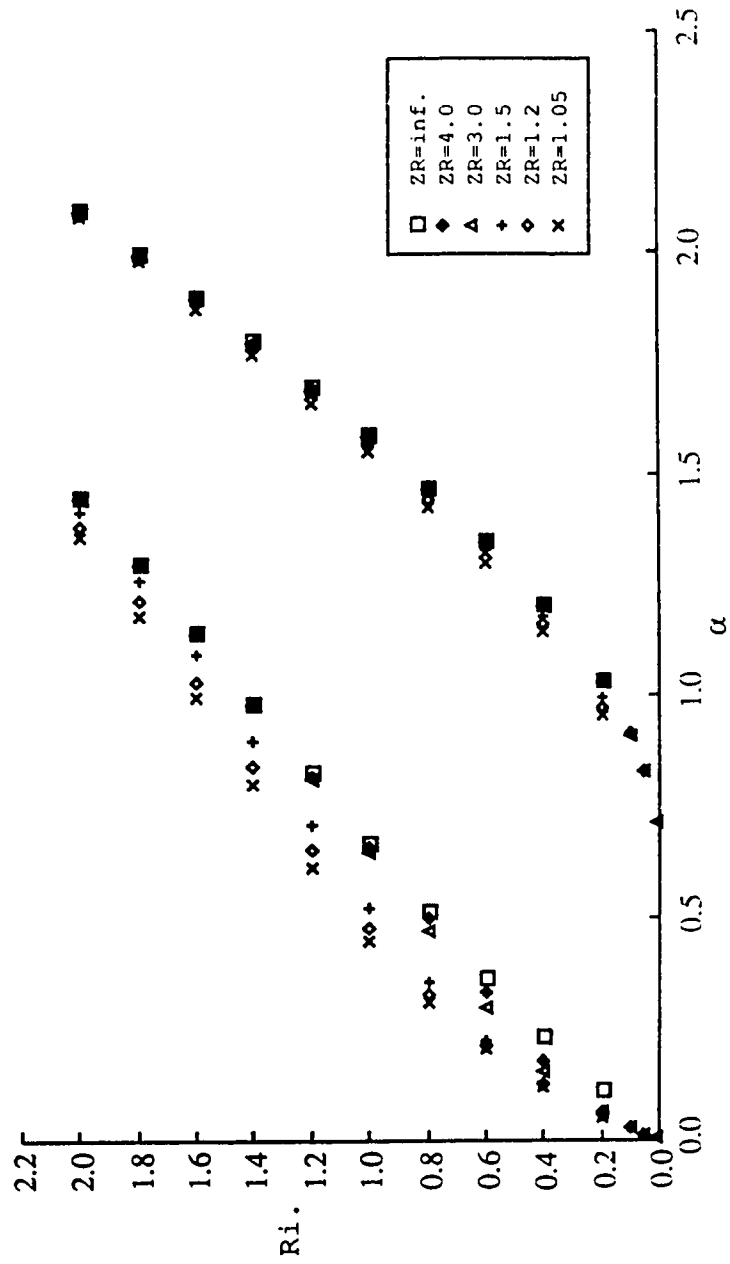


(a) SVA solution

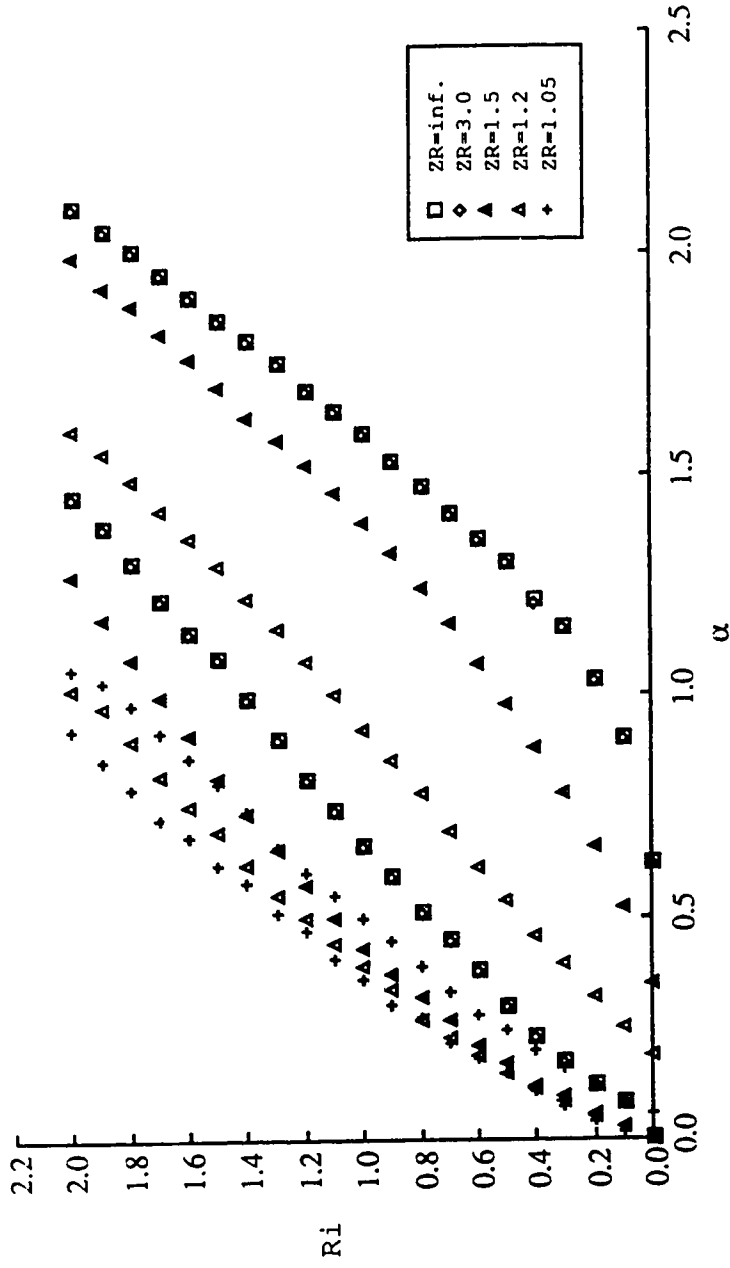


(b) SVB solution

Figure 2.8 (a)-(b). Neutral boundaries VS. lower layer thickness ZR

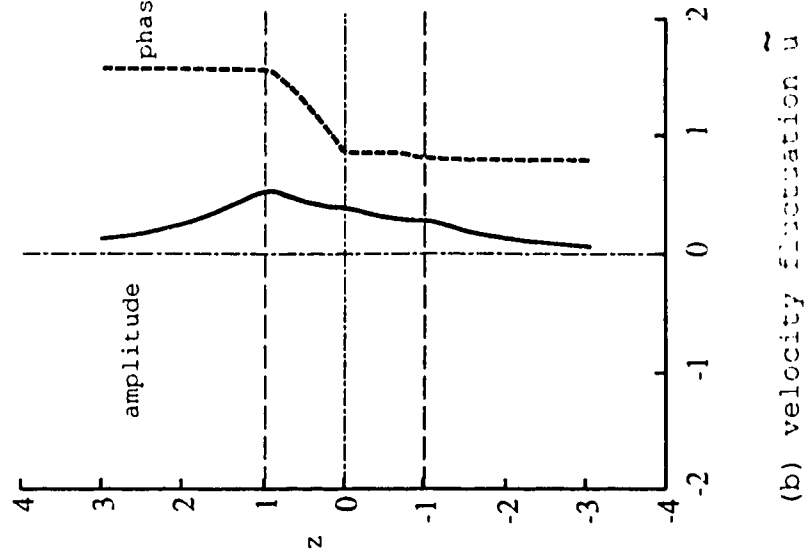
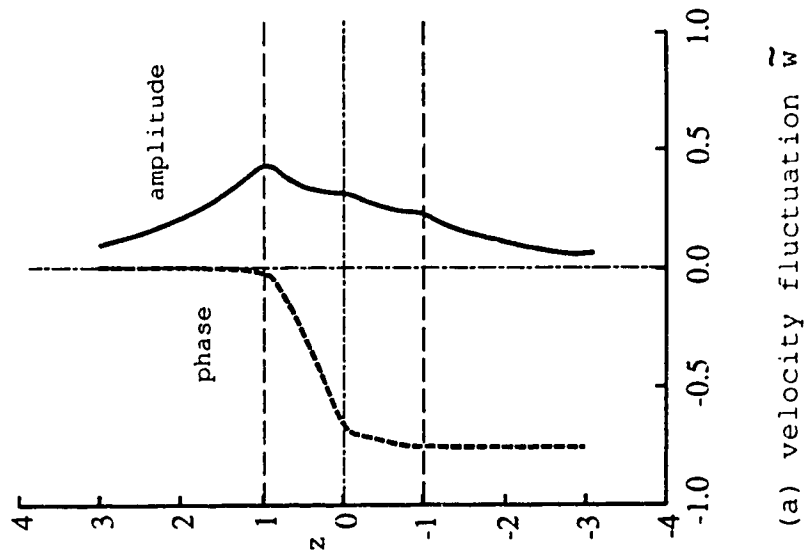


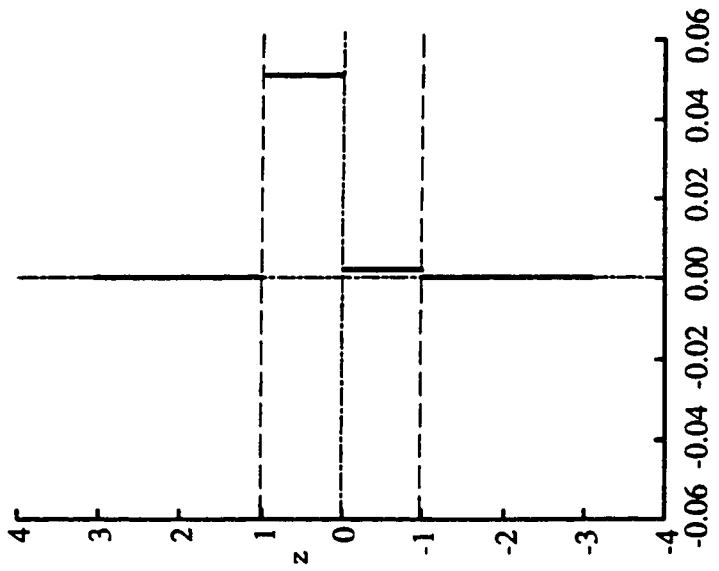
(a) SVA solutions



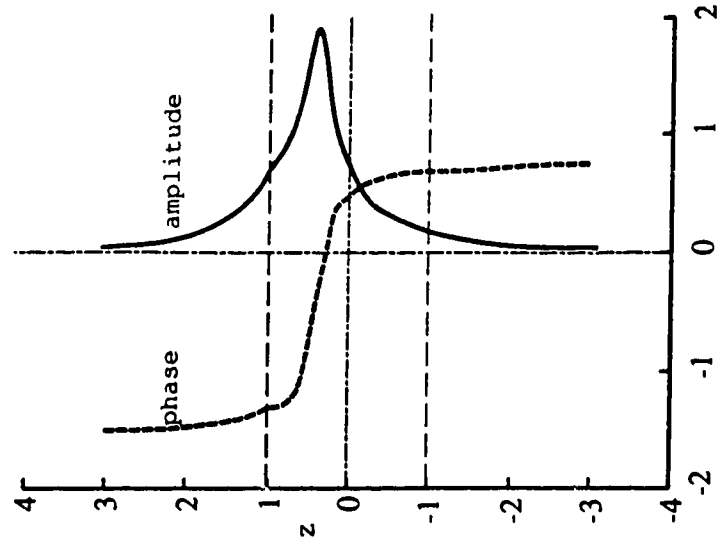
(b) SVB solutions

Figure 2.9 (a)-(d). The perturbation quantities. $Ri=0.2$ $\alpha=0.8$
 $c=(0.388, 0.161)$ Unbounded case



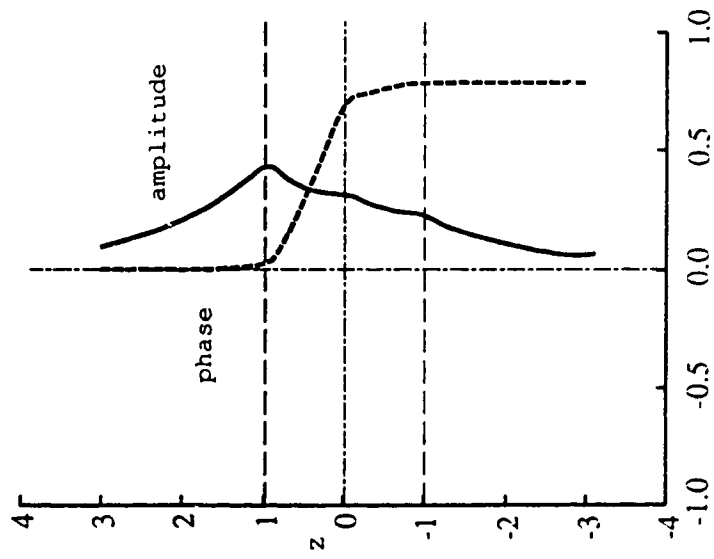


(c) Reynolds stress τ

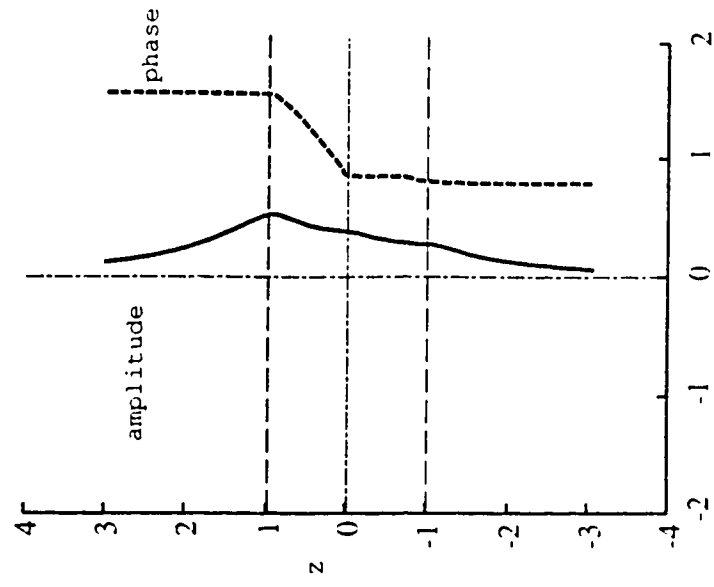


(d) displacement η

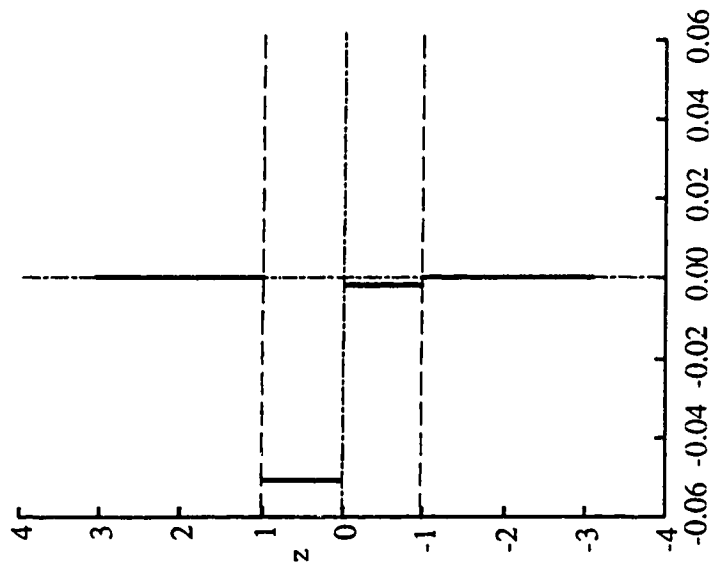
Figure 2.10 (a)-(d). The perturbation quantities. $Ri=0.2$ $\alpha=0.8$
 $c=(0.388, -0.161)$ Unbounded case



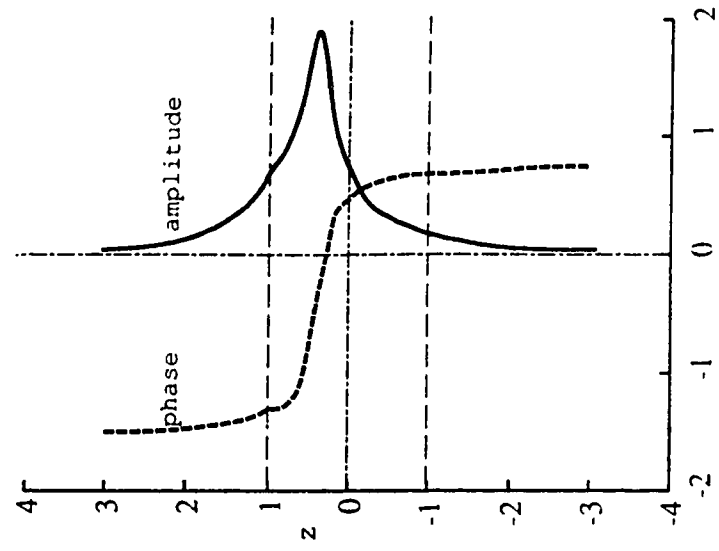
(a) velocity fluctuation \tilde{w}



(b) velocity fluctuation \tilde{u}

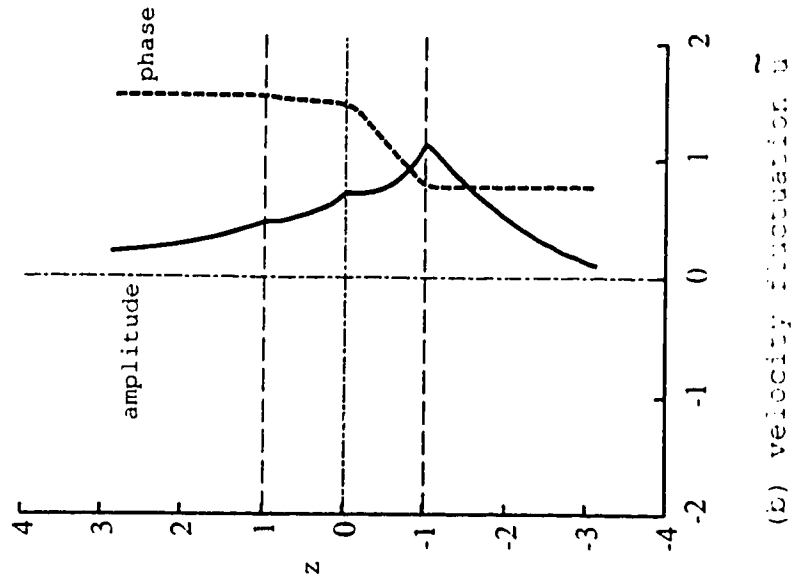
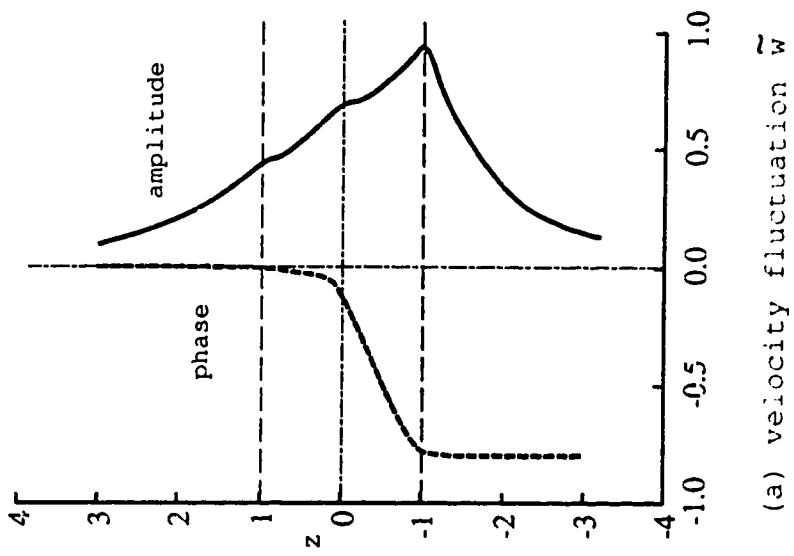


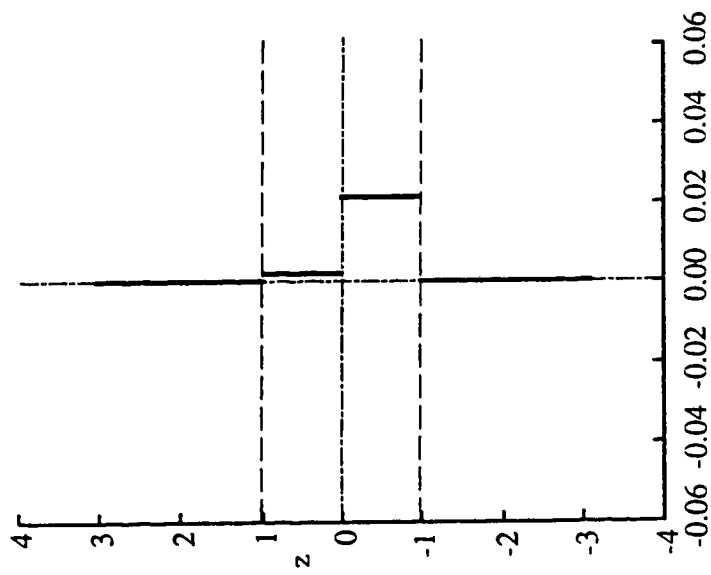
(c) Reynolds stress τ



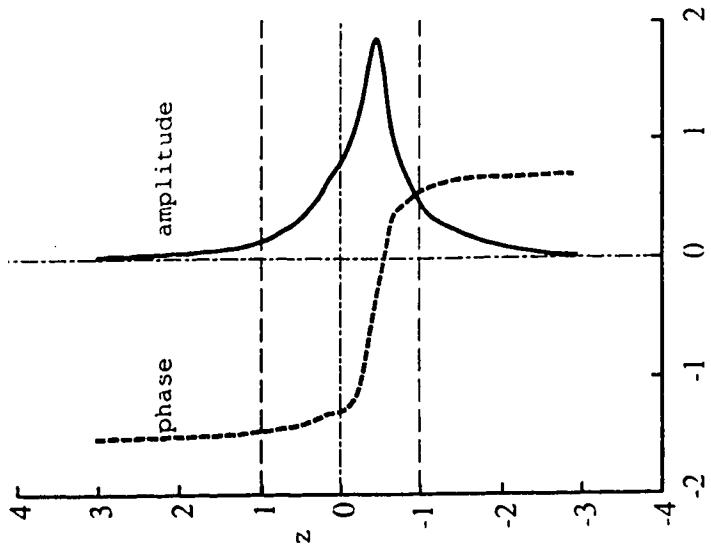
(d) displacement η

Figure 2.11 (a)-(d). The perturbation quantities. $Ri=0.2$ $\alpha=0.8$
 $c=(.389, 0.162)$ Unbounded case



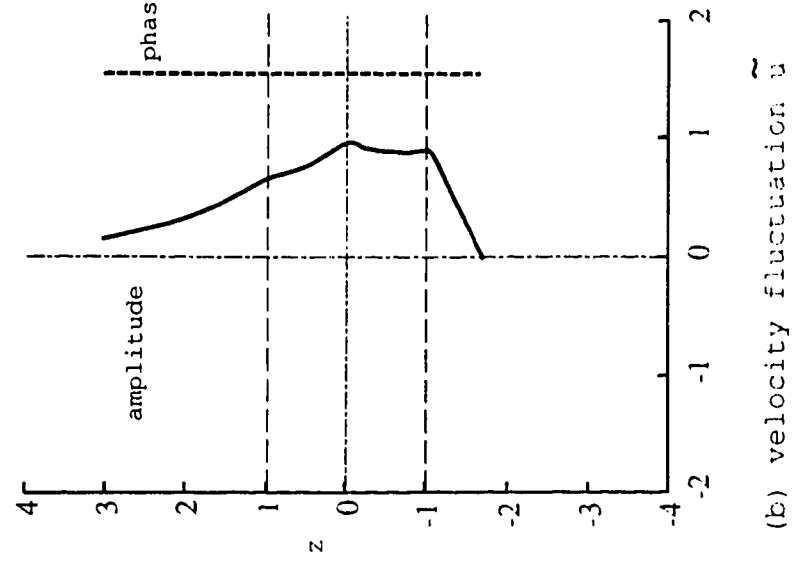
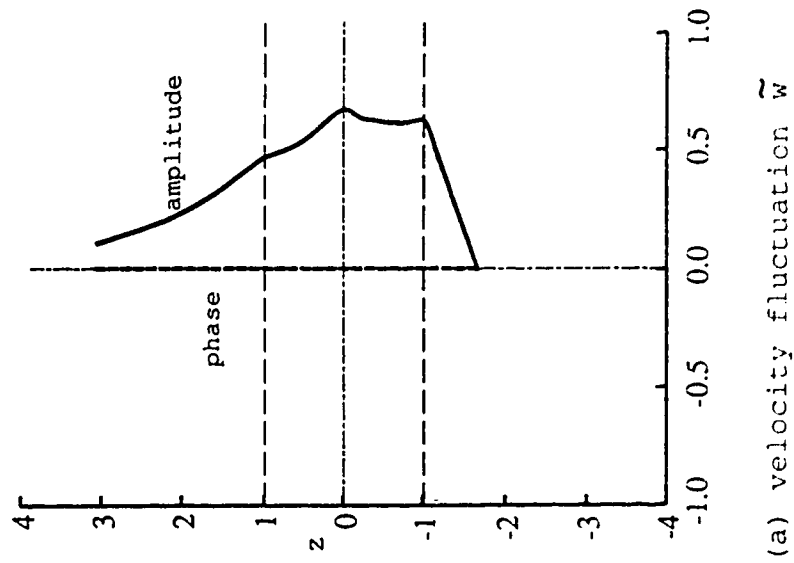


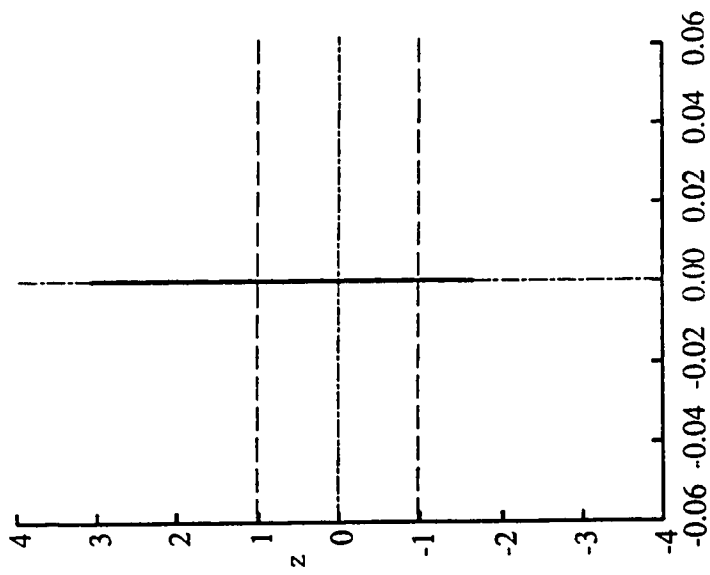
(c) Reynolds stress τ



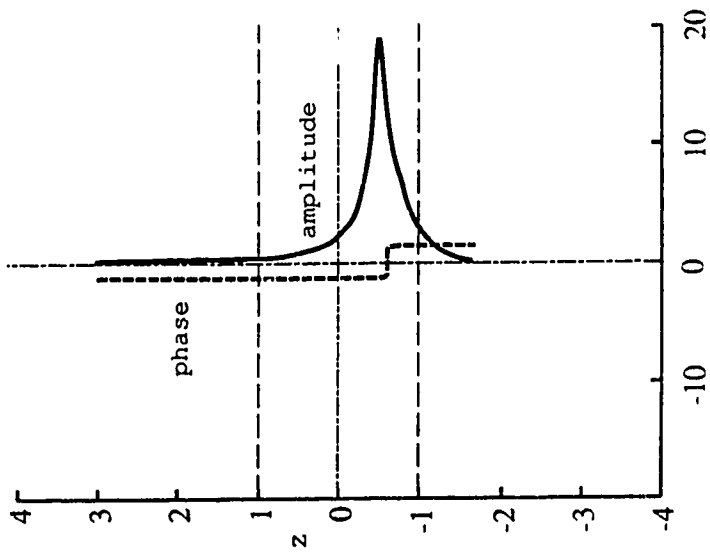
(d) displacement η

Figure 2.12 (a)-(d). The perturbation quantities. $Ri=0.2$ $\alpha=0.8$
 $c=(-0.459, 0.0)$ $ZR=1.68$ case





(c) Reynolds stress τ



(d) displacement η

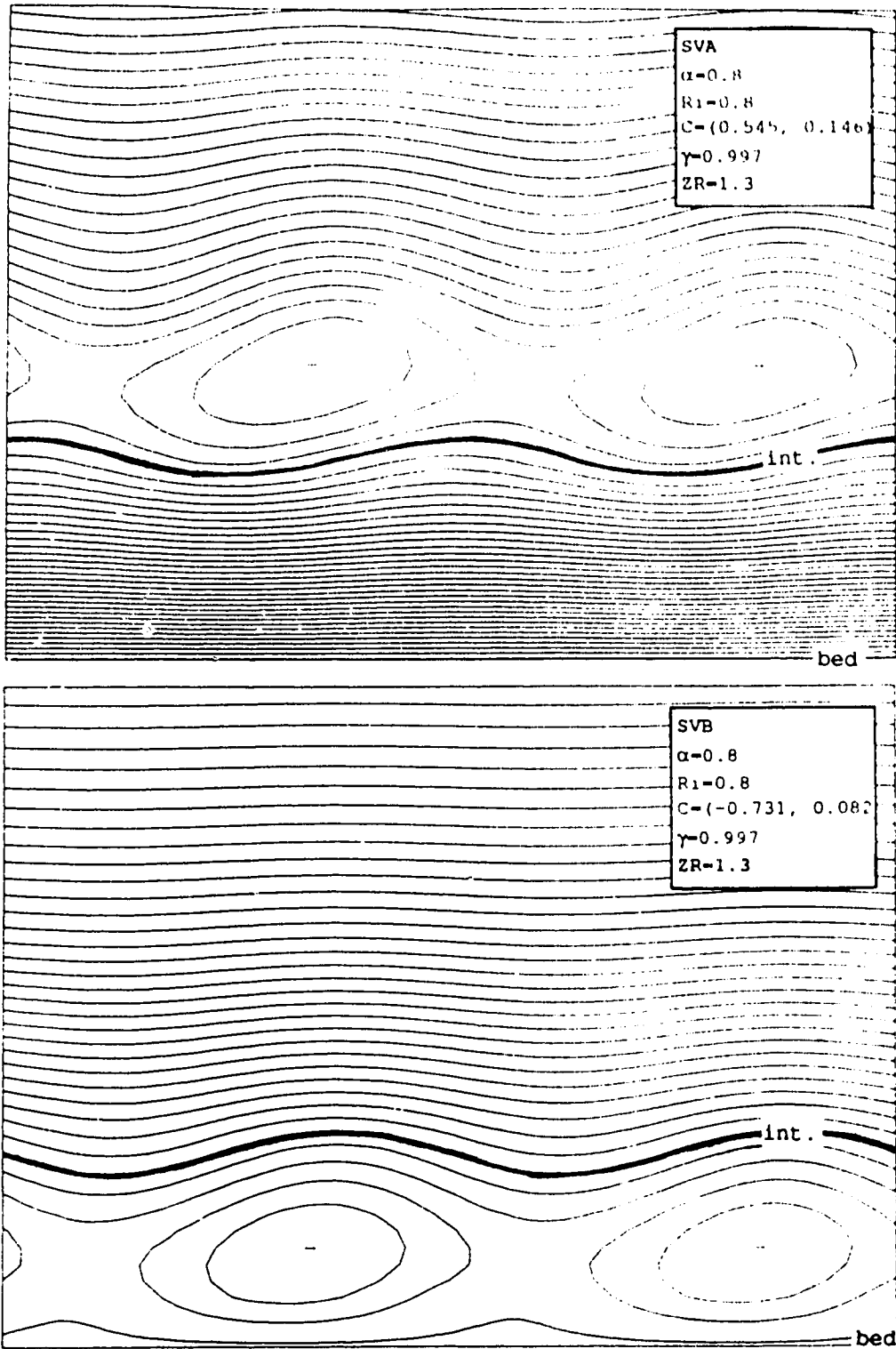


Figure 2.13. Stream lines of SVA and SVB solutions
(on the system moving with C_r)

2.4 MODEL II: EFFECTS OF VARIATIONS OF BOUNDARY VELOCITY

2.4.1 Formulation

The main objective of this section is to evaluate the effects of variations of boundary velocity on the stability of flow. This is actually a slight modification of section 2.3. In addition to the existence of a rigid boundary, it is assumed that the velocity on the rigid boundary can be U_w instead of being restricted to -1.0. Since observations show that the minimum velocity is located slightly above the bottom in most cases, this assumption allows a more reasonable model. Again, to model the system, four layers with piecewise linear velocity profile as shown in Figure 2.14 will be used. As the formulation of the system stability equations is almost identical to that in section 2.3, in this section only a brief additional explanation will be given.

The governing equation for this model is

$$\frac{d^2\hat{w}}{dz^2} - \alpha^2\hat{w} = 0 \quad (2.4.1)$$

And the solutions for each layer become as follows:

$$\hat{w}_I = A_1 \exp(-\alpha z) \quad , \quad (2.4.2)$$

$$\hat{w}_{II} = A_2 \exp(\alpha z) + A_3 \exp(-\alpha z) \quad , \quad (2.4.3)$$

$$\hat{w}_{III} = A_4 \exp(\alpha z) + A_5 \exp(-\alpha z) \quad , \quad (2.4.4)$$

$$\hat{w}_{IV} = A_6 \sinh(\alpha(z+z_R)) \quad , \quad (2.4.5)$$

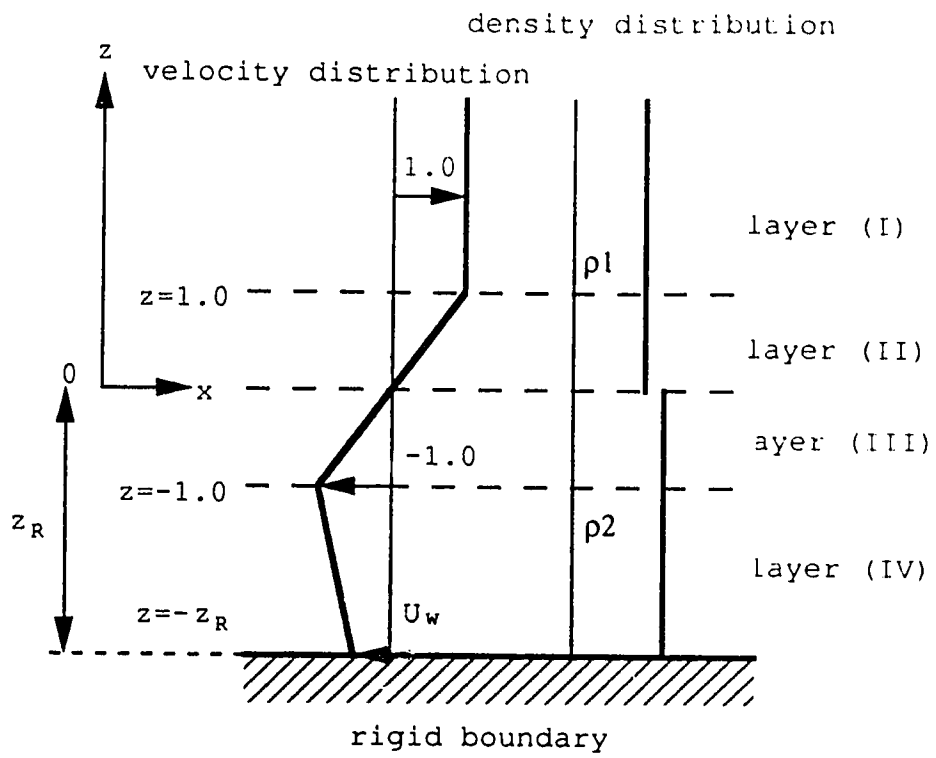


Figure 2.14. Velocity and density distribution of Model II

where A_1, A_2, \dots are coefficients and \hat{w}_i is solution in layer (I).

If the kinematic (2.2.40) and dynamic (2.2.57) matching conditions are now applied to these solutions,

at $z=1.0$

$$A_1 \exp(-\alpha) - A_2 \exp(\alpha) - A_3 \exp(-\alpha) = 0, \quad (2.4.6)$$

$$A_1 \{ \alpha(1-c) \exp(-\alpha) \} + A_2 \{ \alpha(1-c) - 1 \} \exp(\alpha) + A_3 \{ -\alpha(1-c) - 1 \} \exp(-\alpha) = 0, \quad (2.4.7)$$

at $z=0$

$$A_2 + A_3 - A_4 - A_5 = 0, \quad (2.4.8)$$

$$A_2 \gamma \left\{ \alpha c + 1 - \frac{g_*}{c} \right\} + A_3 \gamma \left\{ -\alpha c + 1 - \frac{g_*}{c} \right\} + A_4 \left\{ -\alpha c - 1 + \frac{g_*}{c} \right\} + A_5 \left\{ \alpha c - 1 + \frac{g_*}{c} \right\} = 0. \quad (2.4.9)$$

And at $z=-1.0$

$$A_4 \exp(-\alpha) + A_5 \exp(\alpha) - A_6 \sinh(\alpha(z_R-1)) = 0, \quad (2.4.10)$$

$$A_4 \gamma \{ \alpha(1+c) + 1 \} \exp(-\alpha) + A_5 \gamma \{ -\alpha(1+c) + 1 \} \exp(\alpha) + A_6 \left\{ -\alpha(1+c) \cosh(\alpha(z_R-1)) + \frac{U_w+1}{1-z_R} \sinh(\alpha(z_R-1)) \right\} = 0, \quad (2.4.11)$$

where

$$\gamma = \frac{\rho_1}{\rho_2}, \quad g_* = \frac{Ri_0}{1-\gamma}, \quad Ri_0 = \frac{(1-\gamma)gL}{v^2}.$$

If U_w is the non-dimensionalized velocity on the rigid boundary, these conditions may be written in the following matrix form.

$$\begin{pmatrix} & & & & & \\ & & & & & \\ & & & & & \\ & & & & & \\ & & & & & \\ & & & & & \\ & & & & & \\ & & & & & \\ & & & & & \\ & & & & & \\ \mathbf{M} & & & & & \end{pmatrix} \begin{pmatrix} A_1 \\ A_2 \\ A_3 \\ A_4 \\ A_5 \\ A_6 \end{pmatrix} = \begin{pmatrix} 0 \\ 0 \\ 0 \\ 0 \\ 0 \\ 0 \end{pmatrix} , \quad (2.4.12)$$

For non-trivial solutions, the $\det \mathbf{M} = 0$ must be satisfied, and the dispersion relationship may be written as

$$a_4 c^4 + a_3 c^3 + a_2 c^2 + a_1 c + a_0 = 0 , \quad (2.4.13)$$

where

$$\begin{aligned} a_4 &= \gamma B_4 + B_4^\# , \\ a_3 &= \gamma B_3 + B_3^\# , \\ a_2 &= \gamma B_2 + B_2^\# , \\ a_1 &= \gamma B_1 + B_1^\# , \\ a_0 &= \gamma B_0 + B_0^\# , \end{aligned} \quad (2.4.14)$$

$$\begin{aligned} B_4 &= R_1 R_5 , & B_4^\# &= R_1^\# R_5^\# , \\ B_3 &= R_1 R_6 + R_2 R_5 , & B_3^\# &= R_1^\# R_6^\# + R_2^\# R_5^\# , \\ B_2 &= R_2 R_6 + R_3 R_5 , & B_2^\# &= R_2^\# R_6^\# + R_3^\# R_5^\# , \\ B_1 &= R_3 R_6 + R_4 R_5 , & B_1^\# &= R_3^\# R_6^\# + R_4^\# R_5^\# , \\ B_0 &= R_4 R_6 , & B_0^\# &= R_4^\# R_6^\# , \end{aligned} \quad (2.4.15)$$

$$\begin{aligned} R_1 &= 2\alpha^2 , \\ R_2 &= -\alpha(2\alpha + 1 - \exp(-2\alpha)) , \\ R_3 &= 2\alpha + 2\alpha g_* - 1 + \exp(-2\alpha) , \\ R_4 &= -g_*(2\alpha - 1 + \exp(-2\alpha)) , \\ R_5 &= \alpha(\alpha \sinh(\alpha z_R - \alpha) + \sinh(\alpha) \cosh(\alpha z_R - \alpha)) , \end{aligned}$$

$$\begin{aligned}
R_6 &= R_5 - \left(1 + \frac{U_W + 1}{1 - z_R}\right) \sinh(\alpha) \sinh(\alpha z_R - \alpha) , \\
R_1^\# &= \alpha^2 (\cosh(\alpha z_R) \cosh(\alpha z_R - \alpha) + \sinh(\alpha) \sinh(\alpha z_R - \alpha)) , \\
R_2^\# &= R_1^\# - R_5 - \alpha \left(1 + \frac{U_W + 1}{1 - z_R}\right) \cosh(\alpha z_R) \sinh(\alpha z_R - \alpha) , \\
R_3^\# &= (1 - g_*) R_5 - \left(1 + \frac{U_W + 1}{1 - z_R}\right) \sinh(\alpha) \sinh(\alpha z_R - \alpha) , \\
R_4^\# &= -g_* \left(R_5 - \left(1 + \frac{U_W + 1}{1 - z_R}\right) \sinh(\alpha) \sinh(\alpha z_R - \alpha) \right) , \\
R_5^\# &= 2\alpha , \\
R_6^\# &= -(2\alpha - 1 + \exp(-2\alpha)) . \tag{2.4.16}
\end{aligned}$$

As with the previous model, the same procedure was used to solve this dispersion relationship, and a stability criterion of $C_I=0$ was used to conform with the governing equation and boundary conditions.

2.4.2. Solution

In this model, the parameter ranges studied were $1.0 \leq z_R \leq \infty$, $0.0 \leq \alpha \leq 5.0$, $1.0 \leq Ri \leq 2.0$ and $-1.0 \leq U_W \leq 1.0$ and the calculations were performed using the same facilities as in previous model. Since the cases involving $U_W = -1.0$ were presented in section 2.3.3, only the effects of $U_W > -1.0$ will be described in this section.

Figure 2.15 presents the effect of U_W on the stability boundaries. It is clear that as U_W increases SVB waves tend to get shorter and that SVA waves tend to have additional

unstable modes with extremely long wave length. Also of interest, when $Uw > -1.0$, SVB waves have a tendency to increase their wave number with decreasing Z_R , an effect which is opposite to the $Uw = -1.0$ case. SVA solutions seem unaffected by Uw except for some additional unstable modes. These modes are relatively small when Uw is close to -1.0 , but as Uw exceeds 0.0 , they start growing as an independent unstable region, the details of which will be discussed later.

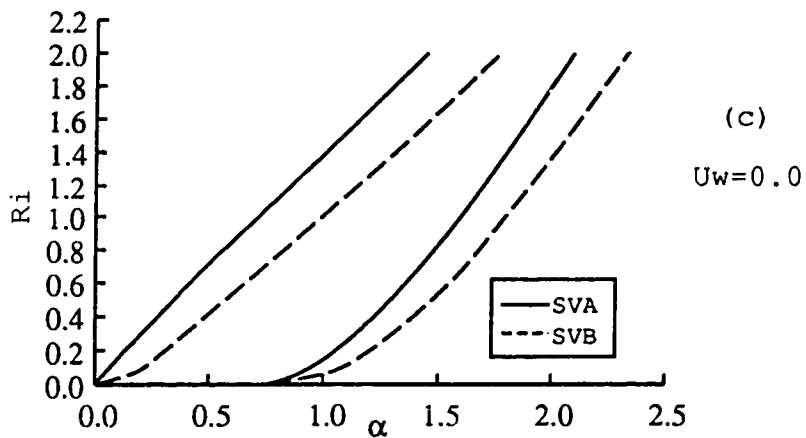
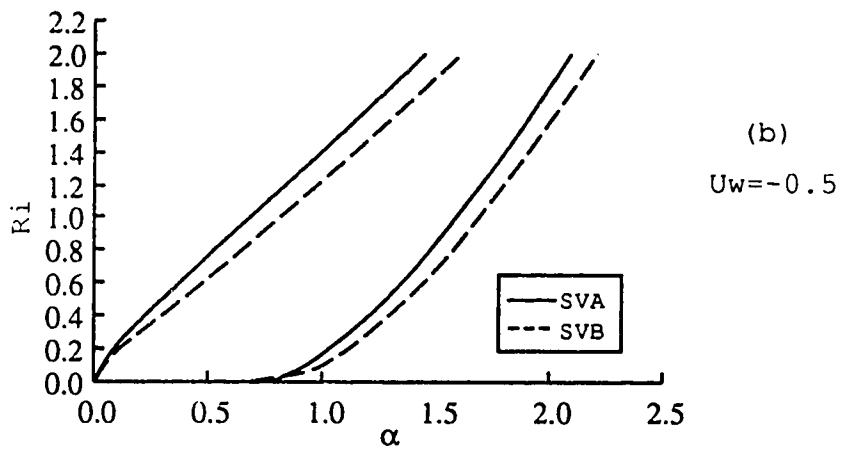
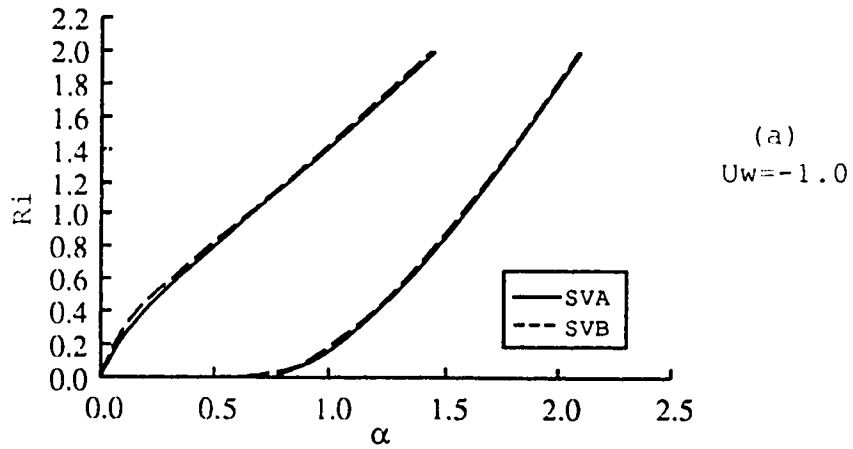
Figures 2.19 and 2.20 present the phase velocity of waves. Again, SVB waves are significantly influenced by Uw and tend to get slower for the same wave number as SVA when Uw increases. These same effects were found for decreasing Z_R in the previous section. By contrast, phase velocities of SVA solutions remain almost unchanged both Z_R and Uw vary. The additional unstable modes cannot be found on these phase velocity diagrams.

In order to investigate the additional unstable modes, the details of the dispersion relationship on the α - Ri plane are shown in Figures 2.21 and 2.22. They show that these modes have very small growth rates and phase velocities of approximately zero, implying that the instabilities will occur around the density interface and should rarely be observed in the flow due to other faster growing unstable modes.

Figures 2.23 and 2.24 show the perturbation quantities of SVA and the additional unstable modes. Despite the

displacement η of these additional modes is of very large amplitude, their growth rates are relatively small. These large amplitudes are simply due to the singularity of equation (2.2.102) which appears as c becomes a real number.

Figure 2.15 (a)-(e). Neutral boundaries V.S. Velocity at wall:
 $ZR=4.0$ case



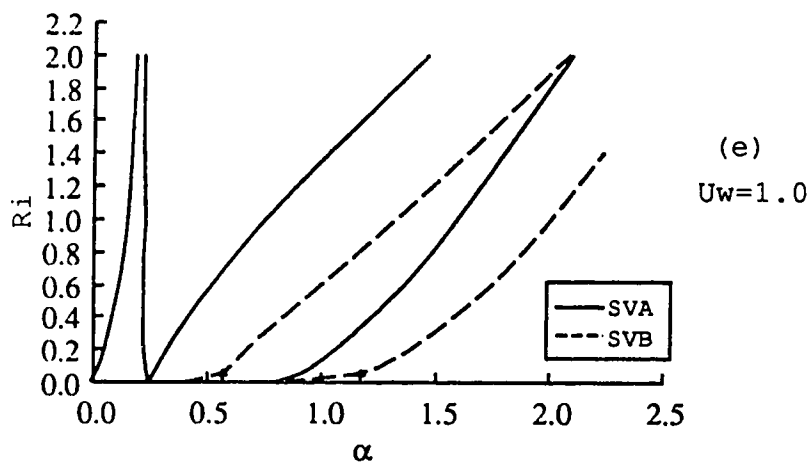
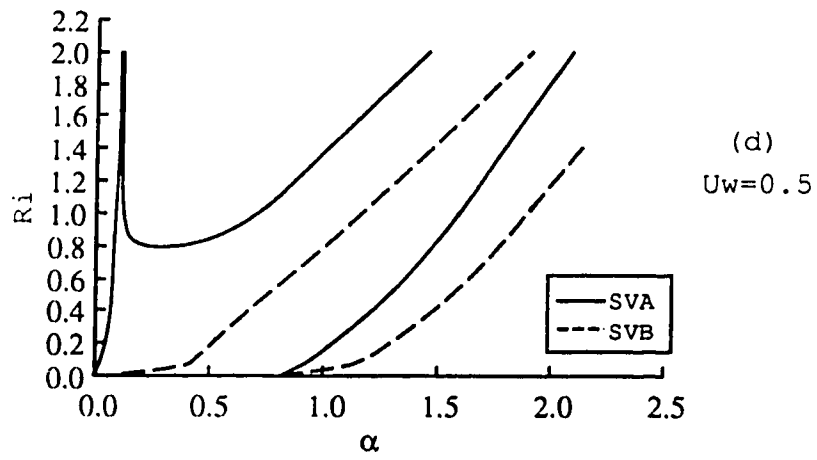
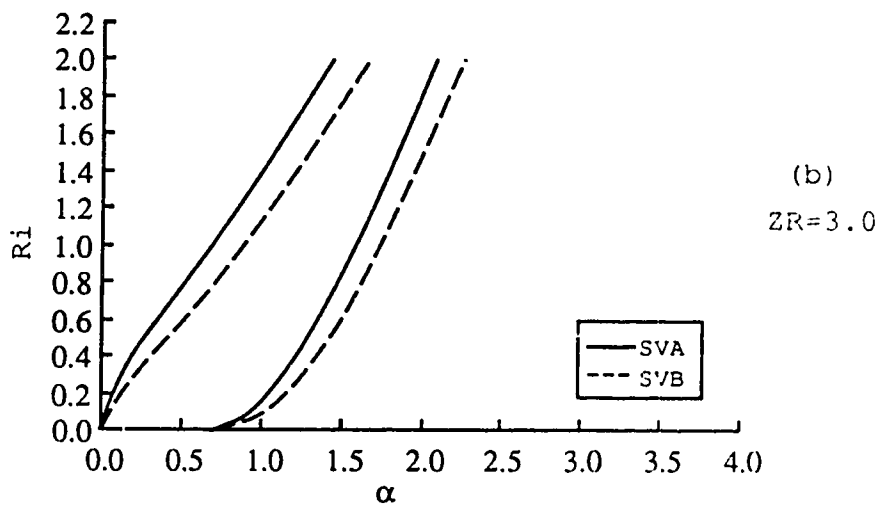
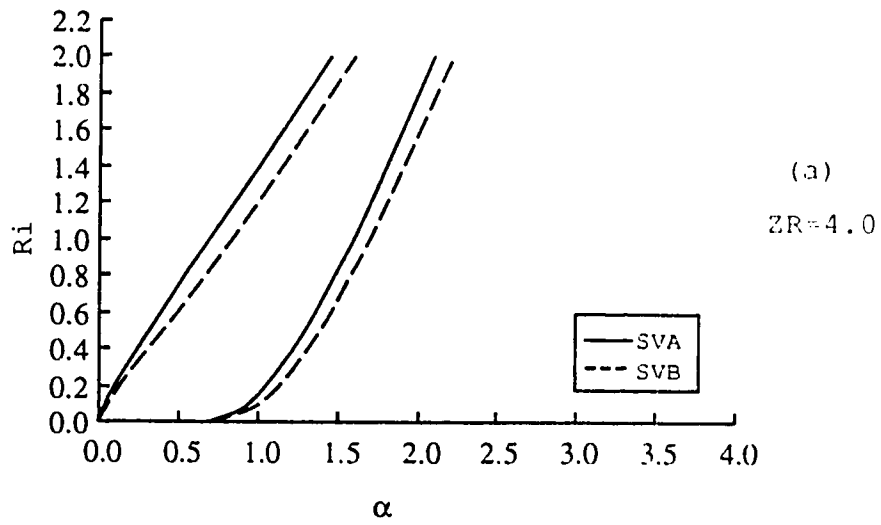
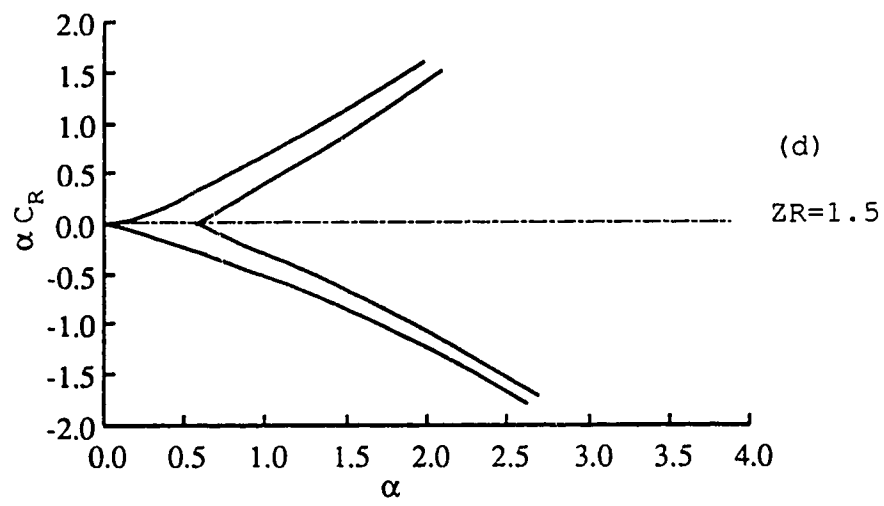
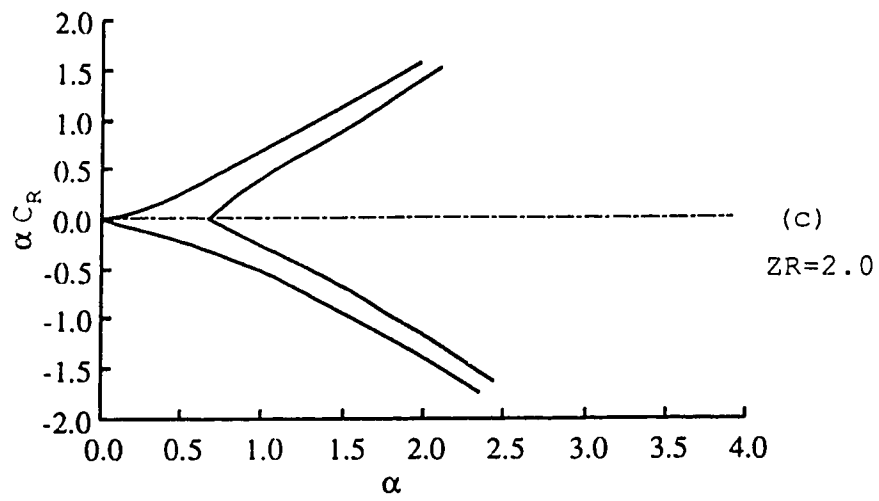
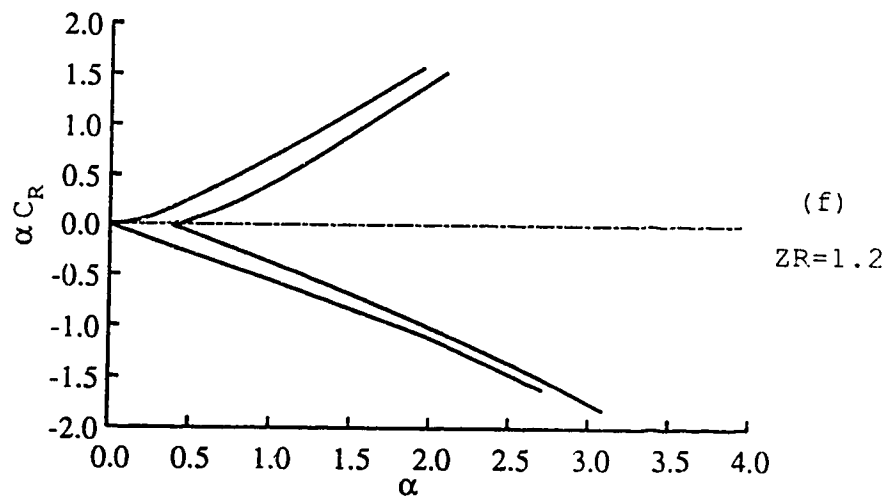
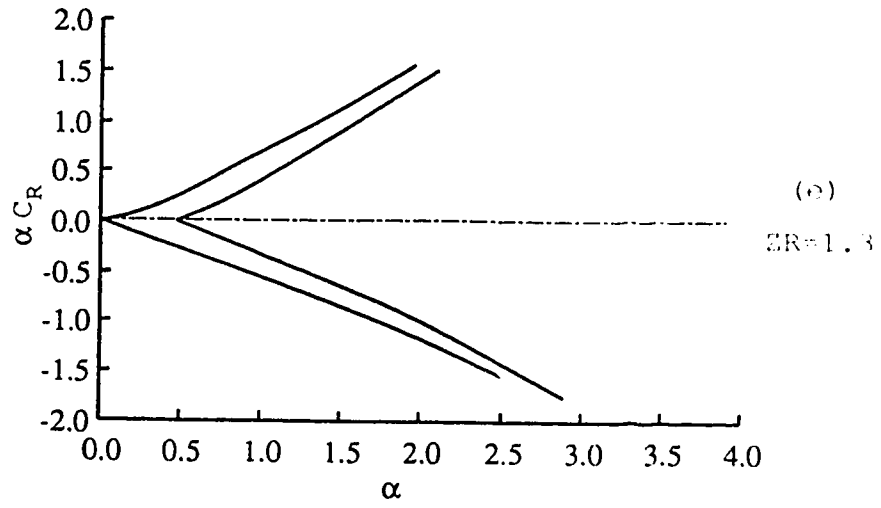


Figure 2.16 (a)-(h). Neutral boundaries. $U_w = -0.5$ cases







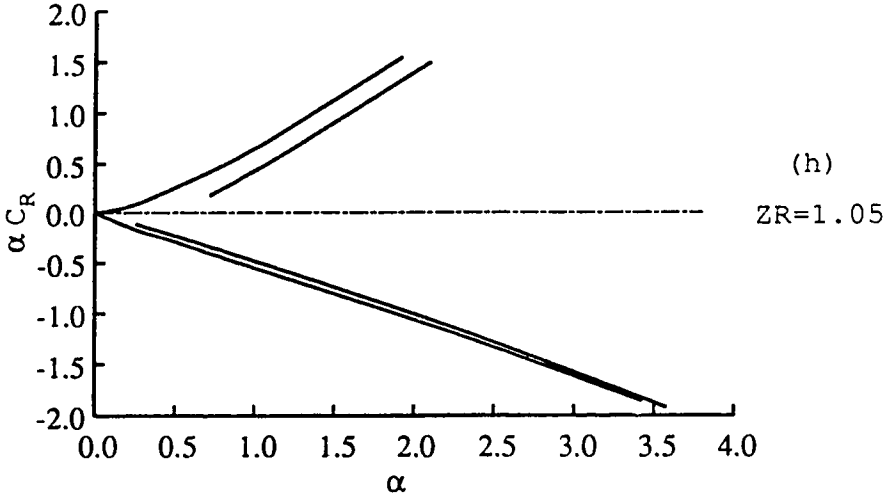
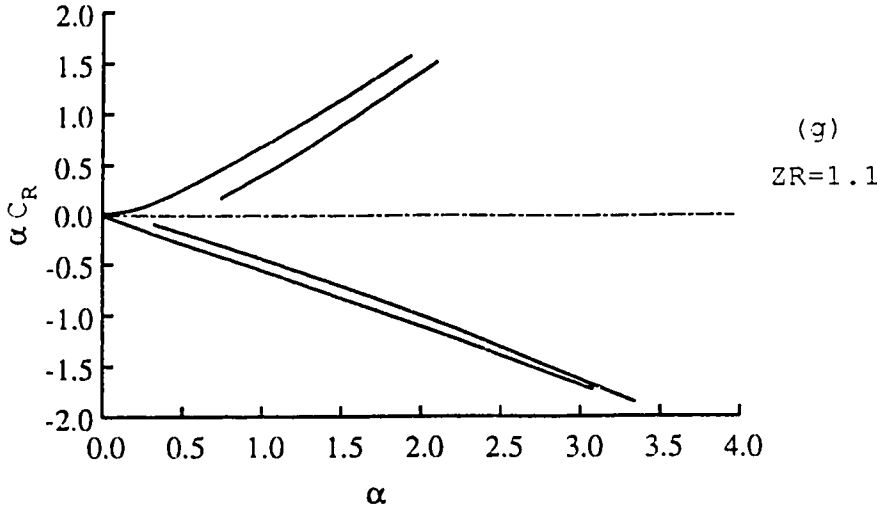
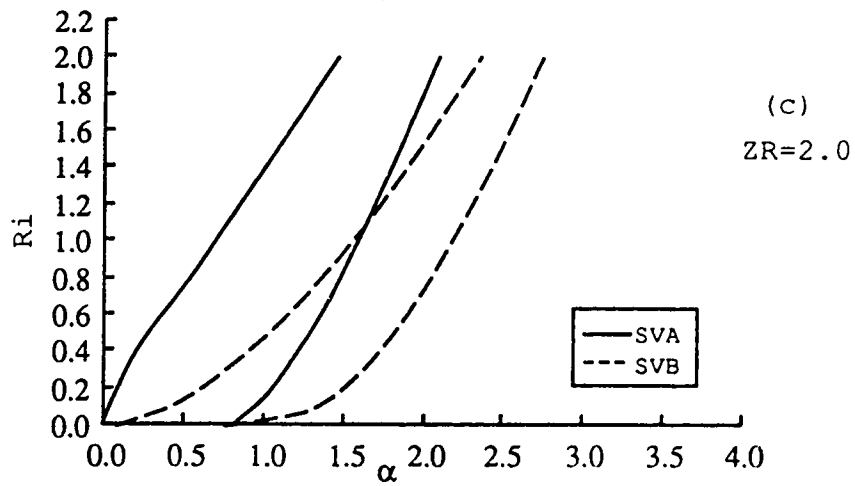
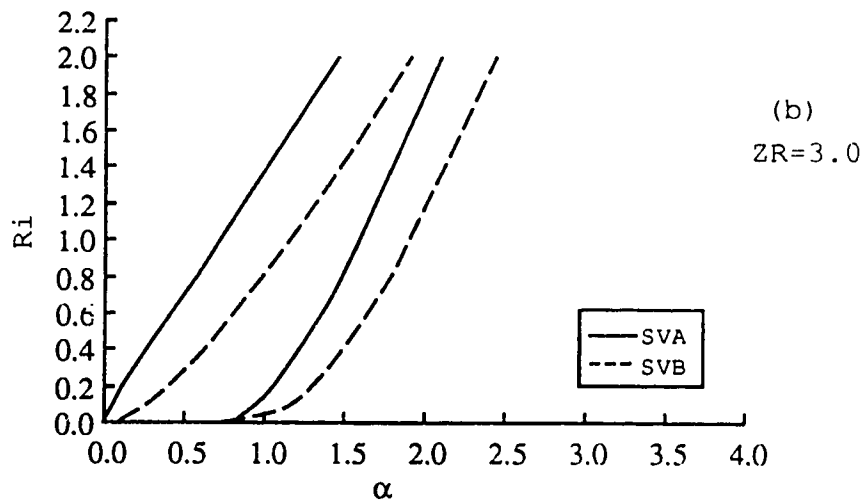
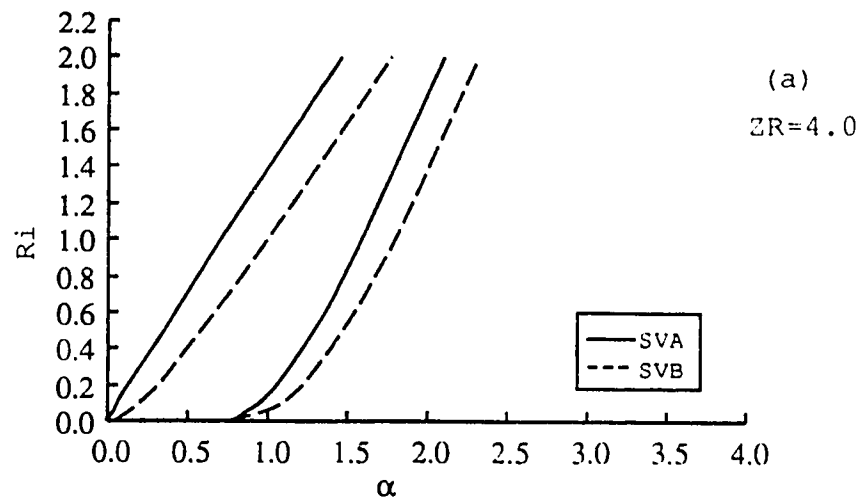
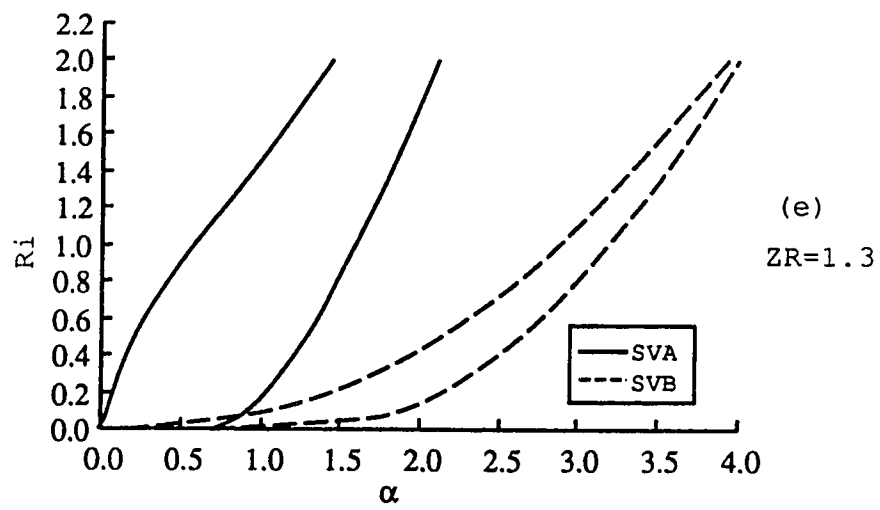
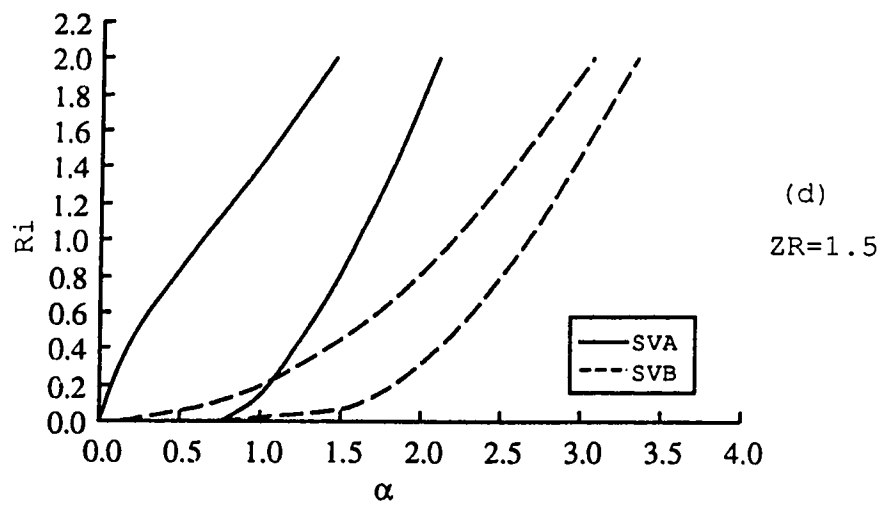


Figure 2.17 (a)-(g). Neutral boundaries. $U_w=0.0$ cases



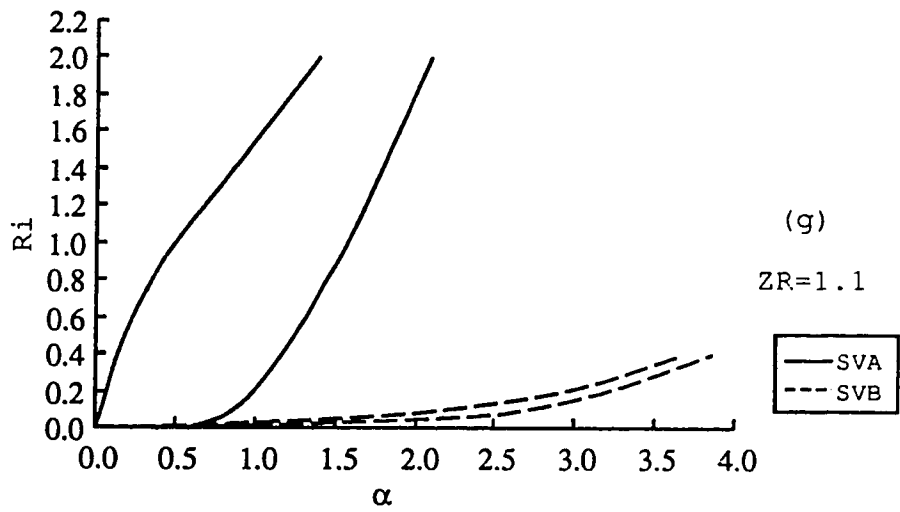
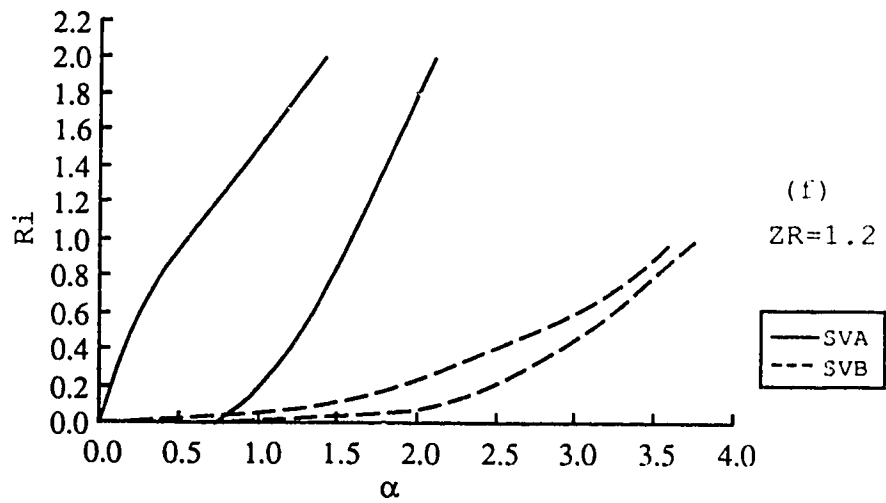
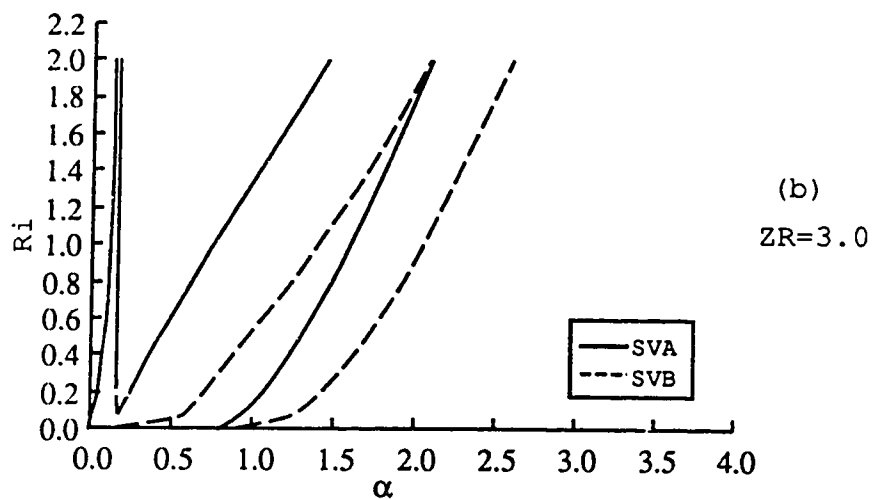
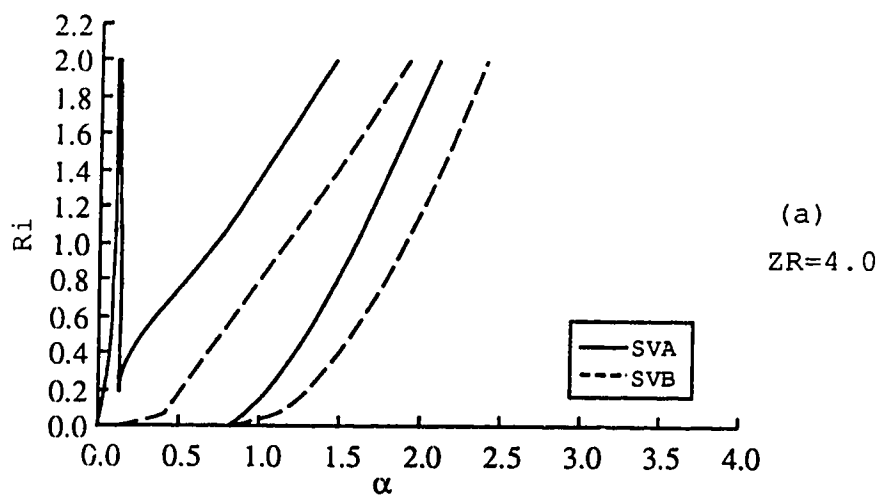
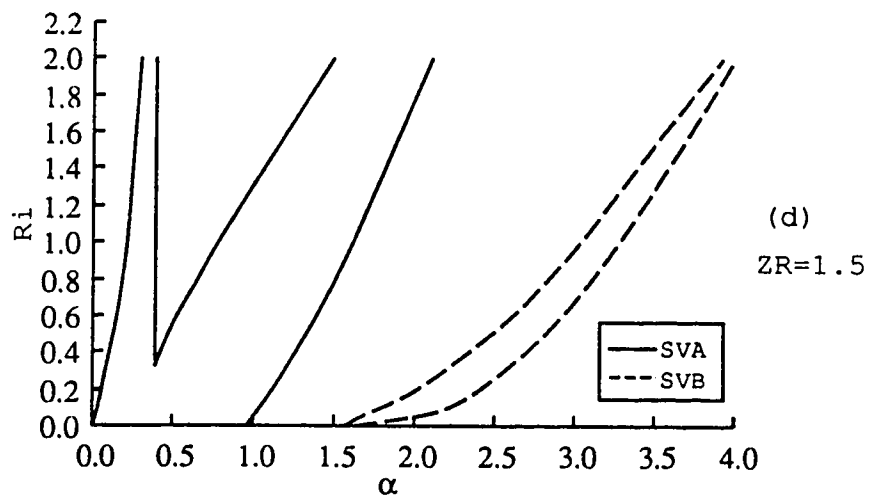
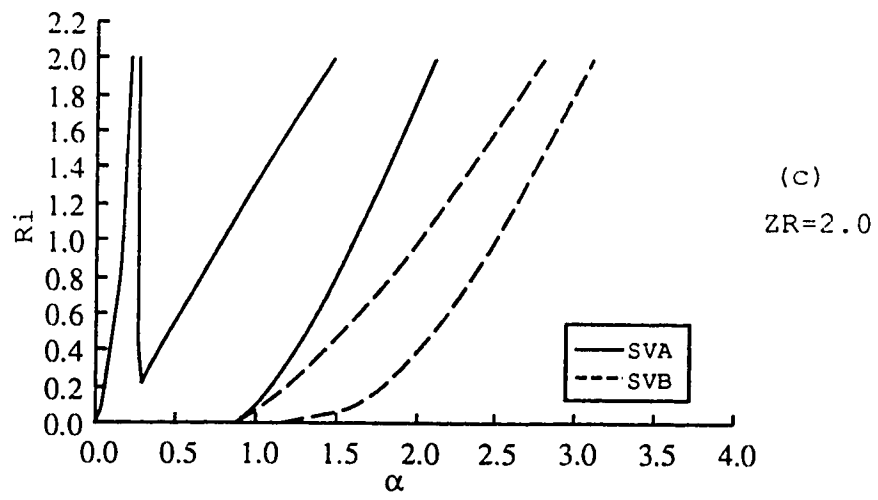
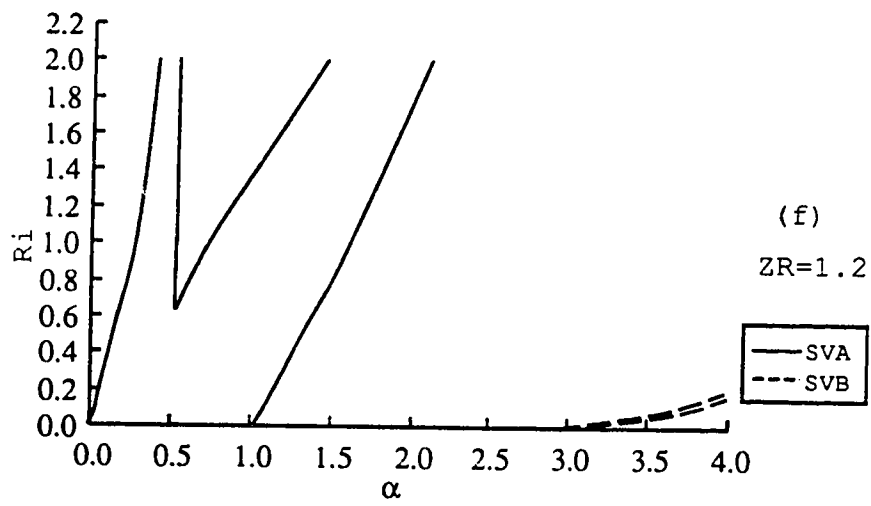
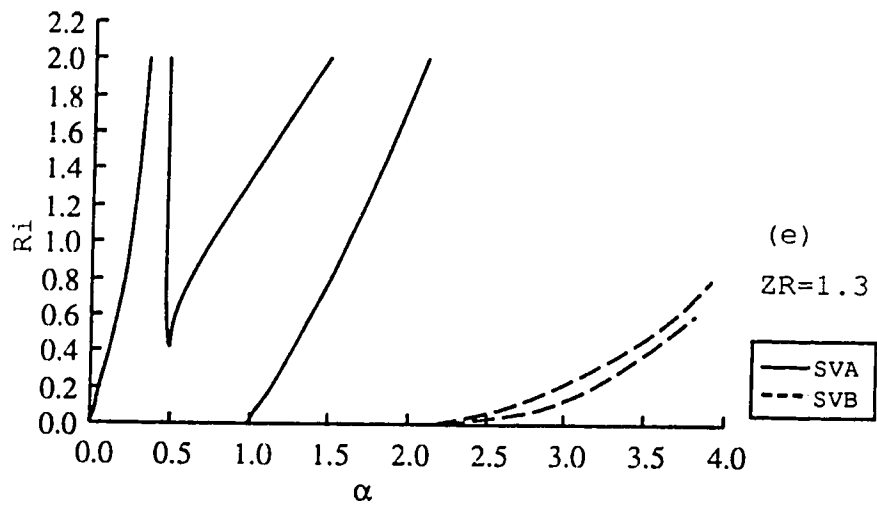


Figure 2.18 (a)-(h). Neutral boundaries. $U_w=0.5$ cases





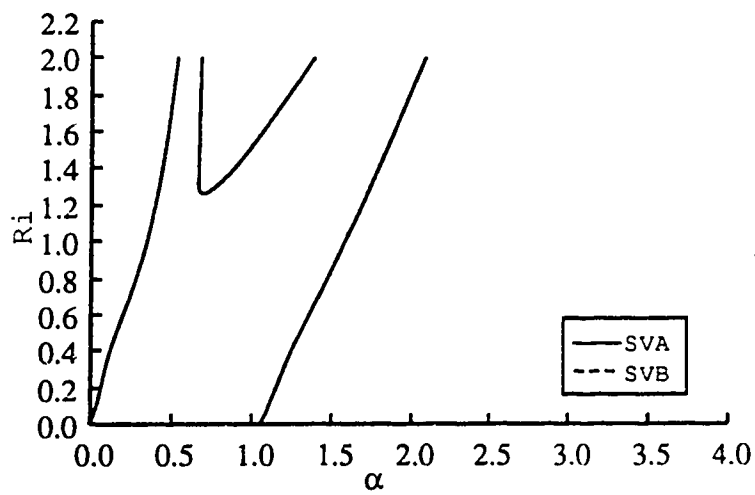
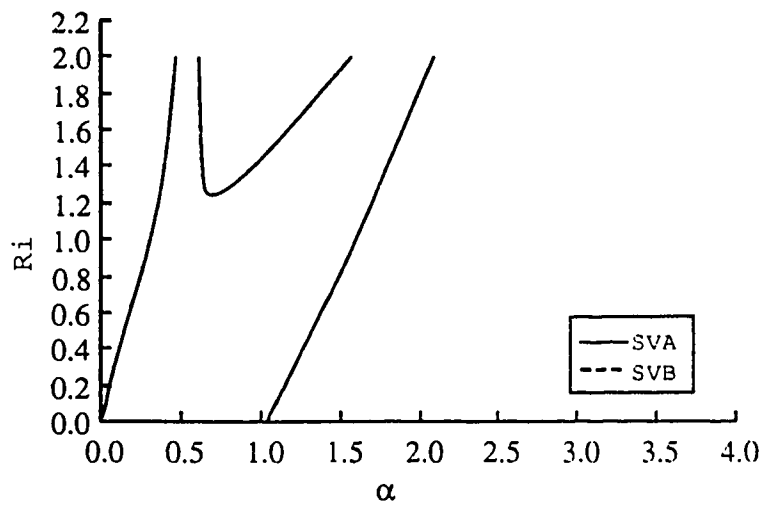
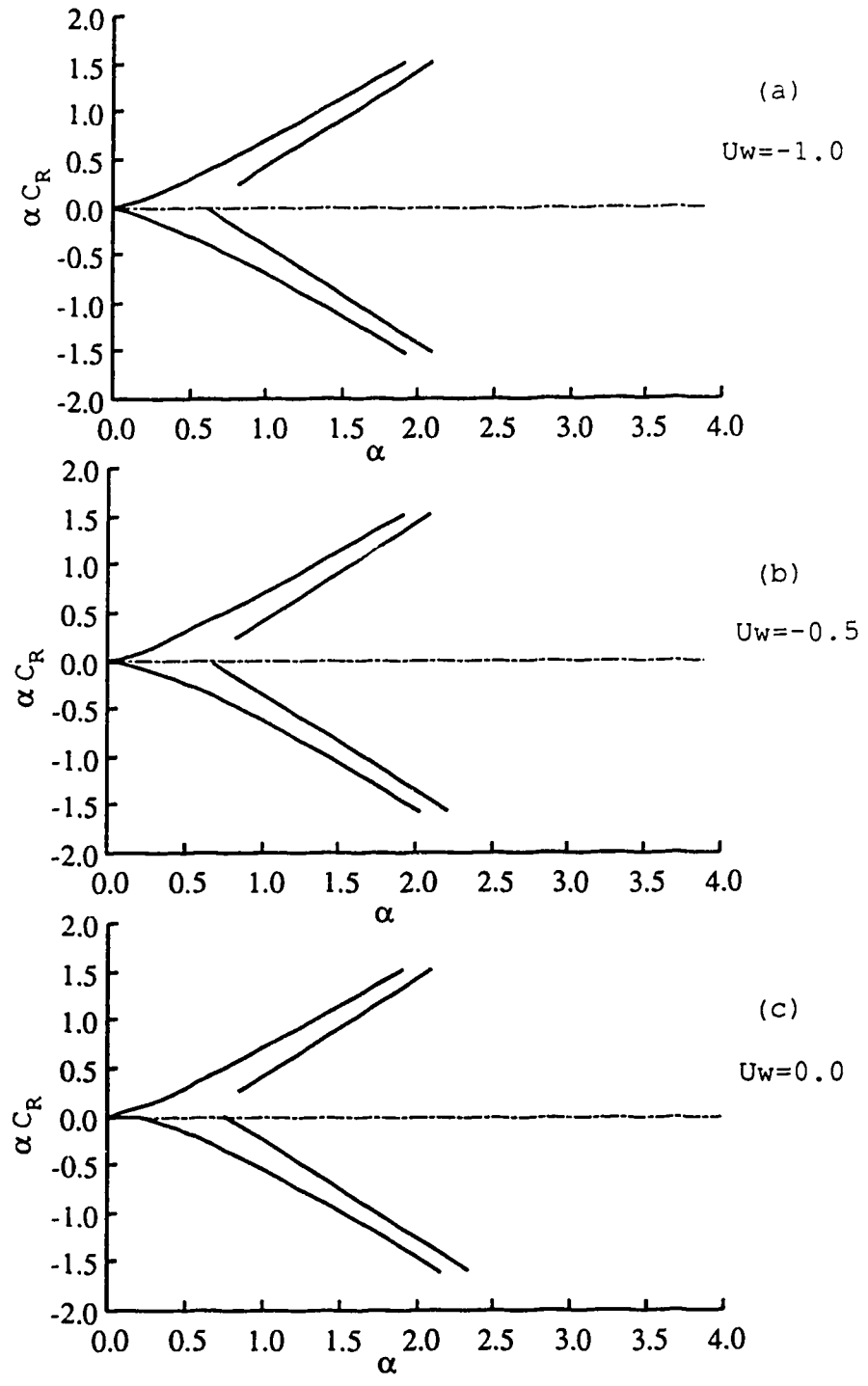


Figure 2.19 (a)-(e). Neutral boundaries on α - α_{CR} plane. $ZR=4.0$ cases



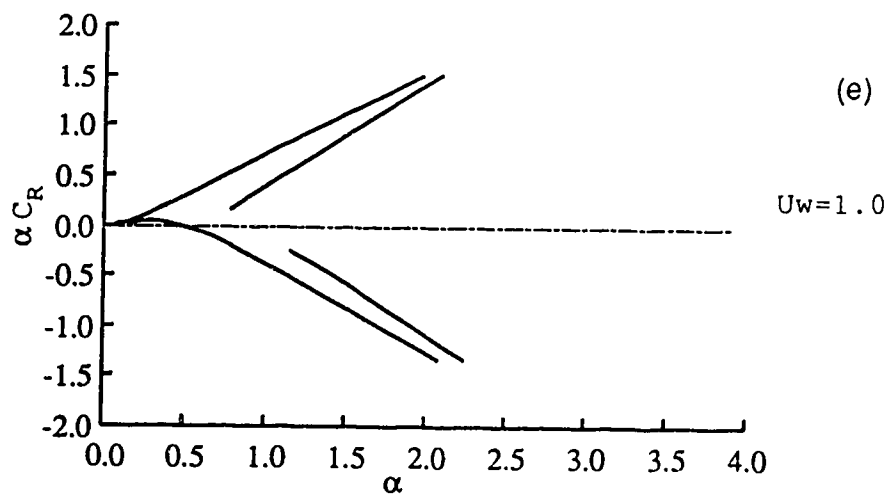
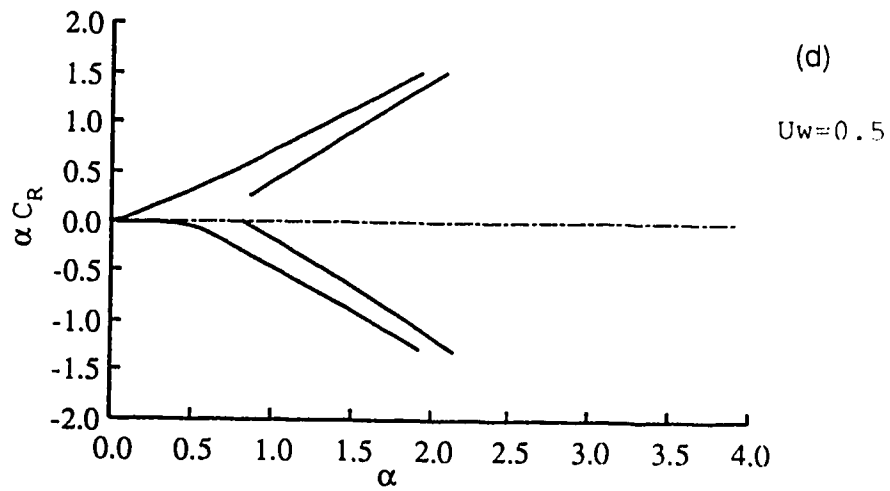
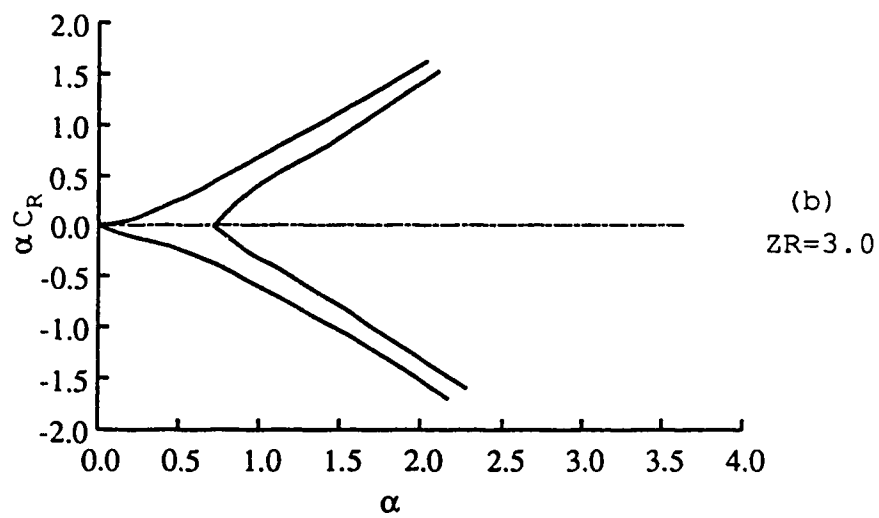
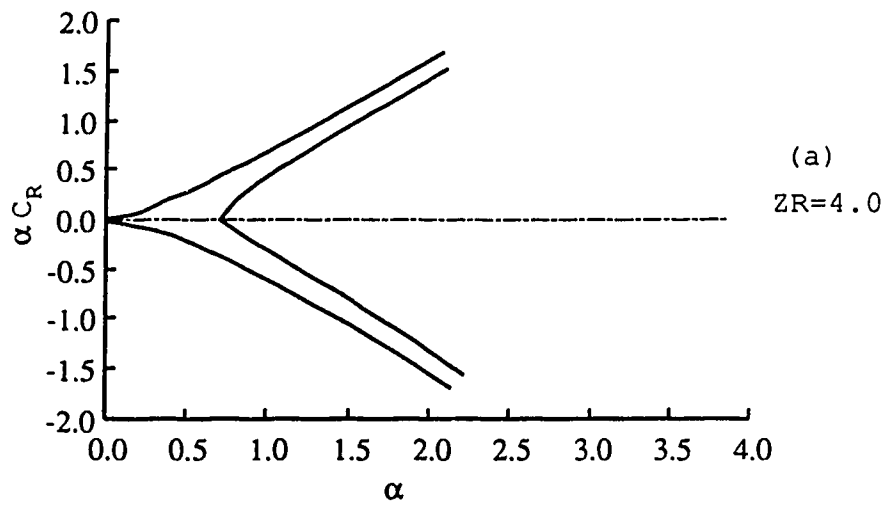
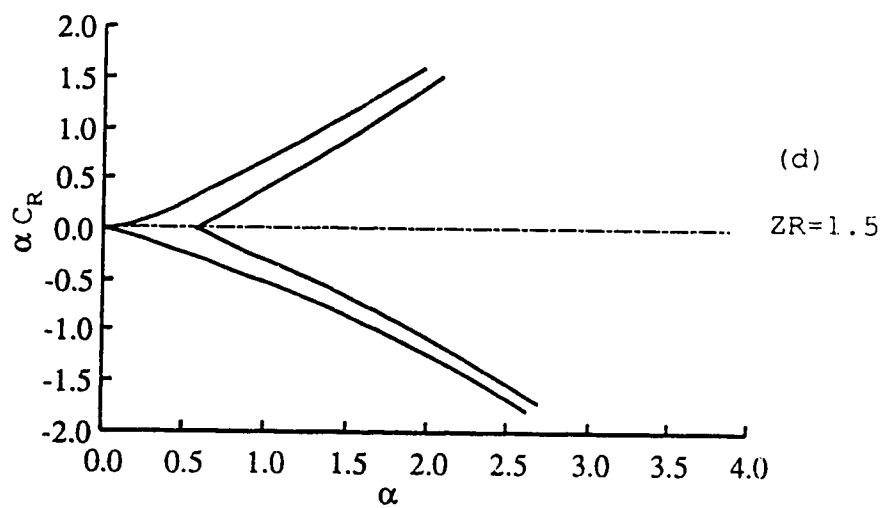
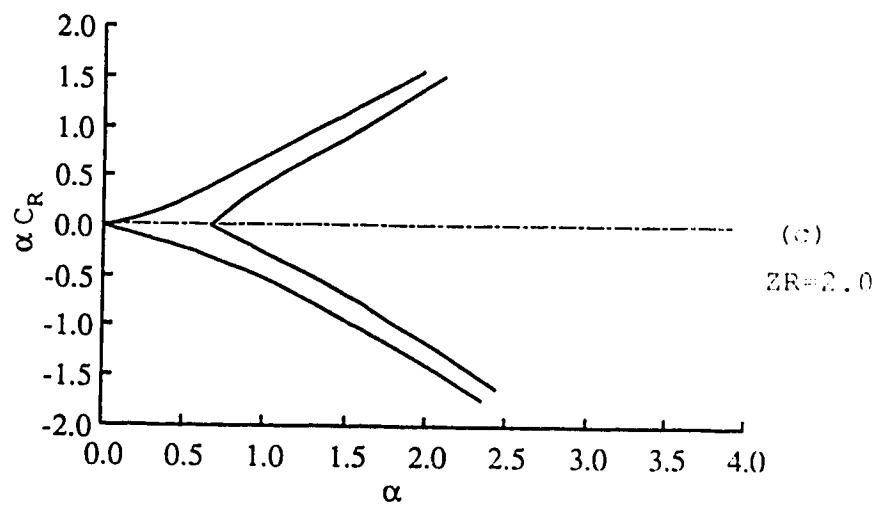
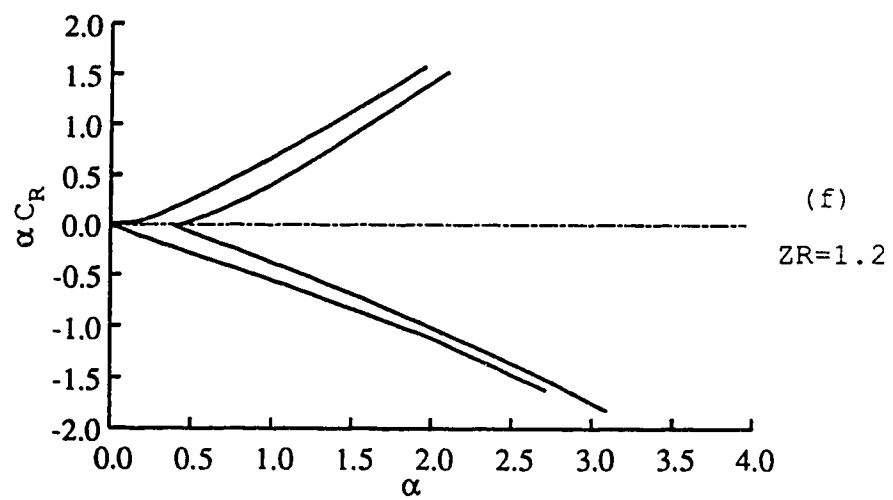
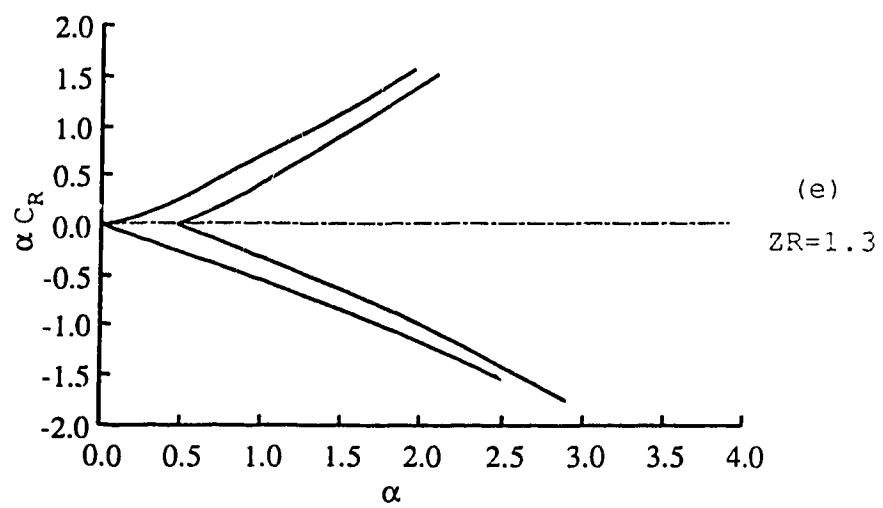


Figure 2.20 (a)-(h). Neutral boundaries on α - αC_R plane. $U_w = -0.5$ cases







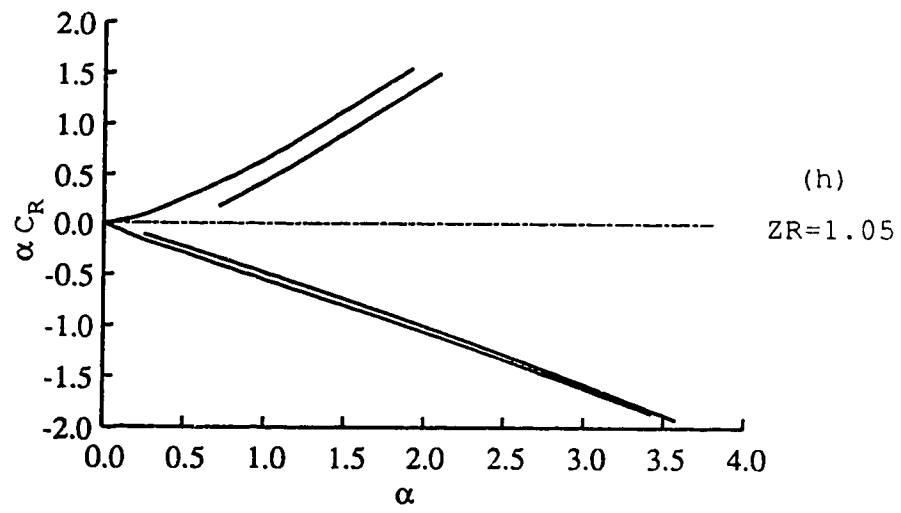
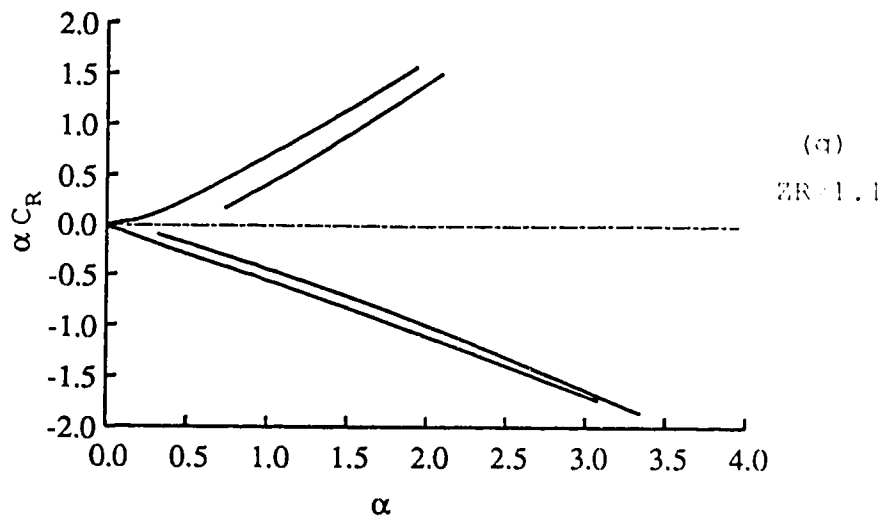
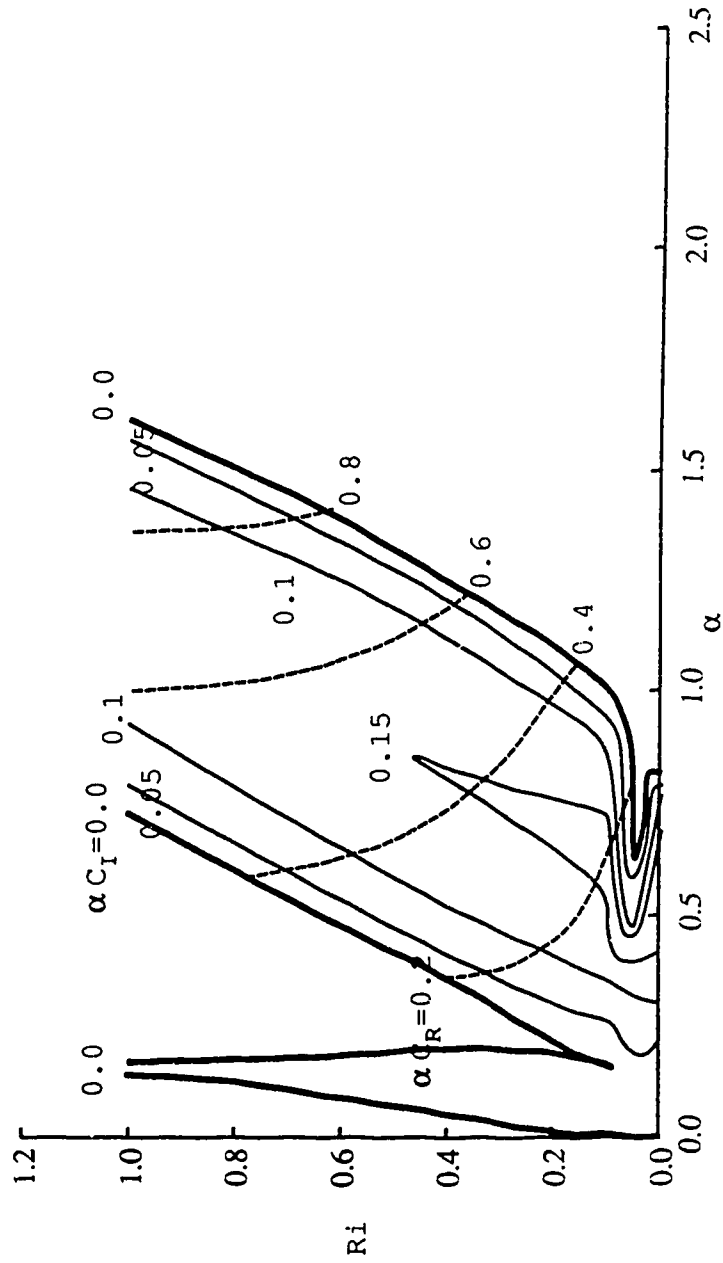
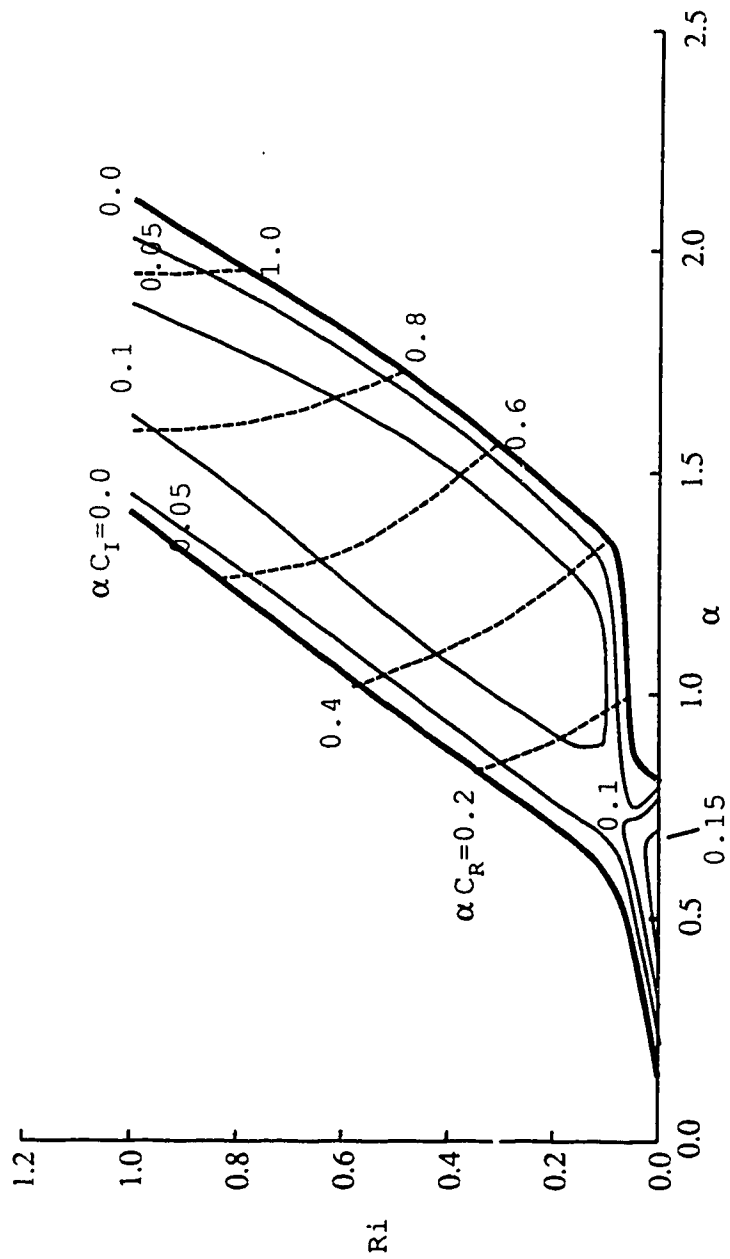


Figure 2.21 (a)-(b) Dispersion relationship for $ZR=3.0$
 $UW=1.0$

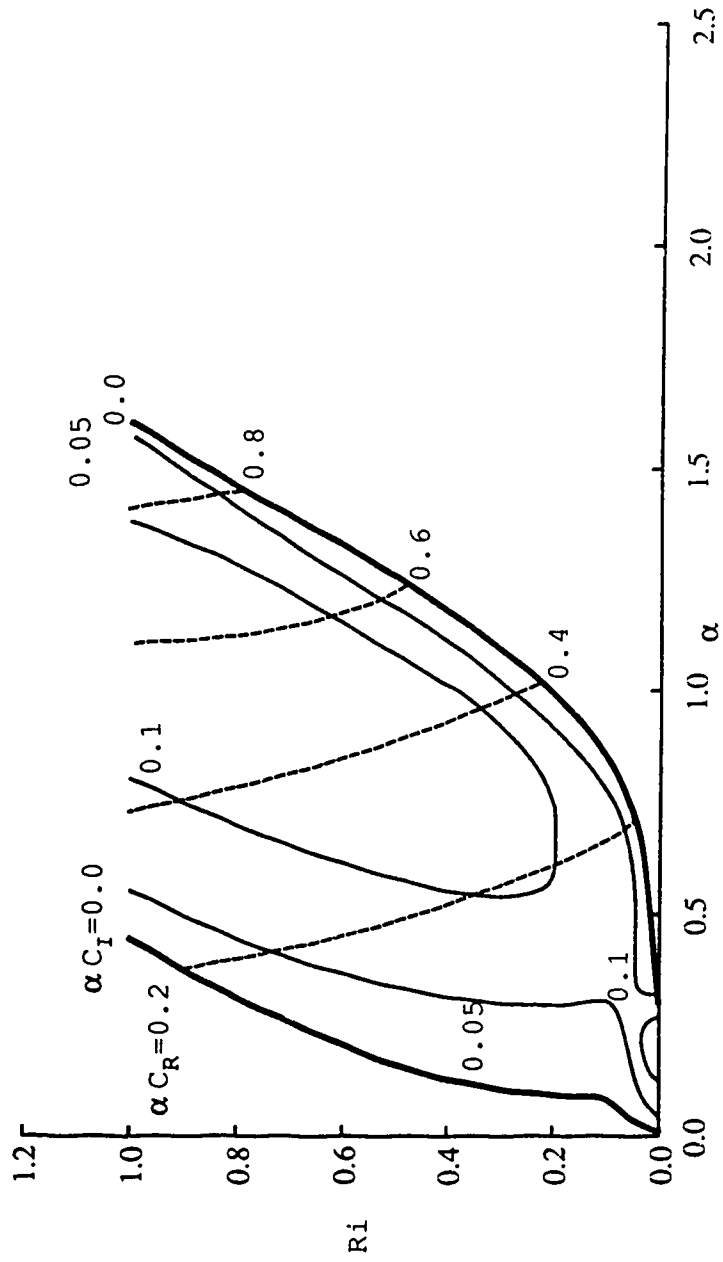


(a) SVA solutions

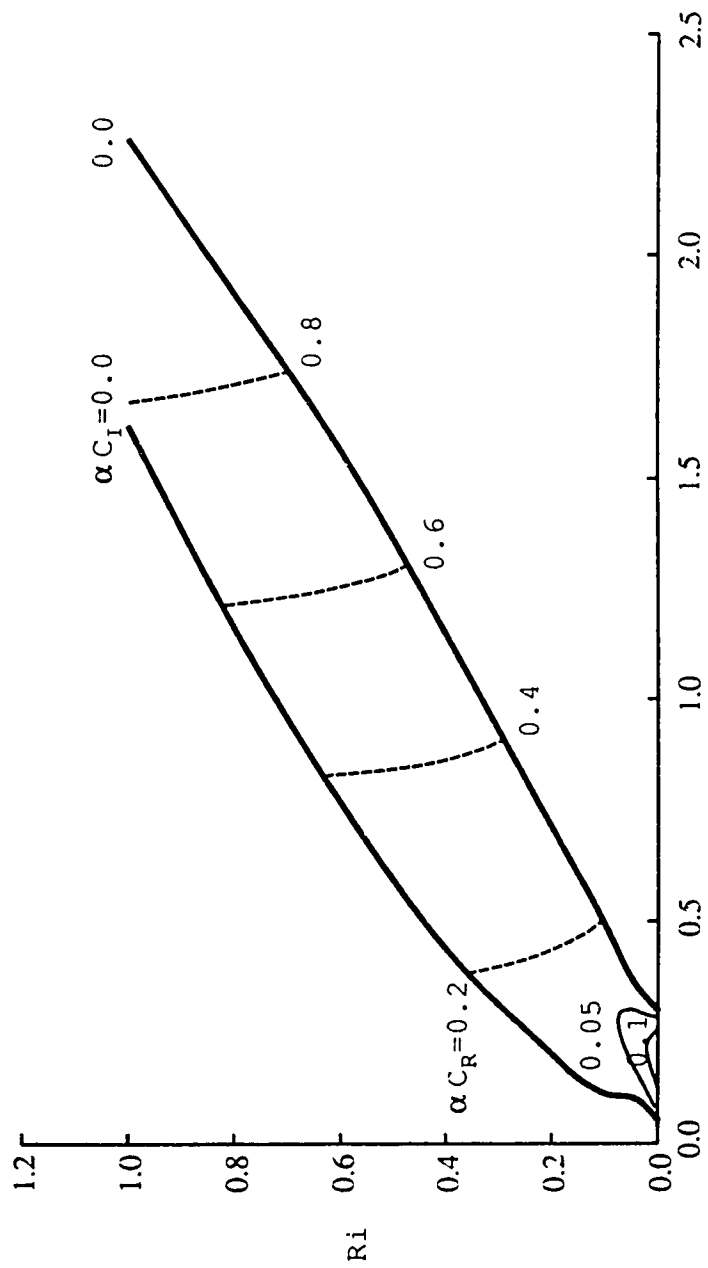


(b) SVB solutions

Figure 2.22 (a)-(b) Dispersion relationship for
 $ZR=1.05$ $Uw=-0.5$

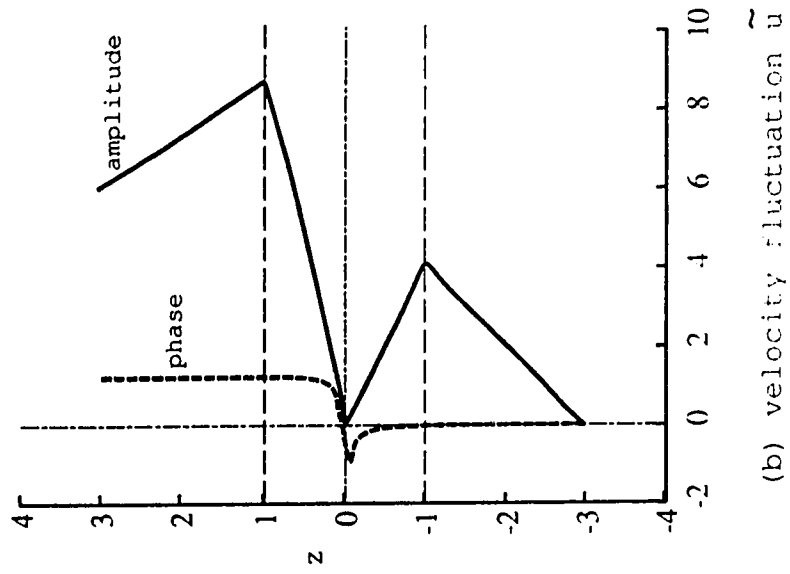
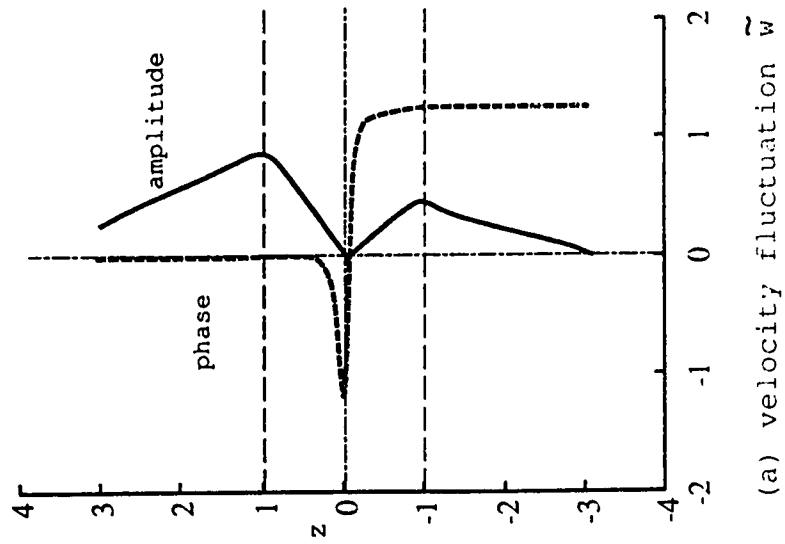


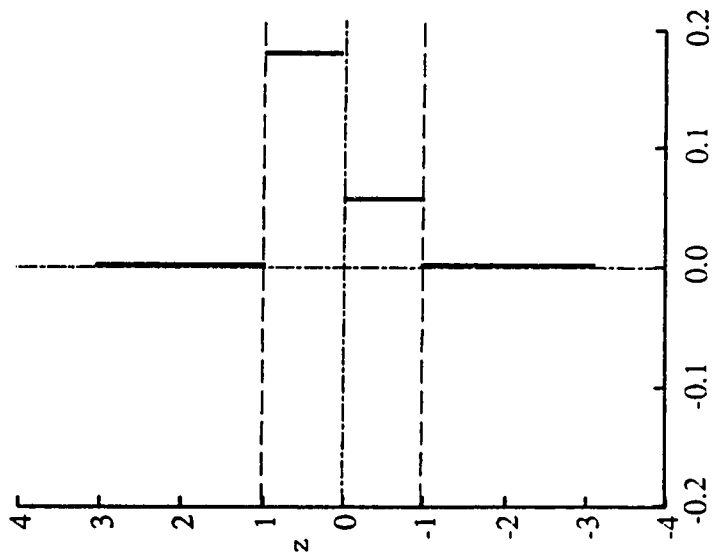
(a) SVA solutions



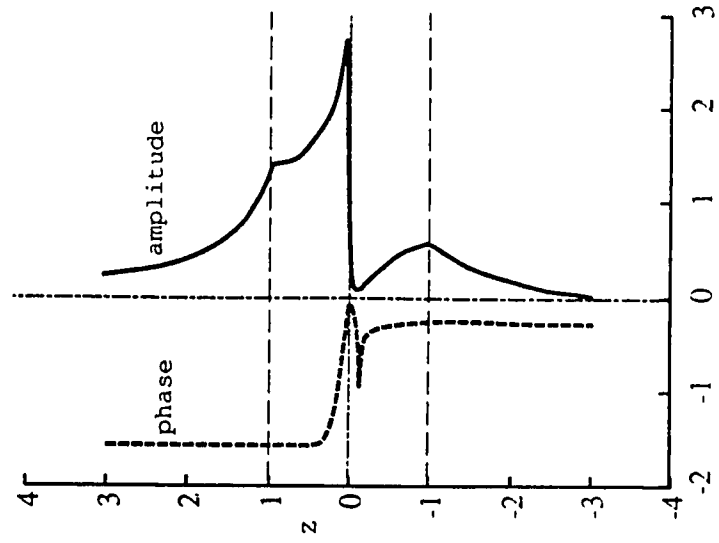
(b) SVB solutions

Figure 2.23 (a)-(d). The perturbation quantities. $Ri=0.3$ $\alpha=0.1$
 $c=(0.108, 0.034)$ $ZR=3.0$ $Uw=0.5$ case



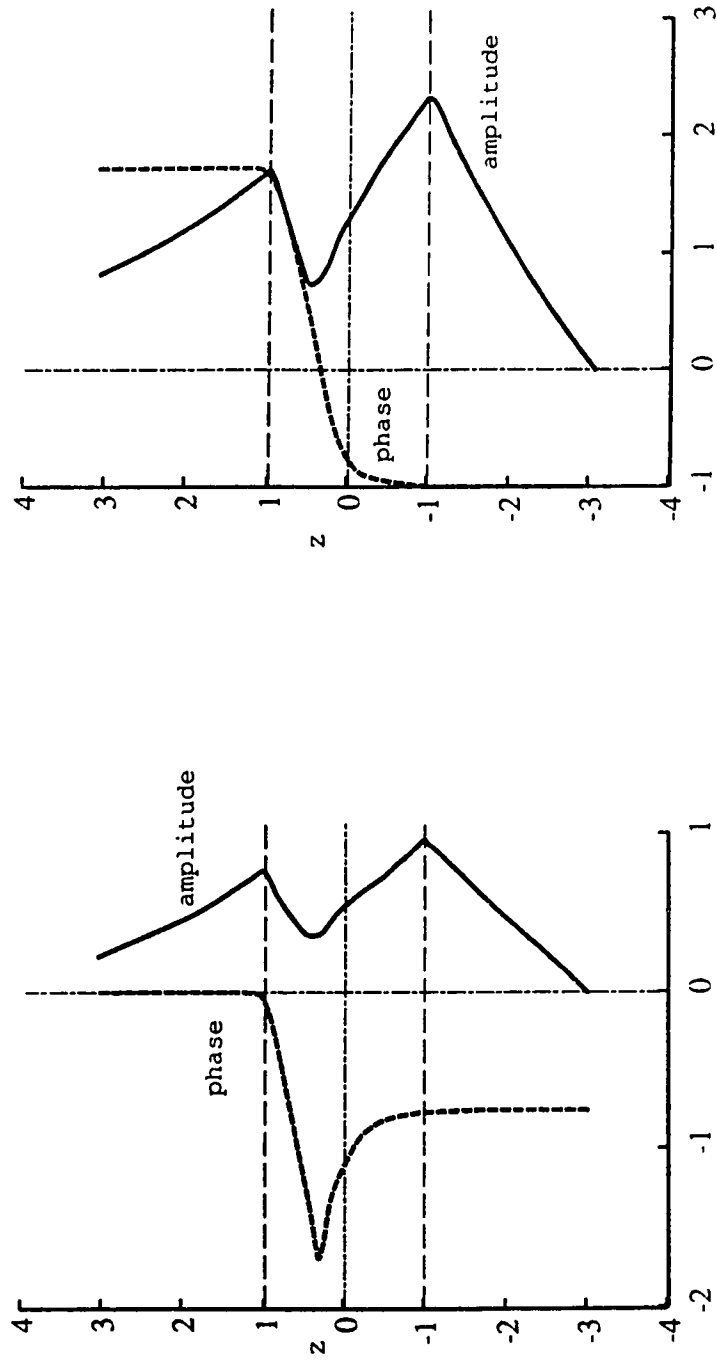


(c) Reynolds stress τ



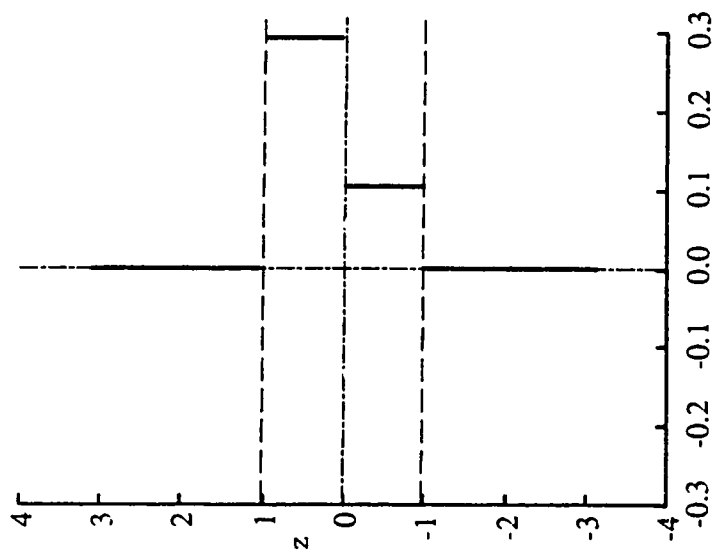
(d) displacement η

Figure 2.24 (a)-(d). The perturbation quantities. $Ri=0.4$ $\alpha=0.4$
 $c=(0.517, 0.121)$ $ZR=3.0$ $Uw=0.5$ case

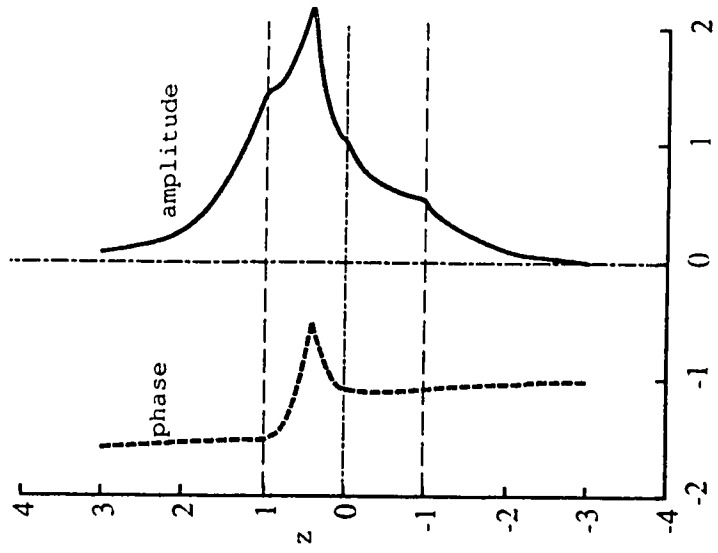


(a) velocity fluctuation \tilde{w}

(b) velocity fluctuation \tilde{u}



(c) Reynolds stress τ



(d) displacement η

2.5 DISCUSSION

Solutions of Models I and II show that unstable regions of small Richardson number waves get smaller as Z_R decreases. Particularly for $Z_R < 1.2$, waves in the range $0.4 < Ri < 1.0$ appear to be more unstable than homogeneous ones ($Ri = 0.0$), and at $Z_R = 1.0$, these homogeneous solutions disappear completely. This sounds contradictory since density stratification usually has a stabilizing effect and it is usually expected that homogeneous solutions are the most unstable.

To investigate this problem, the eigen equations (dispersion relationships) for $Ri = 0.0$ and $g = 1.0$ were derived for both $Z_R > 1.0$ and $Z_R < 1.0$. These equations are second order in terms of the complex phase velocity c , and may be written as

$$A_2 c^2 + A_1 c - A_0 = 0, \quad \text{for } Z_R > 1.0 \quad (2.5.1)$$

$$B_1 c (c + B_2) = 0, \quad \text{for } Z_R < 1.0 \quad (2.5.2)$$

where

$$\begin{aligned} A_0 = & (2\alpha^2 - \alpha) e^{\alpha} (\cosh(\alpha(Z_R - 1)) + \sinh(\alpha(Z_R - 1))) \\ & + e^{-3\alpha} (\cosh(\alpha(Z_R - 1)) - \sinh(\alpha(Z_R - 1))) \\ & - (2\alpha^2 e^{\alpha} + (e^{-3\alpha} - e^{\alpha})) \sinh(\alpha(Z_R - 1)), \end{aligned} \quad (2.5.3)$$

$$A_1 = \alpha (e^{-3\alpha} - e^{\alpha}) (\cosh(\alpha(Z_R - 1)) - \sinh(\alpha(Z_R - 1))), \quad (2.5.4)$$

$$A_2 = -2\alpha^2 e^{\alpha} (\cosh(\alpha(Z_R - 1)) + \sinh(\alpha(Z_R - 1))), \quad (2.5.5)$$

$$B_1 = (\sinh(\alpha) + \cosh(\alpha)) \alpha^2 (\cosh(\alpha Z_R) + \sinh(\alpha Z_R)), \quad (2.5.6)$$

$$B_2 = \frac{\alpha (\sinh(\alpha) \cosh(\alpha Z_R) + \cosh(\alpha) \sinh(\alpha Z_R))}{B_1}. \quad (2.5.7)$$

Therefore, both cases have the following solution

$$c_R = - \frac{A_1}{2A_2} , \quad (2.5.8)$$

$$c_i = \pm \frac{\sqrt{4A_2A_0 - A_1^2}}{2A_2} \quad \text{for } Z_R > 1.0 , \quad (2.5.9)$$

$$c = 0 \text{ or } c = -B_2 \quad \text{for } Z_R < 1.0 , \quad (2.5.10)$$

illustrating that c cannot be complex for $Z_R < 1.0$ (i.e., no unstable solution can exist).

Figure 2.25 presents the dispersion relationship for $Z_R > 1.0$ case. It is obvious that an unstable region fades out as Z_R approaches to 1.0. The reason why there is no unstable solution when $Z_R < 1.0$ is due to the velocity profile. This type of piece-wise linear velocity cannot satisfy one of the necessary conditions of instability; the so-called "Fjortoft's theory" (Fjortoft 1950) which states "Suppose instability occurs, and let $Z^* \in (0, 1)$ for which $U'' = 0$. Define $U^* = U_0(Z^*)$, then a necessary condition for instability is

$$U_0'' (U_0 - U^*) < 0 \quad \text{somewhere in the flow.}"$$

This theory was derived from Rayleigh's stability equation (homogeneous case of the Taylor-Goldstein equation (2.2.37)) and Rayleigh's theory. For a piece-wise linear velocity profile, a slight modification is required as follows:

The Rayleigh equation is

$$(U_0 - c) (\phi'' - \alpha^2 \phi) - U_0'' \phi = 0 , \quad (2.5.11)$$

where ϕ is the stream function of perturbation velocity, U_0 is mean velocity profile which is function of z .
If there is instability, then c becomes a complex number and

$$\phi'' - \alpha' \phi - \frac{U_0'' \phi}{(U_0 - c)} = 0 \quad (2.5.12)$$

By multiplying ϕ^* and integrating through the domain, then

$$\int_0^1 \phi^* \left(\phi'' - \alpha' \phi - \frac{U_0'' \phi}{(U_0 - c)} \right) dz = 0 \quad (2.5.13)$$

where $c = \frac{\omega}{\alpha} = c_R + ic_i$.

And taking the real part of this integration will always yield

$$\int_0^1 \frac{U_0''(U_0 - c_R)}{|U_0 - c|^2} |\phi|^2 dz = - \int_0^1 (|\phi'|^2 + \alpha^2 |\phi|^2) dz < 0 \quad (2.5.14)$$

But, from the Rayleigh's theory

$$(c_R - U^*) \int_0^1 \frac{U_0''}{|U_0 - c|^2} dz = 0 \quad (2.5.15)$$

therefore, the necessary condition becomes

$$\int_0^1 \frac{U_0''(U_0 - U^*)}{|U_0 - c|^2} |\phi|^2 dz < 0 \quad (2.5.16)$$

For $Z_R > 1.0$, there are two singular points which have both $U_0'' = \infty$ and $U_0'' = -\infty$ in the domain, thus they can satisfy this necessary condition. However, for $Z_R < 1.0$, it is impossible to fulfill this condition and, therefore, there is no instability in the flow. In order to achieve reasonable solutions for $Z_R \leq 1.0$, either the viscosity or some other

continuous velocity profile has to be employed. This kind of analysis will be presented in next section.

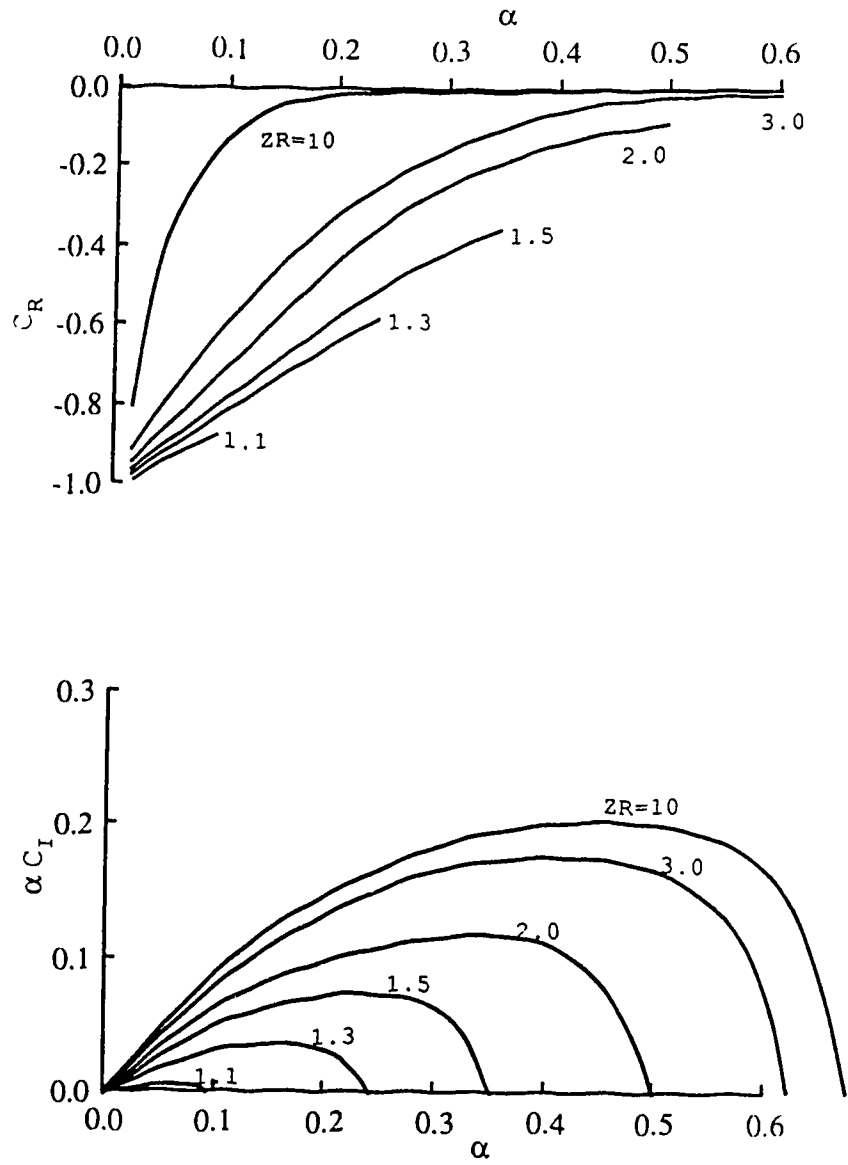


Figure 2.25. Dispersion relationship of homogeneous case ($Ri=0.0$)

2.6 CONCLUSIONS

In this section, analytical models based on a perturbed, inviscid, linearized Navier-Stokes equation have been presented. Model I, which evaluates the effects of the lower layer thickness Z_R , shows that SVB waves are influenced by a reduction in Z_R , but this is not true for SVA cases. Generally, SVB waves tend to have a smaller wave number as Z_R decreases which is opposite to our intuition. By contrast, Model II, which tests the effects of the boundary velocity on the stability, shows that SVB waves with $U_w > -1.0$ get shorter in wave length as Z_R decreases. It was also found that SVA waves have additional unstable modes in the extremely small wave number region when the value of U_w exceeds 0.0. These modes, however, have a very small growth rate and are not expected to be able to appear in the flow.

The results of Models I and II seem to contradict each other in the area of thickness effects, but they indicate an obvious sensitivity of flow stability to velocity profiles. The weakest part of this analysis involves the stability of small Richardson number flow which tend to be over estimated by failing one of the necessary conditions for instability when Z_R gets closer to 1.0. Another problem is that these models were inviscid and could not predict any Reynolds number dependency as observed in experiments.

In summary, the analysis presented in this section explains many features of a flow with a rigid boundary,

although appropriate experiments need to be performed to verify these characteristics, and more extensive analysis should be done to ensure reasonable predictions. In the next section, viscosity will be introduced and a continuous velocity profile will be employed to improve the analysis.

3. PART THREE: NUMERICAL ANALYSIS (VISCOUS MODELS)

3.1 INTRODUCTION

In the previous section, inviscid piece-wise linear velocity profile models were investigated in order to clarify instability mechanisms involving a rigid boundary. However, the simplifications used in these models created problems with their dispersion relationship. Based on the results from these models and the previous experiments, there were indications that the flow stability was dependent on Reynolds number and that there also existed a critical Richardson number.

In this section, the effects of viscosity and a continuous velocity profile will be considered. To simulate the velocity profile, a hyperbolic tangent function will be employed since this function agrees very well with experimental observations. To model the density distribution, it is felt that a two-layer system is a reasonable approximation to that known to exist in a salt wedge type flow.

To model this type of flow, the governing equation, called the Orr-Sommerfeld equation, will be derived from the two-dimensional Navier-Stokes equation by applying infinitesimally small perturbations to the system, and will be solved numerically using two models with appropriate boundary conditions. A third model will evaluate the rigid

boundary effects and a fourth model will investigate the stability of the flow when the density interface is displaced from the center of shear layer (in this model the flow is unbounded). Since these models have much more realistic velocity and density profiles because viscosity is considered, they are expected to have better agreement with experimental results.

3.2 GOVERNING EQUATIONS

3.2.1 Basic Assumptions and Governing Equations

As in the previous section, a system of equations based upon the Cartesian co-ordinate system will be used. The only difference is that we will now include the effect of viscosity. As before, we will assume incompressibility of flow, i.e.

$$\frac{D\rho}{Dt} = 0, \quad (3.2.1)$$

reducing the continuity equation to

$$\nabla \cdot \mathbf{v} = 0, \quad (3.2.2)$$

and the momentum equation to

$$\frac{D\mathbf{v}}{Dt} + \frac{1}{\rho} \nabla p + g \widehat{\mathbf{e}}_3 - \nu \nabla^2 \mathbf{v} = 0, \quad (3.2.3)$$

where $\mathbf{v}=(u,v,w)$ is the velocity vector, g is the gravitational acceleration and $\widehat{\mathbf{e}}_3$ is the unit vector in the vertical direction.

It will also be assumed that the hydrostatic balance between $\rho_0(z)$ and $p_0(z)$ is as follows,

$$\frac{dp_0(z)}{dz} = - \rho_0(z) g, \quad (3.2.4)$$

where the subscript "o" represents quantities in a steady state condition or at rest.

Moreover, since our model (see Figure 3.2) does not have a gradual density stratification in each layer, Squire's theory

may be applied. This means that the system of equations may be reduced to two-dimensional form as

$$\frac{\partial}{\partial y} = 0, \quad v=0 \quad (3.2.5)$$

From these assumptions and conditions, the governing equations become

$$\frac{\partial u}{\partial x} + \frac{\partial w}{\partial z} = 0, \quad (3.2.6)$$

$$\frac{\partial \rho}{\partial t} + u \frac{\partial \rho}{\partial x} + w \frac{\partial \rho}{\partial z} = 0, \quad (3.2.7)$$

$$\rho \left(\frac{\partial u}{\partial t} + u \frac{\partial u}{\partial x} + w \frac{\partial u}{\partial z} \right) - \rho \nu \left(\frac{\partial^2 u}{\partial x^2} + \frac{\partial^2 u}{\partial z^2} \right) + \frac{\partial p}{\partial x} = 0, \quad (3.2.8)$$

$$\rho \left(\frac{\partial w}{\partial t} + u \frac{\partial w}{\partial x} + w \frac{\partial w}{\partial z} \right) - \rho \nu \left(\frac{\partial^2 w}{\partial x^2} + \frac{\partial^2 w}{\partial z^2} \right) + \frac{\partial p}{\partial z} + \rho g = 0, \quad (3.2.9)$$

$$\frac{dp_0(z)}{dz} = -\rho_0(z)g \quad (3.2.10)$$

3.2.2. Orr-Sommerfeld Equation

As in section 2.2.2, we will apply infinitesimally small perturbations to the steady state solutions. By observing their behavior, the stability of this system can be determined. Following this procedure, let us first assume that the steady state solutions are as follows:

$$u = U_0(z), \quad (3.2.11)$$

$$w = 0 , \quad (3.2.12)$$

$$\rho = \rho_0(z) , \quad (3.2.13)$$

$$p = p_0(z) , \quad (3.2.14)$$

where

$$\frac{dp_0(z)}{dz} = - \rho_0(z) g . \quad (3.2.15)$$

Let us now introduce perturbation quantities which are denoted by the superscript tilde.

$$u = U_0(z) + \tilde{u}(x, z, t) , \quad (3.2.16)$$

$$w = 0 + \tilde{w}(x, z, t) , \quad (3.2.17)$$

$$\rho = \rho_0(z) + \tilde{\rho}(x, z, t) , \quad (3.2.18)$$

$$p = p_0(z) + \tilde{p}(x, z, t) . \quad (3.2.19)$$

Substituting these into the governing equations, we will neglect quadratic terms of the perturbation quantities since it is assumed that these quantities and their derivatives have relatively small amplitude. Then

$$\frac{\partial \tilde{u}}{\partial x} + \frac{\partial \tilde{w}}{\partial z} = 0 , \quad (3.2.20)$$

$$\frac{\partial \tilde{\rho}}{\partial t} + U_0 \frac{\partial \tilde{\rho}}{\partial x} + \tilde{w} \frac{\partial \rho_0}{\partial z} = 0 , \quad (3.2.21)$$

$$\frac{\partial \tilde{u}}{\partial t} + U_0 \frac{\partial \tilde{u}}{\partial x} + \tilde{w} \frac{\partial U_0}{\partial z} - v \frac{\partial^2 U_0}{\partial z^2} - v \left(\frac{\partial^2 \tilde{u}}{\partial x^2} + \frac{\partial^2 \tilde{u}}{\partial z^2} \right) + \frac{1}{\rho_0} \frac{\partial \tilde{p}}{\partial x} = 0 , \quad (3.2.22)$$

$$\frac{\partial \tilde{w}}{\partial t} + U_0 \frac{\partial \tilde{w}}{\partial x} - v \left(\frac{\partial^2 \tilde{w}}{\partial x^2} + \frac{\partial^2 \tilde{w}}{\partial z^2} \right) + \frac{1}{\rho_0} \frac{\partial \tilde{p}}{\partial z} + \frac{\tilde{p}}{\rho_0} g = 0 . \quad (3.2.23)$$

If we now consider the perturbation quantities, let us assume wavelike perturbations as

$$\begin{aligned}\tilde{u} &= (\hat{u}(z) \exp(i\alpha x - i\omega t) + \text{c.c.}) / 2 \\ &= (\hat{u}(z) \exp(i\alpha(x-ct)) + \text{c.c.}) / 2 ,\end{aligned}\quad (3.2.24)$$

$$\tilde{w} = (\hat{w}(z) \exp(i\alpha(x-ct)) + \text{c.c.}) / 2 , \quad (3.2.25)$$

$$\tilde{\rho} = (\hat{\rho}(z) \exp(i\alpha(x-ct)) + \text{c.c.}) / 2 , \quad (3.2.26)$$

$$\tilde{p} = (\hat{p}(z) \exp(i\alpha(x-ct)) + \text{c.c.}) / 2 , \quad (3.2.27)$$

where

$$c = \frac{\omega}{\alpha} = c_r + ic_i . \quad (3.2.28)$$

As explained in section 2.2.2, the imaginary part of the complex phase velocity c indicates the stability of the system. Namely, if $c_i > 0$, the perturbation grows with time and the system is unstable. If $c_i = 0$, then the system is neutrally stable, and if $c_i < 0$, the system is stable. By introducing these wavelike perturbations, the governing equations become a set of ordinary differential equations as shown below:

$$i\alpha \hat{u} + \frac{d\hat{w}}{dz} = 0 , \quad (3.2.29)$$

$$i\alpha (U_0 - c) \hat{p} + \frac{d\rho_0}{dz} \hat{w} = 0 , \quad (3.2.30)$$

$$\rho_0 \left(i\alpha (U_0 - c) \hat{u} + \frac{dU_0}{dz} \hat{w} \right) + \rho_0 v \left(\alpha^2 \hat{u} - \frac{d^2 \hat{u}}{dz^2} \right) - \hat{p} v \frac{d^2 U_0}{dz^2} + i\alpha \hat{p} = 0 , \quad (3.2.31)$$

$$\rho_0 i\alpha (U_0 - c) \hat{w} + \rho_0 v \left(\alpha^2 \hat{w} - \frac{d^2 \hat{w}}{dz^2} \right) + \frac{d\hat{p}}{dz} + \hat{p} g = 0 . \quad (3.2.32)$$

Since the flow is two-dimensional, we can introduce the stream function of the perturbation velocity field, which is

$$\begin{aligned}\tilde{\phi} &= \hat{\phi}(z) \exp(i\alpha x - i\omega t) \\ &= \hat{\phi}(z) \exp(i\alpha(x - ct))\end{aligned}\quad (3.2.33)$$

Then, by definition,

$$\tilde{u} = \frac{\partial \tilde{\phi}}{\partial z}, \quad (3.2.34)$$

$$\tilde{w} = -\frac{\partial \tilde{\phi}}{\partial x} = -i\alpha \tilde{\phi}. \quad (3.2.35)$$

Substituting these relations into equations (3.2.29), (3.2.30), (3.2.31) and (3.2.32), eliminating \hat{p} and \hat{p}' and applying Boussinesq's approximation, we get the following expression,

$$(U_0 - c) \left(\hat{\phi}'' - \hat{\phi} \right) + \left(-\frac{g}{\rho_0} \frac{d\rho_0}{dz} - U_0'' \right) \hat{\phi} = \frac{v}{i\alpha} \left\{ \hat{\phi}^{(3)} - 2\alpha \hat{\phi}'' + \alpha^2 \hat{\phi} \right\}, \quad (3.2.36)$$

where a superscript of prime denotes d/dz .

If we non-dimensionalize this equation by using characteristic length and velocity scales, the following equation is produced.

$$(U_0 - c) \left(\widehat{\phi}''' - \widehat{\phi} \right) + \left(\frac{N^2}{U_0 - c} - U_0'' \right) \widehat{\phi} = \frac{1}{i\alpha Re} \left\{ \widehat{\phi}^{IV} - 2\alpha \widehat{\phi}'' + \alpha^4 \widehat{\phi} \right\}, \quad (3.2.37)$$

where N is the Brunt-Väisälä frequency and Re is the Reynolds number.

Since this model has no density stratification in either layer, the Brunt-Väisälä frequency becomes zero and the equation may be simplified to

$$(U_0 - c) \left(\widehat{\phi}''' - \widehat{\phi} \right) - U_0'' \widehat{\phi} = \frac{1}{i\alpha Re} \left\{ \widehat{\phi}^{IV} - 2\alpha \widehat{\phi}'' + \alpha^4 \widehat{\phi} \right\}. \quad (3.2.38)$$

Equation is the so-called 'Orr-Sommerfeld' equation, which is actually just the vorticity equation obtained by eliminating the pressure p from the momentum equations. As one model is essentially a superposition of two homogeneous fluid flow systems, let us use the subscripts 1 and 2 to define the stream function and Reynolds number for the upper(1) and lower(2) layer quantities. Thus,

$$(U_0 - c) \left(\widehat{\phi}_1''' - \widehat{\phi}_1 \right) - U_0'' \widehat{\phi}_1 = \frac{1}{i\alpha Re_1} \left\{ \widehat{\phi}_1^{IV} - 2\alpha \widehat{\phi}_1'' + \alpha^4 \widehat{\phi}_1 \right\}, \quad (3.2.39)$$

$$(U_0 - c) \left(\widehat{\phi}_2''' - \widehat{\phi}_2 \right) - U_0'' \widehat{\phi}_2 = \frac{1}{i\alpha Re_2} \left\{ \widehat{\phi}_2^{IV} - 2\alpha \widehat{\phi}_2'' + \alpha^4 \widehat{\phi}_2 \right\}. \quad (3.2.40)$$

3.3 BOUNDARY CONDITIONS

There are three boundaries we have to consider here. They are: the bottom boundary which is rigid a wall at $z=-z_R$, the density interface which is a flexible boundary at $z=\eta$, and the upper boundary at $z = \text{infinity}$. Because of viscosity, the no-slip condition must be applied on both the rigid surface and the density interface which is main difference between this model and the previous inviscid model. Therefore, at $z=-z_R$, the boundary condition is simply

$$\hat{\phi}_2 = \hat{\phi}_2' = 0 \quad \text{at } z=-z_R, \quad (3.3.1)$$

where a superscript of prime denotes d/dz .

At the density interface, since each velocity, pressure and shear stress component must be continuous, the boundary condition may be expressed as:

$$\tilde{w}_1 = \tilde{w}_2, \quad (3.3.2)$$

$$\tilde{u}_1 = \tilde{u}_2, \quad (3.3.3)$$

$$v_1 \left(\frac{\partial \tilde{w}_1}{\partial x} + \frac{\partial \tilde{u}_1}{\partial z} \right) = v_2 \left(\frac{\partial \tilde{w}_2}{\partial x} + \frac{\partial \tilde{u}_2}{\partial z} \right), \quad (3.3.4)$$

$$-\tilde{p}_1 + 2\rho_1 v_1 \frac{\partial \tilde{w}_1}{\partial z} = -\tilde{p}_2 + 2\rho_2 v_2 \frac{\partial \tilde{w}_2}{\partial z} - T \frac{\partial^2 \eta}{\partial x^2}, \quad \text{at } z=\eta \quad (3.3.5)$$

where the subscripts 1 and 2 refer to upper and lower layer quantities respectively and T is the surface (interfacial) tension.

If we take a Taylor expansion around $z=0$, and neglect higher order terms of η , and non-dimensionalize by using a characteristic length scale L and velocity scale V , then

$$\widehat{\phi}_1 = \widehat{\phi}_2, \quad (3.3.6)$$

$$\widehat{\phi}_1' - \frac{U_0'}{U_0 - c} \widehat{\phi}_1 = \widehat{\phi}_2' - \frac{U_0'}{U_0 - c} \widehat{\phi}_2, \quad (3.3.7)$$

$$\frac{\gamma}{\text{Re}_1} \left\{ \widehat{\phi}_1'' - \left(\frac{U_0''}{U_0 - c} - \alpha^2 \right) \widehat{\phi}_1 \right\} = \frac{1}{\text{Re}_2} \left\{ \widehat{\phi}_2'' - \left(\frac{U_0''}{U_0 - c} - \alpha^2 \right) \widehat{\phi}_2 \right\}, \quad (3.3.8)$$

$$\begin{aligned} \frac{i\gamma}{\alpha \text{Re}_1} \widehat{\phi}_1''' + \gamma \left\{ (U_0 - c) - \frac{3i\gamma}{\text{Re}_1} \right\} \widehat{\phi}_1' - \gamma U_0' \widehat{\phi}_1 = \\ \frac{i}{\alpha \text{Re}_2} \widehat{\phi}_2''' + \left\{ (U_0 - c) - \frac{3i\gamma}{\text{Re}_2} \right\} \widehat{\phi}_2' - U_0' \widehat{\phi}_2 - \frac{\text{Ri} + \alpha^2 S}{U_0 - c} \widehat{\phi}_2, \end{aligned} \quad (3.3.9)$$

where

$$\gamma = \frac{\rho_1}{\rho_2}, \quad (3.3.10)$$

$$\text{Re}_i = \frac{VL}{v_i}, \quad (3.3.11)$$

$$\text{Ri} = \frac{(1-\gamma)gL}{v^2}, \quad (3.3.12)$$

where γ is the relative density, Ri is the (global) Richardson number, Re is the Reynolds number and S is the non-dimensional surface (interfacial) tension.

For the boundary at $z=\infty$, the boundary condition can be assumed to be the same the boundary condition at $z=-Z_R$. It should be noted, however, that this may produce some difficulties for our numerical analysis. A more complete treatment of this boundary condition will be discussed in the next section.

3.4 CALCULATION METHOD OF EIGENVALUES

3.4.1 Eigen Equation

The governing equations are fourth order and require four independent solutions in each layer. However, because of the boundary conditions at $z=\infty$ and $z=-z_R$, we will only need to determine two arbitrary solution constants instead of four. To solve these equations, we will perform two computing passes in which we will integrate the governing equations numerically from the boundaries to the density interface. These calculations will be performed in the upper and lower layers separately, then, by examination, the conditions that permit a perfect matching of these solutions at the interface will be determined. Some values of α and γ , as well as some tentative values of C_R and C_I must be chosen to start the calculation, and then, if they satisfy the matching conditions, the system stability can be determined by judging sign of C_I .

Let us assume that the form of the upper and lower layer solutions is as below,

$$\hat{\phi}_1 = A_1 \phi_{11} + A_2 \phi_{12} , \quad (3.4.1)$$

$$\hat{\phi}_2 = A_3 \phi_{21} + A_4 \phi_{22} , \quad (3.4.2)$$

where ϕ_{i1}, ϕ_{i2} are independent solutions for the Orr-Sommerfeld equation and the first subscript i denotes the layer.

If we know the values of ϕ_{i1}, ϕ_{i2} at the density interface, then by substituting them into the matching conditions (3.3.6),

(3.3.7), (3.3.8) and (3.3.9), we will obtain the following matrix

$$\left(\begin{array}{cccc} & & & \\ & & & \\ a_{ij} & & & \\ & & & \end{array} \right) \begin{pmatrix} A_1 \\ B_1 \\ A_2 \\ B_2 \end{pmatrix} = \begin{pmatrix} 0 \\ 0 \\ 0 \\ 0 \end{pmatrix},$$

(3.4.3)

where

$$a_{11} = \phi_{11},$$

$$a_{12} = \phi_{12},$$

$$a_{13} = -\phi_{21},$$

$$a_{14} = -\phi_{22},$$

$$a_{21} = \phi_{11}' - \left(\frac{U_0'}{U_0 - c} \right) \phi_{11},$$

$$a_{22} = \phi_{12}' - \left(\frac{U_0'}{U_0 - c} \right) \phi_{12},$$

$$a_{23} = -\phi_{21}' + \left(\frac{U_0'}{U_0 - c} \right) \phi_{21},$$

$$a_{24} = -\phi_{22}' + \left(\frac{U_0'}{U_0 - c} \right) \phi_{22},$$

$$a_{31} = \frac{\gamma}{\text{Re}_1} \phi_{11}'' - \frac{\gamma}{\text{Re}_1} \left(\frac{U_0'}{U_0 - c} - \alpha^2 \right) \phi_{11},$$

$$a_{32} = \frac{\gamma}{\text{Re}_1} \phi_{12}'' - \frac{\gamma}{\text{Re}_1} \left(\frac{U_0'}{U_0 - c} - \alpha^2 \right) \phi_{12},$$

$$\begin{aligned}
a_{11} &= -\frac{1}{Re_1} \phi_{11}'' + \frac{1}{Re_1} \left(\frac{U_0'}{U_0 - c} - \alpha^2 \right) \phi_{21}, \\
a_{14} &= -\frac{1}{Re_1} \phi_{12}'' + \frac{1}{Re_1} \left(\frac{U_0'}{U_0 - c} - \alpha^2 \right) \phi_{22}, \\
a_{41} &= \frac{i\gamma}{\alpha Re_1} \phi_{11}'' + \gamma \left((U_0 - c) - \frac{3i\alpha}{Re_1} \right) \phi_{11}' - \gamma U_0 \phi_{11}, \\
a_{42} &= \frac{i\gamma}{\alpha Re_1} \phi_{12}'' + \gamma \left((U_0 - c) - \frac{3i\alpha}{Re_1} \right) \phi_{12}' - \gamma U_0 \phi_{12}, \\
a_{31} &= -\frac{i}{\alpha Re_2} \phi_{21}'' - \left((U_0 - c) - \frac{3i\alpha}{Re_2} \right) \phi_{21}' + \left(U_0 + \frac{Ri + \alpha^2 S}{U_0 - c} \right) \phi_{21}, \\
a_{34} &= -\frac{i}{\alpha Re_2} \phi_{22}'' - \left((U_0 - c) - \frac{3i\alpha}{Re_2} \right) \phi_{22}' + \left(U_0 + \frac{Ri + \alpha^2 S}{U_0 - c} \right) \phi_{22}.
\end{aligned} \tag{3.4.4}$$

Therefore, for non-trivial solutions, the determinant of this matrix (a_{ij}) must be zero and the associated eigenvalue equation may be written as

$$\det(\Delta(\alpha, c; Re_1, Re_2, Ri, \gamma)) = 0. \tag{3.4.5}$$

To simplify the calculation, it is assumed that the kinematic viscosity takes almost the same value in both layers (i.e. $Re_1 = Re_2$) and the non-dimensional surface (interfacial) tension $S=0$ which can be easily estimated its effects by investigating the effect of the Richardson number Ri on the system stability. With this simplification, the eigen equation becomes

$$\det(\Delta(\alpha, c; Re, Ri, \gamma)) = 0 \quad . \quad (3.4.6)$$

3.4.2 Parasitic Growth Problems and Orthonormalization

Now, let us consider the problem of determining values for Φ_{11} , Φ_{12} at the density interface in order to solve this eigen equation. Although there are several possible methods, we will employ the method of direct integration since we know the values of Φ_{11} , Φ_{12} at boundaries. This reduces the problem into a one-point boundary problem, for which the method of direct integration gives high accuracy and also makes it possible to solve for situation involving relatively high Reynolds numbers.

If we follow the method developed by Betchov and Criminale (1967), from the boundary conditions, we choose the initial values of Φ_{11} , Φ_{12} to be

$$\Phi_{11} = (\phi_{11}, \phi_{11}', \phi_{11}'', \phi_{11}''') = (0, 0, 1, 0) \quad , \quad (3.4.7)$$

$$\Phi_{12} = (\phi_{12}, \phi_{12}', \phi_{12}'', \phi_{12}''') = (0, 0, 0, 1) \quad , \quad (3.4.8)$$

$$\Phi_{21} = (\phi_{21}, \phi_{21}', \phi_{21}'', \phi_{21}''') = (0, 0, 1, 0) \quad , \quad (3.4.9)$$

$$\Phi_{22} = (\phi_{22}, \phi_{22}', \phi_{22}'', \phi_{22}''') = (0, 0, 0, 1) \quad , \quad (3.4.10)$$

where Φ_{ij} is vector form of solutions.

However, since the upper layer is assumed to be unbounded, it is difficult to calculate Φ_{11} , Φ_{12} by integrating the equations from $z=\infty$ to $z=0$ without sacrificing accuracy.

Fortunately, our model uses the hyperbolic tangent velocity profile and in the $z \gg 1$ region, the coefficients of the Orr-

Sommerfeld equation are zero or constant. Therefore, the asymptotic solutions for $z \gg 1$ can be obtained as

$$\phi_{11} = \exp\left(-\left(\alpha^2 + \frac{U_c''}{U_c - c}\right)^{1/2} z\right), \quad (3.4.11)$$

$$\phi_{12} = \exp\left(-\left(\alpha^2 + i\alpha \operatorname{Re}(U_c - c)\right)^{1/2} z\right). \quad (3.4.12)$$

In our calculations, we use the values of these asymptotic solutions at $z=5$ as the starting values of integration. By using the Runge-Kutta-Gill numerical integration method with a calculation step $\Delta z = 0.005$ to 0.025 , we obtain the values of ϕ_{11} , ϕ_{12} and their derivatives at the density interface $z=0$. As the computer proceeds toward $z=0$, however, the solutions occasionally develop characteristic oscillations and the two solutions, ϕ_{11} and ϕ_{12} , become dependent. This phenomena, so-called parasitic growth problem, occurs more often when the system has either a large Reynolds number Re or wave number α .

To avoid this problem, several techniques have been developed. A few of them which are the filter method, the re-orthogonalization method, and the Riccati method (see Gersting & Jankowski (1972), Davey (1973 and 1977)). In this model, we will use the modified filter method which is based upon the method suggested by Kaplan (1964). The basic idea of this method is to maintain a right angle between the two

vectors Φ_{11} and Φ_{12} by subtracting Φ_{12} element from Φ_{11} . This produces

$$\Phi_{11N} = \Phi_{11} - K_1 \Phi_{12} , \quad (3.4.13)$$

where Φ_{11N} is the new vector which has been re-orthogonalized against Φ_{12} and K_1 is a modification coefficient.

Since the coefficients of the Orr-Sommerfeld equation can be considered to be constant locally, the solutions should have the same forms as the $z \rightarrow \infty$ case, i.e.

$$\overline{\Phi} = A_i \overline{\Phi_{ij}} , \quad (3.4.14)$$

where $\overline{\Phi_{ij}}$ is the solution matrix

$$\overline{\Phi_{ij}} = \begin{pmatrix} \Phi_{11} & \Phi_{11} & \Phi_{11} & \Phi_{11} \\ \Phi_{12} & \Phi_{12} & \Phi_{12} & \Phi_{12} \\ \Phi_{21} & \Phi_{21} & \Phi_{21} & \Phi_{21} \\ \Phi_{22} & \Phi_{22} & \Phi_{22} & \Phi_{22} \end{pmatrix} , \quad (3.4.15)$$

$$A_i = (A_1, A_2, A_3, A_4) , \quad (3.4.16)$$

$$\Phi_{11} = \exp(B_1 z) , \quad (3.4.17)$$

$$\Phi_{12} = \exp(B_2 z) , \quad (3.4.18)$$

$$\Phi_{21} = \exp(B_3 z) , \quad (3.4.19)$$

$$\Phi_{22} = \exp(B_4 z) , \quad (3.4.20)$$

$$B_1 = - \left(\alpha^2 + \frac{U_0''}{U_0 - c} \right)^{1/2} , \quad (3.4.21)$$

$$B_2 = - \left(\alpha^2 + j \alpha \text{Re}(U_0 - c) \right)^{1/2} , \quad (3.4.22)$$

$$B_3 = -B_1 , \quad (3.4.23)$$

$$B_4 = -B_2 \quad (3.4.24)$$

Then

$$A_1 = \overline{\Phi \cdot \Phi_{11}} \quad (3.4.25)$$

Therefore,

$$A_1 = \begin{pmatrix} \frac{\exp(B_1 z)}{2B_1(B_2^2 - B_1^2)} (\phi''' - B_1 \phi'' - B_2^2 \phi' + B_1 B_2^2 \phi) \\ \frac{-\exp(B_2 z)}{2B_2(B_2^2 - B_1^2)} (\phi''' - B_2 \phi'' - B_1^2 \phi' + B_2 B_1^2 \phi) \\ \frac{\exp(B_3 z)}{2B_3(B_4^2 - B_3^2)} (\phi''' - B_3 \phi'' - B_4^2 \phi' + B_3 B_4^2 \phi) \\ \frac{-\exp(B_4 z)}{2B_4(B_4^2 - B_3^2)} (\phi''' - B_4 \phi'' - B_3^2 \phi' + B_4 B_3^2 \phi) \end{pmatrix} \quad (3.4.26)$$

where A_1, \dots, A_4 represent the magnitude of each element of a particular solution within the solutions Φ .

Thus, the modified solutions should satisfy the following relationship,

$$A_2(\Phi_{11N}) = A_4(\Phi_{11N}) = 0 \quad (3.4.27)$$

and the modification coefficients K_i become

$$K_1 = \frac{A_2(\Phi_{11})}{A_2(\Phi_{12})} \quad \text{for } z > 0 \quad (3.4.28)$$

$$K_2 = \frac{A_4(\Phi_{21})}{A_4(\Phi_{22})} \quad \text{for } z < 0 \quad (3.4.29)$$

Thus, the modified solutions may be written as

$$\Phi_{z+N} = \Phi_{z:} - \frac{A_3(\Phi_{z:})}{A_4(\Phi_{z:})} \Phi_{z:} \quad \text{for } z > 0$$

(3.4.30)

$$\Phi_{z+N} = \Phi_{z:} - \frac{A_3(\Phi_{z:})}{A_4(\Phi_{z:})} \Phi_{z:} \quad \text{for } z < 0 \quad (3.4.31)$$

By using this method in every several calculation step, the accumulation of the truncation errors can be avoided.

3.4.3 Determination of Eigenvalues

In previous sections (3.4.1 and 3.4.2), the eigenvalue problem is presented in terms of the 6 parameters α , C_R , C_I , R_i , R_e and γ . It is convenient to regard four of the parameters as given, and to present the determinant values on the plane of the other two. In this analysis, we will choose two possible combinations. In the first, we fix C_I , R_i , R_e , γ and plot the determinant values on α - C_R plane, while in the second, we fix α , R_i , R_e , γ and plot on C_R - C_I plane.

For example, if we use the second combination, the program will require α , R_i , R_e and γ as given values, and a tentative range for C_R and C_I including the calculation steps ΔC_R and ΔC_I . Based on these values, the computer will perform the numerical integration from the boundaries toward the interface, and map the real and imaginary parts of the left-hand-side of the eigen equation (3.4.6). For convenience, let us define these parts as D_R and D_I . When the mapping is completed on the C_R - C_I plane, depending on the sign

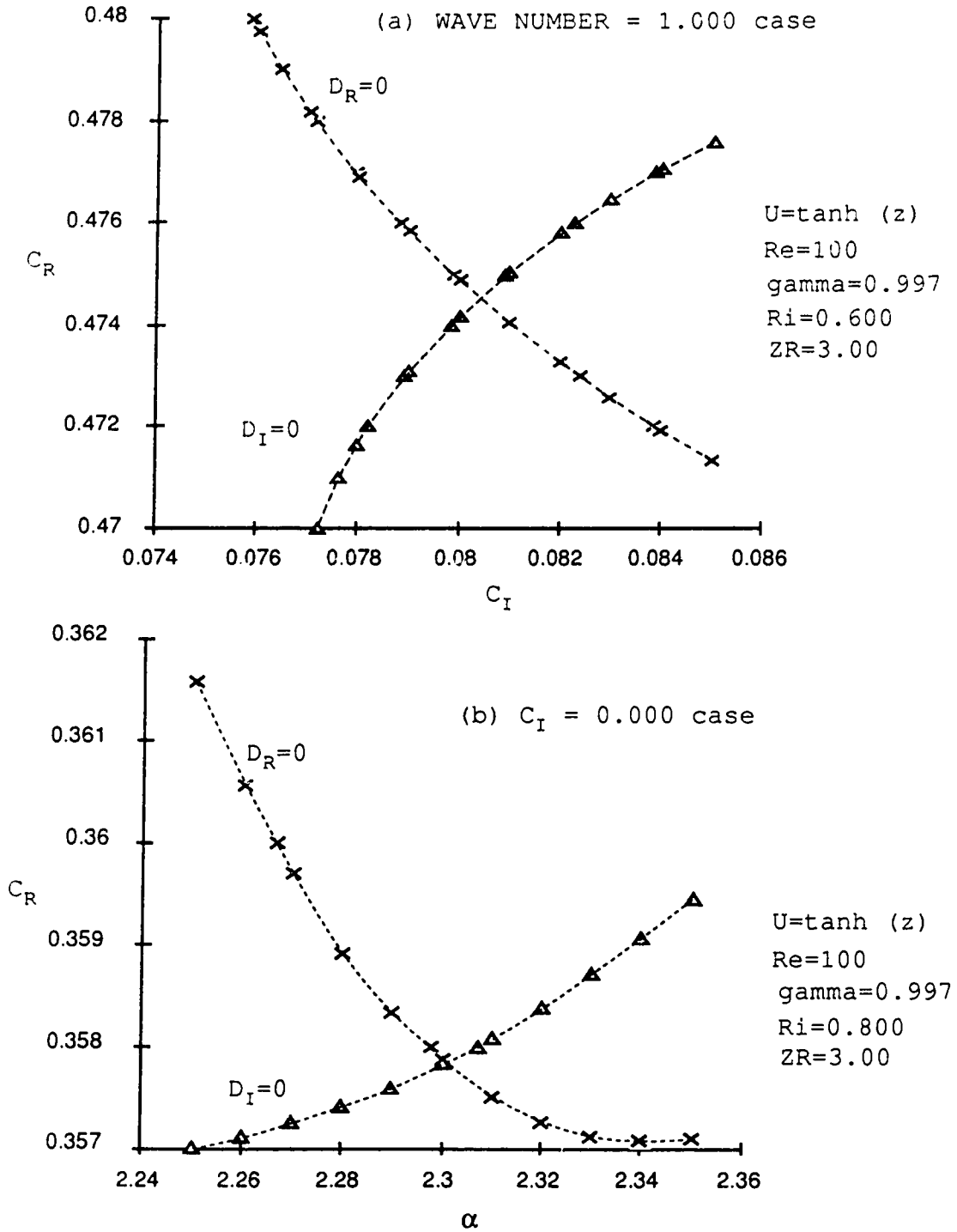


Figure 3.1. Determination of eigenvalues

of D_R and D_I , the computer will determine the points where $D_R=0$ and $D_I=0$. By connecting these points, we can make contour curves of $D_R=0$ and $D_I=0$ on C_R-C_I plane, with their points of intersection representing the eigenvalues (C_R, C_I) . By evaluating the expected values of C_R and C_I from this map, with the aid of computer, we can achieve solutions with higher accuracy. If the first combination of variables is used, the program works in same way except C_I is fixed instead of the wave number α . (see Figure 3.1(a) and (b))

3.4.4 Perturbation Quantities of the Flow

To obtain the eigen function $\Phi(z)$, we will use the following process. First, calculate the values of $\Phi(z)$ at the density interface based upon the eigenvalues. While the numerical integration is performed, calculated values of $\Phi(z)$ in each step are stored in memory as well as the modification coefficients K_i if the modifications are required. Using the matrix equation (3.4.26), we determine the coefficients A_1, \dots, A_4 , and by calculating these values from $z=0$ to the boundaries, the eigen function $\hat{\Phi}$ will be determined. It is important to note that this eigen function $\hat{\Phi}$ is defined as the stream function of the perturbation velocity field, therefore, we can find the perturbation quantities from $\hat{\Phi}$ as follows,

$$\tilde{u} = \left(\frac{d\hat{\Phi}}{dz} \exp(i\alpha(x-ct)) + \text{c.c.} \right) / 2 \quad (3.4.32)$$

$$\tilde{w} = \left(-i\alpha\hat{\phi} \exp(i\alpha(x-ct)) + \text{c.c.} \right) / 2 \quad (3.4.33)$$

$$\eta = \left(-\frac{i}{U_1 - c} \hat{\phi} \exp(i\alpha(x-ct)) + \text{c.c.} \right) / 2 \quad (3.4.34)$$

$$\tau = \left(-\overline{\tilde{u}\tilde{w}} + \text{c.c.} \right) / 2 \quad (3.4.35)$$

$$\varepsilon = \left(\frac{\overline{\tilde{u}^2} + \overline{\tilde{w}^2}}{2} + \text{c.c.} \right) / 2 \quad (3.4.36)$$

where τ is the Reynolds stress (averaged over the wave length) and ε is the turbulent kinetic energy.

3.5 MODEL III: THICKNESS EFFECTS

3.5.1 Formulation

Figure 3.2 shows the velocity and density profiles used in model III which was designed to investigate the effect of the rigid boundary and the lower layer thickness Z_R on the flow stability (The computer program for this problem and its flow-chart are listed in appendix B). It should be noted that the structure of this program allows it to calculate any type of velocity profile simply by changing the form of the function in subroutine FUNC. This feature allows us to investigate the stability of other velocity profiles in later sections. For this model the $\tanh(z)$ function was employed since it has been found that measured mean velocity profiles tend to match either the \tanh or error functions very well (see section 1.2.2). The calculations were performed on the University of Alberta Computing Service's Amdhal 5870 system with the FORTRAN77 programming language. It took about 20 sec. of CPU time to determine each eigenvalue on either the $\alpha-C_R$ or C_R-C_I plane. These solutions will be present in next sub-section.

3.5.2 Solutions

The proceeding problems were solved numerically for the parameter ranges $0.4 \leq Z_R \leq 5.0$, $0.0 \leq \alpha \leq 3.0$, $0.0 \leq Ri \leq 2.0$. Figures 3.3 to 3.18 summarize the results obtained including the dispersion relationship, neutral boundaries and the

perturbation quantity profiles. Figure 3.3 illustrates the dispersion relationship for the $Z_p = \infty$ case and is identical to the solutions arrived at by Nishida & Yoshida (1987). For this condition, the SVA and SVB waves are identical.

Figures 3.4 and 3.5 evaluate the rigid boundary effects and, again, both the SVA and SVB solutions have the same dispersion relationship, although they show that the additional unstable modes in the low wave number region. This is very similar to the inviscid cases presented in the previous sections as well as the Lalas & Einaudi (1976) results. These modes are, however, Holmboe modes instead of Kelvin-Helmholtz modes as in the Lalas' case. Figure 3.5 shows that the growth rates in the $\alpha C_i = 0.05$ region shrink as the Richardson number decreases, a phenomena noted in both models I and II. Eventually, the most unstable modes appear in the area where the Richardson number is about 0.4 and wave number is 0.8. This tendency is maintained until $Z_R = 0.4$, and will be discussed in the following section.

The dispersion relationship of SVA and SVB waves starts to separate at $Z_R = 1.7$; a phenomena which can be clearly seen in Figure 3.6. Similar to the inviscid model results, SVA waves are not influenced by a thinning of the lower layer thickness Z_R , except in the region of very low wave number or small Richardson number. As Z_R becomes smaller than 1.0, a numerical instability occurs for very small Richardson number flow and makes it impossible to calculate the dispersion

relationship, although these unstable regions eventually shrink as is presented in Figure 3.11.

Instead of testing the entire range of parameters, $\alpha=0.8$ and $Ri=0.4$ have been chosen as the most unstable mode and examined for stability. Figure 3.12 implies that this system will be stabilized when $Z_R < 0.43$. By contrast, SVB waves are much more stable against decreasing Z_R and for these waves, the criterion is met at approximately $Z_R=1.07$. This value is very close to that obtained from the inviscid models in the previous sections. Thus, it indicates that the viscosity effects on the system stability is in the order of 3 to 4%. This result is similar to the conclusions of Maslowe & Thompson (1972) and Nishida & Yoshida (1987).

Figures 3.13 to 3.17 illustrate the variation of the perturbation quantity profiles with Z_R . The Reynolds stress shows an obvious relationship between stability and energy transfers. The phase change of the displacement η also shows that the perturbation field must lie into the mean flow field in order to become unstable, which corresponds to the sign of Reynolds stress.

Figure 3.18 shows the stream line of the unstable modes of the SVA and SVB waves. It is obvious that SVB waves are deformed by the existence of the rigid boundary. Most of the features are identical with the inviscid case; except for smaller growth rates.

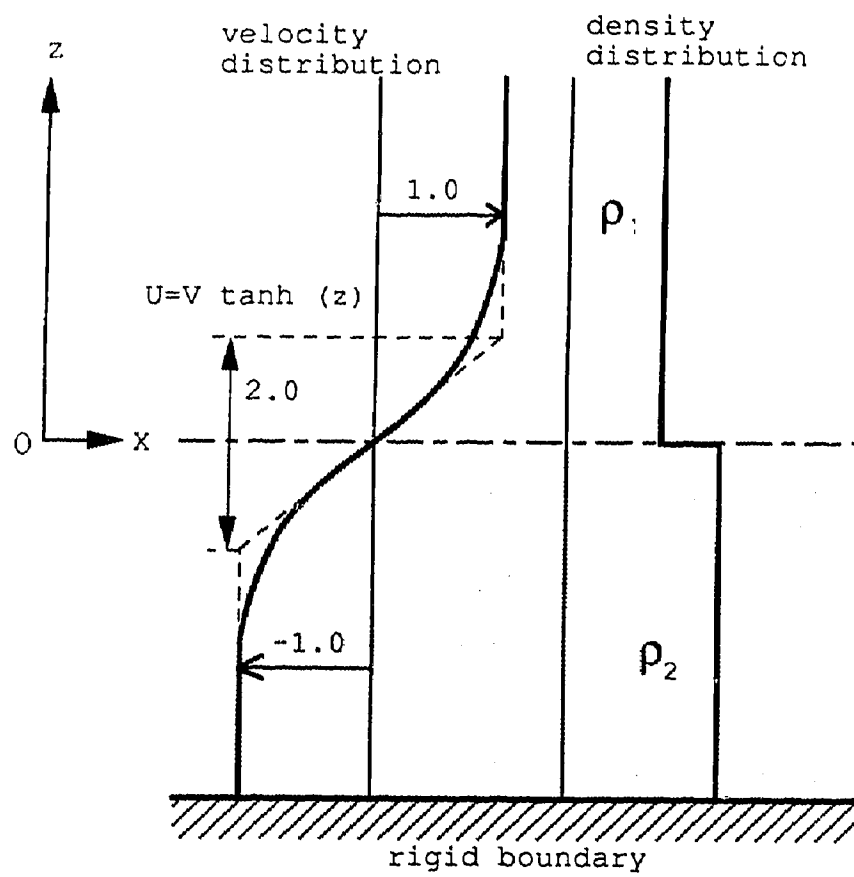


Figure 3.2. Velocity and density distributions of Model III

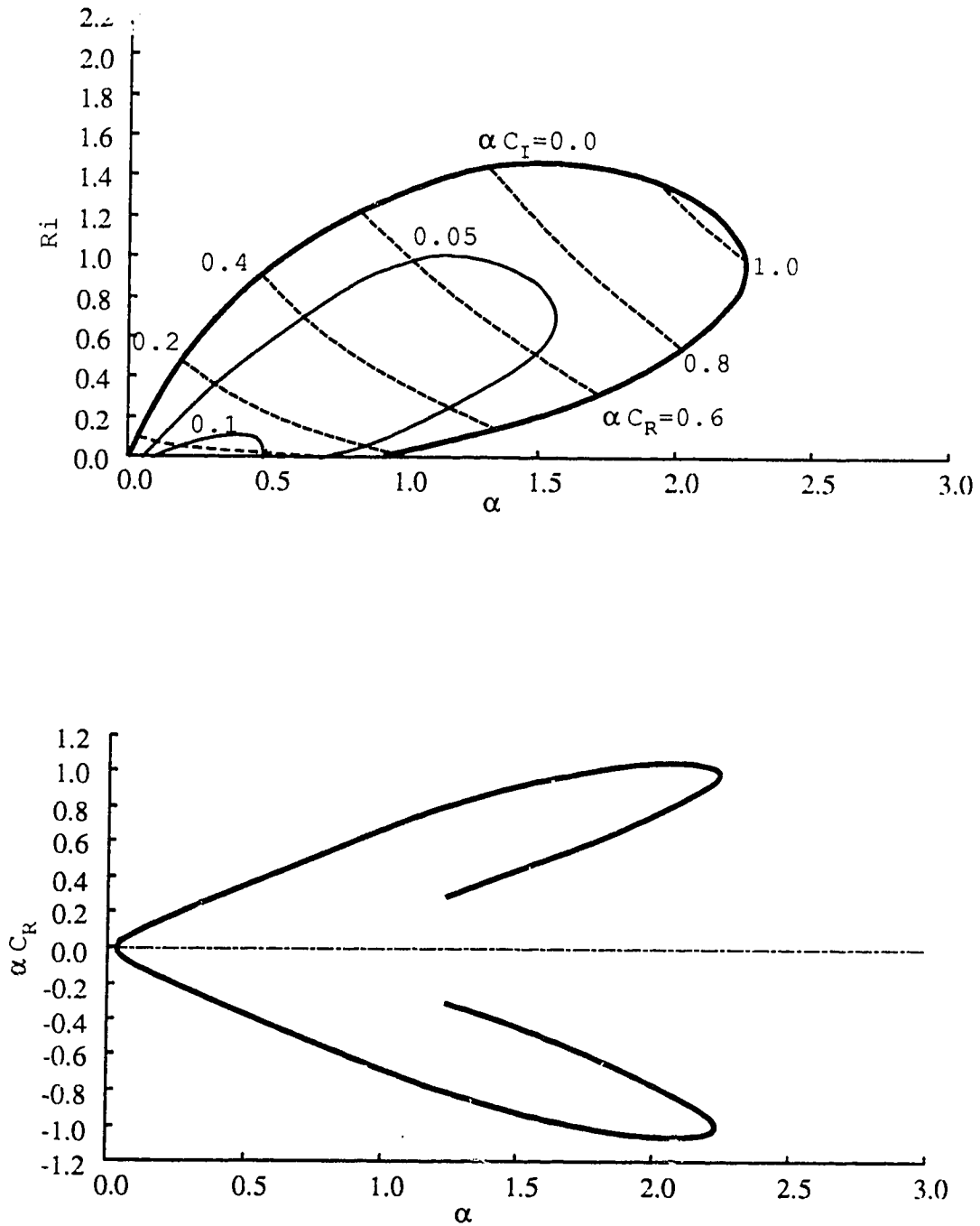


Figure 3.3. Dispersion relationship for $ZR=\infty$ case

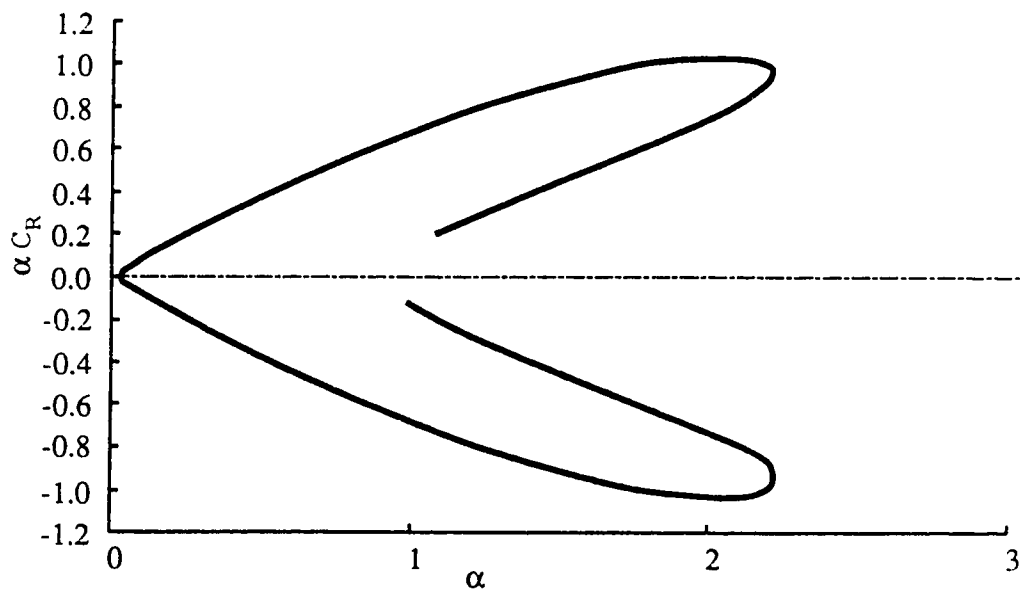
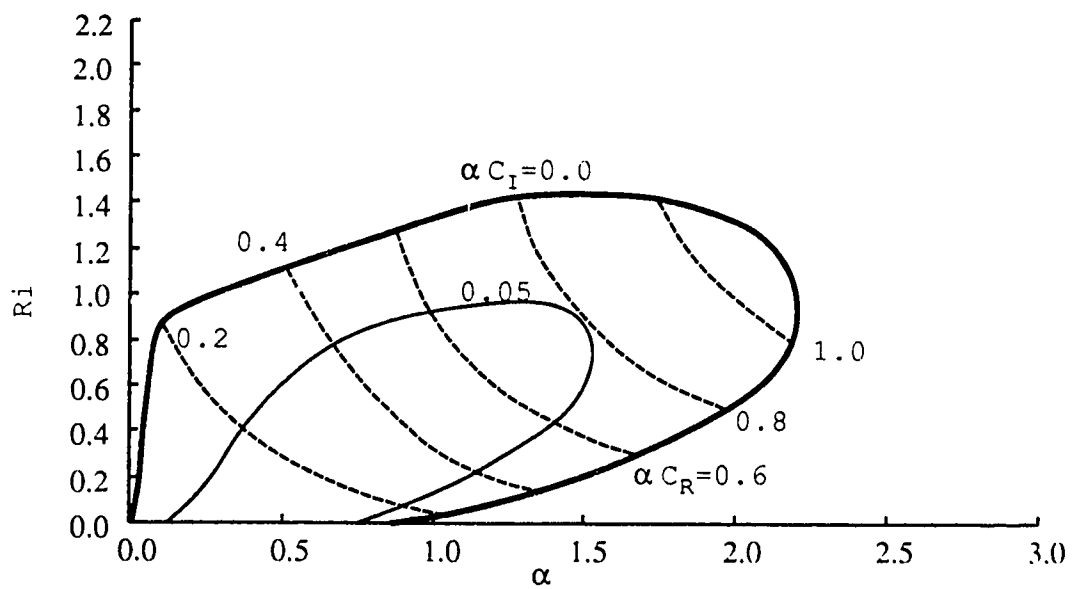


Figure 3.4. Dispersion relationship for $ZR=3.0$ case

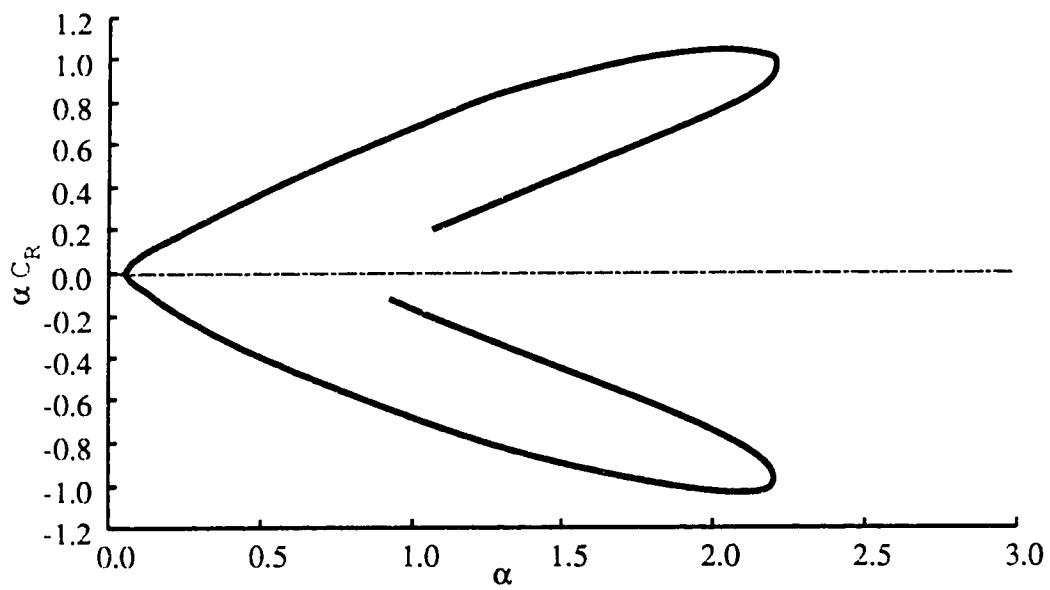
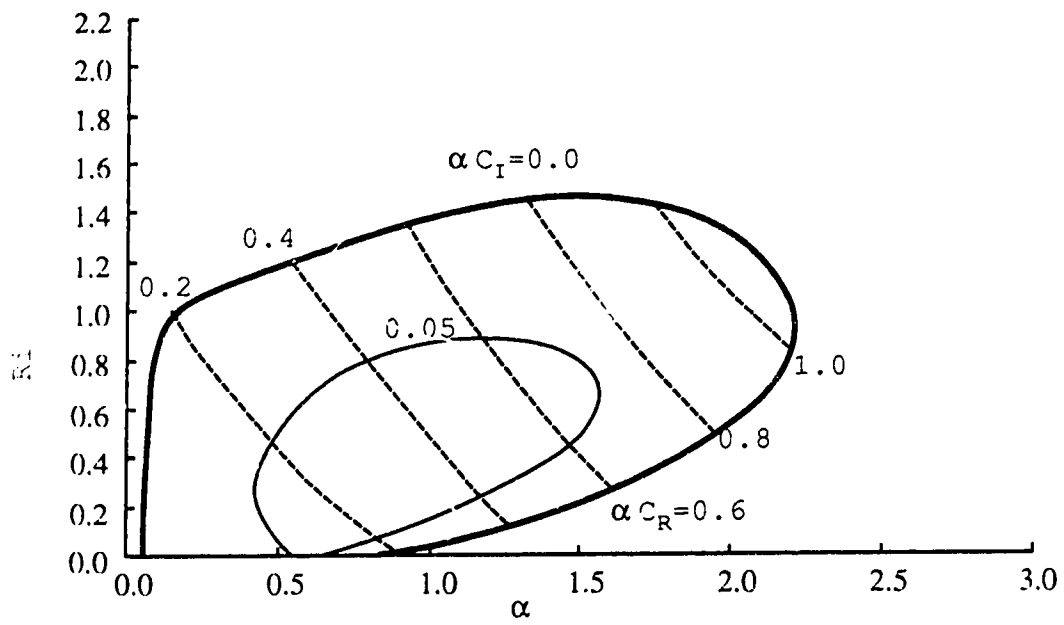


Figure 3.5. Dispersion relationship for $ZR=2.0$ case

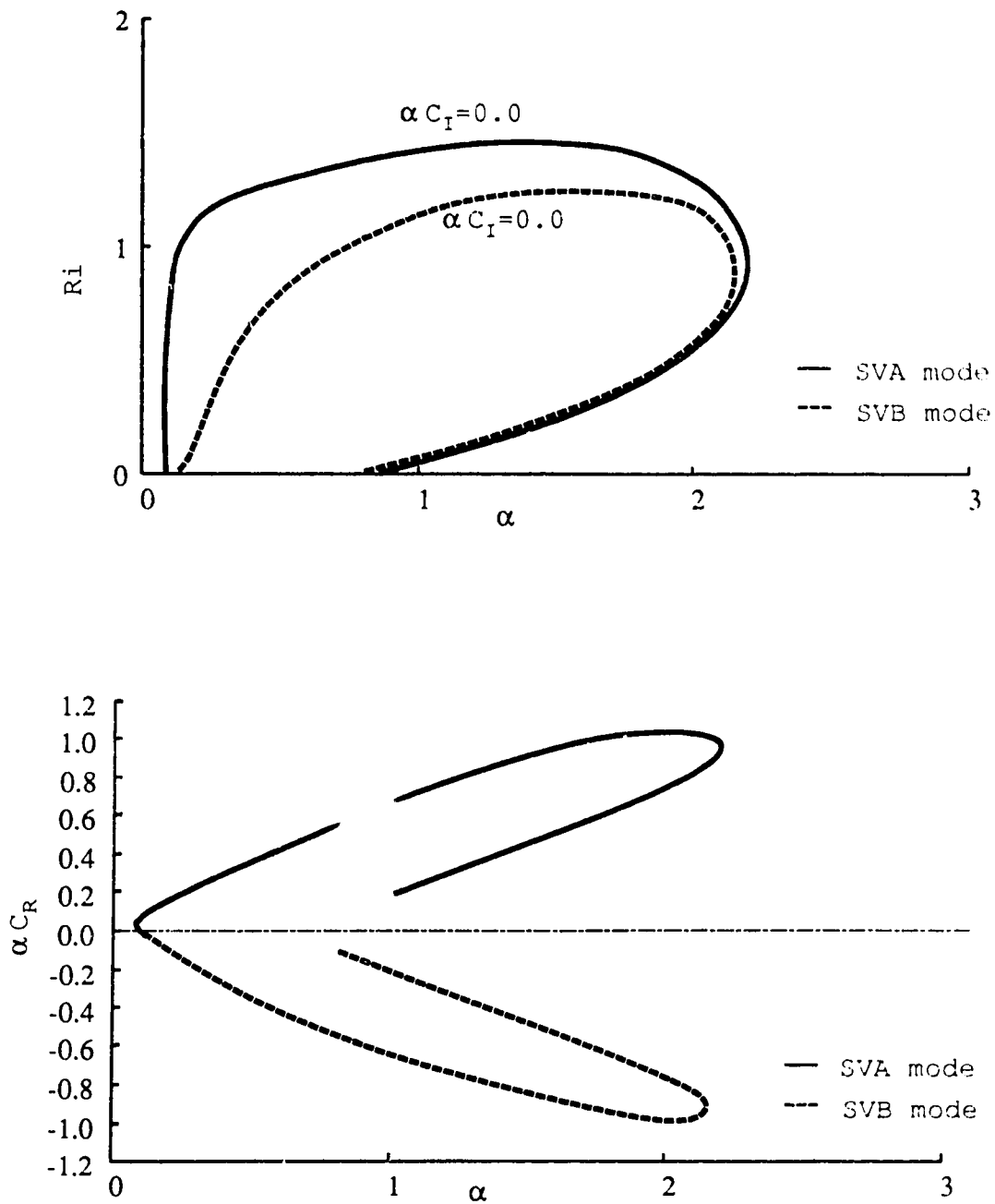


Figure 3.6. Neutral boundaries of $ZR=1.5$ case

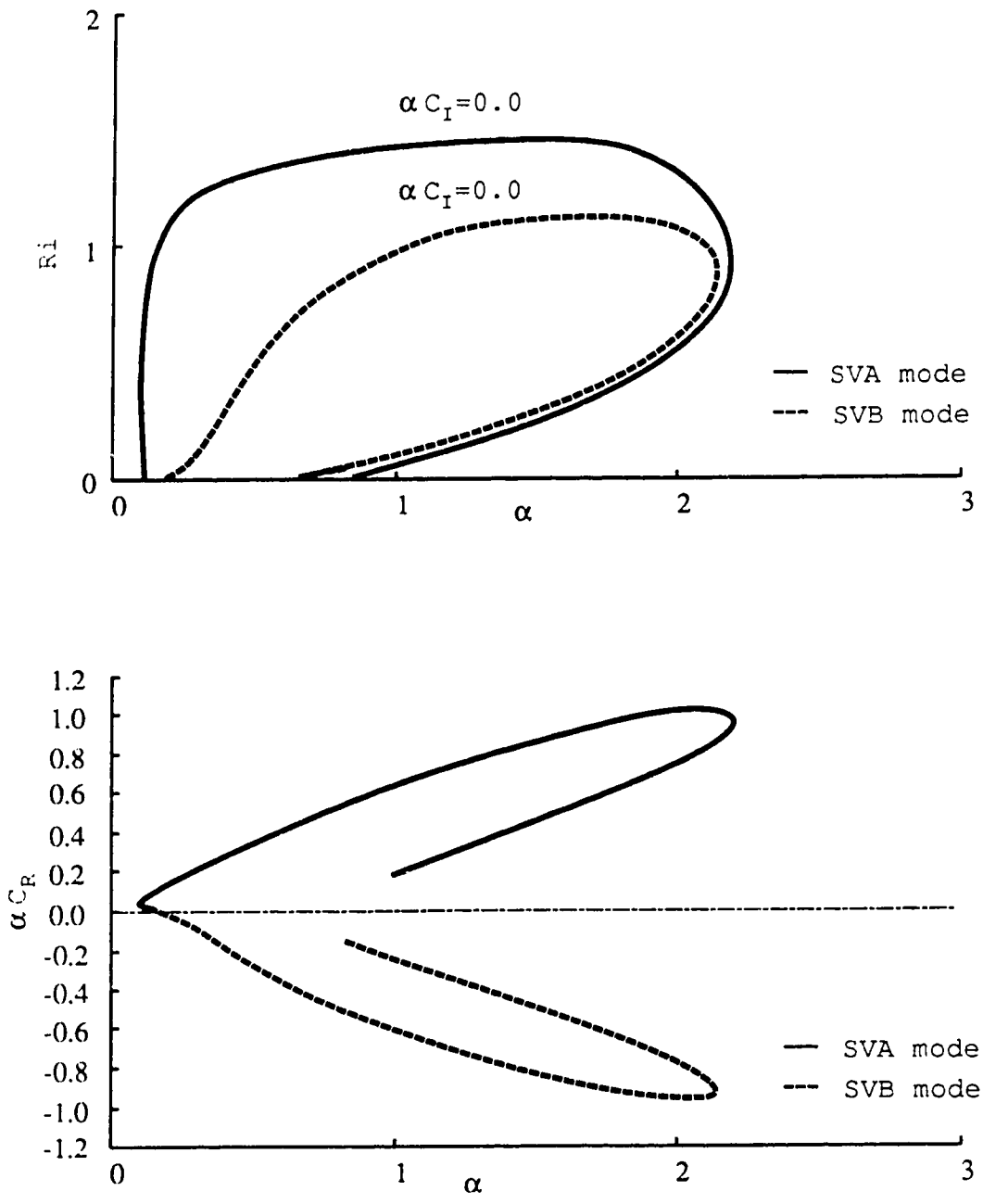


Figure 3.7. Neutral boundaries of ZR=1.3 case

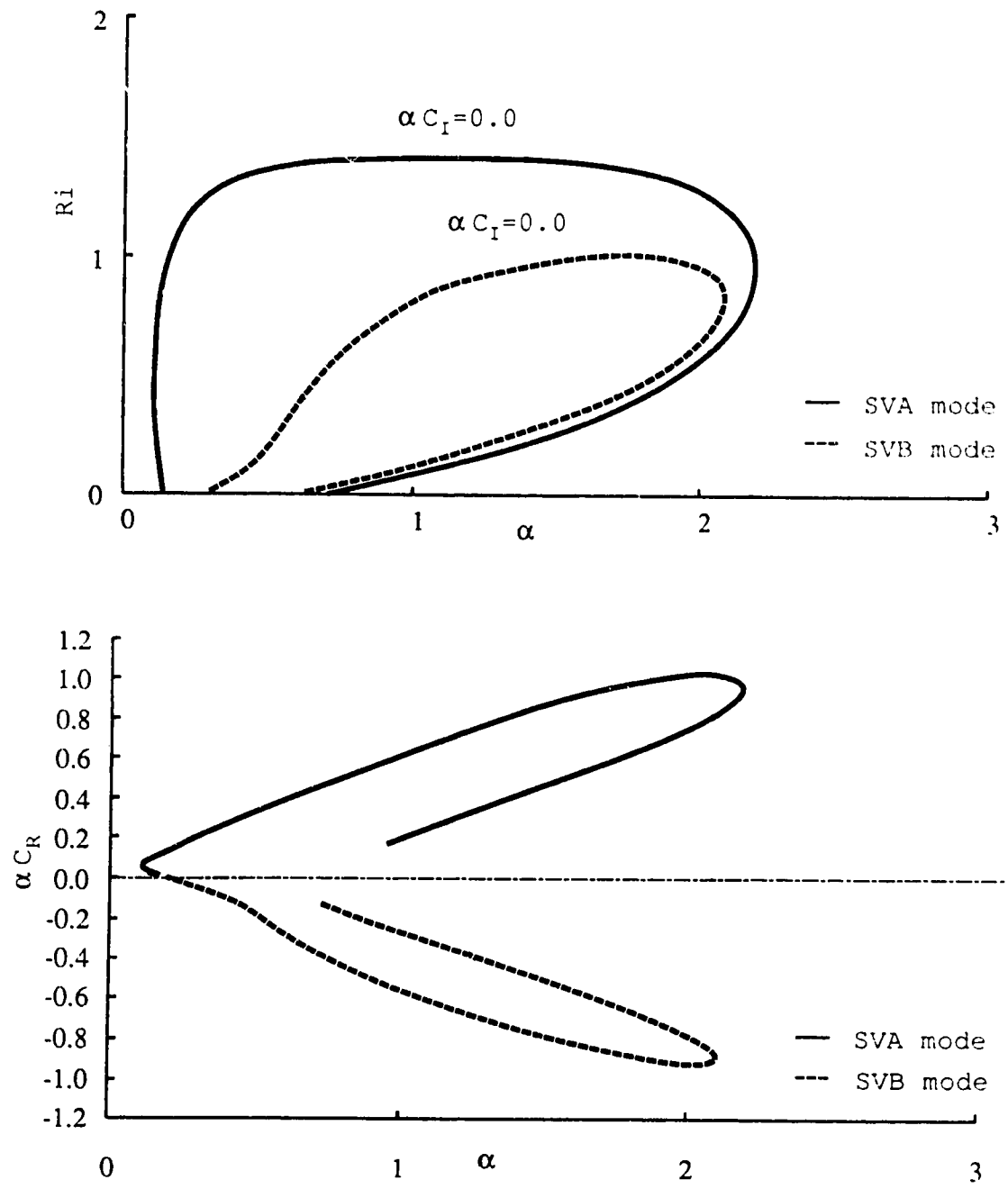
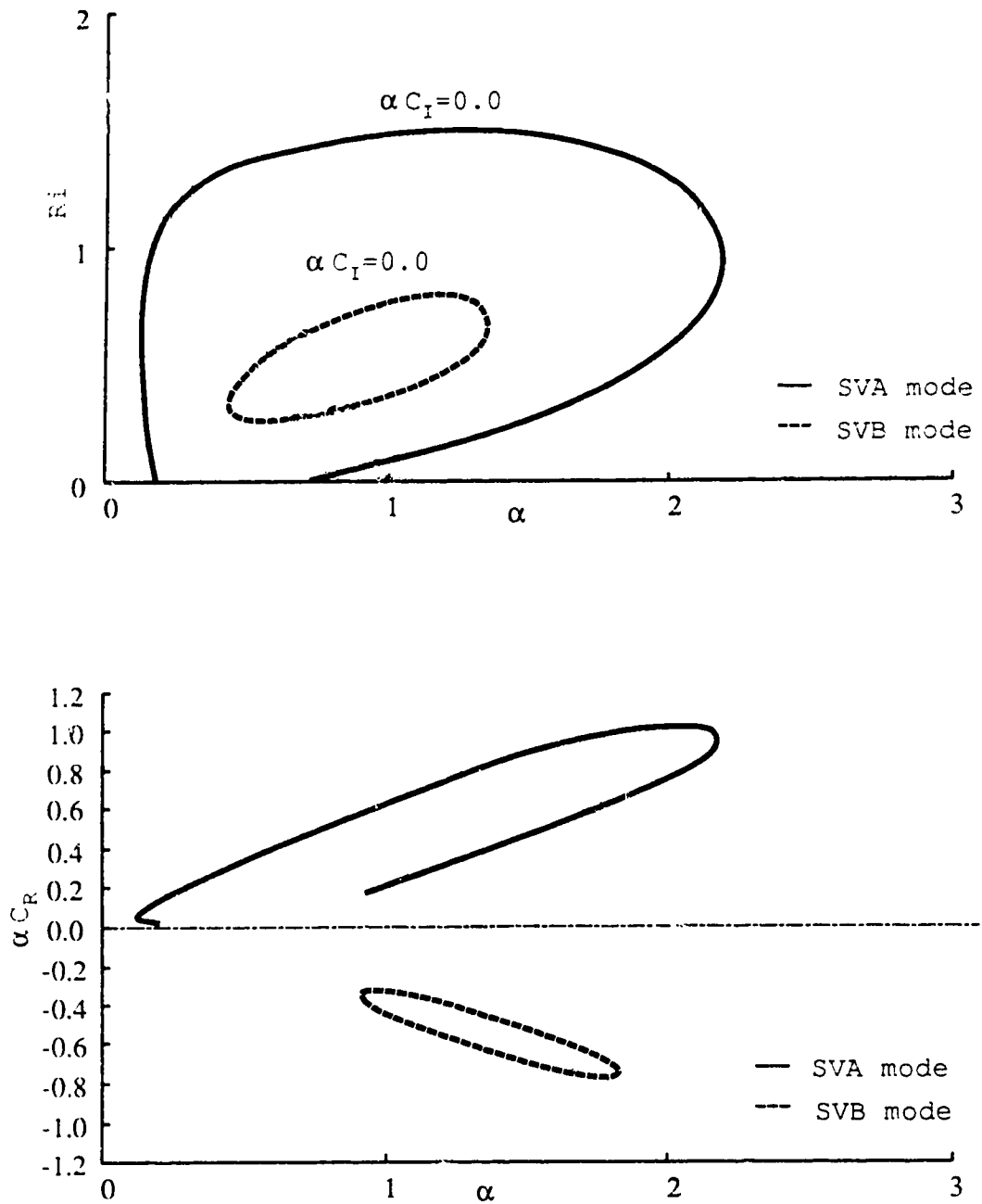


Figure 3.8. Neutral boundaries of ZR=1.2 case

Figure 3.9. Neutral boundaries of $ZR=1.1$ case

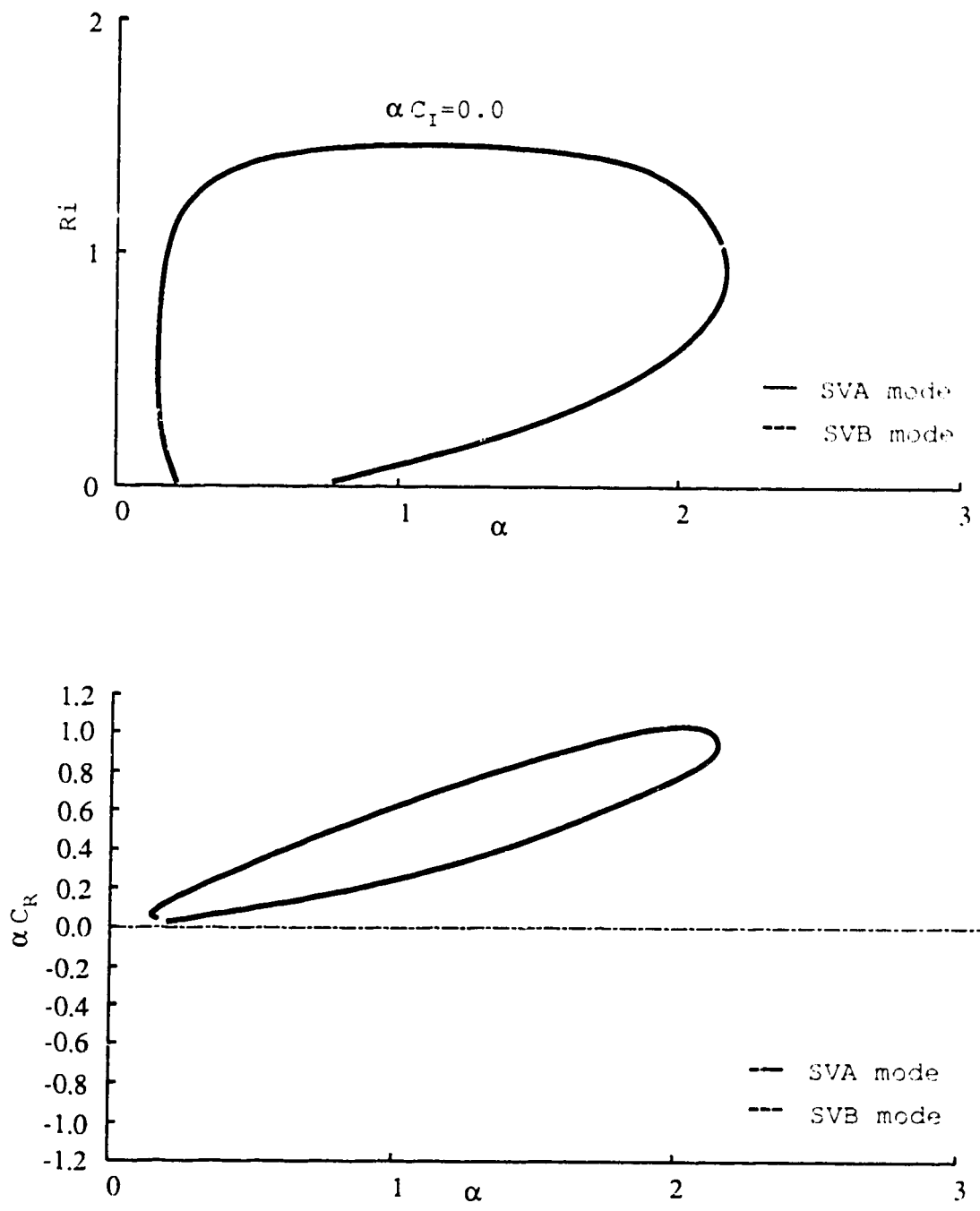
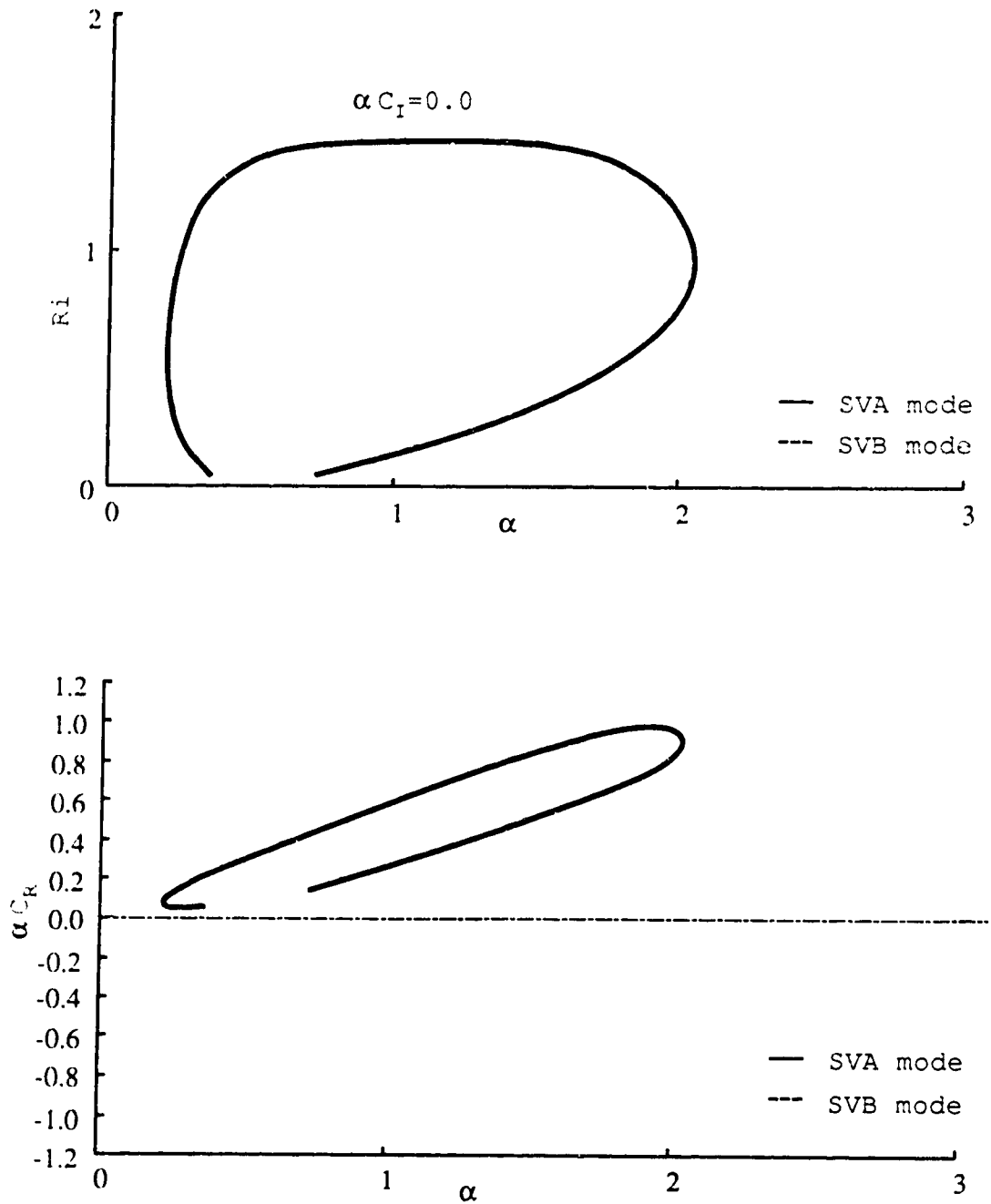


Figure 3.10. Neutral boundaries of ZR=1.0 case

Figure 3.11. Neutral boundaries of $ZR=0.7$ case

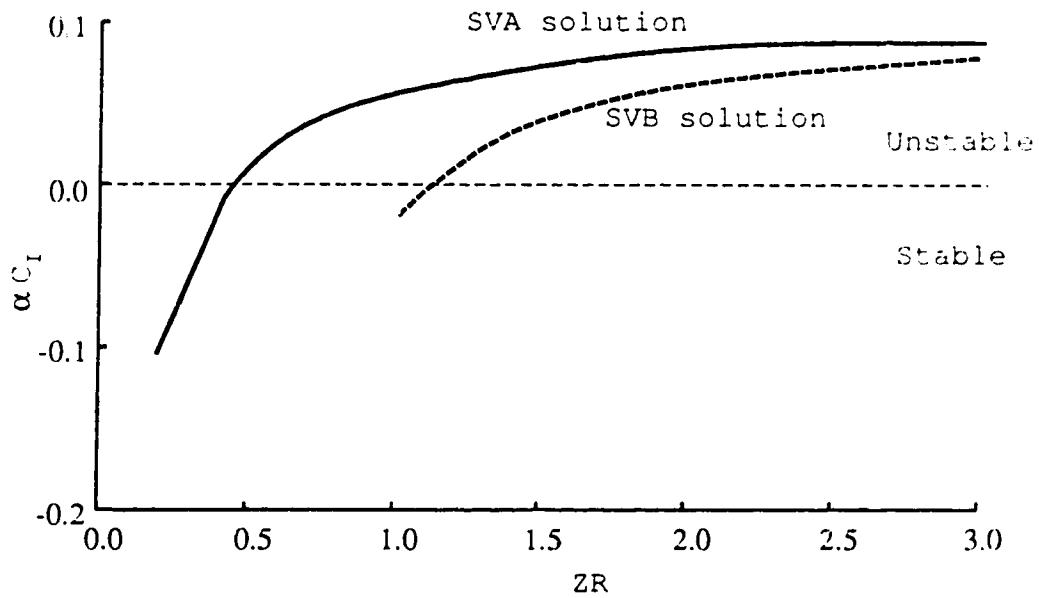
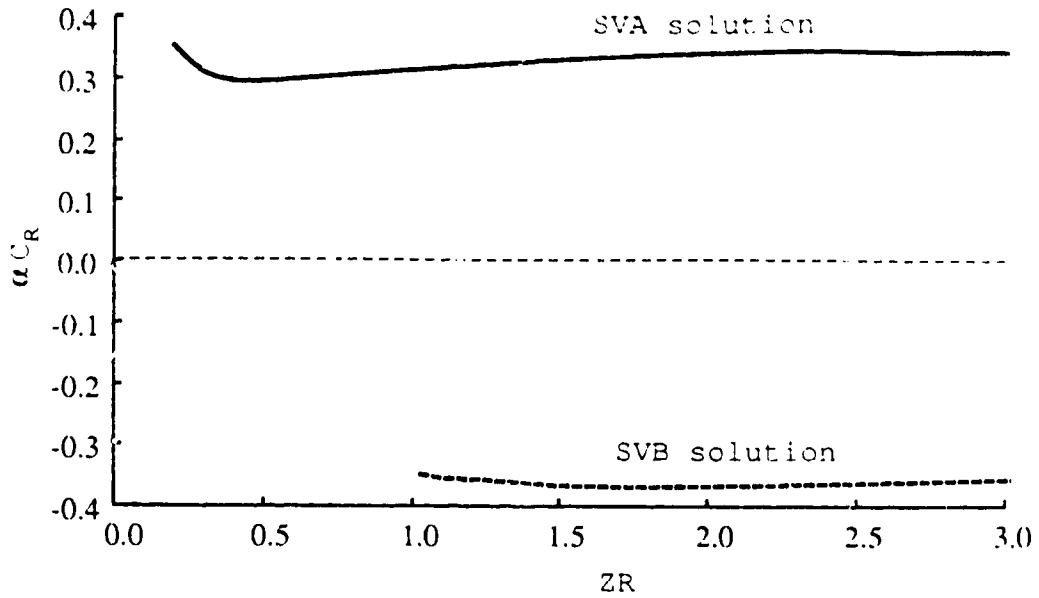
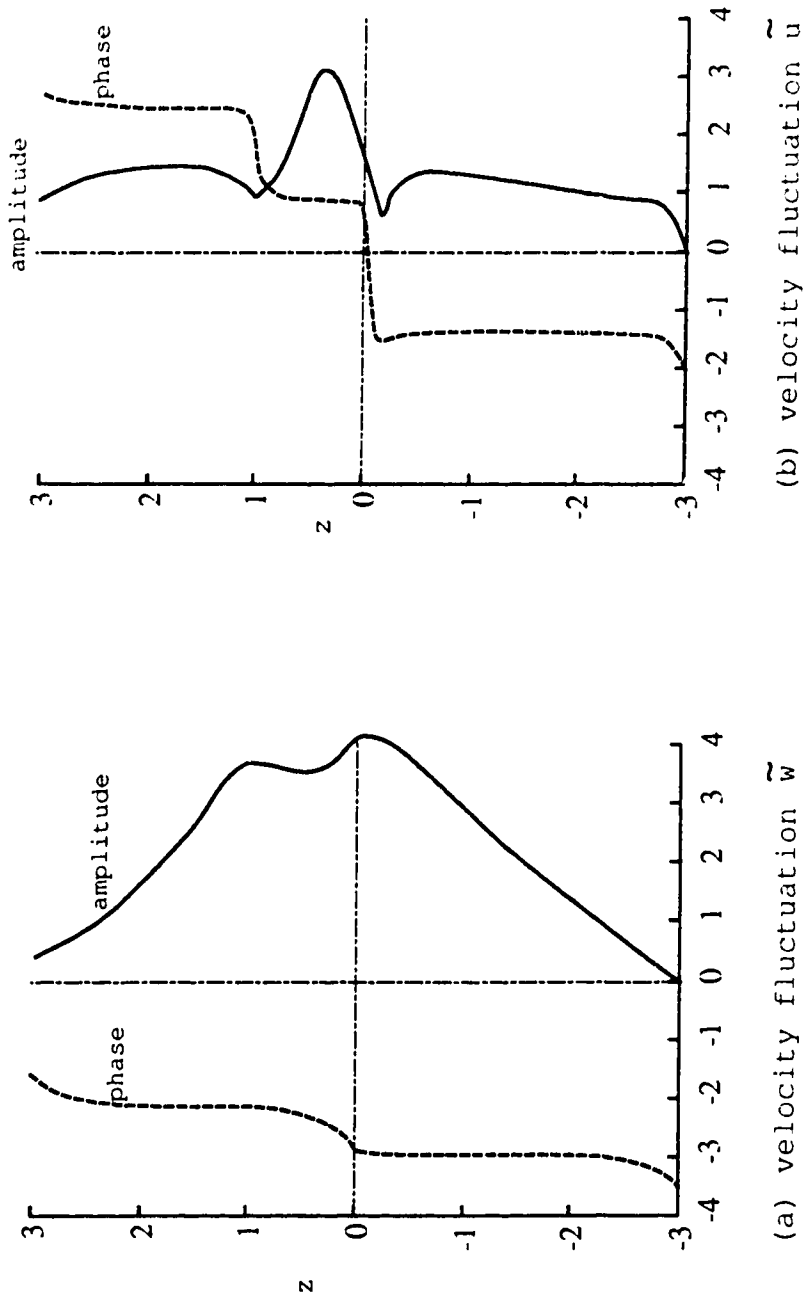
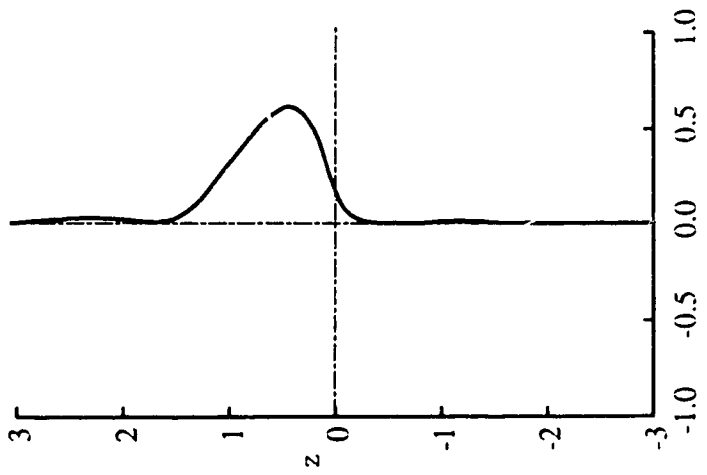


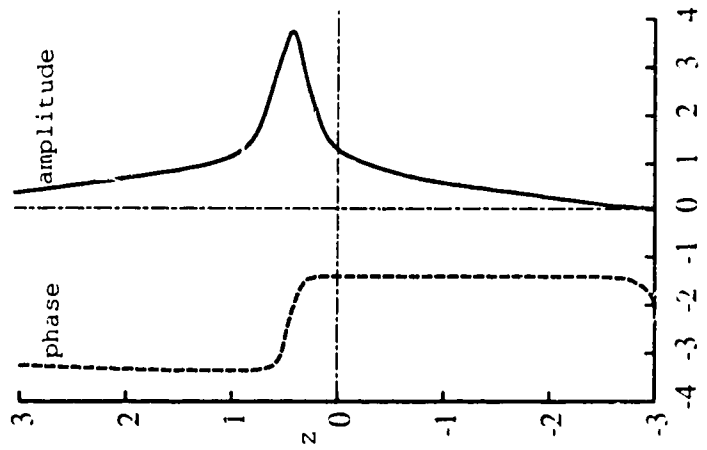
Figure 3.12. Relationship between lower layer thickness ZR and Phase velocity, growth rate.

Figure 3.13 (a)-(e) The perturbation quantities of the flow.
 $\alpha=0.8$ $Ri=0.4$ $C_R=0.432$ $\alpha C_I=0.084$ $ZR=3.0$ case.

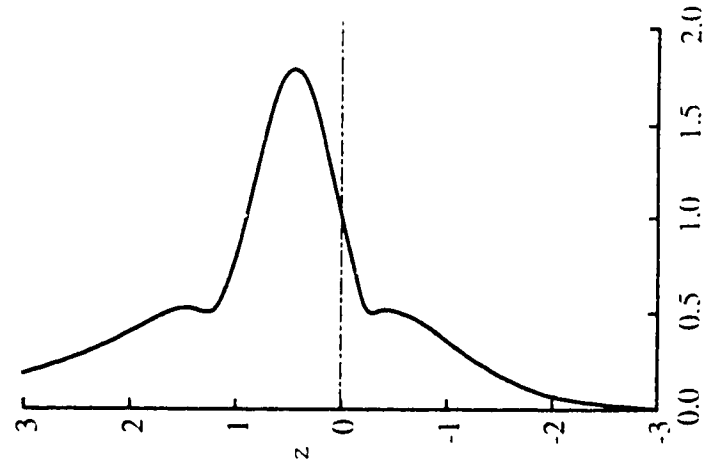




(c) Reynolds stress τ

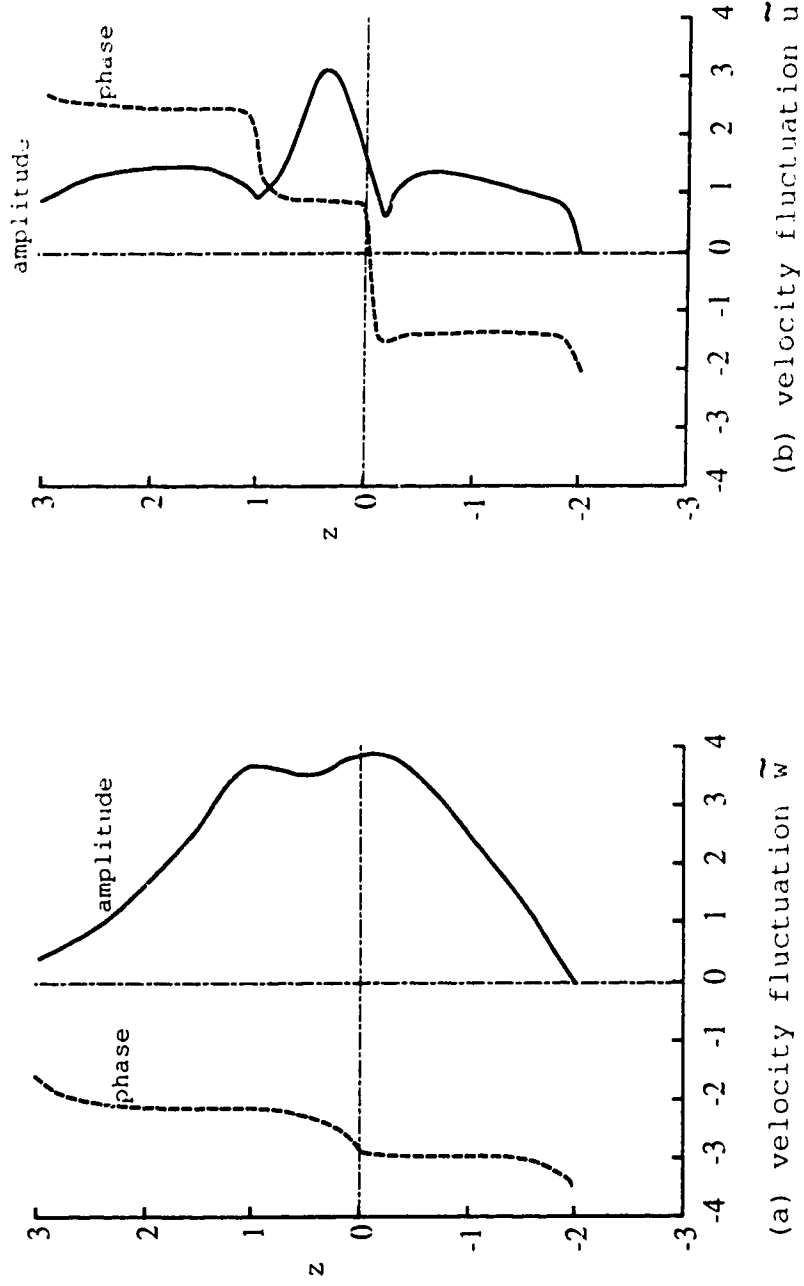


(d) Displacement η



(e) Turbulence energy ϵ

Figure 3.14 (a)-(e) The perturbation quantities of the flow.
 $\alpha=0.8$ $Ri=0.4$ $C_p=0.432$ $\alpha C_I=0.084$ $ZR=2.0$ case.



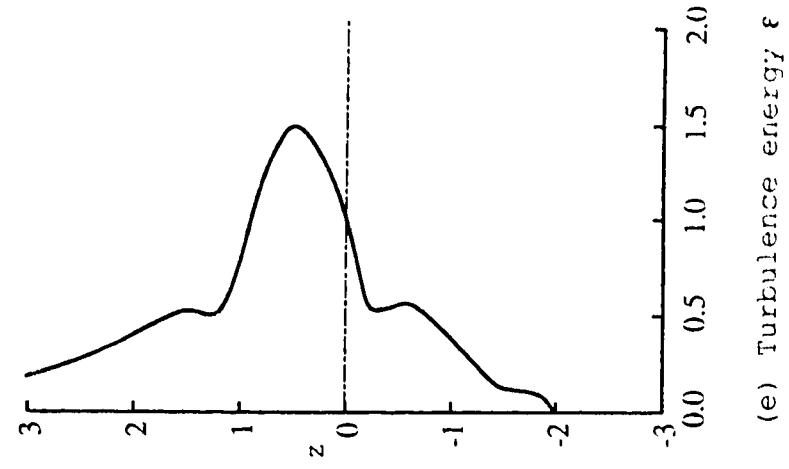
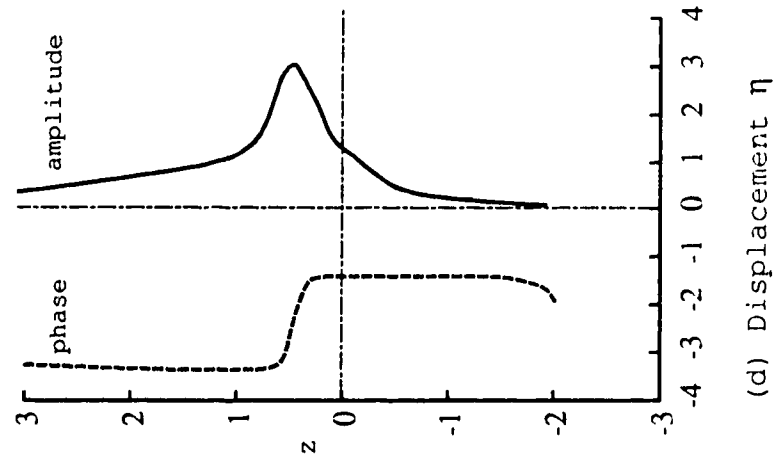
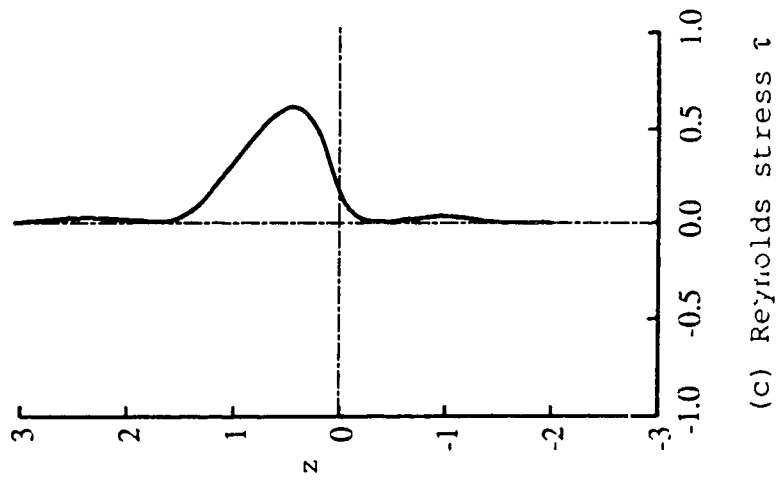
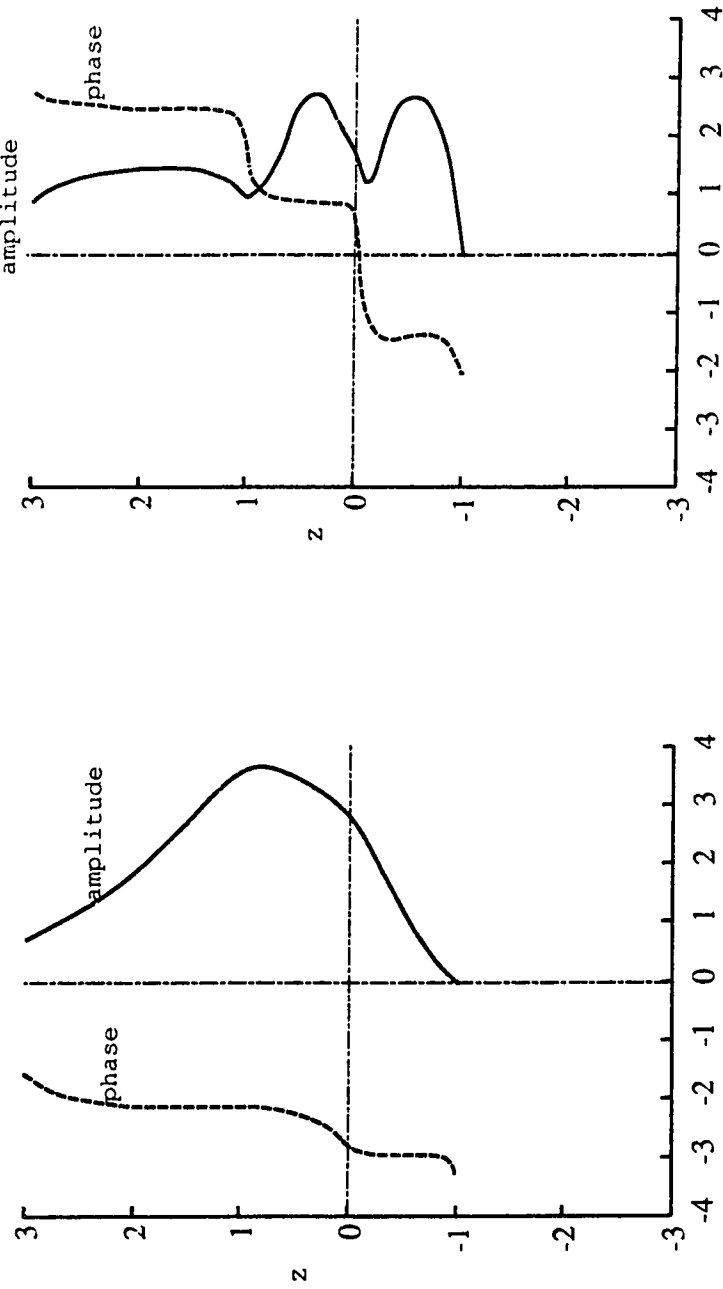


Figure 3.15 (a)-(e) The perturbation quantities of the flow.
 $\alpha=0.8$ $Ri=0.4$ $C_R=0.393$ $\alpha C_I=0.056$ $ZR=1.0$ case.



(a) velocity fluctuation \tilde{w}

(b) velocity fluctuation \tilde{u}

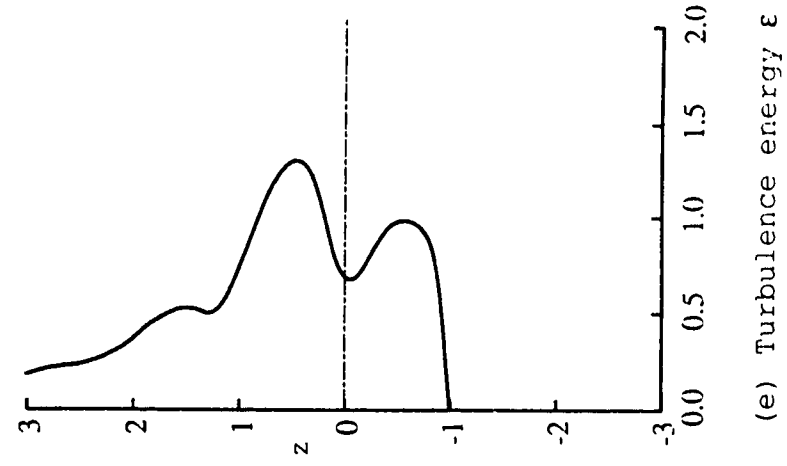
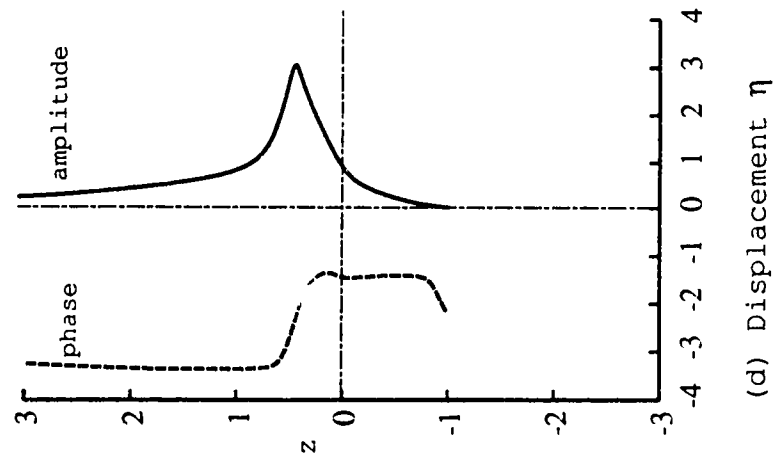
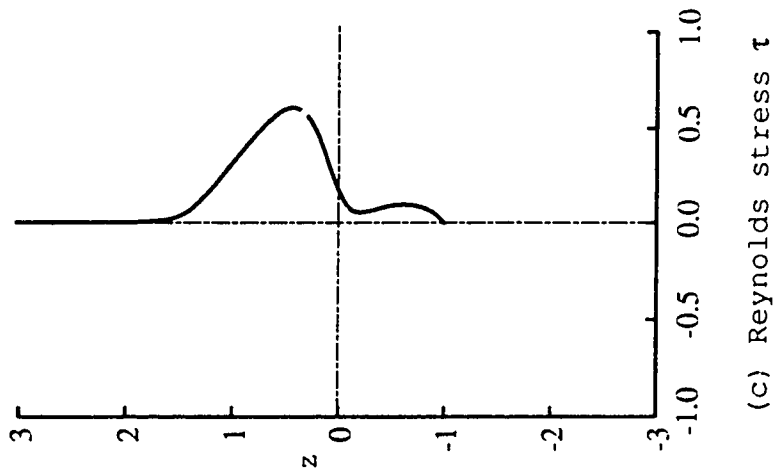
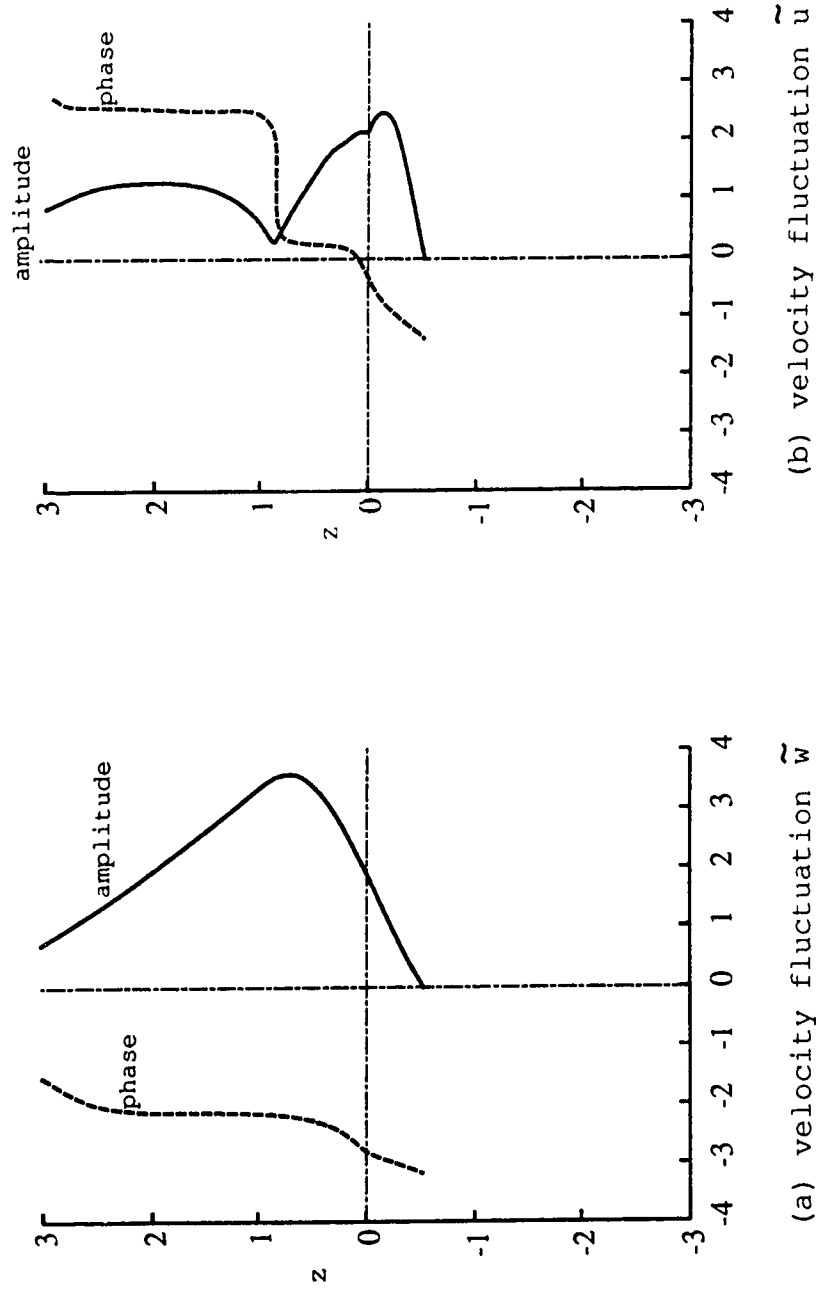


Figure 3.16 (a)-(e) The perturbation quantities of the flow.
 $\alpha=0.8$ $Ri=0.4$ $C_R=0.371$ $\alpha C_I=0.011$ $ZR=0.5$ case.



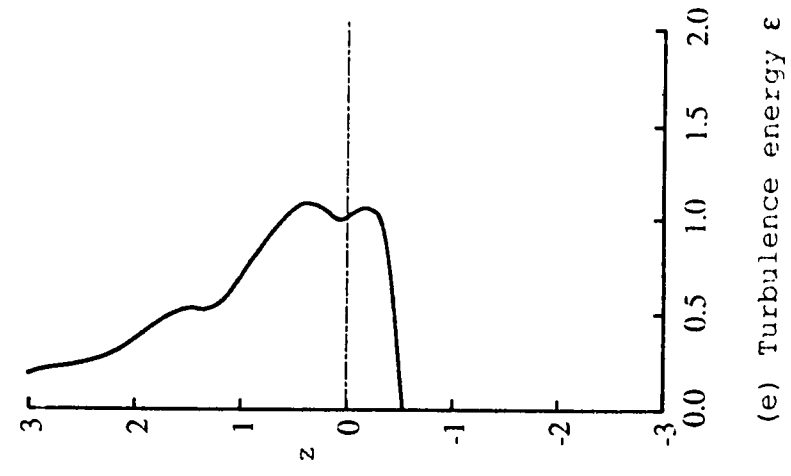
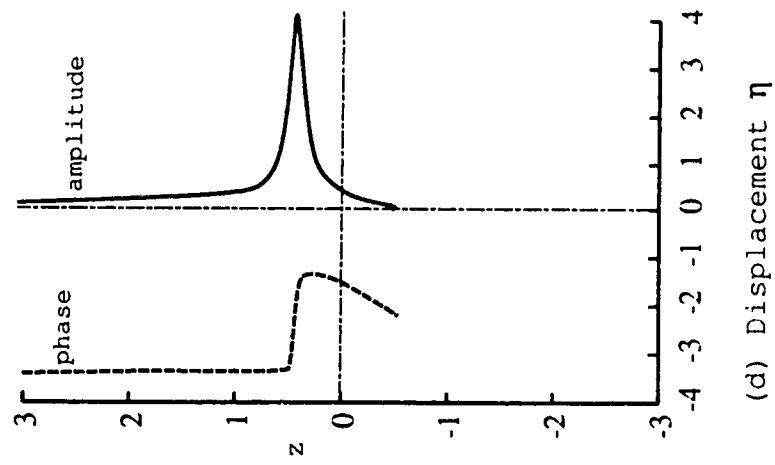
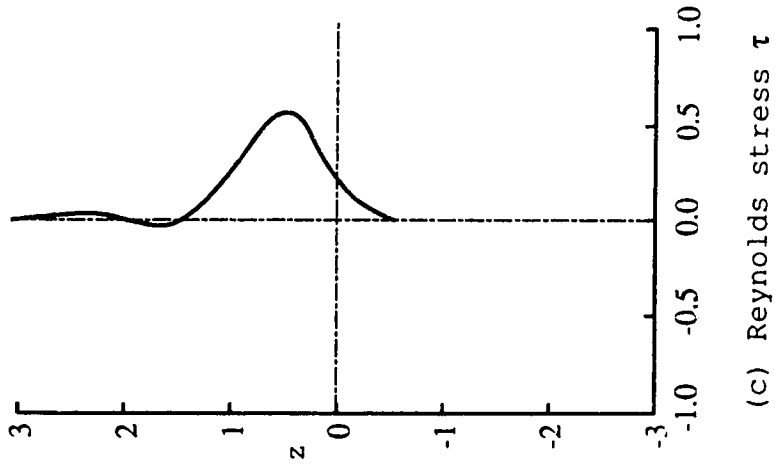
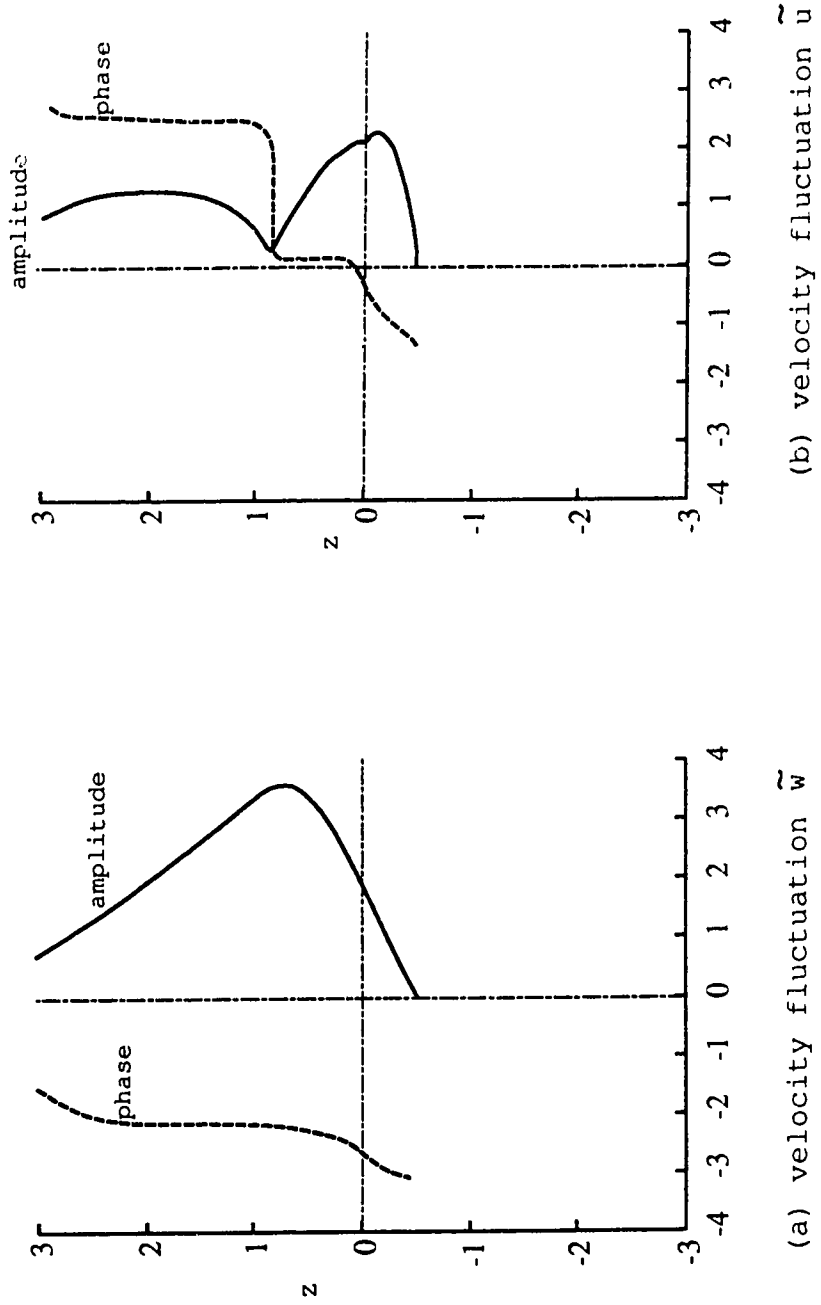
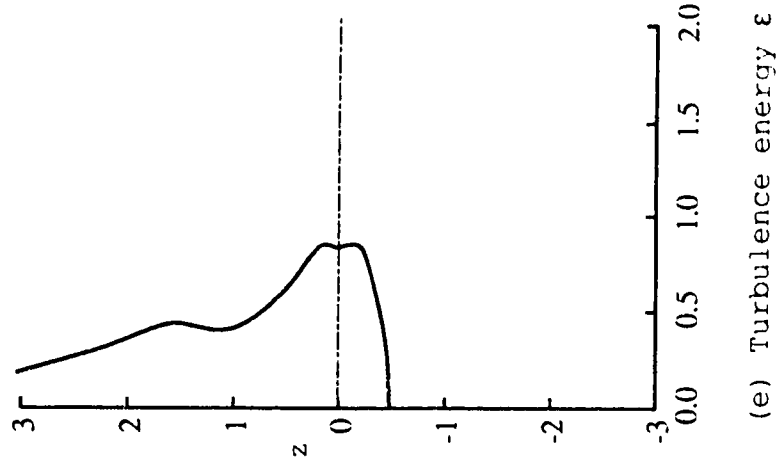
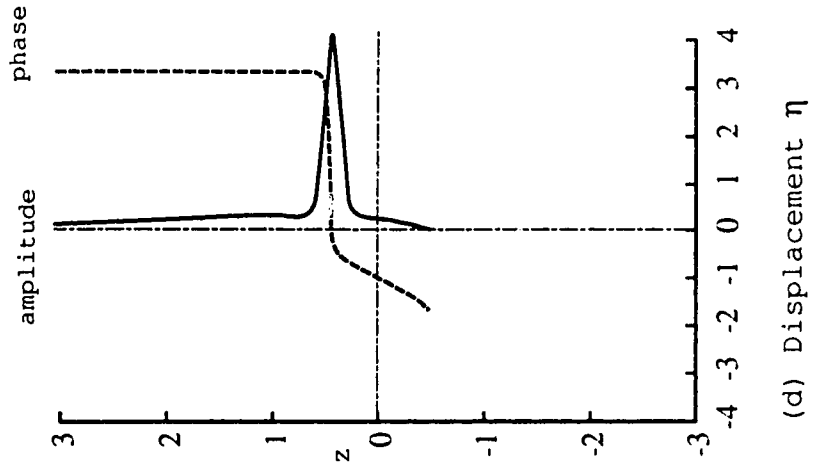
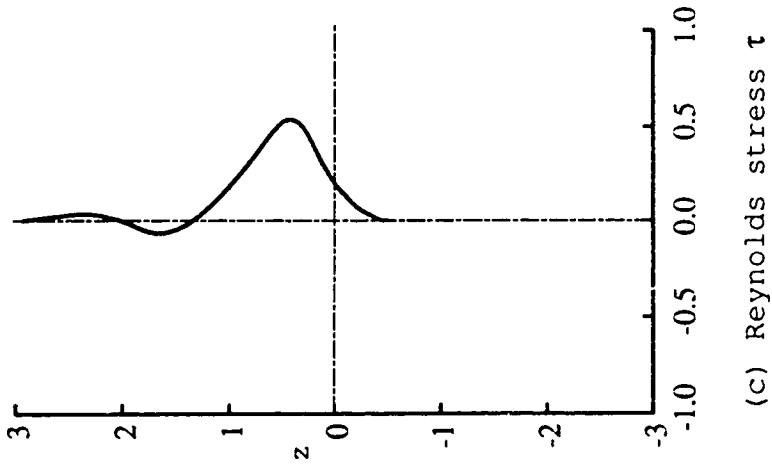


Figure 3.17 (a)-(e) The perturbation quantities of the flow.
 $\alpha=0.8$ $Ri=0.4$ $C_R=0.370$ $\alpha C_I=-0.0016$ $ZR=0.45$ case.





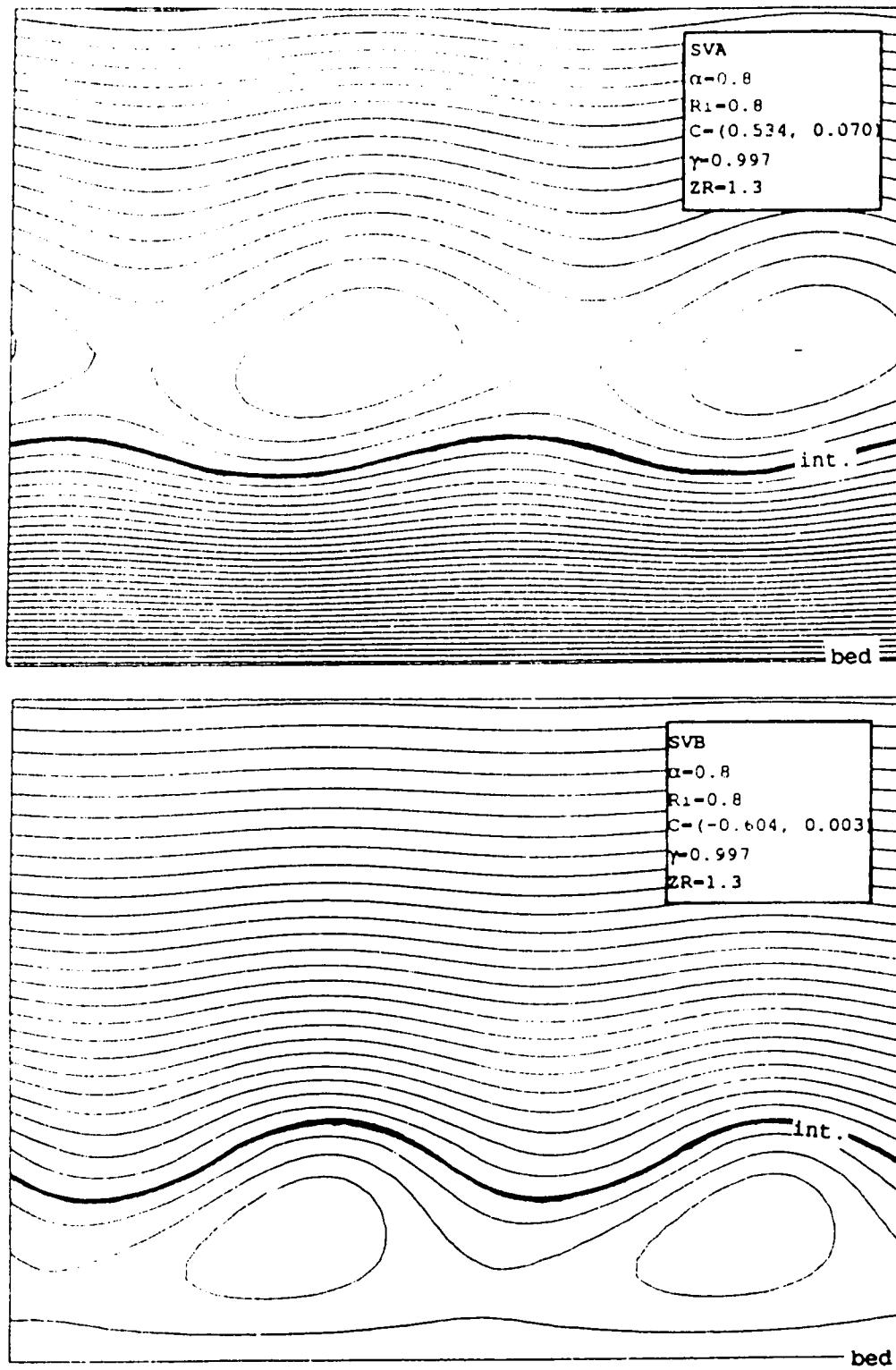


Figure 3.18. Stream lines of SVA and SVB solutions
(on the system moving with C_R)

3.6 MODEL IV: DENSITY INTERFACE SHIFTING EFFECTS

3.6.1 Formulation

This problem is very similar to that researched by Lawrence, Browand & Redekopp (1991). Figure 3.19 shows the velocity and density profiles used in this model. Since these profiles are similar to the preceding model, program changes will only be required in the subroutine FUNC and in some boundary conditions. To make the density interface shifting effects clear, an unbounded boundary condition will be used; an assumption supported by experiments since velocity distributions displaying this feature were observed when the lower layer thickness $Z_R > 3.0$. With the rigid boundary, it is expected that the dispersion relationship may show some additional unstable modes in the low wave number region; this will be discussed in section 3.7.

3.6.2 Solutions

In this model, the parameter ranges studied were $d=0.5$, $Re=100$, $0.0 \leq \alpha \leq 3.0$ and $0.0 \leq Ri \leq 2.5$, which were chosen based on previous experimental research (Yonemitsu (1986)), and the calculations were performed using the same facilities as used in the previous models. Figure 3.20 illustrates the neutral boundaries and dispersion relationship of unstable modes. Under this condition, it was found that only one type of wave can be unstable. Since this wave also has a negative propagation speed, by definition, these waves must be called

SVB modes. As Figure 3.21 shows, the perturbation quantities imply an instability level located lower than the point of inflection, which was expected to be the point of greatest instability.

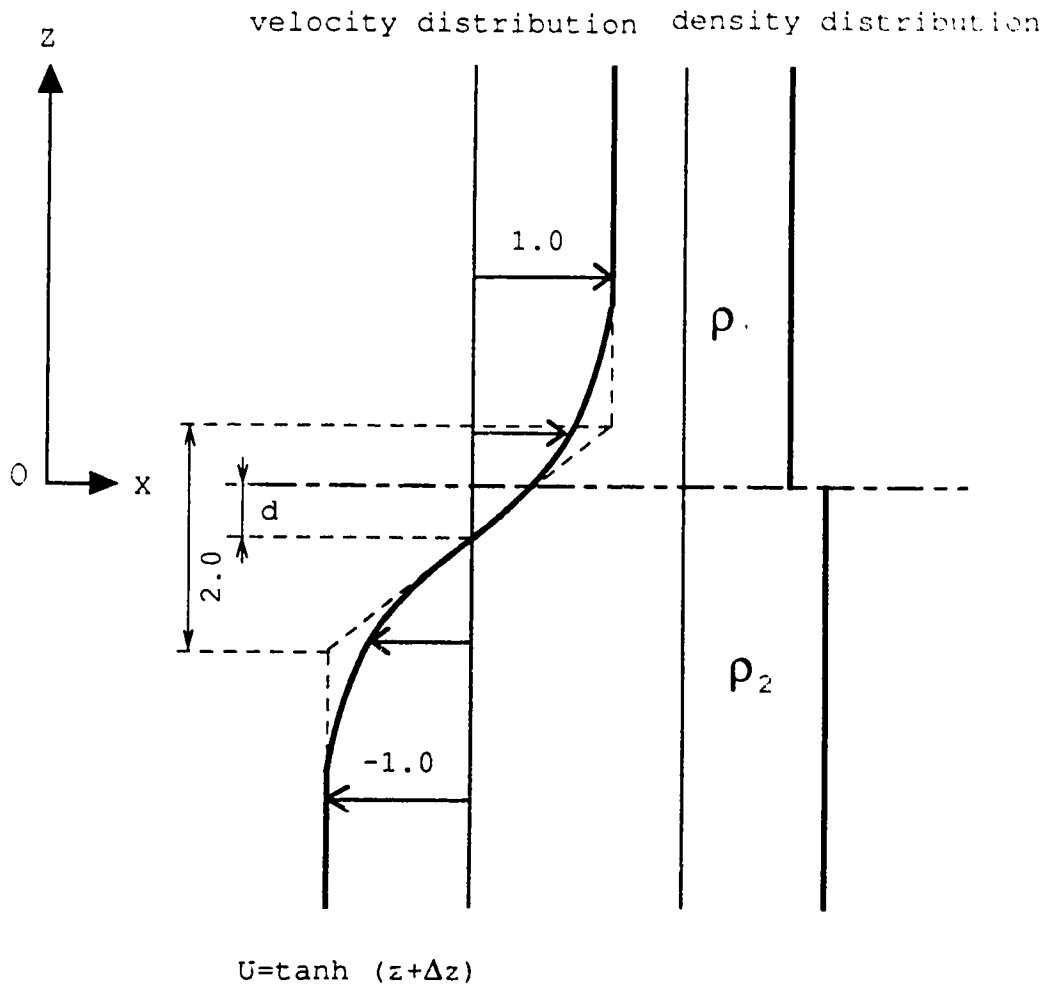


Figure 3.19. Velocity and density distribution of Model IV

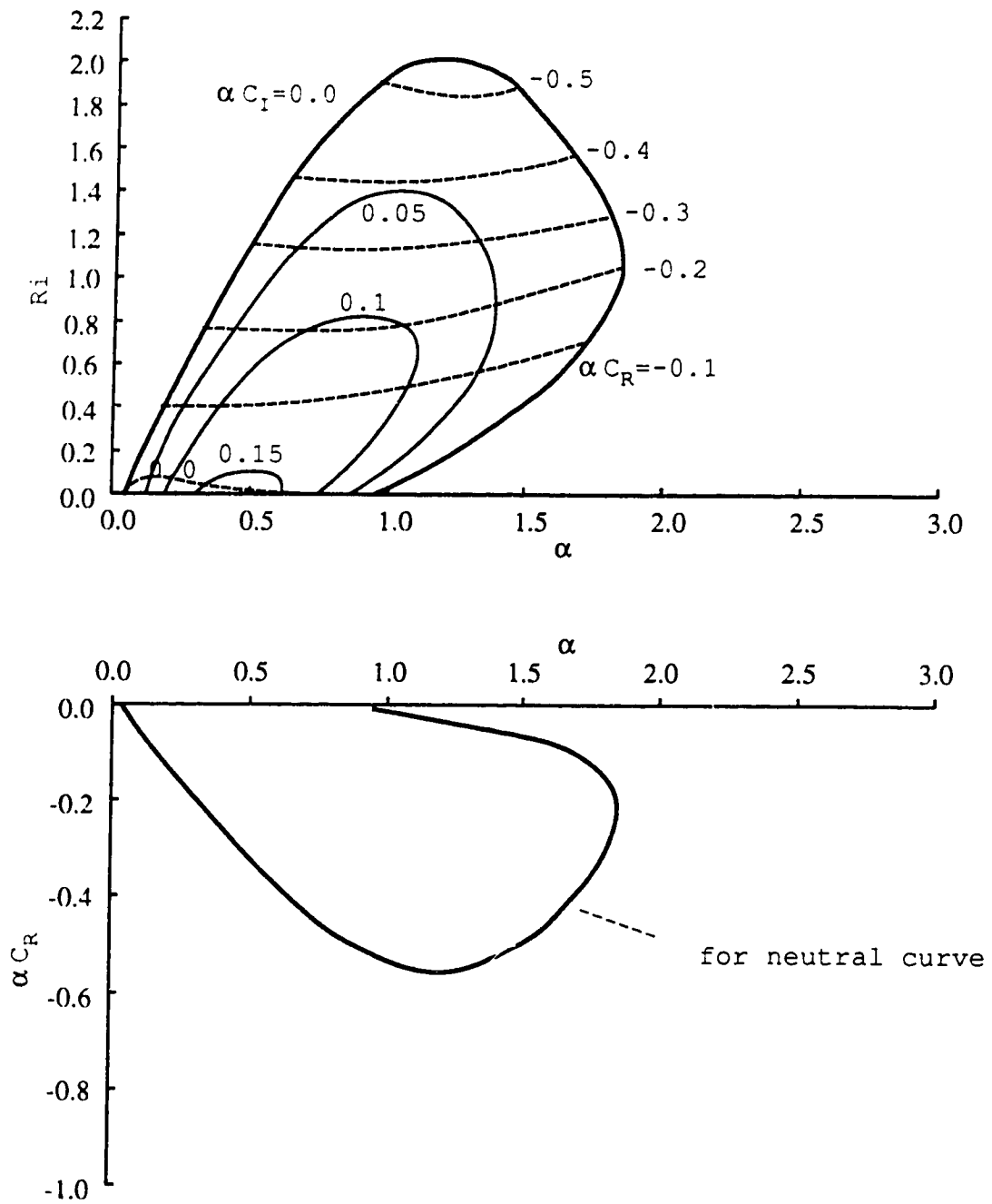
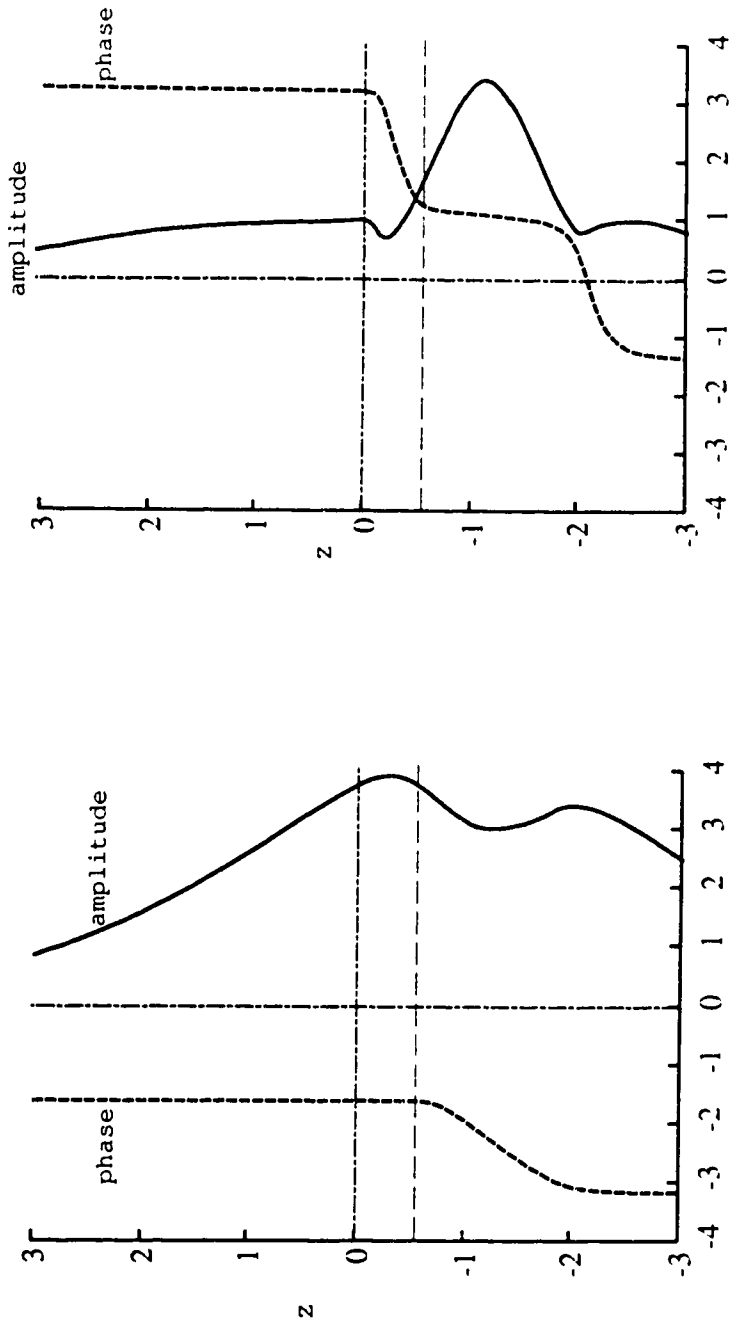


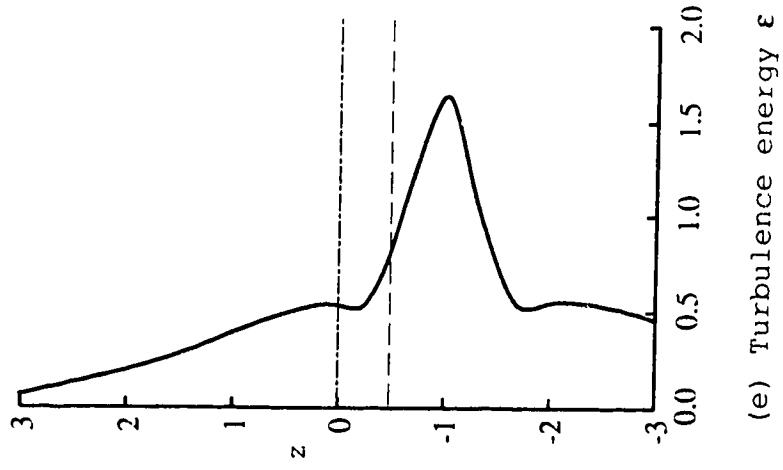
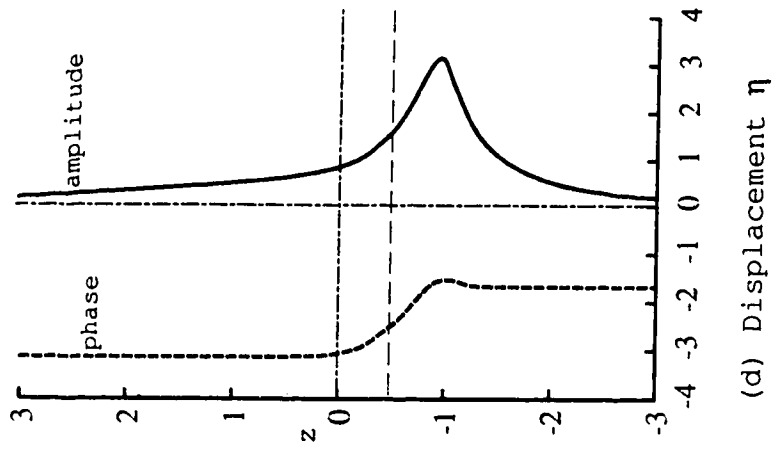
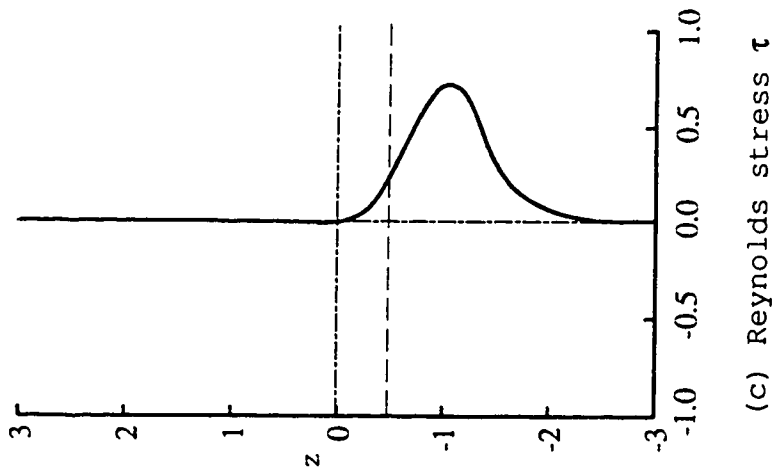
Figure 3.20. Dispersion relationship for density interface displaced case ($Re=100$, $d=0.5$ case)

Figure 3.21 (a) - (e) The perturbation quantities of the flow.
 $\alpha=0.6$ $Ri=0.4$ $C_R=-0.225$ $\alpha_{C_I}=0.135$ $ZR=3.0$ case.



(a) velocity fluctuation \tilde{w}

(b) velocity fluctuation \tilde{u}



3.7 DISCUSSION

Solutions of model III show the effects of viscosity on the flow stability. By comparing to the result of inviscid models, it can be seen that a large Richardson number region is stabilized and that the neutral boundaries now have closed forms. This is a more reasonable solution since the previous experiments indicated the existence of a critical Richardson number for the Holmboe modes but the inviscid theories could not explain it.

Despite the fact that model III included significant improvements over the inviscid models in terms of the velocity profile and the evaluation of the viscosity effects, the dispersion relationship on the α -Ri plane indicates that the most unstable modes tend to appear around $\alpha=0.8$ and $Ri=0.4$ for the bounded cases; a result similar to that predicted by the inviscid models in section 2.3. This finding is consistent with the results obtained by Lawrence et.al. (1991) who employed an inviscid piece-wise linear velocity profile model. It is interesting that the most unstable modes get closer to the axis ($Ri=0.0$) as Z_R increases, and, as was mentioned before, they appear on the axis in the unbounded case. This fact implies that model III may be using a slightly different mechanism to determine the most unstable modes in an off-axis location, when compared to Lawrence's model, he mentioned that this phenomena may be due to the existence of more unstable three dimensional primary

instability in the flow. However, present knowledge is insufficient to answer this question; it is suggested that experiments be performed to consider the three dimensional wave structure (see Smyth and Peltier 1989, 1990).

Model III also shows that the lower layer thickness Z_R affects the stability of SVB waves, but does not seem to affect SVA waves until it becomes less than 1.0. By contrast, in the inviscid models, the most unstable modes of SVB waves do not move their location on α - Ri plane with the variation of Z_R . This implies that the stability of SVB waves is sensitive not only to the velocity profile but also to the viscosity. SVA waves obtained the additional unstable modes similar to the inviscid models, but over a much larger area. Unfortunately, as was found by Lalas & Einaudi (1976), it is impossible to distinguish the boundaries between these additional modes. Since investigation of the perturbation quantities showed no over-reflection type of phenomena in these modes, more precise calculations need to be done in this region to find the mechanism of the additional modes. Experimental investigations would be difficult since it is expected that these modes would not be seen in the flow due to their extremely small growth rates.

Model IV illustrates the dispersion relationship for situation in which the density interface is displaced from the center of the shear layer. Lawrence's inviscid models show unstable Holmboe mode solutions in the region with small Richardson numbers and large wave numbers, but these

solutions cannot be seen in Figure 3.20. This may be due to viscosity damping effects, since the growth rate predicted in an inviscid solution is relatively small and occurs at a large wave number. Figure 3.20 also shows that the critical value of the Richardson number is larger than that predicted by model III. This result is reasonable, since the strongest shear occurs at the center of shear layer and far from the density interface. Thus, the stabilizing effects of buoyancy are much smaller than in the non-displaced cases. Another contrast between this model and non-displaced models is that only SVB waves can exist when the Richardson number exceeds about 0.2. This implies that the perturbation only appears in the lower layer, which agrees with observations by Browand & Winant (1973), Koop & Browand (1979) and Lawrence et.al.(1990).

3.8 CONCLUSION

In this section, the effect of viscosity was introduced into the previous models, and a hyperbolic tangent velocity profile was employed in order to improve the evaluation of the flow stability.

Model III, which evaluates the effects of the lower layer thickness Z_R , shows the damping and stabilizing effects of viscosity on high Richardson number flows. This is a much more reasonable solution than the inviscid one, since the previous experiments indicated the existence of a critical Richardson number of about 1.5 to 2.0. It was also found that the viscosity destabilizes the low wave number region, as was illustrated by the additional unstable modes.

Model III also shows that SVB waves are strongly influenced by the reduction in Z_R , but neutral boundaries and the most unstable modes behave slightly differently from those in the inviscid solutions. The most unstable modes appear around $\alpha=0.8$ $Ri=0.4$ and do not move with variation of Z_R . These models (I, II and III) imply a sensitivity of SVB wave stability on the lower layer thickness Z_R and velocity profile U_0 . By contrast, SVA waves are only slightly influenced by Z_R and U_0 ; a result very similar to the inviscid case, which may suggest an independence of SVA waves from the lower layer flow.

Model IV, which tests effects of the displacement between the interface and the center of the shear layer,

shows that only one Holmboe mode (SVB) can exist in the channel. Although the model did not cover the entire range of parameter variation (especially the displacement d), the results imply mechanisms for the instability that are quite reasonable (in particular, the larger critical Richardson number). This model also showed that the additional unstable modes obtained by Lawrence et.al. are stabilized by viscosity.

In summary, viscosity and continuous velocity profiles exhibit significant influences on flow stability. However, some of the features predicted by both the inviscid and viscous models are contradictory. In the next section, appropriate experiments will verify these problems and the stability of the salt-wedge will be examined.

4. PART FOUR: EXPERIMENTAL STUDY

4.1 INTRODUCTION

In the previous section, several flow models, designed for different flow patterns in the channel, were investigated for their stability features. However, as was mentioned in Part I, few experimental and field observational data are available to verify the waves and flow structures in the channel, due mainly to the incompleteness of data sets.

In this section, experiments to produce complete data sets (i.e. information such as wedge shape, velocity and density profiles, wave length and its phase velocity, interface displacement d and the lower layer thickness Z_R) will be described. Measurements were made using LDA (Laser Doppler Anemometry), a conductivity-salinity meter, and a wave detector; all controlled by a computerized data acquisition system. Also a flow visualization technique was used to identify the flow structure and density interface. The parameter ranges were carefully controlled by choosing the salt water density ρ_2 and fresh water velocity U_0 to produce an appropriate flow situation for observing the waves and results referred to in previous sections. The details will be explained in the following sub-sections.

4.2 FACILITIES AND PROCEDURES

4.2.1 Flume

The layout of the flume used in the experiments is shown in Figure 4.1. It consists of a straight channel section 3.05 m long and 16 cm wide connected to a large downstream reservoir which is 81 cm long, 82 cm wide and 10 cm deep. At the end of reservoir there is an overflow weir to maintain a constant water level. The depth of the channel section is maintained at 6.7 to 7 cm for all cases. Although the slope is adjustable by using a jack located at the upstream end of the channel, it was set at zero for the experiments.

The flume was constructed of plexiglass supported by aluminum frames to prevent bending and torsion due to its own weight. The bed of flume is supported over the desk top about 40 cm high in order to move the LDA system. These supports were arranged to minimize interference with the measuring system except for the region very near the river mouth. At the upstream end, two sets of flow straighteners (which were made of 7 cm long plastic honeycomb and fiber hog) were installed in order to obtain uniform flow by destroying the large eddy structure in the channel. By employing this method, the turbulence intensity in the channel was of the order of 10 to 20% of the mean flow velocity at the upstream end.

The salt wedges for our experiments were formed using the following procedure. First, the flume was filled with

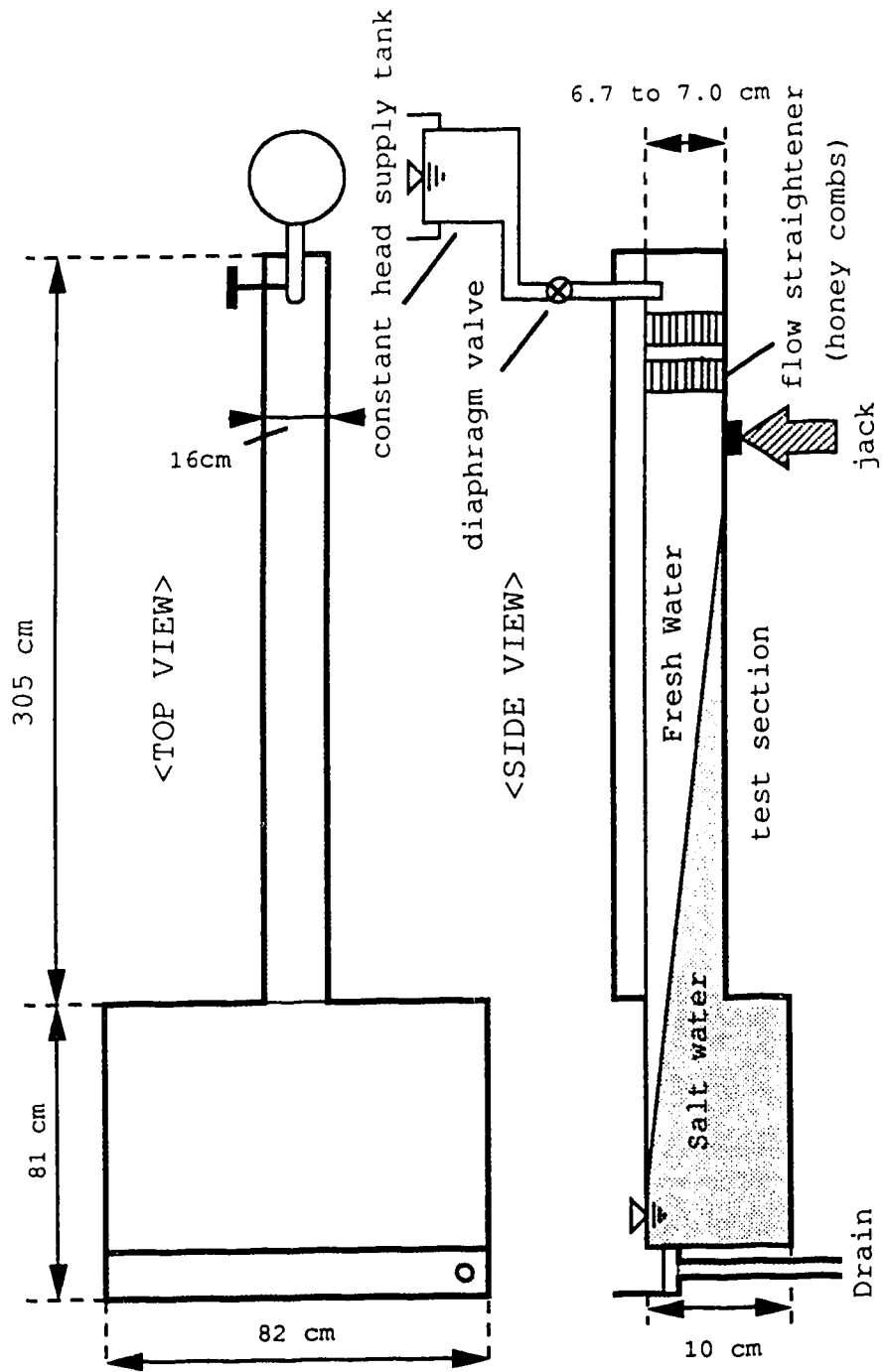


Figure 4.1. Schematics of the apparatus

salt water while the upstream end of the channel was elevated about 5 cm higher than downstream end and the depth of water was about 2 cm. Then, fresh water was introduced into the channel from the upstream end using a very small discharge, in order to prevent any mixing phenomena right at the beginning. Once a distinct fresh water layer had been established over the salt water, the discharge was increased and at the same time the slope was slowly reduced. The combination of discharge and bed slope was carefully chosen such that the location of the front end of the salt wedge (so-called tip region) would be maintained about 10 to 20 cm downstream of the flow straighteners. After the bed slope reached zero, and a constant discharge of the fresh water was established, the salt wedge tip continued to move until it reached a station approximately 200 cm from the channel mouth. At this point, the movement of the salt wedge slowed down significantly, reaching an average velocity of about 5 to 30 cm/hour (Quasi-steady state).

The measurements were made after a steady state condition had been obtained, which was ascertained by constancy of the salt wedge tip location. Measurements included visualization of interfacial details through dye injection, velocity profiles taken by the LDA system, interfacial wave phase velocity C_R and wave length λ determined by the wave detector. The density profile measurements were made with the conductivity probe and by

sampling. Details of these measurements and their equipment will be described in following sub-sections.

4.2.2 Laser Doppler Anemometer

The Laser Doppler Anemometry (LDA) technique is one of the most widely utilized velocity measurement systems. It is a non-intrusive, instantaneous measurement without any calibration even though its signal processing gives several mathematical and electrical difficulties. For a general review of the history, theories and applications, refer to the work by Durst, Melling & Whitelaw (1981), in the Von Karman Institute Lecture series 1981-3 entitled 'Laser velocimetry' (1981). Technical details of the system can be found in the DISA manuals.

The method utilized in the experiments is the "dual beam forward scatter" method (fringe mode) shown in Figure 4.2. The advantage of this method, compared to the common back scatter type LDA, is a smaller power requirement for the laser tube, and easy maintenance. In particular, the ease with which the optics could be adjusted was a very important feature of this method since the density stratification often refracted the laser beams, making it necessary to re-focus the photo detector during experiments. A minor adjustment of the detector focusing was necessary every time the system went across the density interface. Since the photomultiplier was conveniently located slightly higher than the beam

focusing plane (see Figure 4.2), it was impossible to measure the velocity at points a few millimetres below the interface.

When using this method, velocity is given by following equation,

$$U = \frac{\lambda_L}{2\sin(\theta_c/2)} f_D, \quad (4.2.1)$$

where λ_L is the wavelength of laser light (632.8 nm (He-Ne tube)), θ_c is the crossing angle of the two beams (measured as 5.52 deg.), and f_D is the Doppler shift frequency.

This equation implies that measured velocity values are completely independent of the location and set-up of photo detectors.

Figure 4.3 is a schematic diagram of the main components of the LDA system, as well as the data acquisition system. The laser tube was composed of a 35mW He-Ne laser with a 632.8 nm red line, requiring significantly less power than other comparable systems. Using the beam splitter, the laser beam was split into two distributed beams of approximately equal power. The frequency of one of these beams was shifted 40MHz (plus-minus a few KHz) by passing it through the Bragg cell (acousto-optical frequency shifting system) in order to detect flow direction. A focusing lens ($f=310\text{mm}$ $\theta_c=5.52\text{deg.}$) crossed these two beams at a point which was positioned in the flow by moving the entire optical system (mounted on the optical bench). Accuracy of positioning in the vertical and transverse direction was 0.5 mm.

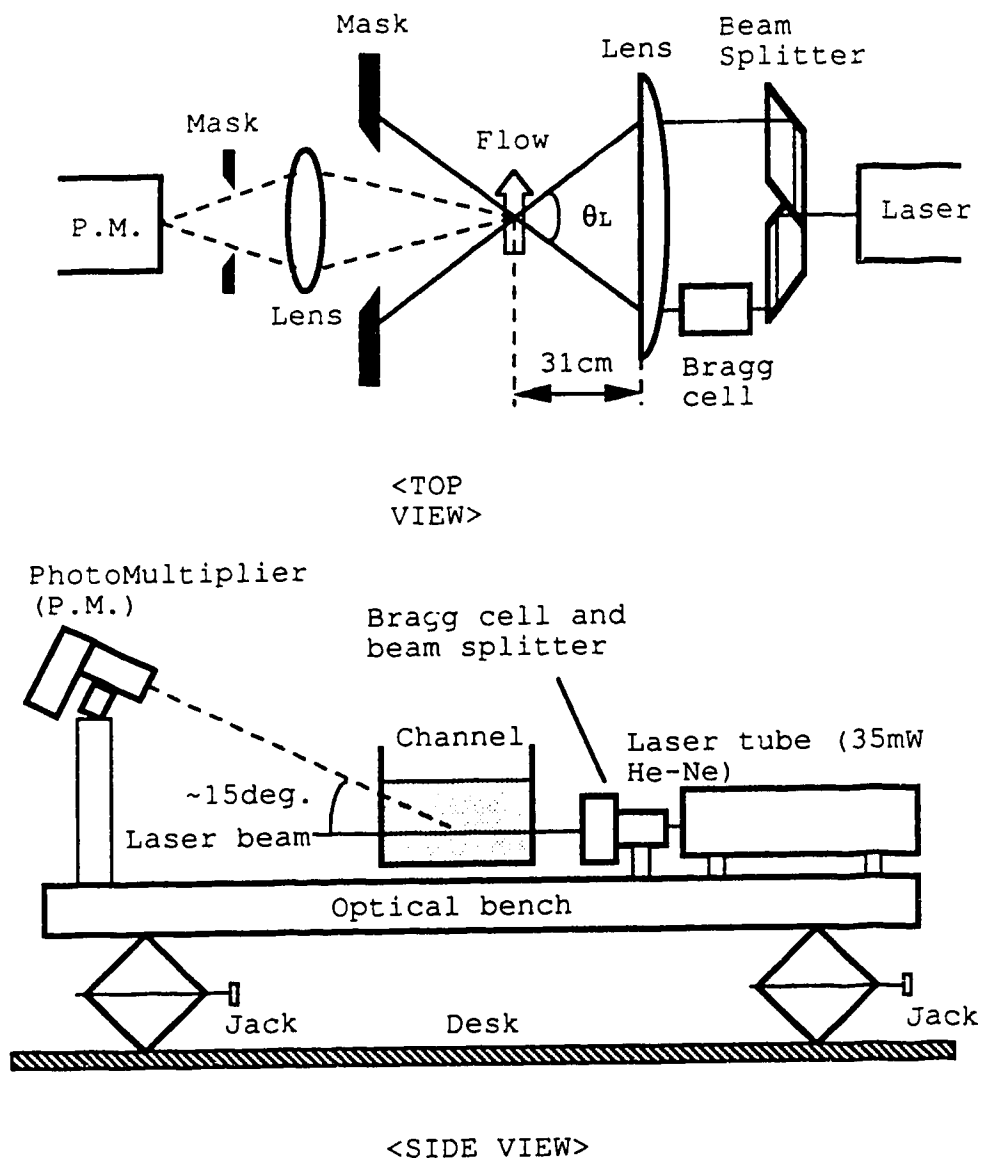


Figure 4.2. Laser optics set up.

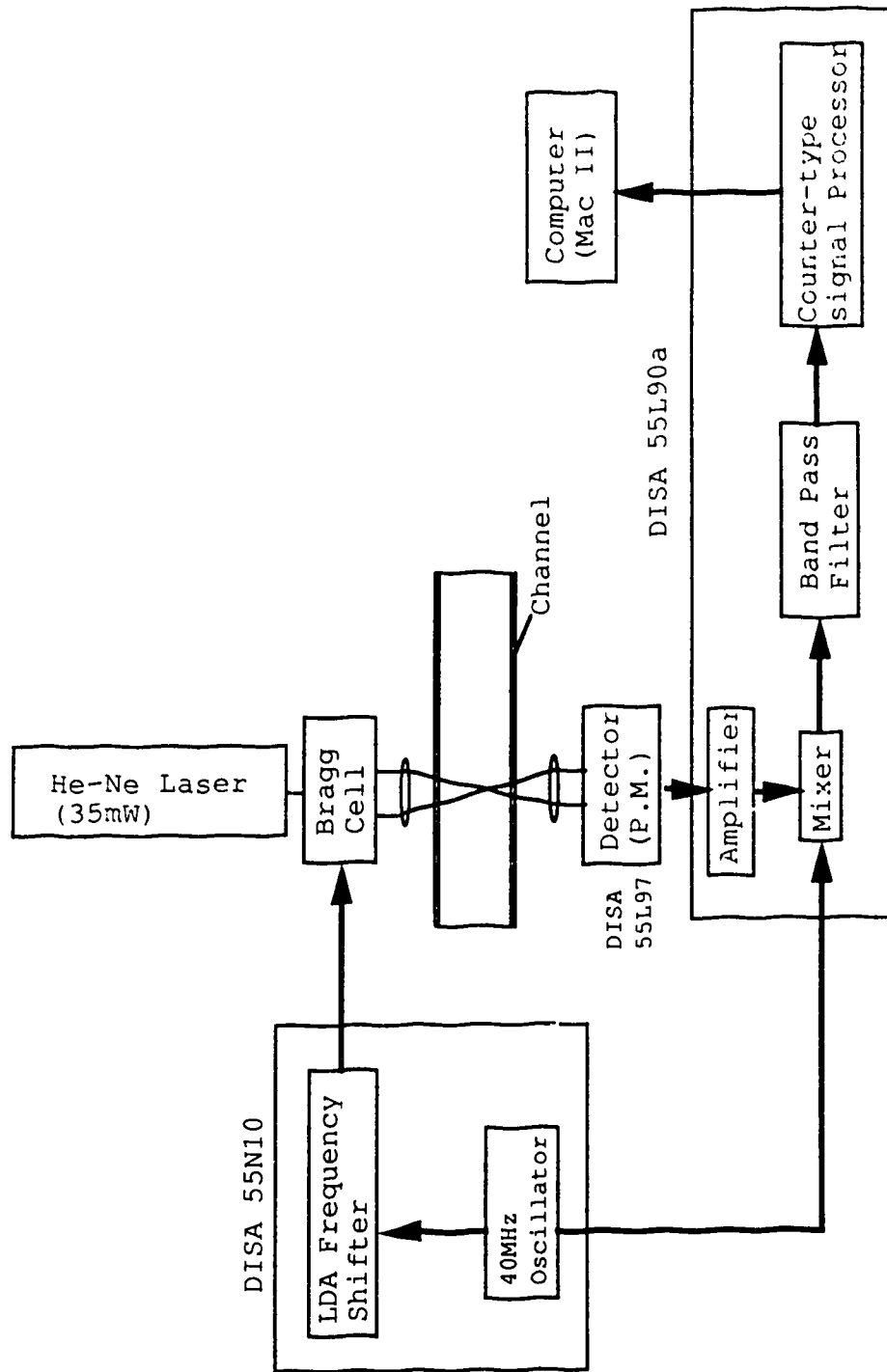


Figure 4.3. Block diagram of Laser Doppler Anemometry system.

Since the system operates by analyzing the scattered light from minute particles within the flow, the flow was seeded with skim milk powder in very small concentrations, the required quantity being determined by monitoring the raw signal output of the photomultiplier with pre-amplifier and band-pass filters. The scattered light was collected by the photomultiplier located opposite the laser on the same optical bench as the laser-Bragg cell-focusing system. This scattered light was converted into an electrical signal, which was processed by the counter type frequency analyzer after passing through pre-amplifier and band-pass filters. This counter evaluated the Doppler frequency f_D in each burst and displayed these values on its front panel. Also, since the digital output was sent to a D-A convertor and output amplifier, the velocity values could be monitored as a voltage by using appropriate instruments such as a syncroscope.

As can be imagined, this system generates a large amount of data and necessitates the use of a data acquisition system. The system we used consisted of an A-D convertor (NB-MIO-16L-9), an amplifier and a computer (Macintosh II with 4MB of memory). The analog signal could be sampled by this system at an arbitrary sampling rate which was totally controlled by computer software, and, although this system was capable of a sampling interval of 10 MHz, the experiments did not require such a high speed sampling since the flow was

quasi-laminar. Other settings of importance to the operation of this system are presented in Table 4.1.

Table 4.1 LDA system setting

band pass filters	1 to 256 kHz
pre-amp. gain	-3 to -7 db
threshold window	7 db
computation accuracy	1.5 to 3 %
ensemble width	1 to 4096
Frequency shift	40 MHz+20kHz
output amp. reduce gain	3 to 7 db
AD conv. amp. gain (Mac)	100 db
sampling rate (Mac)	50 Hz ($\Delta t=0.02$ sec.)
FFT smpling (Mac)	1024 data points

The sampled data was processed by the utility program package 'LabView', which controlled data acquisition, calculations and data storage. Essentially, two types of information were collected; the time-averaged velocity U_0 and the root-mean-square of fluctuations \tilde{u} . The averaging was performed over a time interval represented by 4000 to 40000 data points at a sampling interval $\Delta t=0.02$ seconds. Thus, it took about 2 minutes at each location to get one averaged velocity. At the same time, the statistical package included with LabView determined the standard deviation of velocity which corresponds to rms (\tilde{u}). In addition to velocity information, the power spectrum was obtained simultaneously

by using the FFT (Fast Fourier Transform) program in the LabView. All this information could be monitored on the computer display screen and was automatically stored on a floppy disk in spread sheet format.

4.2.3 Wave Detector

The interfacial waves were detected using an instrument similar to a conductivity meter. Figure 4.4 shows a schematic diagram of this instrument, designed and built by the Department of Applied Physics at Hokkaido University in 1984. This device measures the conductivity difference between two wires by detecting the unbalance across a Wheatstone bridge and amplifying the output. A 5 KHz alternating current was applied to the bridge to avoid the electrolysis of water, and the output of this circuit responded linearly to conductivity change. To maximize the sensitivity of this device to interface movement, the pair of wires was positioned such that the ends were half submerged into the salt water.

Two completely independent sets of sensors were located longitudinally in the stream, separated by a known distance (10cm). A FFT and cross-correlation of outputs gave enough information to evaluate the interfacial wave length λ and its phase velocity C_R (see Appendix C). These measured values were compared with flow visualization results in order to confirm the information. Unfortunately, it was impossible to measure the growth rate of waves αC_I , because these two sensors had to be electrically independent and could not

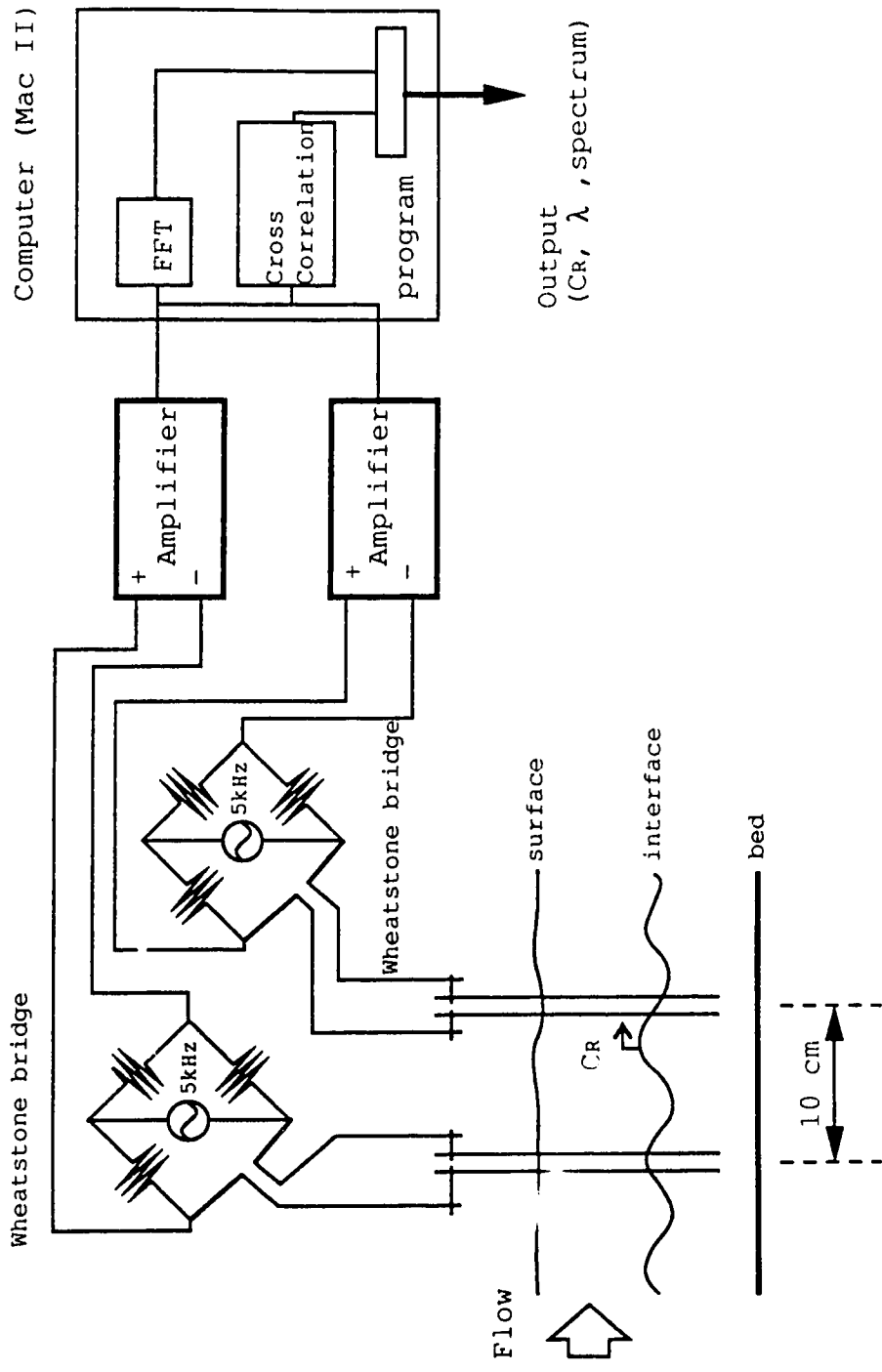
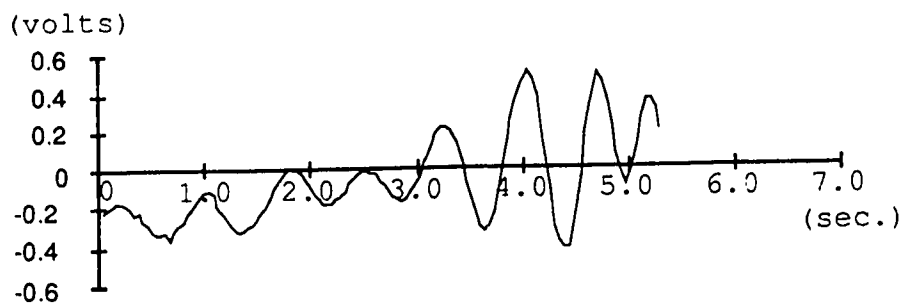
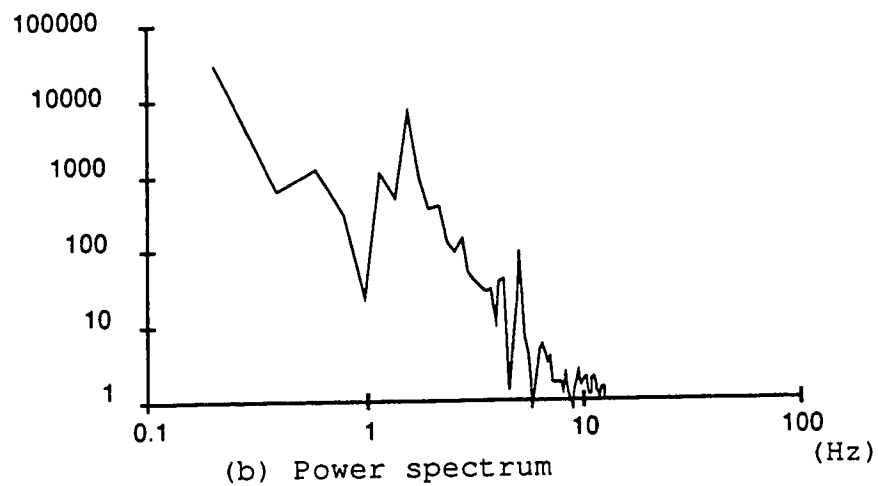


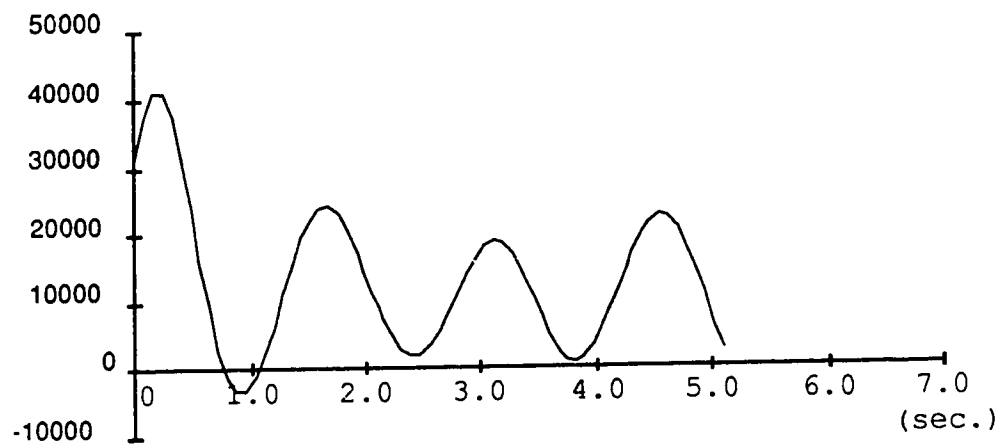
Figure 4.4. Block diagram of the wave detector.



(a) Interfacial waves



(b) Power spectrum



(c) Cross correlation

Figure 4.5. Wave detector output and processed data.
 (90.6.9(1) case. $\lambda^* = 2.10$ cm, $C_R^* = 3.20$ cm/sec.)

match their output characteristics completely. The FFT and cross-correlation were performed using the same computer system as was used for velocity measurements. (see Figure 4.5)

4.2.4 Conductivity-Salinity Meter

It is well known that conductivity-salinity measurements are one of the most difficult aspects of experimental instrument design and usually are not reliable unless sensors are calibrated every time they are used. The difficulty is mainly due to the change of sensor effective surface area by salt, and also the sensitivity of the sensor and circuit to temperature fluctuations. Also, entrainment of sampling water by the sensor makes the situation even more difficult. (see Sargent & Jirka (1987)).

In order to avoid these technical problems, the following two methods were employed. In the first method, a sensor designed and built in the Department of Mechanical Engineering at the University of Alberta was used. This had a tip designed to be very small and sleek to prevent entrainment, yet large enough to achieve high accuracy and sensitivity during experiments. This sensor was moved slowly and located at each measuring point for a sufficient length of time to obtain stable readings. The process required one to two minutes for each reading, depending on the flow velocity. By employing this method, it was found that

$$y = - 6.2461e-3 + 4.0802e-3x \quad R^2 = 0.998$$

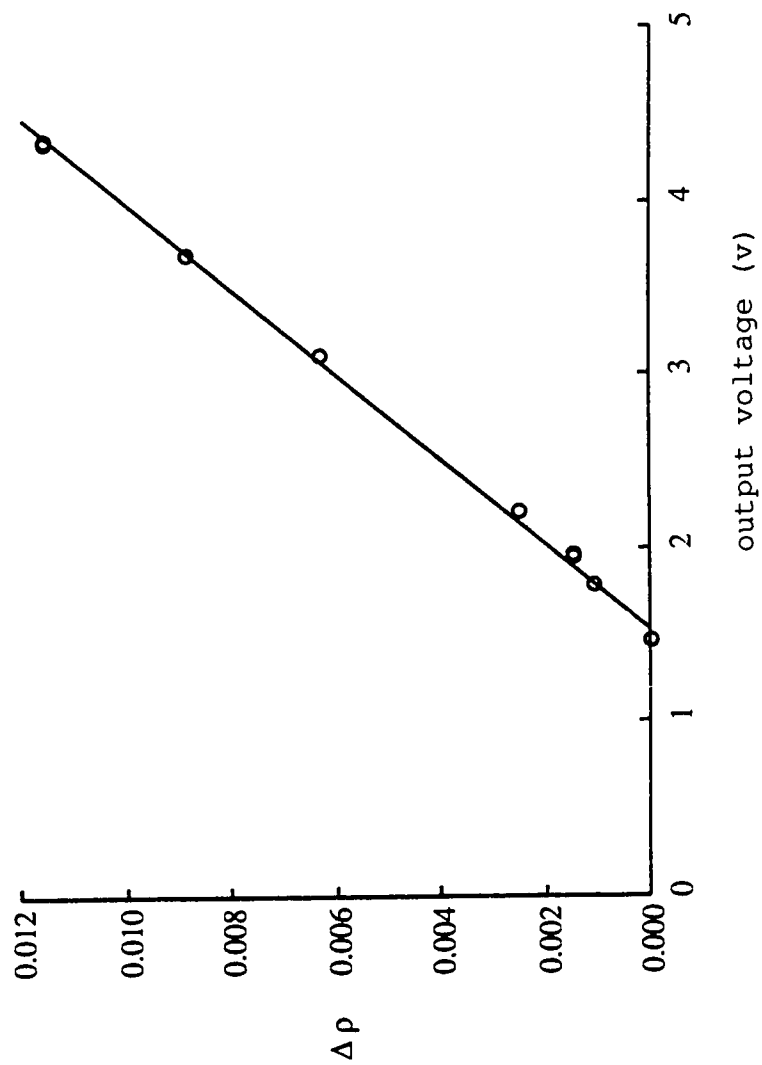


Figure 4.6. Calibration of the Conductivity-salinity sensor

reading values were very consistent and reliable regardless of the direction of sensor travel.

In the second method, the density of the upper and lower layers was determined by taking 100ml samples of fresh and salt water before and after the experiments. By measuring the weight of each sample using an electric scale (which can read up to 10 mg), and averaging several readings, the maximum and minimum densities in the flow were obtained. From these values, $\Delta\rho$ and γ were obtained.

As shown in Figure 4.6, this sensor showed excellent linearity, implying a similarity of density profiles and output velocity profiles. Based on this figure, we feel very confident of our measurements of density distributions and the density interface location, which was defined as the level at which ρ_{AV} is located. The vertical resolution of this sensor was 0.1mm in location and it was accurate enough to examine the density structure of the interface and shear layer.

4.3 EXPERIMENTAL RESULTS

Figure 4.7 is a schematic diagram of a typical salt wedge profile observed during the experiments. On the basis of their detailed experimental data, Sargent & Jirka (1987) suggested a longitudinal subdivision of the wedge into three regions (see part one) which are (1) the tip region, (2) the quasi-equilibrium region and (3) the exit region, based upon the force distribution on the interface. Although the overall dynamics of the salt wedge is mainly controlled by the quasi-equilibrium region, it was found that the tip and exit region contribute to wave generation as well. Therefore, it was necessary to perform velocity and density profile measurements in all three regions.

As it was mentioned before, the flow in the channel has a very complicated three-dimensional structure as is shown schematically in Figure 4.8. These structures were observed using a combination of flow visualization, conductivity measurements and LDA (see Figure 4.8 and 4.9). It is obvious that the secondary flow in the channel creates the transverse flow structures, and it is because of these structures that the stability of the system cannot be described by width-averaged or centerline velocity profiles as was the common practice with previous researchers. Moreover, the LDA measurement of the velocity distribution in the transverse direction, shown in Figure 4.9, indicates the existence of a slightly different structure in the salt water

compared to that observed in the fresh water. Therefore, the experiments were performed with consideration of not only longitudinal subdivisions but also transverse subdivision such as the high speed region and low speed region.

Let us now introduce new longitudinal subdivisions based upon wave and interfacial phenomena (Figure 4.7). If we consider Figure 4.8 it can be seen that SVA waves are located in the high speed region and, by contrast, SVB waves are always found in the low speed region.

In addition to velocity profiles (see Figure 4.8), the thickness of the salt wedge was also measured in the transverse direction, and it was found that only very small changes (about 0.2mm) in thickness existed. This fact implies that it is very difficult to determine the flow structure by measuring interfacial deformation. Therefore, it is necessary to clearly specify the locations of flow measurements if we are to understand and evaluate flow stability.

Figure 4.10. shows typical interfacial waves (here SVA) in this flume. Here, the salt water layer was dyed with food color to visualize the density interface ((a) and (b)). Also in (b), this dye was injected into fresh water layer about 1cm above the interface and it indicated the series of vortices which correspond to SVA waves. Both photographs were taken in the quasi-equilibrium region and over-all Richardson number was around $Ri_0=0.6$.

In the analysis of vertical velocity profiles, they were non-dimensionalized using the characteristic length and velocity scales as defined in Figure 4.11. These scales are based upon the hyperbolic tangent function velocity profile and the step function which describes the density profile. Figure 4.12 summarizes the velocity profiles and shows good agreement with $\tanh(z)$ especially around the density interface. It can be seen that velocities tend not to match well in the $z < -1.0$ region, which is due to the existence of the rigid boundary. The upper layer velocities also show some disagreement with $\tanh(z)$ since the shear stress near the density interface was considered as the first priority for velocity matching. Also, it should be mentioned that we have tried to minimize the displacement d (which is defined as the distance between the density interface and the center of the shear layer) unless it was too big. The effects of this velocity approximation technique on the evaluation of the stability will be discussed in the next section.

Figure 4.13 shows a typical vertical density distribution and implies that a two-layer model for the salt wedge is quite reasonable. The profiles maintained their sharp density interface through the entire section of flume, and it was found that the visual interface and the steepest density gradient point always matched each other very well.

The significant details of the experiments performed are summarized in Table 4.2, where the superscript "*" indicates a dimensional quantity. X and Y represent the location of

measurement points as distance from the mouth and left wall, respectively, V_{int} and D_{int} represent the velocity and depth of the density interface, D represents the total depth of the location and d represents the density interface displacement from the center of the shear layer. Some of the experiments in this table were performed in a different flume by Yonemitsu (1986) and are listed for comparison. The ranges of the global parameters such as the Reynolds number and the Richardson number were wide enough to cover entire range of results from the previous analysis ($29 < Re < 549$, $0.15 < Ri < 3.96$).

Figure 4.14 shows three typical velocity profiles measured in stable and unstable situations. It can be seen that the fluctuations ($rms(\tilde{u})$) tend to have three peaks in their amplitude; a feature that may be considered to be proof of the instability mechanism since it is a very unique feature predicted in sections 3.5 and 3.6. Moreover, the spectrum of these fluctuations appears to be identical with the interfacial wave spectrum predicted for the case involving unstable flow conditions. On the other hand, the stable case shows that the maximum fluctuation peaks are significantly far from the density interface and seem to be stabilized by stronger buoyancy effects. Another problem of $rms(\tilde{u})$ was that the data rates in lower layer, particularly near the bed, were not significantly high to obtain reliable value of deviation, which was mainly due to the feature of our counter type signal processor. Details of this problem can be found in the DISA manual. Also, it can be seen that

the amplitude of $\text{rms}(\tilde{u})$ in the lower layer exceeds 100% of the mean velocity and, therefore, we must conclude that by using the velocity approximation, $\tanh(z)$, we may be introducing problems into the analysis. These problems will be evaluated in the next section.

Figures 4.15 to 4.20 summarize the results obtained by the experiments. Each of them combines experimental results with the theoretical and numerical analysis performed in the previous sections and by Nishida & Yoshida (1987). If we consider Figure 4.15, this figure indicates a strong dependence between Reynolds number and the unstable wave number and, since most results are below the line, the experiments show good agreement with the numerical results (unbounded case). Also, it should be noted that SVB waves tend to have larger wave numbers than SVA waves which may be due to the effects of the rigid boundary.

A strong influence of Reynolds number on stability can be seen in Figure 4.16 which illustrates Z_R effects on the stability of the flow. The inviscid analysis performed by several researchers (Hazel et.al. see section 1.3.3.) matches with experiment when $Re > 250$, however, for the smaller Re , the results seem to indicate that viscosity effects should also be considered.

Figure 4.17 presents the relationship between wave number α and phase speed αC_R . Obviously, the numerical analysis underestimates the phase velocity of SVB waves even though the solid line is for the $Z_R = 3.0$ case. This type of

mismatch of phase velocity of SVB waves is common amongst most of the experimental results reported (Yoshida & Kashiwada 1988 and Hino & Hung 1982). Although several explanations (including non-linear effects) have been given for this problem, none of them have been verified.

Figure 4.18 illustrates the stability boundaries on the α - Ri plane. It is easily seen that the critical Richardson number Ri_c is about 2.0, which is slightly larger than that predicted by both the unbounded and bounded cases. This is also commonly found in experiments: it has been suggested that the intermittency of wave generation is related to this overestimation. Two other observations that can be made from this diagram are as follows. First, the numerical analysis gives reasonable agreement for SVA waves in terms of the most unstable modes. Second, SVB waves appear to be much shorter (i.e. larger wave number) than predicted values: again, several explanations exist and will be discussed later.

The critical Richardson number Ri_c and its Z_R dependence are shown in Figure 4.19. As in Figure 4.18, there is an indication of slight overestimation on Ri_c and, therefore, some of these points, which have extremely large Richardson numbers, may result from same mechanism. However, except for these points, experiments show relatively good matching with numerical analysis and the existence of a cut-off value for Z_R can be seen clearly.

Figure 4.20 shows the relationship between Re and Ri . Agreement is good except for several SVA waves which are the same outlines as in previous figures.

The experiments have revealed some of the basic mechanisms relevant to the interfacial wave phenomena in terms of the hydrodynamic stability. Yet, a few problems still remain, such as the underestimation of the critical Richardson number Ri_c and the SVB wave phase velocity. In the next section, these questions will be discussed from the point of view of velocity approximation problems.

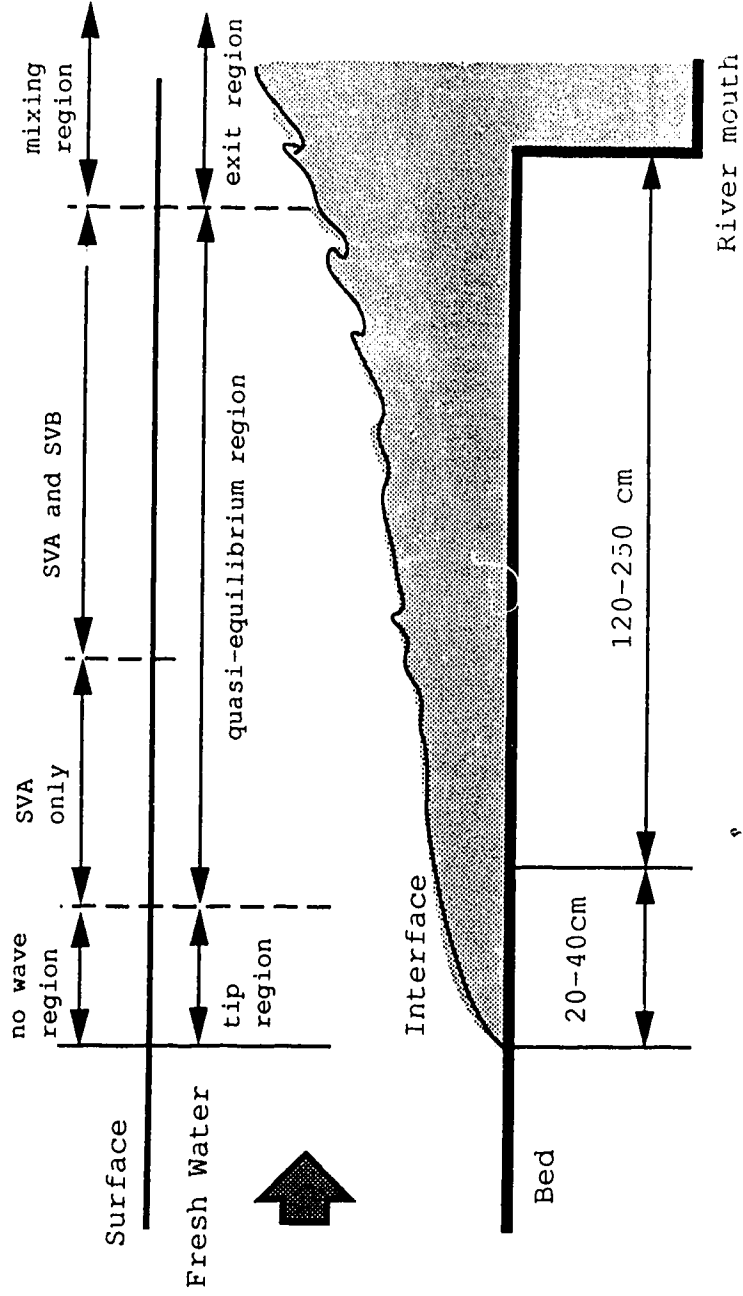


Figure 4.7. Side view of the salt-wedge and wave phenomena.

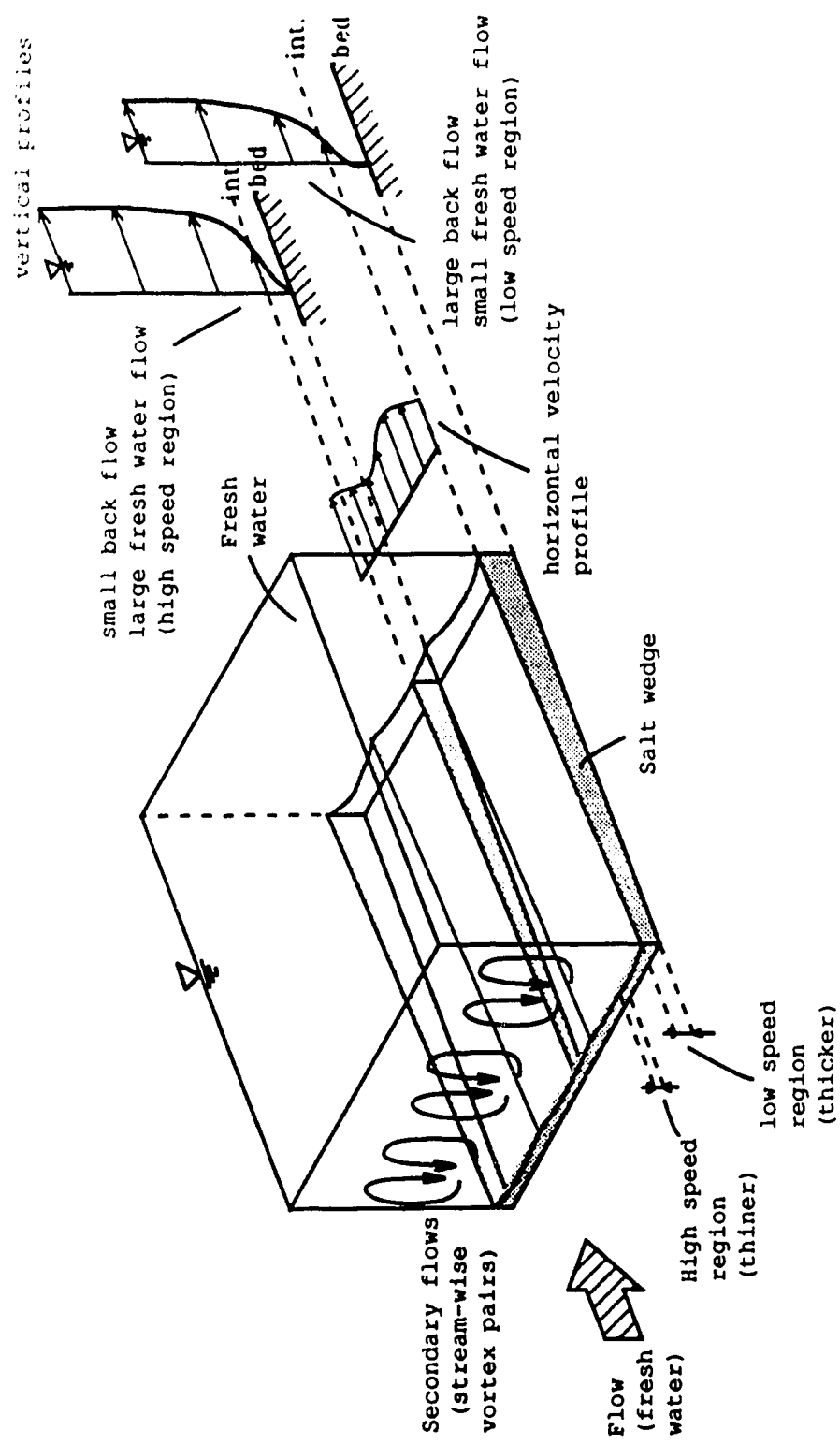


Figure 4.8. Three-Dimensional structure on the salt wedge.

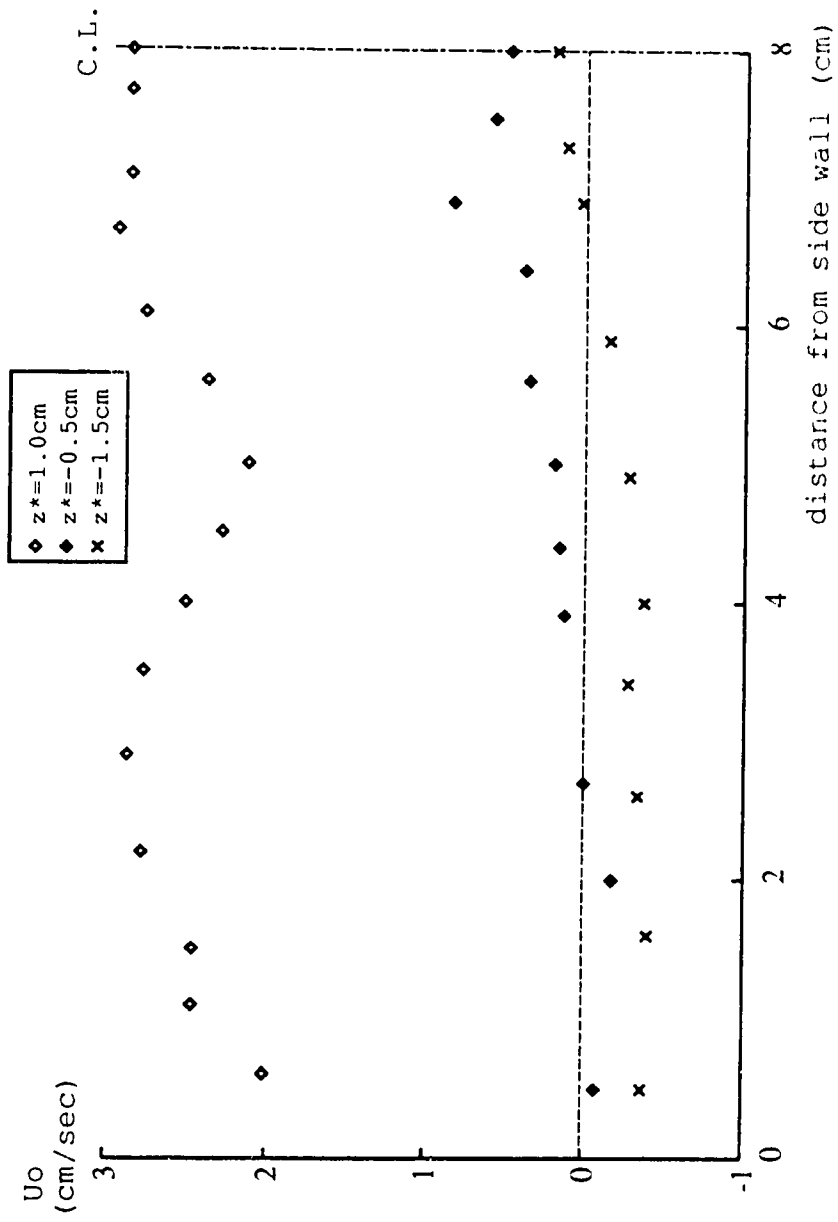
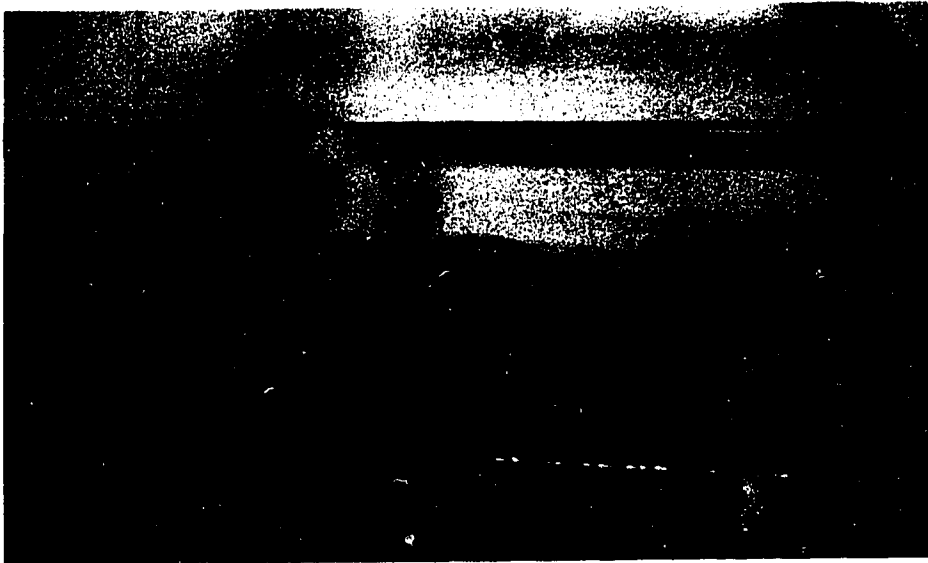


Figure 4.9. Secondary flow structure in the channel (40cm from the mouth, total depth=7.0 cm, salt water depth=2.0cm, $\rho_2=1.032\text{g/cc}$. case)



(a)



(b)

Figure 4.10 SVA waves in the flume
(quasi-equilibrium region)

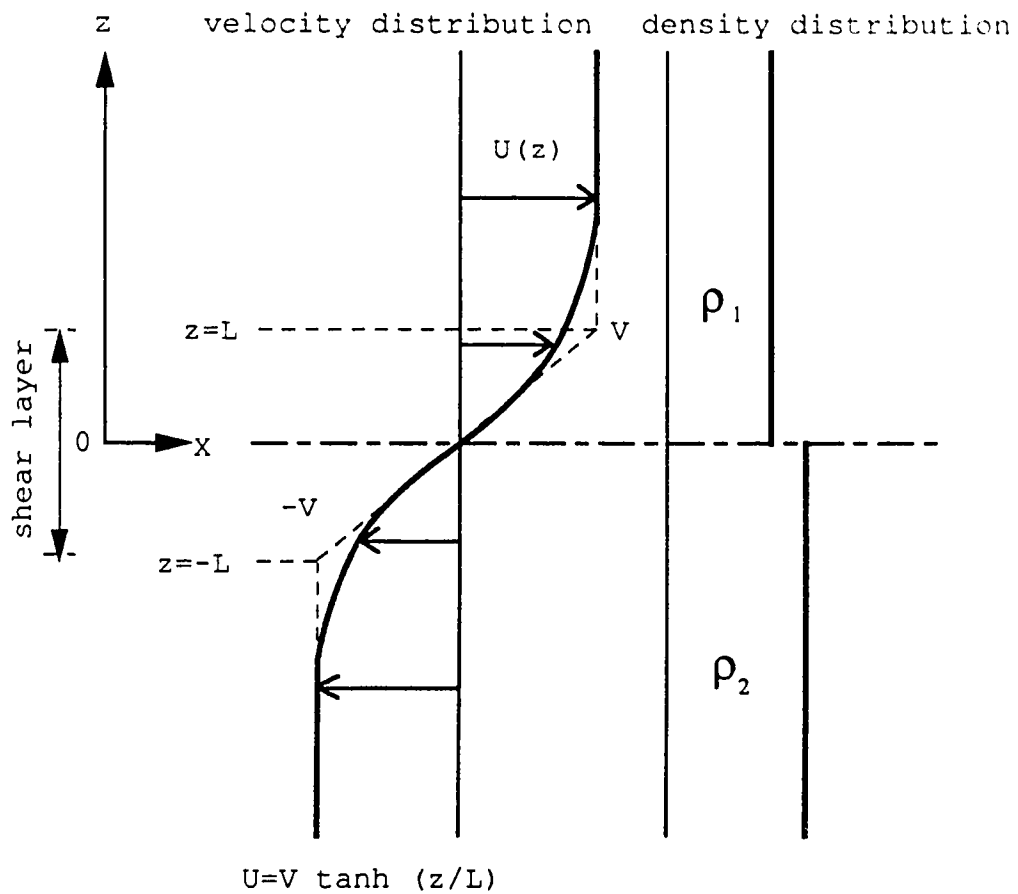


Figure 4.11. Definitions of the characteristic length and velocity scale

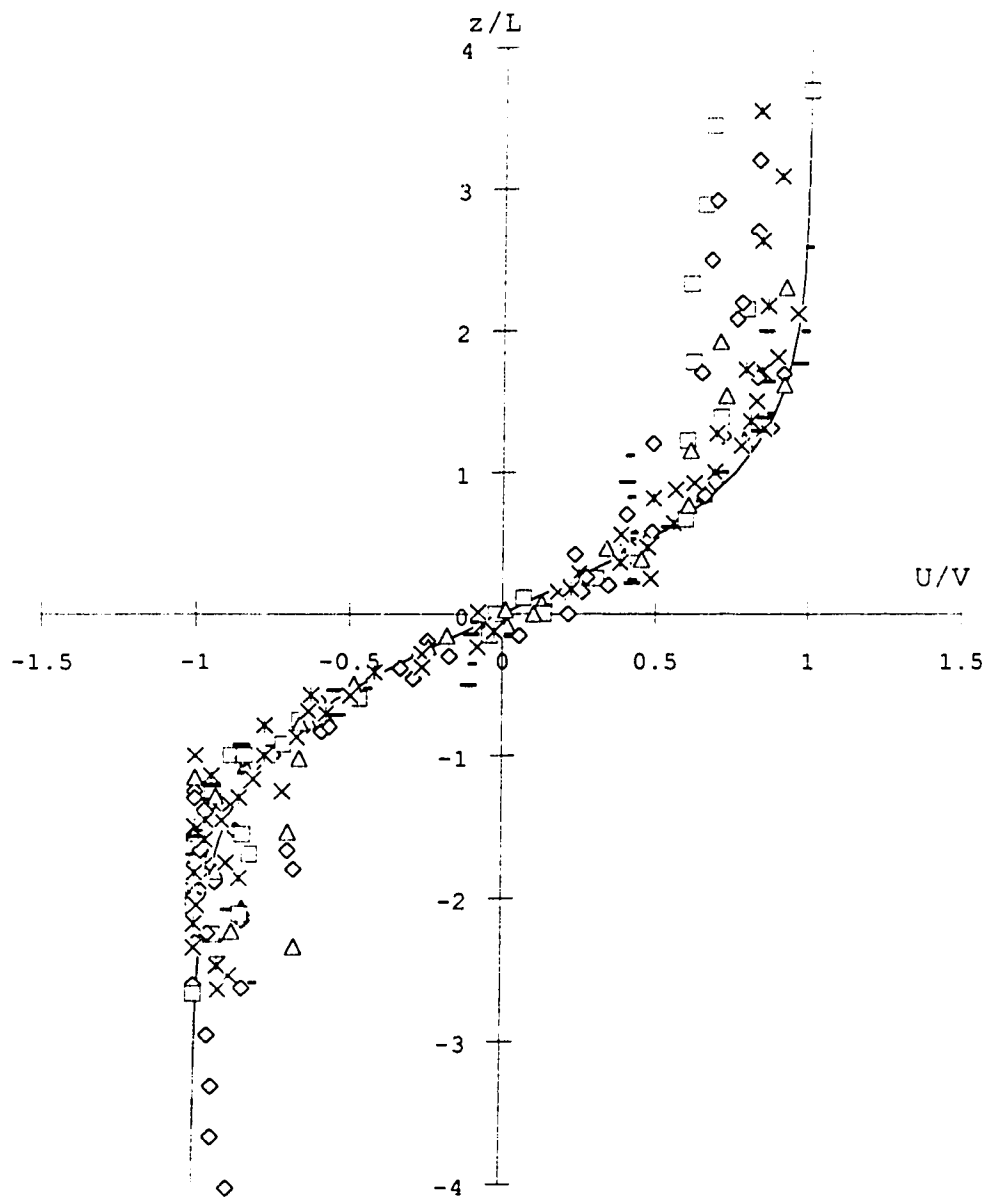


Figure 4.12. Non-dimensionalized velocity profiles

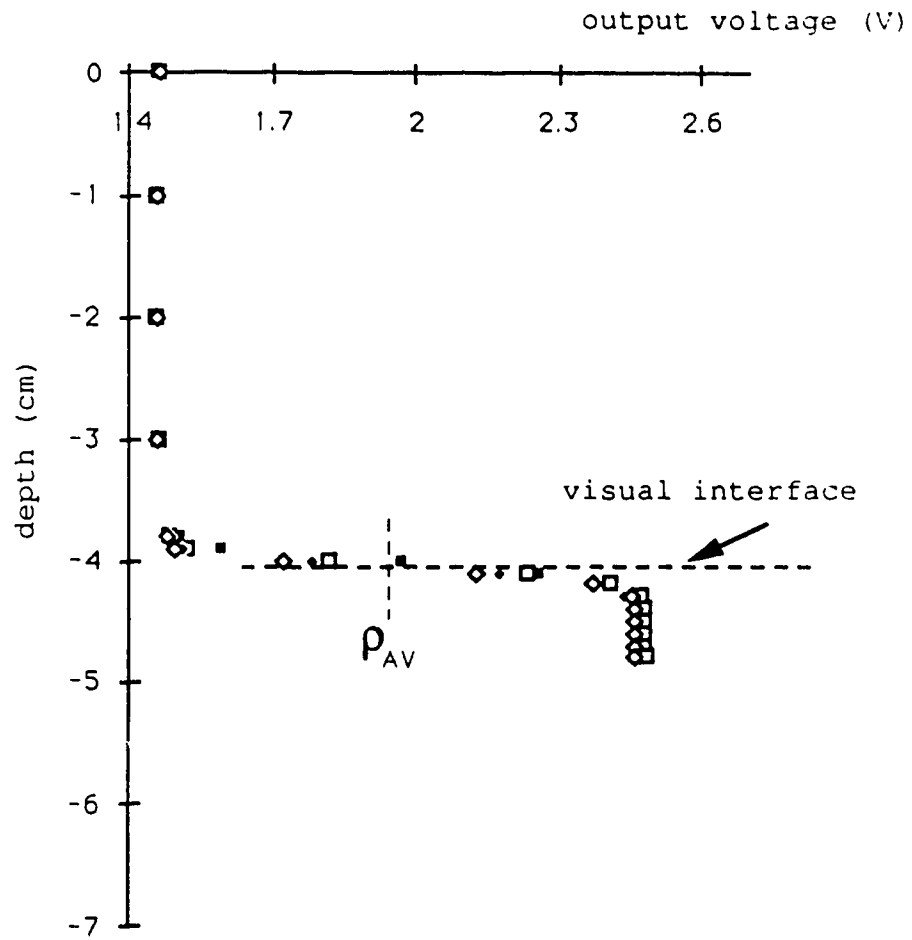


Figure 4.12. Conductivity profile as output voltage.
 (at 80cm from river mouth and 2.0cm from left wall)

Table 4.1. Summary details of the experiments.

date	Ap	µp	Σm	item	weight	count	log ₁₀ (count)	σ _{count}	σ _{log₁₀(count)}}	σ _{log₁₀(count)/Σm}	σ _{log₁₀(count)/Σm}	σ _{log₁₀(count)/Σm}
89.12.11	0.0047	1.00	1.20	0.65	0.95	5.00	78.00	2.07	stable	N	N	N
89.12.12	0.0047	1.31	1.45	0.80	0.70	5.40	88.55	1.74	stable	N	N	N
89.12.13	0.0047	1.31	1.30	0.70	0.90	5.20	69.47	1.90	stable	N	N	N
89.12.14	0.0024	1.31	1.10	0.90	0.55	5.10	75.57	1.75	stable	N	N	N
89.12.15	0.0035	1.32	1.33	0.80	0.65	5.40	80.61	1.55	stable	N	N	N
89.12.17	0.0059	1.27	1.45	0.93	1.00	4.40	106.18	2.54	stable	N	N	N
89.12.18	0.0047	1.35	1.60	0.80	0.90	5.35	94.81	1.43	stable	N	N	N
89.12.19	0.0095	1.27	1.60	1.10	1.20	4.45	138.58	3.96	stable	N	N	N
89.12.20	0.0071	1.36	1.50	0.85	1.30	4.40	93.75	2.61	stable	N	N	N
89.12.21	0.0071	1.34	1.40	0.80	1.30	3.50	83.58	2.82	stable	N	N	N
90.1.3	0.0059	1.23	1.25	0.95	1.10	4.05	96.54	3.49	stable	N	N	N
90.1.8(1)	0.0059	1.27	1.15	0.75	1.25	4.15	67.91	3.26	stable	N	N	N
90.1.8(2)	0.0059	1.27	1.20	0.80	1.10	4.15	75.59	3.19	stable	N	N	N
90.6.6	0.0210	1.09	3.50	1.10	2.05	5.60	353.21	1.81	SVA, SVB	3.00	2.85	2.85
90.6.7	0.0200	1.07	4.70	1.25	1.10	6.00	549.07	1.09	stable	N	N	N
90.6.8	0.0200	1.10	2.80	0.60	1.80	5.50	152.73	1.47	SVA, SVB	3.50	3.58	3.58
90.6.9(1)	0.0290	1.10	3.00	0.65	1.80	5.70	177.27	1.99	SVA, SVB	2.10	3.20	3.20
90.6.9(2)	0.0290	1.10	3.10	0.60	1.28	5.80	169.09	1.72	stable	N	N	N
90.6.11	0.0304	1.10	4.30	0.80	1.00	5.80	312.73	1.25	SVA, SVB	2.50	3.24	3.24
90.6.12	0.0258	1.09	3.30	0.80	2.30	5.60	242.20	1.81	SVA, SVB	2.60	3.24	3.24
90.6.14	0.0295	1.14	3.10	0.55	2.90	5.70	149.56	1.61	SVA, SVB	2.30	5.00	5.00
90.6.20	0.0057	1.08	2.40	0.60	2.25	5.30	133.33	0.58	SVA, SVB	4.00	2.43	2.43
90.6.21	0.0098	1.09	2.90	1.00	1.55	5.50	266.06	1.13	SVA, SVB	3.00	2.40	2.40
90.6.22	0.0097	1.08	2.90	0.85	1.55	5.50	228.24	0.95	SVA, SVB	4.00	2.66	2.66
90.6.23	0.0082	1.03	3.00	1.00	1.50	5.50	291.26	0.89	SVA, SVB	4.00	2.70	2.70
90.6.24	0.0111	1.01	3.00	0.90	1.50	5.90	267.33	1.08	stable	N	N	N
90.6.26	0.0073	1.02	2.60	0.78	1.45	5.60	198.82	0.82	SVA, SVB	3.00	2.23	2.23
90.6.28	0.0073	1.01	2.80	1.10	1.40	5.60	304.95	1.00	SVA, SVB	3.50	2.11	2.11

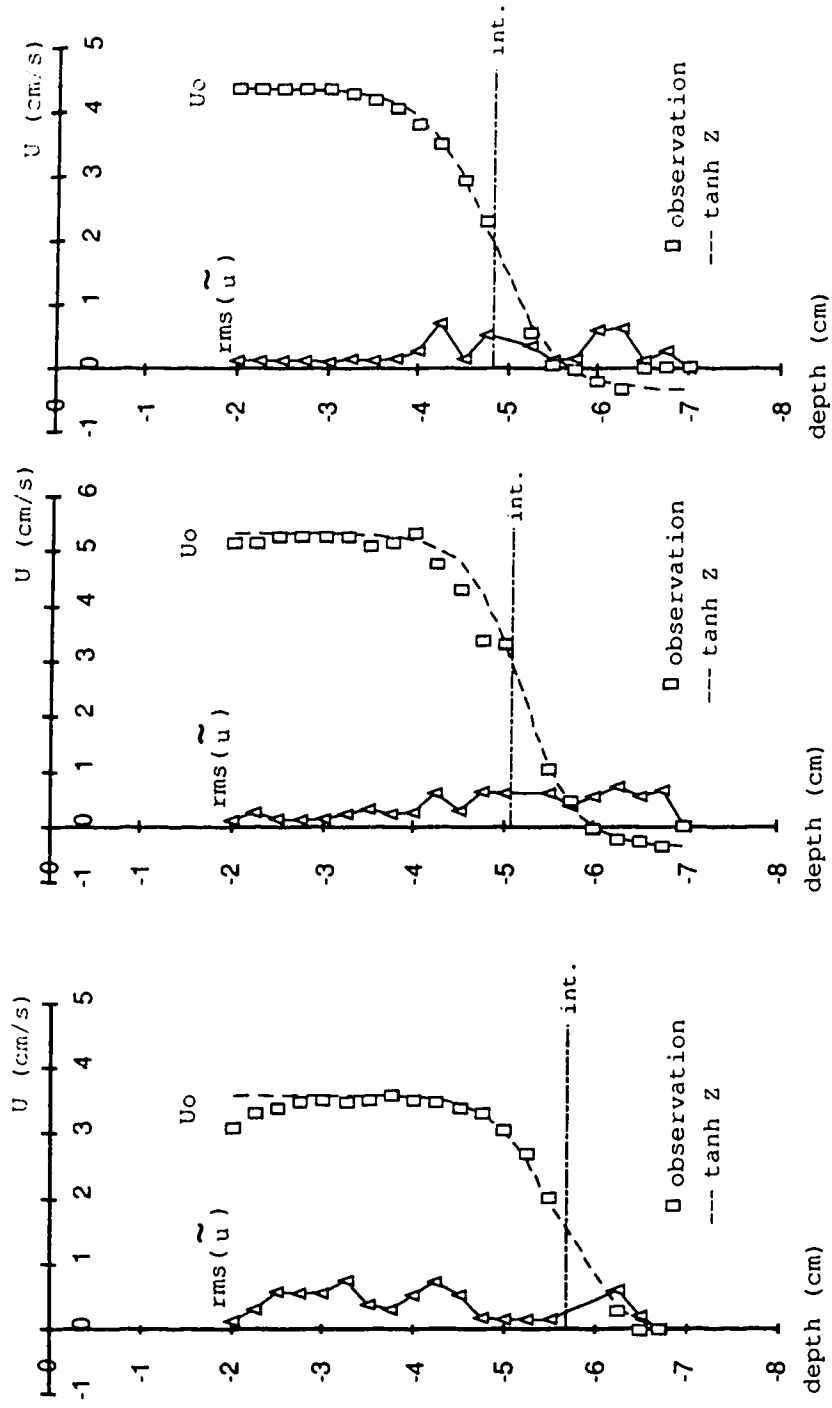
date	Δp	μp	V (cm/s)	L (cm)	vint. (cm/s)	Dint. (cm)	Reynolds #	Richardson #	Flow type	λ^*	Cr'
90.7.5(1)	0.0046	1.09	2.50	1.20	1.30	5.50	275.23	0.86	stable	N	N
90.7.5(2)	0.0046	1.09	0.80	0.40	0.75	5.20	29.36	2.80	stable	N	N
90.7.8	0.0129	1.04	2.55	0.75	1.60	5.70	183.89	1.44	stable	N	N
90.7.10	0.0088	1.00	2.30	0.80	1.15	5.70	184.00	1.29	SVA, SVB	2.80	2.02
90.7.11	0.0023	1.00	1.75	0.90	0.90	5.70	157.50	0.66	SVA, SVB	4.00	1.64
90.7.12	0.0078	1.00	2.50	1.00	1.35	5.60	250.00	1.21	SVA, SVB	3.50	2.25
90.7.16	0.0083	0.98	2.20	0.85	1.40	5.80	190.82	1.42	stable	N	N
90.7.23	0.0002	0.97	0.89	0.60	0.69	4.60	55.05	0.15	SVB	2.00	0.00
90.7.25	0.0019	0.98	1.68	0.50	1.41	5.20	85.71	0.33	SVB	2.20	0.13
90.7.26	0.0032	1.00	2.07	0.75	1.61	5.00	155.25	0.55	SVA, SVB	4.00	0.50
90.7.28	0.0064	0.98	1.97	0.50	1.78	5.10	100.51	0.80	SVB	1.50	0.00
90.7.31	0.0128	0.98	2.85	0.60	2.48	5.05	174.49	0.91	SVA, SVB	2.50	0.00
90.8.1	0.0027	0.95	2.01	0.40	1.68	4.45	84.63	0.26	SVB	3.00	0.00
90.8.2	0.0077	0.97	2.45	0.75	1.90	4.85	189.43	0.94	SVA	4.50	2.53
90.8.3	0.0019	0.97	1.30	0.50	1.30	4.75	67.01	0.55	SVA	2.50	1.43
90.8.5	0.0072	0.96	2.00	0.43	1.65	5.05	89.58	0.75	SVA	2.60	2.32
85.....							32.00	0.33	SVA		
85.....							42.00	0.28	SVA		
85.....							41.00	0.37	SVA		
85.....							83.00	0.38	SVA		
85.....							79.00	0.32	SVA		
85.....							92.00	0.58	SVA		
85.....							58.00	0.49	SVA		
85.....							60.00	0.94	SVA		
85.....							81.00	0.54	SVA		
85.....							100.00	0.80	SVA		
95.....							89.00	0.64	SVA		
85.....							69.00	0.95	SVA		
85.....							95.00	0.77	SVA		

date	Ap	µP	VI (M/S)	1 (EM)	WIND	OR	SUBST.	(EMPLOYEES)	•	FEEDBACK	•	FIN	TYPE	•	OP
85.....								108.00		0.63			SVA		
85.....								90.00		0.90			SVA		
85.....								145.00		0.58			SVA		
85.....								182.00		0.43			SVA		
85.....								126.00		0.59			SVA		
85.....								138.00		0.68			SVA		

date	α	C1	a	C1	X (cm)	Y (cm)	note	D (cm)	ZR* (cm)	ZR (ZR*, L)	d*	d
89.12.11	N	N	N	N	70	8		6.5	1.5	2.31	0.10	0.15
89.12.12	N	N	N	N	70	8		6.5	1.1	1.37	0.30	0.28
89.12.13	N	N	N	N	70	8		6.5	1.3	1.86	0.15	0.21
89.12.14	N	N	N	N	70	8		6.5	1.4	1.56	0.25	0.28
89.12.15	N	N	N	N	70	8		6.5	1.1	1.37	0.20	0.25
89.12.17	N	N	N	N	70	8		6.5	2.1	2.26	0.10	0.11
89.12.18	N	N	N	N	70	8		6.5	1.15	1.44	0.20	0.25
89.12.19	N	N	N	N	70	8		6.5	2.05	1.86	0.20	0.18
89.12.20	N	N	N	N	70	8		6.5	2.1	2.47	-0.05	-0.06
89.12.21	N	N	N	N	70	8		6.5	3	3.75	-0.18	-0.23
90.1.3	N	N	N	N	70	8		6.5	2.45	2.58	-0.13	-0.14
90.1.8(1)	N	N	N	N	70	8		6.5	2.35	3.13	-0.11	-0.15
90.1.8(2)	N	N	N	N	70	8		6.5	2.35	2.94	-0.25	-0.31
90.6.6	2.30	0.23	0.53		85	6	high speed region	6.7	1.1	1.00	0.40	0.36
90.6.7	N	N	N		85	6	high speed region	6.7	0.7	0.56	0.60	0.48
90.6.8	1.08	0.64	0.68		85	6	high speed region	6.7	1.2	2.00	0.20	0.33
90.6.9(1)	1.94	0.47	0.91		85	6	high speed region	6.7	1	1.54	0.20	0.31
90.6.9(2)	N	N	N		85	6	high speed region	6.7	0.9	1.50	0.20	0.33
90.6.11	2.01	0.52	1.05		85	6	high speed region	6.7	0.9	1.13	0.30	0.38
90.6.12	1.93	0.28	0.55		85	12.5	high speed region	6.7	1.1	1.38	-0.10	-0.13
90.6.14	1.50	0.68	1.02		85	12.5	high speed region	6.7	1	1.82	0.00	0.00
90.6.20	0.94	0.08	0.07		85	12.5	high speed region	6.7	1.4	2.33	0.00	0.00
90.6.21	2.09	0.29	0.61		85	12.5	high speed region	6.7	1.2	1.20	0.15	0.15
90.6.22	1.34	0.38	0.51		85	12.5	high speed region	6.7	1.2	1.41	0.10	0.12
90.6.23	1.57	0.40	0.63		85	12.5	high speed region	6.7	1.2	1.20	0.25	0.25
90.6.24	N	N	N		85	12.5	high speed region	6.7	0.8	0.99	0.10	0.11
90.6.26	1.63	0.30	0.49		85	12.5	high speed region	6.7	1.1	1.41	0.20	0.26
90.6.28	1.97	0.25	0.50		85	12.5	high speed region	6.7	1.1	1.00	0.30	0.27

date	a	CI	a	CI	Y	rate	DP	DP	DP	DP	DP	DP
90.7.5(1)	N	N	N	N	85	12.5	high speed region	6.7	1.2	1.00	0.20	0.17
90.7.5(2)	N	N	N	N	85	12.5	high speed region	6.7	1.5	3.75	0.20	0.50
90.7.8	N	N	N	N	85	12.5	high speed region	6.7	1	1.33	0.15	0.20
90.7.10	1.80	0.38	0.68	0.68	85	12.5	high speed region	6.7	1	1.25	0.25	0.31
90.7.11	1.41	0.42	0.60	0.60	85	12.5	high speed region	6.7	1	1.11	0.20	0.22
90.7.12	1.80	0.36	0.65	0.65	85	12.5	high speed region	6.7	1.1	1.10	0.20	0.20
90.7.16	N	N	N	N	85	12.5	high speed region	6.7	0.9	1.06	0.25	0.29
90.7.23	1.88	-0.78	-1.46	-1.46	30	11	low speed region	7	2.40	4.00	-0.05	-0.08
90.7.25	1.43	-0.76	-1.09	-1.09	30	11	low speed region	7	1.80	3.60	-0.03	-0.06
90.7.26	1.18	-0.54	-0.63	-0.63	30	11	low speed region	7	2.00	2.67	0.00	0.00
90.7.28	2.09	-0.90	-1.89	-1.89	9	11	low speed region	7	1.90	3.80	0.00	0.00
90.7.31	1.51	-0.87	-1.31	-1.31	9	11	low speed region	7	1.95	3.25	-0.13	-0.22
90.8.1	0.84	-0.84	-0.70	-0.70	9	11	low speed region	7	2.55	6.38	0.05	0.13
90.8.2	1.05	0.26	0.27	0.27	9	11	low speed region	7	2.15	2.97	0.00	0.00
90.8.3	1.26	0.10	0.13	0.13	9	11	low speed region	7	2.25	4.50	0.00	0.00
90.8.5	1.04	0.34	0.35	0.35	9	11	low speed region	7	1.95	4.53	0.00	0.00
85....	0.35	NA	NA	NA							NA	NA
85....	0.39	NA	NA	NA							NA	NA
85....	0.43	NA	NA	NA							NA	NA
85....	0.58	NA	NA	NA							NA	NA
85....	0.60	NA	NA	NA							NA	NA
85....	0.63	NA	NA	NA							NA	NA
85....	0.66	NA	NA	NA							NA	NA
85....	0.74	NA	NA	NA							NA	NA
85....	0.76	NA	NA	NA							NA	NA
85....	0.77	NA	NA	NA							NA	NA
85....	0.87	NA	NA	NA							NA	NA
85....	0.88	NA	NA	NA							NA	NA
85....	0.94	NA	NA	NA							NA	NA

date	α	C1	a	Cj	X (cm)	Y (cm)	note	D (cm)	ZR* (cm)	ZR (ZR* L)	d*	u
85.1.1	0.98	NA			NA						NA	NA
85.1.1	0.98	NA			NA						NA	NA
85.1.1	0.99	NA			NA						NA	NA
85.1.1	1.06	NA			NA						NA	NA
85.1.1	1.10	NA			NA						NA	NA
85.1.1	1.11	NA			NA						NA	NA



(a) Stable case (90-7-16 data.Ri=1.42) (b) SVB case (90-7-31 data.Ri=0.91 Cr=-0.870) (c) SVA case (90-8-02 data.Ri=0.94 Cr=0.260)

Figure 4.14 (a)-(c) Typical velocity profiles and velocity fluctuations

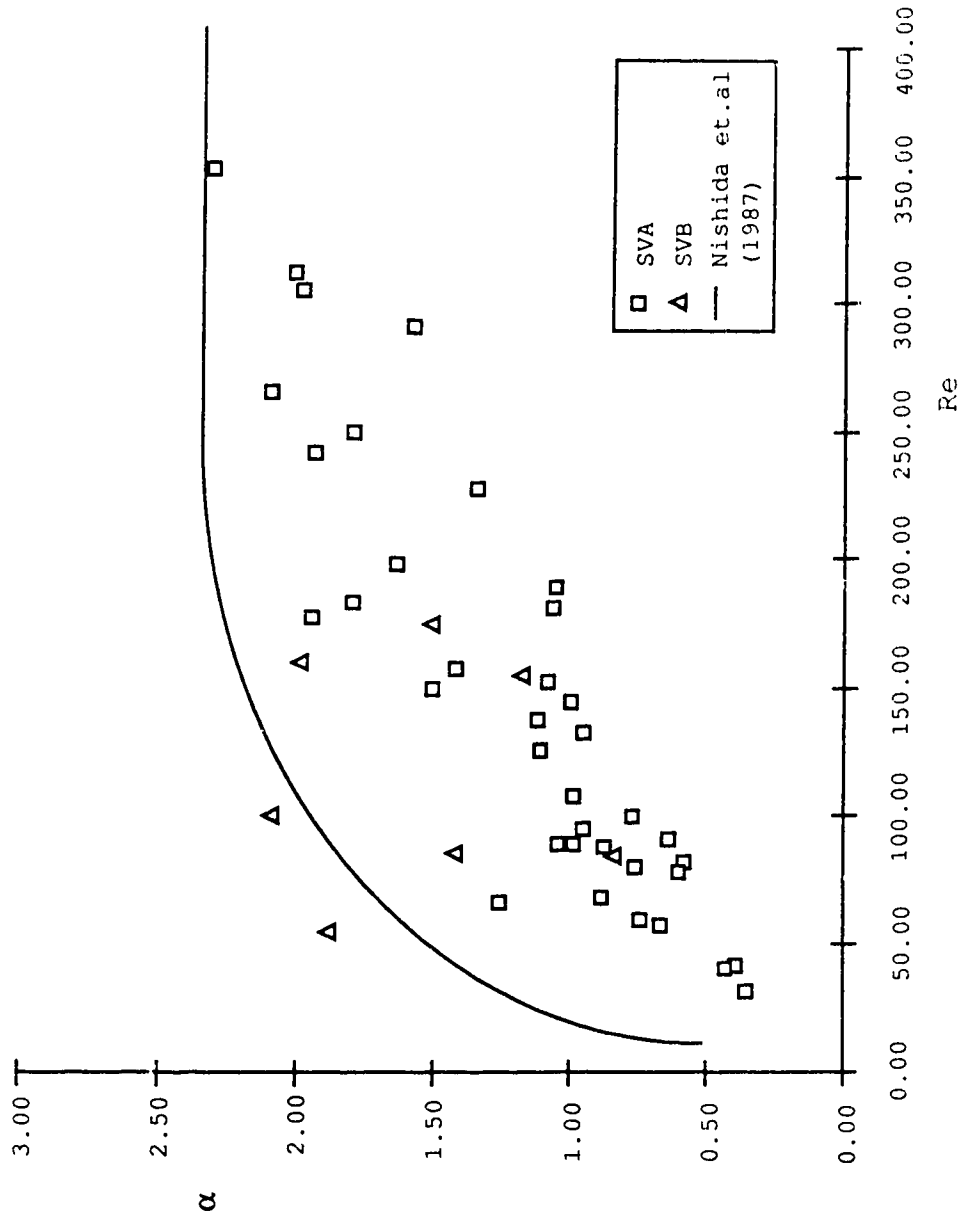


Figure 4.15. α -Re relationship

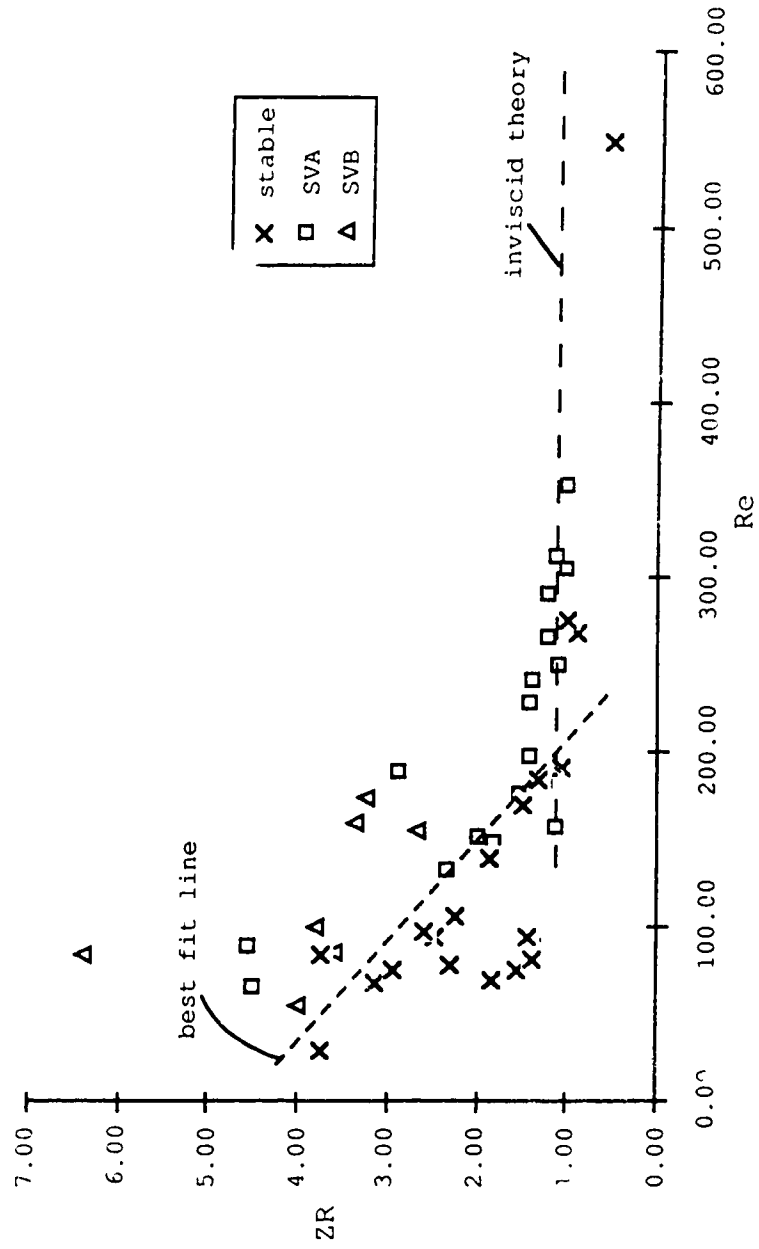


Figure 4.16. Re-ZR relationship

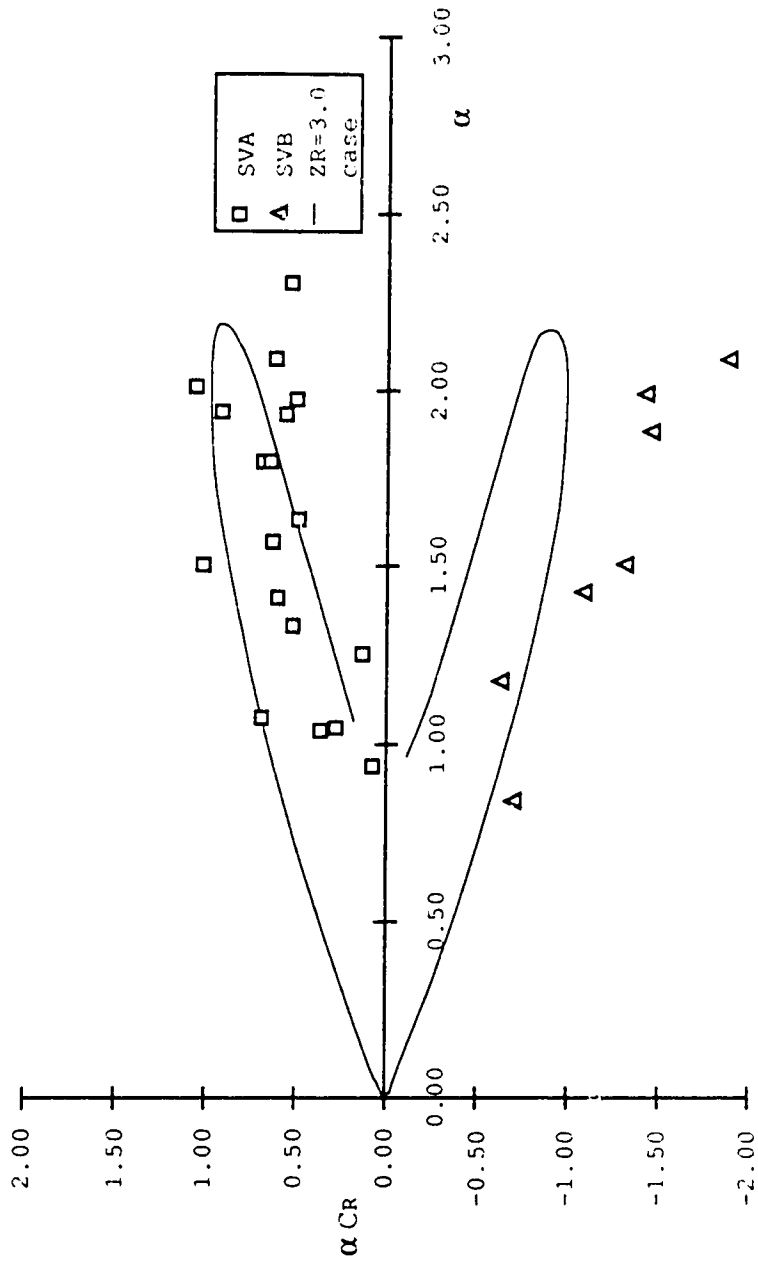


Figure 4.17. α - α CR relationship

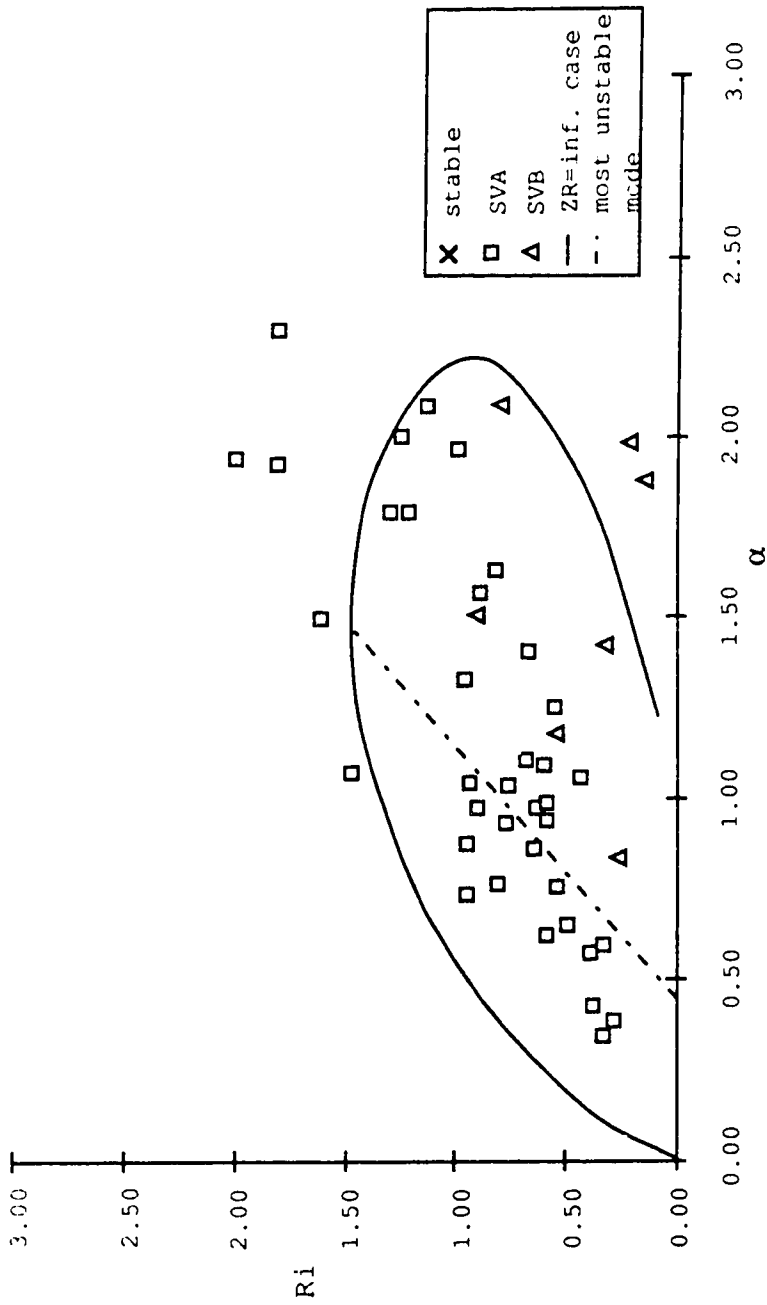


Figure 4.18. α - Ri relationship

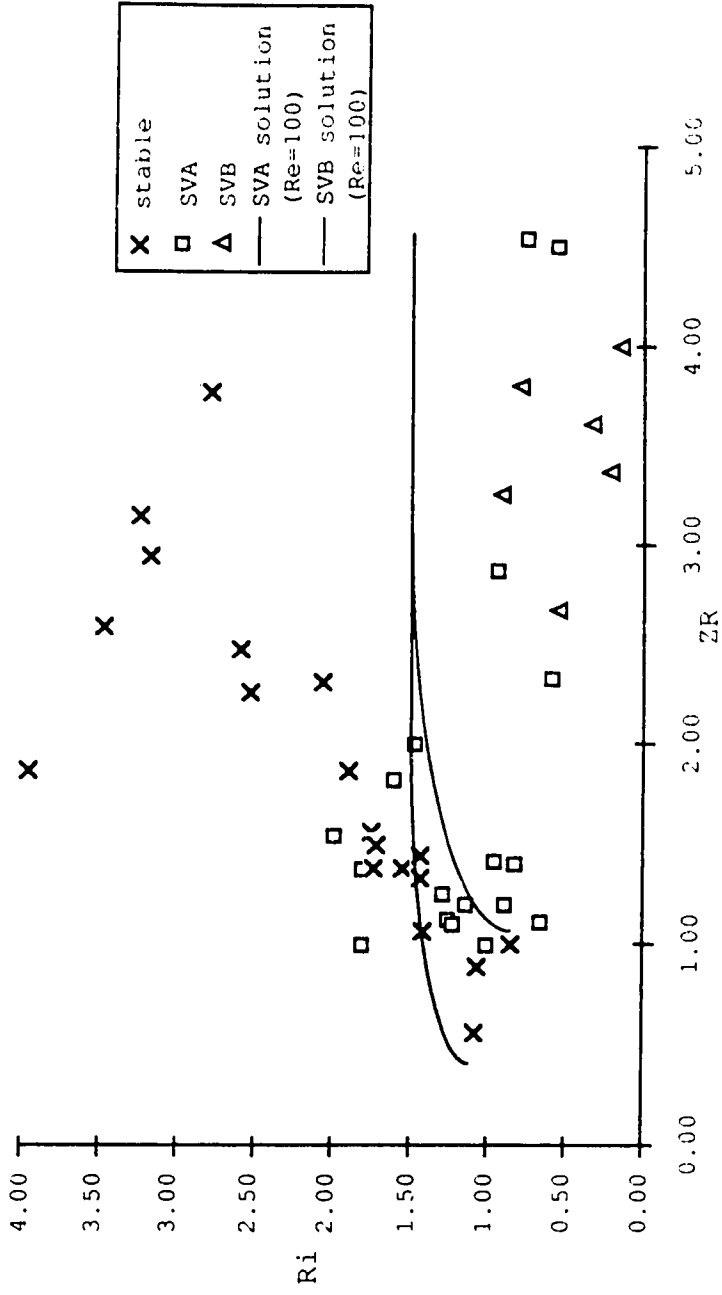


Figure 4.19. Ri-ZR relationship

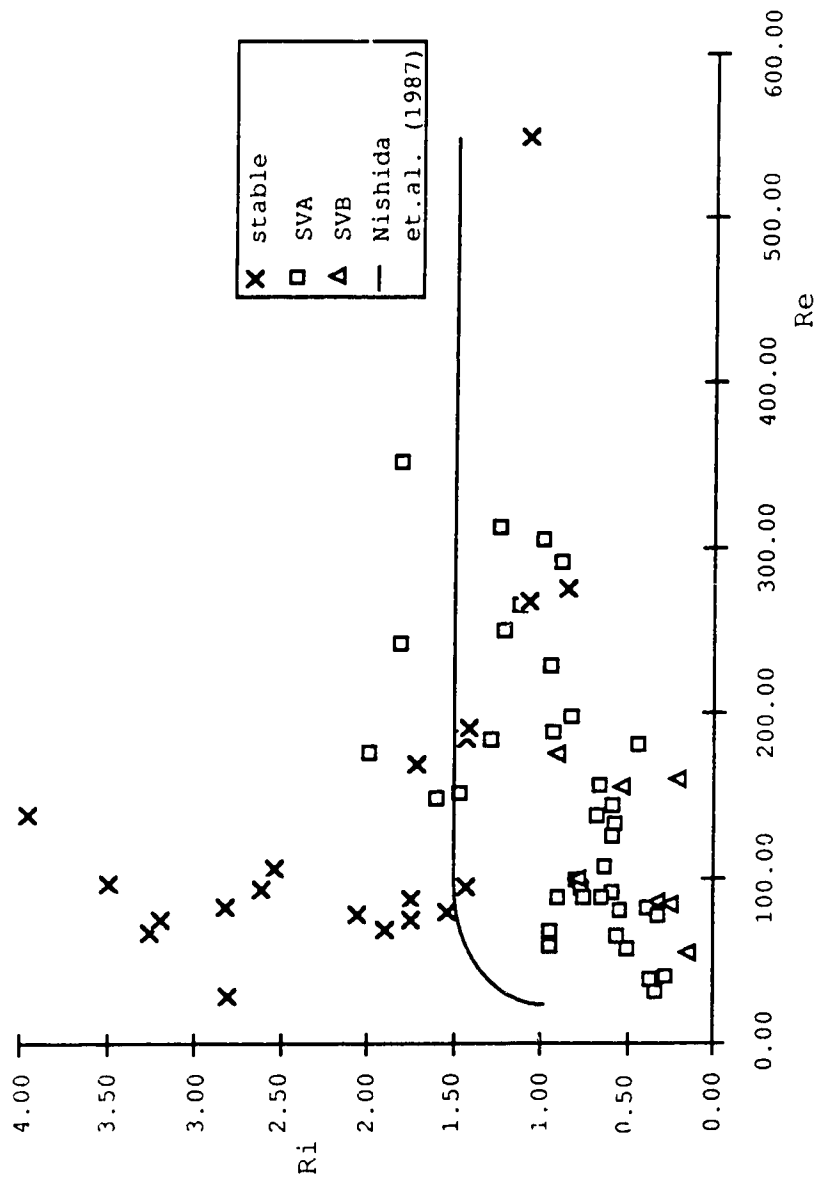


Figure 4.20. Re-Ri relationship

4.4 DISCUSSION

The previous section indicates that the hydrodynamic stability analysis explains the interfacial wave phenomena very well. However, several problems also arise, examples of which are the velocity approximation, the critical Richardson number and the phase velocity. In this section some explanations will be given from the velocity approximation point of view.

As was mentioned in Part One, it was believed that the mean velocity profiles fit a $\tanh(z)$ function reasonably well and that the inflection point (i.e. the center of the shear layer) always matches the location of the density interface. This is true if a width averaged, center line velocity is considered. However, the actual flow structure is far more complicated and this idea of width averaging may not be appropriate for all the cases. Therefore, the velocity approximation should be re-considered in order to evaluate the flow stability correctly.

In section 4.3, the velocity profile was approximated by the $\tanh(z)$ function on the basis of the following assumptions: (1) The inflection points of the velocity profile (i.e. $z=0$) occur at the density interface except in the flow region near the mouth region. (2) The velocity gradient is of greater importance to a stability evaluation than the maximum-minimum values of velocity. Figure 4.12 and Table 4.2 were obtained using these assumptions and they

provide the most important criteria for flow parameter determination. However, if we relax these conditions and let the interface displacement d be non-zero, a better approximation can be obtained as shown in Figure 4.21. Table 4.3 contains re-calculated parameters based on this new approximation: it can be seen that most of values are identical to Table 4.2 except for d .

As was found in the numerical analysis and Lawrence's results, the displacement d has strong effects on the flow stability, particularly on the wave number and phase velocity. In order to evaluate the influence of d , the Richardson number Ri and wave number α were plotted against d as in Figure 4.22. This figure indicates that the unstable modes tend to have larger Richardson numbers and wave numbers as d increases. This is very reasonable in terms of the critical Richardson number, since the prediction of model IV showed $Ri_c=2.2$ at $d=0.5$ ($Ri_c=1.5$ for $d=0.0$ case). On the other hand, model IV showed that the unstable wave numbers tend to be unchanged or slightly smaller than the $d=0$ cases; a result which is completely different from the behavior of SVB waves in Figure 4.22.

These experimental results seem to support Lawrence's inviscid analysis. SVA waves showed relatively good agreement with the viscous model and any differences may be explained as follows: (1) SVA waves showed larger critical Richardson numbers mainly due to the displacement effects predicted by model IV; (2) SVB waves tend to have larger wave

numbers than were predicted by the viscous models (III and IV). However, it may be reasonable to say that the viscosity effects are relatively small since the lower layer thickness Z_0 was large for these cases. Thus, the inviscid model does a better job of prediction (see also Figure 4.23). (3) Another possible explanation for these phenomena is that the non-slip boundary conditions (model II) make the SVB wave number larger as U_w (relative velocity of the rigid boundary to the mean flow) increases. This also seems reasonable since model II is inviscid.

It should also be mentioned that the critical Richardson number observed in most of the previous experimental works tends to be large since the wave phenomenon is intermittent. Also, if the mean velocity profile is employed to examine the stability, the shear stress was likely underestimated and the critical Richardson number overestimated. This suggests that instantaneous velocity profile measurements must be employed to improve the accuracy of the prediction, although our experiments did reveal the details of the mechanism of the interfacial wave phenomena very well.

Figure 4.24 shows the relationship between the density difference $\Delta\rho$ and the characteristic length and velocity scales. It is interesting that the length scale L is almost independent of $\Delta\rho$ variation, while the velocity scale V is significantly influenced by $\Delta\rho$. The variation of V also shows that V cannot be large enough to maintain their small Richardson number for unstable waves as $\Delta\rho$ increases. On the

other hand, smaller values of $\Delta\rho$ allow a certain amount of variation in V and therefore, most of the unstable situations were observed in the $0 < \Delta\rho < 0.015$ region. This fact suggests that it is very difficult to obtain an instability in experimental channels with a high density difference such as provided by sea water ($\Delta\rho = 0.029 - 0.033$).

The phase velocity mismatch of SVB waves is another problem. However, there is no clear explanation for this problem mainly due to the lack of appropriate analysis. It can be seen (based on models I, III) that the SVB waves have a slightly larger phase velocity in the smaller wave number region if a rigid boundary is present than in the unbounded case and this may be one of the reasons. The possibility of non-linear effects on these waves has been examined by Yoshida & Kashiwada (1988), but this analysis did not improve the situation either. This is certainly a problem to be solved in the future.

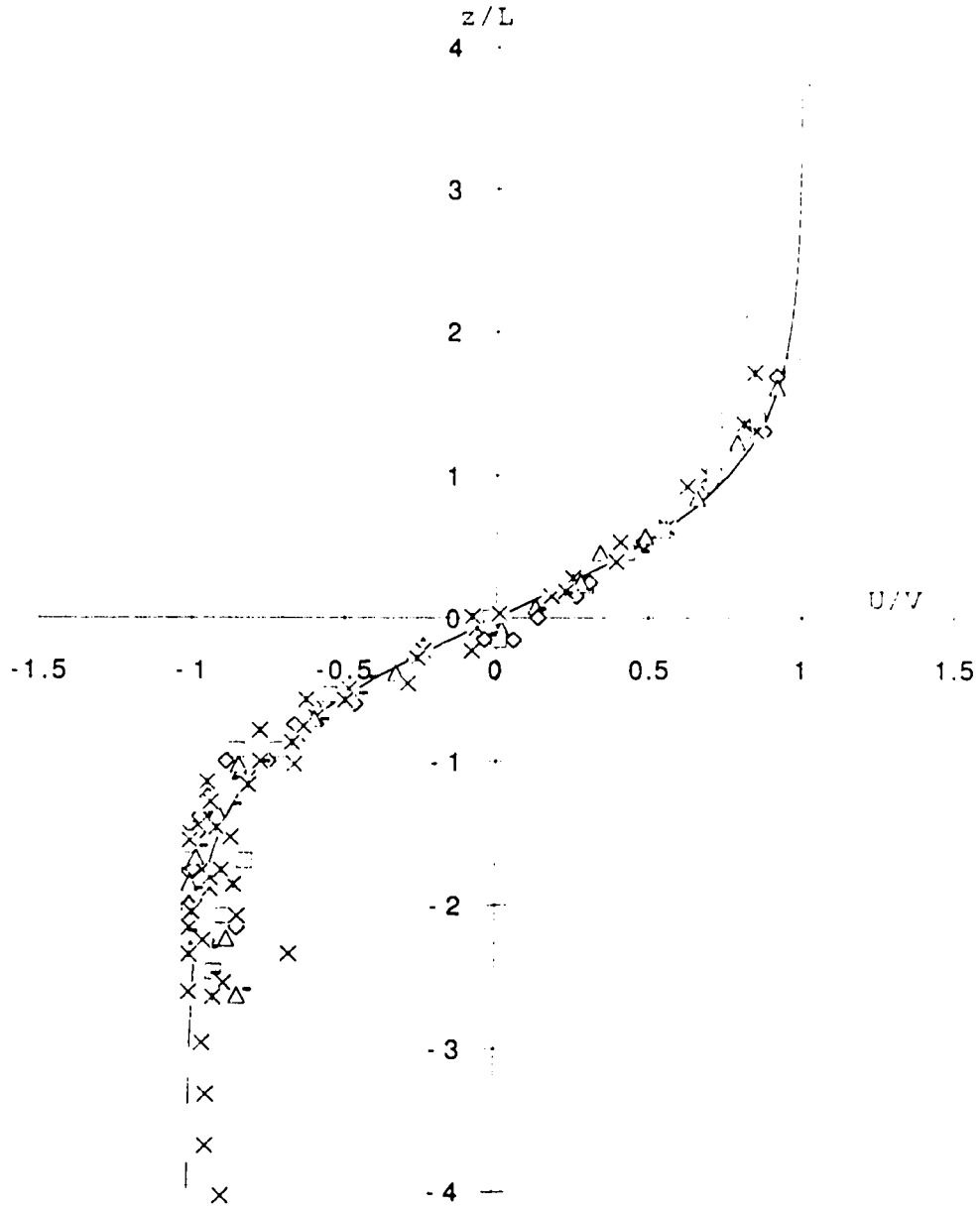


Figure 4.21. Non-dimensionalized velocity profile
(with non-zero d approximation)

date	Ap	µP	V(cm.s)	L(cm)	Wint.(cm/s)	Dia.t.(cm)	Reynolds #	Fachartson #	Flow type	λ*	Gr*
90.6.22	0.0097	1.08	2.90	0.85	1.35	5.50	228.24	0.95	SVA,SVB	4.00	2.66
90.6.23	0.0082	1.03	3.00	1.00	1.50	5.50	291.26	0.89	SVA,SVB	4.00	2.70
90.6.26	0.0073	1.02	2.60	0.78	1.45	5.60	198.82	0.82	SVA,SVB	3.90	2.23
90.6.28	0.0073	1.01	2.80	1.10	1.40	5.60	304.95	1.00	SVA,SVB	3.50	2.11
90.7.10	0.0088	1.00	2.30	0.80	1.15	5.70	184.00	1.29	SVA,SVB	2.80	2.02
90.7.11	0.0023	1.00	1.75	0.90	0.90	5.70	157.50	0.66	SVA,SVB	4.00	1.64
90.7.12	0.0078	1.00	2.50	1.00	1.35	5.60	250.00	1.21	SVA,SVB	3.50	2.25
90.8.2	0.0077	0.97	2.45	0.75	1.90	4.85	189.43	0.94	SVA	4.50	2.53
90.8.3	0.0019	0.97	1.30	0.50	1.30	4.75	67.01	0.55	SVA	2.50	1.43
90.8.5	0.0072	0.96	2.00	0.43	1.65	5.05	89.58	0.75	SVA	2.50	2.12
90.7.23	0.0002	0.97	0.69	0.60	0.69	4.60	55.05	1.15	SVB	2.00	1.10
90.7.25	0.0019	0.98	1.68	0.50	1.41	5.20	85.71	0.93	SVB	2.00	1.13
90.7.27	0.0032	1.00	2.07	0.75	1.61	5.00	155.25	1.55	SVA,SVB	4.10	1.50
90.7.28	0.0004	0.98	1.97	0.50	1.79	5.10	100.51	1.80	SVB	1.50	1.10
90.7.31	0.0128	0.98	1.50	0.40	2.46	5.05	174.49	0.91	SVA,SVB	2.50	1.10
90.8.1	0.0027	0.95	1.10	0.40	1.55	4.45	64.63	0.65	SVB	3.10	1.10
85.1.1							30.00	1.30	SVA		
85.1.1							40.00	1.00	SVA		
85.1.1							40.00	1.30	SVA		
85.1.1							50.00	1.00	SVA		
85.1.1							70.00	1.30	SVA		
85.1.1							90.00	1.00	SVA		
85.1.1							100.00	1.30	SVA		
85.1.1							120.00	1.00	SVA		
85.1.1							140.00	1.30	SVA		
85.1.1							160.00	1.00	SVA		
85.1.1							180.00	1.30	SVA		
85.1.1							200.00	1.00	SVA		
85.1.1							220.00	1.30	SVA		
85.1.1							240.00	1.00	SVA		
85.1.1							260.00	1.30	SVA		
85.1.1							280.00	1.00	SVA		
85.1.1							300.00	1.30	SVA		

```

date      dp      kd      item      volume      hydride     fuel      gas      oil
85.---.---  90.000  0.000  0.000  0.000  0.000  0.000  0.000
85.---.---  0.000  0.000  0.000  0.000  0.000  0.000  0.000
85.---.---  0.000  0.000  0.000  0.000  0.000  0.000  0.000
85.---.---  0.000  0.000  0.000  0.000  0.000  0.000  0.000
85.---.---  0.000  0.000  0.000  0.000  0.000  0.000  0.000

```

date	α	Ci	a	C:	X(cm)	Y(cm)	note	D (cm)	ZR*(cm)	ZR(ZR* L)	d*	d
89.12.11	N	N	N	N	70	8		6.5	1.5	2.31	0.10	0.15
89.12.12	N	N	N	N	70	8		6.5	1.1	1.37	0.30	0.38
89.12.13	N	N	N	N	70	8		6.5	1.3	1.86	0.15	0.21
89.12.14	N	N	N	N	70	8		6.5	1.4	1.56	0.25	0.28
89.12.15	N	N	N	N	70	8		6.5	1.1	1.37	0.20	0.25
89.12.17	N	N	N	N	70	8		6.5	2.1	2.26	0.10	0.11
89.12.18	N	N	N	N	70	8		6.5	1.15	1.44	0.20	0.25
89.12.19	N	N	N	N	70	8		6.5	2.05	1.86	0.20	0.18
89.12.20	N	N	N	N	70	8		6.5	1.1	2.47	-0.05	-0.06
89.12.21	N	N	N	N	70	8		6.5	3	3.75	-0.18	-0.23
90.1.3	N	N	N	N	70	8		6.5	2.45	2.58	-0.13	-0.14
90.1.8(1)	N	N	N	N	70	8		6.5	2.35	3.13	-0.11	-0.13
90.1.8(2)	N	N	N	N	70	8		6.5	2.35	2.94	-0.25	-0.31
90.6.7	N	N	N	N	85	6	high speed region	6.7	1.7	0.56	0.53	0.46
90.6.9(2)	N	N	N	N	85	6	high speed region	6.7	1.7	1.50	0.20	0.33
90.6.24	N	N	N	N	85	12.5	high speed region	6.7	1.8	1.89	0.11	0.11
90.7.5(1)	N	N	N	N	85	12.5	high speed region	6.7	1.6	1.60	0.20	0.17
90.7.5(2)	N	N	N	N	85	12.5	high speed region	6.7	1.8	3.13	0.01	0.01
90.7.8	N	N	N	N	85	12.5	high speed region	6.7	1.7	1.89	0.11	0.11
90.7.16	N	N	N	N	85	12.5	high speed region	6.7	1.7	1.6	0.01	0.01
90.6.6	0.50	0.20	0.20	N	85	6	high speed region	6.7	1.7	1.6	0.01	0.01
90.6.8	0.58	0.24	0.24	N	85	6	high speed region	6.7	1.7	1.6	0.01	0.01
90.6.9(1)	0.94	0.47	0.47	N	85	6	high speed region	6.7	1.7	1.6	0.01	0.01
90.6.11	0.51	0.24	0.24	N	85	6	high speed region	6.7	1.7	1.6	0.01	0.01
90.6.12	0.95	0.26	0.26	N	85	6	high speed region	6.7	1.7	1.6	0.01	0.01
90.6.14	0.51	0.26	0.26	N	85	6	high speed region	6.7	1.7	1.6	0.01	0.01
90.6.23	0.94	0.29	0.29	N	85	6	high speed region	6.7	1.7	1.6	0.01	0.01
90.6.24	0.51	0.24	0.24	N	85	6	high speed region	6.7	1.7	1.6	0.01	0.01

date	alpha	beta	gamma	delta	epsilon	zeta	eta	theta	iota	kappa	lambda	mu	nu	xi	omicron	pi	rho	sigma	tau	upsilon	phi	chi	psi	omega	
90.6.22	1.34	0.38	0.51	85	12.5	high speed region	0.0	0.0	0.0	0.0	0.0	0.0	0.0	0.0	0.0	0.0	0.0	0.0	0.0	0.0	0.0	0.0	0.0	0.0	
90.6.23	1.57	0.40	0.61	85	12.5	high speed region	0.0	0.0	0.0	0.0	0.0	0.0	0.0	0.0	0.0	0.0	0.0	0.0	0.0	0.0	0.0	0.0	0.0	0.0	
90.6.26	1.63	0.39	0.49	85	12.5	high speed region	0.0	0.0	0.0	0.0	0.0	0.0	0.0	0.0	0.0	0.0	0.0	0.0	0.0	0.0	0.0	0.0	0.0	0.0	
90.6.28	1.97	0.25	0.50	85	12.5	high speed region	0.0	0.0	0.0	0.0	0.0	0.0	0.0	0.0	0.0	0.0	0.0	0.0	0.0	0.0	0.0	0.0	0.0	0.0	
90.7.10	1.85	0.38	0.68	85	12.5	high speed region	0.0	0.0	0.0	0.0	0.0	0.0	0.0	0.0	0.0	0.0	0.0	0.0	0.0	0.0	0.0	0.0	0.0	0.0	
90.7.11	1.41	0.42	0.60	85	12.5	high speed region	0.0	0.0	0.0	0.0	0.0	0.0	0.0	0.0	0.0	0.0	0.0	0.0	0.0	0.0	0.0	0.0	0.0	0.0	
90.7.12	1.80	0.36	0.65	85	12.5	high speed region	0.0	0.0	0.0	0.0	0.0	0.0	0.0	0.0	0.0	0.0	0.0	0.0	0.0	0.0	0.0	0.0	0.0	0.0	
90.8.2	1.05	0.26	0.27	1	1	low speed region	0.0	0.0	0.0	0.0	0.0	0.0	0.0	0.0	0.0	0.0	0.0	0.0	0.0	0.0	0.0	0.0	0.0	0.0	
90.8.3	1.36	0.19	0.31	1	1	low speed region	0.0	0.0	0.0	0.0	0.0	0.0	0.0	0.0	0.0	0.0	0.0	0.0	0.0	0.0	0.0	0.0	0.0	0.0	
90.8.5	1.54	0.34	0.44	1	1	low speed region	0.0	0.0	0.0	0.0	0.0	0.0	0.0	0.0	0.0	0.0	0.0	0.0	0.0	0.0	0.0	0.0	0.0	0.0	
90.7.13	1.98	0.78	1.19	1	1	low speed region	0.0	0.0	0.0	0.0	0.0	0.0	0.0	0.0	0.0	0.0	0.0	0.0	0.0	0.0	0.0	0.0	0.0	0.0	
90.7.25	1.43	0.79	1.19	1	1	low speed region	0.0	0.0	0.0	0.0	0.0	0.0	0.0	0.0	0.0	0.0	0.0	0.0	0.0	0.0	0.0	0.0	0.0	0.0	
90.7.26	1.24	0.54	0.87	1	1	low speed region	0.0	0.0	0.0	0.0	0.0	0.0	0.0	0.0	0.0	0.0	0.0	0.0	0.0	0.0	0.0	0.0	0.0	0.0	
90.7.28	2.04	0.91	1.27	1	1	low speed region	0.0	0.0	0.0	0.0	0.0	0.0	0.0	0.0	0.0	0.0	0.0	0.0	0.0	0.0	0.0	0.0	0.0	0.0	
90.7.31	1.51	0.87	1.20	1	1	low speed region	0.0	0.0	0.0	0.0	0.0	0.0	0.0	0.0	0.0	0.0	0.0	0.0	0.0	0.0	0.0	0.0	0.0	0.0	
90.8.1	0.84	0.54	0.87	1	1	low speed region	0.0	0.0	0.0	0.0	0.0	0.0	0.0	0.0	0.0	0.0	0.0	0.0	0.0	0.0	0.0	0.0	0.0	0.0	
85.---	0.35	NA	NA	NA	NA	NA	NA	NA	NA	NA	NA	NA	NA	NA	NA	NA	NA	NA	NA	NA	NA	NA	NA	NA	NA
85.---	0.39	NA	NA	NA	NA	NA	NA	NA	NA	NA	NA	NA	NA	NA	NA	NA	NA	NA	NA	NA	NA	NA	NA	NA	NA
85.---	0.43	NA	NA	NA	NA	NA	NA	NA	NA	NA	NA	NA	NA	NA	NA	NA	NA	NA	NA	NA	NA	NA	NA	NA	NA
85.---	0.58	NA	NA	NA	NA	NA	NA	NA	NA	NA	NA	NA	NA	NA	NA	NA	NA	NA	NA	NA	NA	NA	NA	NA	NA
85.---	0.60	NA	NA	NA	NA	NA	NA	NA	NA	NA	NA	NA	NA	NA	NA	NA	NA	NA	NA	NA	NA	NA	NA	NA	NA
85.---	0.62	NA	NA	NA	NA	NA	NA	NA	NA	NA	NA	NA	NA	NA	NA	NA	NA	NA	NA	NA	NA	NA	NA	NA	NA
85.---	0.66	NA	NA	NA	NA	NA	NA	NA	NA	NA	NA	NA	NA	NA	NA	NA	NA	NA	NA	NA	NA	NA	NA	NA	NA
85.---	0.74	NA	NA	NA	NA	NA	NA	NA	NA	NA	NA	NA	NA	NA	NA	NA	NA	NA	NA	NA	NA	NA	NA	NA	NA
85.---	0.76	NA	NA	NA	NA	NA	NA	NA	NA	NA	NA	NA	NA	NA	NA	NA	NA	NA	NA	NA	NA	NA	NA	NA	NA
85.---	0.77	NA	NA	NA	NA	NA	NA	NA	NA	NA	NA	NA	NA	NA	NA	NA	NA	NA	NA	NA	NA	NA	NA	NA	NA
85.---	0.87	NA	NA	NA	NA	NA	NA	NA	NA	NA	NA	NA	NA	NA	NA	NA	NA	NA	NA	NA	NA	NA	NA	NA	NA
85.---	0.88	NA	NA	NA	NA	NA	NA	NA	NA	NA	NA	NA	NA	NA	NA	NA	NA	NA	NA	NA	NA	NA	NA	NA	NA
85.---	0.94	NA	NA	NA	NA	NA	NA	NA	NA	NA	NA	NA	NA	NA	NA	NA	NA	NA	NA	NA	NA	NA	NA	NA	NA
85.---	0.98	NA	NA	NA	NA	NA	NA	NA	NA	NA	NA	NA	NA	NA	NA	NA	NA	NA	NA	NA	NA	NA	NA	NA	NA

date	α	CI	a	Ci	X (cm)	Y (cm)	note	D (cm)	ZR* (cm)	ZR (ZR*/L)	d*	d
85.--.--	0.98	NA	NA	NA	NA	NA					NA	NA
85.--.--	0.99	NA	NA	NA	NA	NA					NA	NA
85.--.--	1.06	NA	NA	NA	NA	NA					NA	NA
85.--.--	1.10	NA	NA	NA	NA	NA					NA	NA
85.--.--	1.11	NA	NA	NA	NA	NA					NA	NA

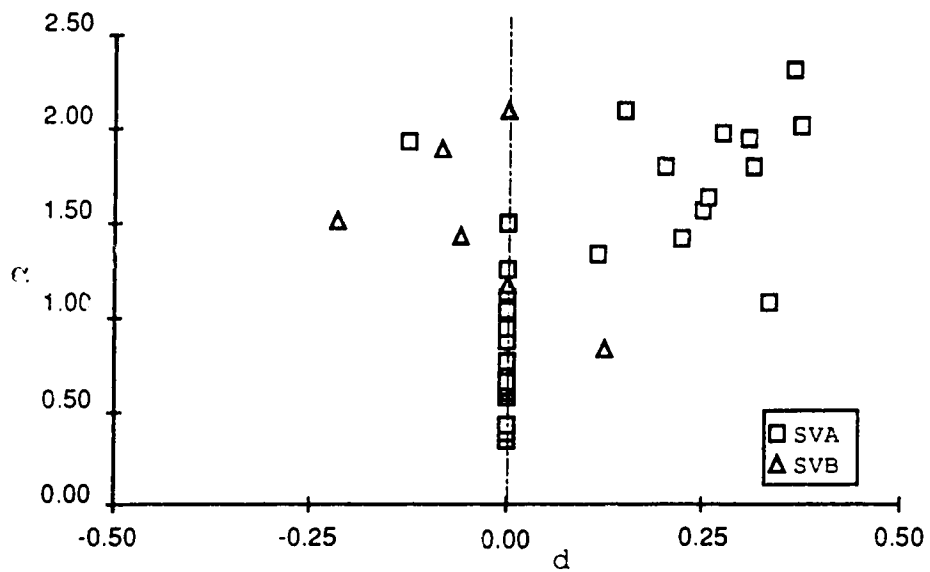
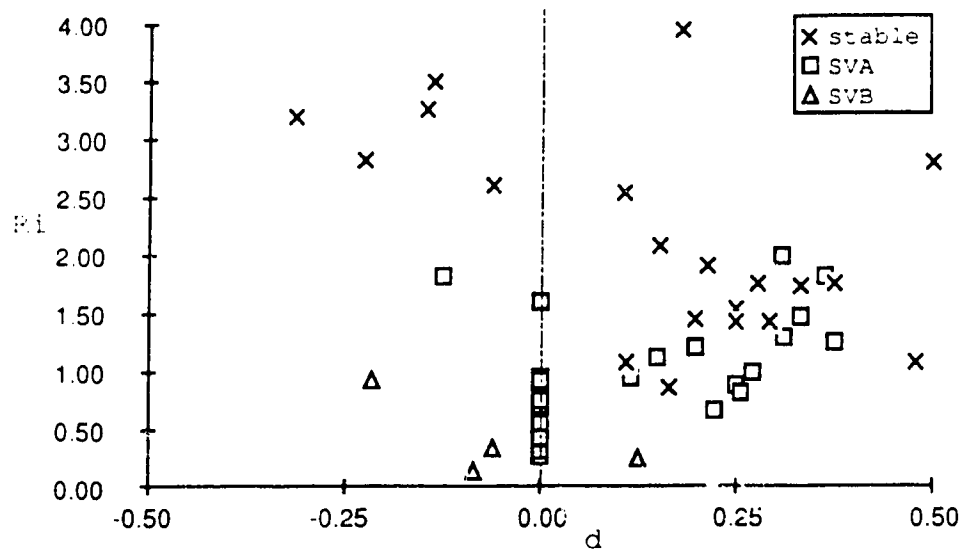


Figure 4.22. Displacement effects on the Richardson number Ri and wave number α

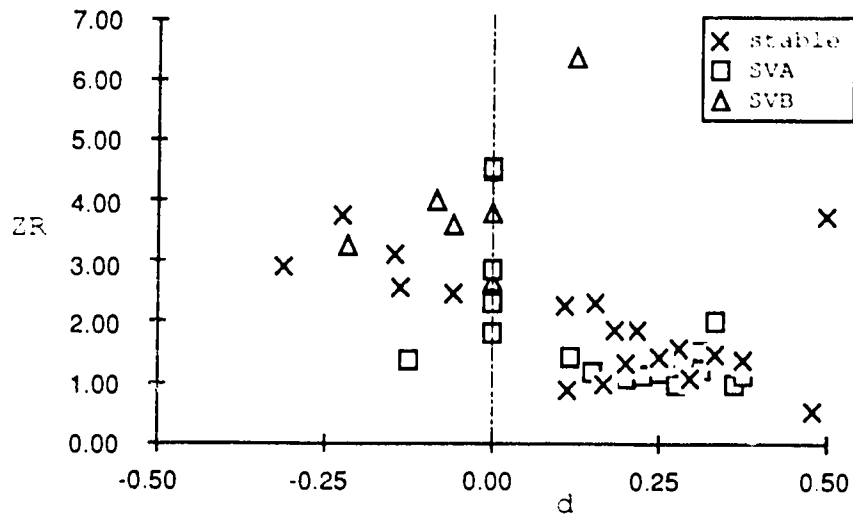


Figure 4.23. Displacement d and the lower layer thickness Z_R

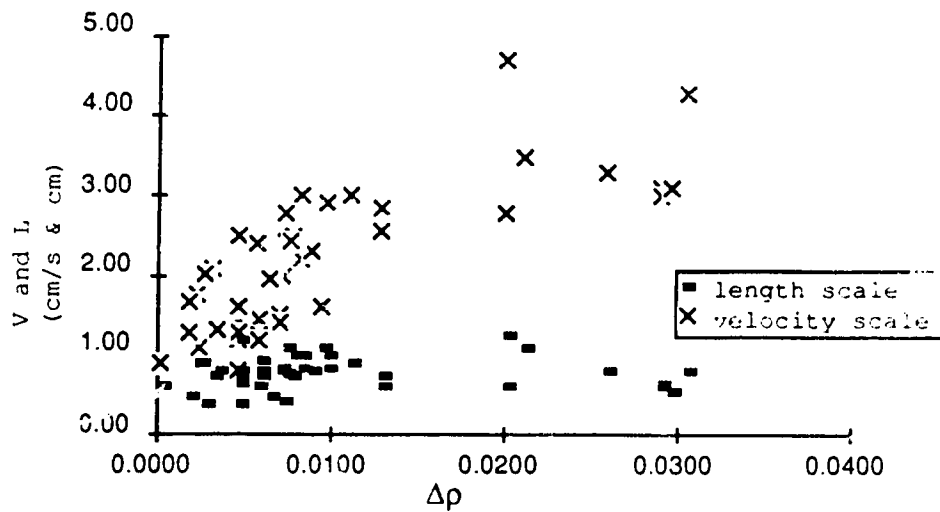


Figure 4.24. Density difference v.s. Characteristic length and velocity scales

4.5 CONCLUSION

In this section, experiments involving the salt wedge type of two layer stratified flow have been discussed. The measurements (from LDA, wave detector, conductivity meter and visualization techniques) investigated the wave phenomena on this type of flow. As the measured mean and fluctuation velocity profiles showed very good agreement with theoretical prediction, this proved that these wave phenomena are strongly associated with the shear instability mechanism. The other flow parameters (the Reynolds number, the Richardson number, wave number and phase velocity) supported this idea by showing very good agreement with analysis. However, a few problems were found related to the critical value of the Richardson number and phase velocity of SVB waves. These are partially caused by problems of the velocity approximation with a $\tanh(z)$ function and to intermittency of the wave phenomena. Also, it was suggested that strong non-linear effects on the phase velocity may affect the measurements. This problem needs further investigation by both theoretical and experimental analysis.

PART FIVE: GENERAL CONCLUSIONS

5.1 CONCLUSIONS

In this study, present knowledge was reviewed with the objective of clarifying relatively weak points in our understanding of instability phenomena on salt wedge flow. The following problems were addressed:

Problem (i): Separation of two Holmboe modes (i.e. SVA and SVB) were observed and this phenomena is called 'one-sidedness'. Present knowledge of stability may explain some stabilizing effects of the rigid boundary conditions, but does not explain the separation of the solutions.

Problem (ii): Previous experiments show that a salt wedge can be divided into three sub-divisions based on their stress distributions. In each region, velocity profiles can be approximated very well by a $\tanh(z)$ function, although the inflection points are often displaced with respect to the density interface. These displacements cause some problems when applying existing hydrodynamic stability theories to the salt wedge.

Problem (iii): Due to the secondary flow structures in channels, high and low speed regions develop which may cause three-dimensional interfacial wave structures. However, few experimental data are available in the case of salt wedge flow, making it difficult to determine the implications of this phenomena.

These problems were investigated by developing appropriate numerical models and through verification of these models with experimental data.

For the problem (i), three models were examined to evaluate the rigid boundary effects on the stability of salt wedge flow. The features of these models can be summarized as follows:

Model I: Inviscid, piece-wise linear velocity profile flow to evaluate the effects of the rigid boundary.

Model II: Same as model I, but provides for the back flow effects in the lower layer by changing the rigid boundary velocity U_w .

Model III: Viscous, $\tanh(z)$ velocity profile flow. Designed to evaluate rigid boundary effects on stability.

The results are:

Model I: Generally SVB waves are stabilized as the lower thickness Z_R decreases, while SVA waves are not affected as strongly. The unstable wave numbers for SVB waves tends to have smaller values as Z_R decreases, which is opposite to intuition.

Model II: It was found that the SVB wave length gets shorter as Z_R decreases when the velocity of the rigid boundary U_w is $U_w > -1.0$. It was also found that SVA waves have additional unstable modes in the extremely small wave number region when the value of U_w exceeds 0.0. These modes, however, have a very small growth rate and are not expected to be able to appear in the flow.

Both models I and II showed some problems when Z_R was smaller than 1.0, since the piece-wise linear velocity profile fails to satisfy one of the necessary conditions for instability.

Model III: In this model the damping and stabilizing effects of viscosity on high Richardson number flow was observed. It was also found that the viscosity destabilized the low wave number region, as was illustrated by the additional unstable modes. This model also shows that SVB waves are strongly influenced by the reduction in Z_R , but neutral boundaries and the most unstable modes behave in a slightly different way when compared to the inviscid solutions. The most unstable modes appear around $\alpha=0.8$ $Ri=0.4$ and do not move with the variation of Z_R . These models (I, II and III) imply a sensitivity of SVB wave stability on the lower layer thickness Z_R and velocity profile U_0 . By contrast, SVA waves are only slightly influenced by Z_R and U_0 ; a result very similar to the inviscid case and may suggest an independence of SVA waves from the lower layer flow.

These numerical results indicate that viscosity and a continuous velocity profile have a significant influence upon the flow stability. In order to verify these results, the experiments including the measurements (from LDA, wave detector, conductivity meter and flow visualization technique) were performed. As the measured mean and fluctuation velocity profiles showed very good agreement with

the numerical results, this proved that wave phenomena on the salt wedge are strongly associated with the shear instability mechanism. Other flow parameters (the Reynolds number, the Richardson number, wave number and phase velocity) supported this idea by showing very good agreement with analysis. It also found, however, that there were a few problems related to the critical value of the Richardson number and the phase velocity of SVB waves. These are partially caused by approximating the velocity profile with a $\tanh(z)$ function and problem associated with intermittency of the wave phenomena. Also, it was suggested that strong non-linear effects on the phase velocity may affect the measurements. This problem needs further investigation by both theoretical and experimental analysis.

For the problem (ii), the displacement of inflection point upon the stability of salt wedge flows were evaluated by numerical model IV, which is: Viscous, $\tanh(z)$ velocity profile and unbounded flow with the inflection point displacement. The results were summarized as:

Model IV: This model showed that only one Holmboe mode (SVB) can exist in an open channel. Although the model did not cover the entire range of parameter variation (especially the displacement d), the results imply mechanisms for the instability that are quite reasonable (in particular, the larger critical Richardson number). This model also showed that the additional unstable modes obtained by Lawrence et al. are stabilized by

viscosity.

The experiments verified significant effects of the inflection point displacement on the waves, particularly 'one-sidedness' phenomenon.

For the problem (iii), careful and precise experiments were performed. By combining the results with the problem (i) and (ii), they showed even more details of flow and wave structures on salt wedge than previous knowledge. The results from these experiments also support the assumption that localization and three-dimensional structures of interfacial waves are strongly related to the channel configuration and three-dimensional flow structures. This fact implies that better prediction of wave phenomena on a salt wedge requires precise details of the flow as opposed to just width averaged or centerline velocity and density profiles.

Therefore, the stability problem of a salt wedge needs further investigation in which precise measurements are taken. These should include the instantaneous velocity profiles and secondary flow structures in the channel.

5.2 DISCUSSION AND SUGGESTIONS

As was mentioned before, the three-dimensional structure of interfacial waves is another commonly observed problem associated with salt wedges. Because of the consequence of Squire's theorem, we have always assumed *a priori* that an initially one-dimensional flow will pass through a distinct two-dimensional state before becoming dependent on the third spatial coordinate (lateral direction). Thus, these three-dimensional wave structures are considered to be the secondary instabilities produced after full development of primary two-dimensional instabilities. However, the salt wedge flow usually does not have the strong non-linearity required, by theory, to induce secondary instabilities and it is this fact that has guided this study in the investigation of three-dimensional flow structure as opposed to focusing on a non-linear treatment of these interfacial waves.

Recently, it was found that the fastest growing three-dimensional primary instability possibly exists when there is increasing viscosity or stratification of the flow. Smyth & Peltier (1990) investigated the stability of stratified, dissipative flows and found these three-dimensional primary instabilities in the Holmboe modes. Although the calculation is performed under quite a limited range of parameters, their results answer some of the questions concerning the stability analysis of stratified flows. For example, the maximum growth rate of Holmboe modes is always obtained around

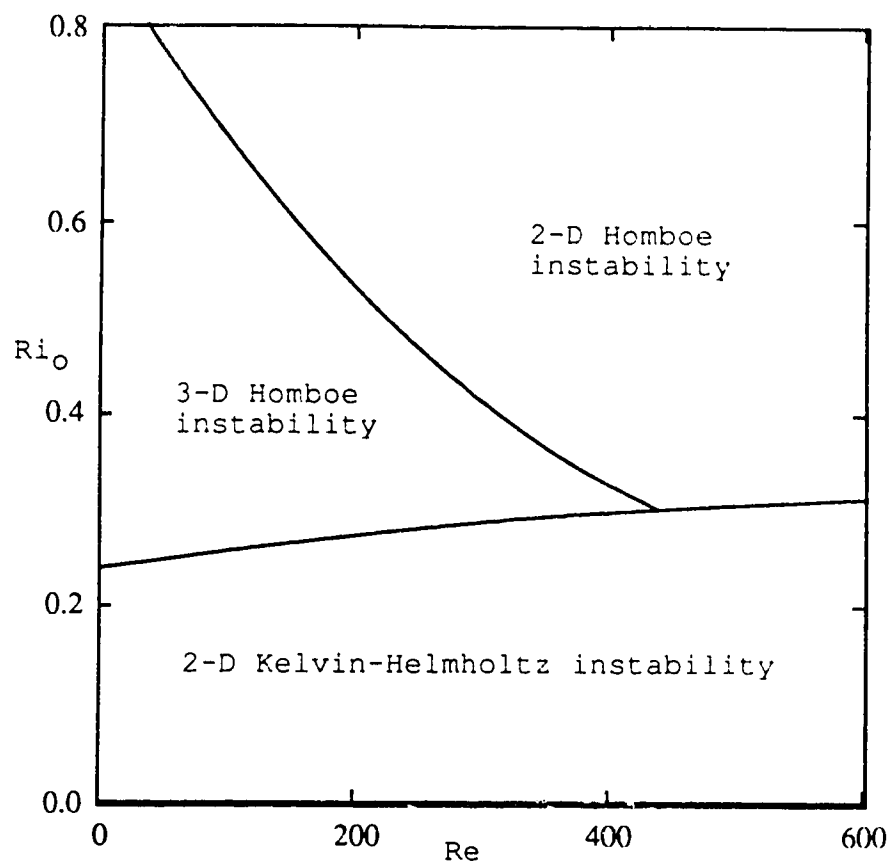


Figure 5.1 Adopted stability diagram of primary three-dimensional instability from Smyth & Peltier (1990). ($R=3.0$, $Pr=9.0$ case)

Fig. 9.4. Although this is intuitively somewhat suspicious, a possible explanation is that the flow tends to be more unstable due to the three-dimensional perturbations when Fig. 9.4.

Figure 5.1 illustrates some of the results obtained by Smyth & Peltier, and shows that when $Re=100$ (which was the case for models III and IV) three-dimensional instabilities can become the most unstable modes. Although their model employs a relatively large density transition thickness compared to the two layer model, the results indicate the necessity for further theoretical investigation to explore the possibility of three-dimensional primary instability. At the present time, we do not have enough evidence to verify the existence of three-dimensional primary instability, and further experimental and theoretical investigation is expected.

BIBLIOGRAPHY

- Abraham, G., M. Karelse and A.G. von Os (1979). On the magnitude of interfacial shear of subcritical stratified flows in relation with interfacial stability. *Journal of Hydraulic Research* **17**, 273-287.
- Arita, M. and G.H. Jirka (1987a). Two-layer model of saline wedge I: Entrainment and interfacial friction. *Journal of Hydraulic Engineering*. **113**, 1229-1247.
- Arita, M. and G.H. Jirka (1987b). Two-layer model of saline wedge II: Prediction of mean properties. *Journal of Hydraulic Engineering*. **113**, 1249-1263.
- Arita, M., G.H. Jirka and N. Tamai (1987). Classification and mixing of two-dimensional bouyant surface discharges. *Journal of Hydraulic Research*. **24**, 333-345.
- Atlas, D., J.I. Metcalf, J.H. Richter and E.E. Gossard (1970). The birth of 'CAT' and microscale turbulence. *Journal of the Atmospheric Sciences*. **27**, 903-913.
- Betchov, R. and W.O. Criminale (1967). 'Stability of parallel flows'. *Academic Press, London*.
- Browand, F.K. and Y.H. Wang (1972). An experimental study of the growth of small disturbances at the interface between two streams of different densities and velocities. *Proceedings of International Symposium on Stratified Flows, Novosibirsk*. 491-498.
- Browand, F.K. and C.D. Winant (1973). Laboratory observations of shear-layer instability in a stratified fluid. *Boundary Layer Meteorology*. **5**, 67-77.
- Davey, A. (1973). A simple numerical method for solving Orr-Sommerfeld problems. *Quaterly Journal of Mechanics and Applied Mathematics*, **26**, 401-411.
- Davey, A. (1977). On the numerical solution of difficult eigenvalue problems. *Journal of Computational Physics*. **24**, 331-338.
- Drazin, P.G. and L.N. Howard (1966). Hydrodynamic stability of parallel flow of inviscid fluids. *Advances in Applied Mechanics*. **9**, Academic Press. 1-89.
- Drazin, P.G. and W.H. Reid (1981). 'Hydrodynamic stability'. *Cambridge University Press*.

- Dronkers, J. & W.V. Leussen (1988). 'Physical Processes in Estuaries', Springer-Verlag, Berlin.
- Durst, F., A. Melling and J.H. Whitelaw (1981). 'Principles and practice of Laser-Doppler Anemometry'. Academic Press.
- Einaudi, F. and D.P. Lalas (1974). Some new properties of Kelvin-Helmholtz waves in an atmosphere with and without condensation effects. *Journal of the Atmospheric Sciences*. **31**, 1995-2007.
- Fjortoft, R. (1950). Application of integral theorems in deriving criteria of stability for laminar flows and for the baroclinic circular vortex. *Geofysiske Publikasjoner*. **17**(6), 1-52.
- Fua, D. and F. Einaudi (1984). On the effect of dissipation on shear instabilities in the stable atmospheric boundary layer. *Journal of the Atmospheric Sciences*. **41**, 888-900.
- Garrett, C. and W. Munk (1979). Internal waves in the ocean. *Annual Review of fluid Mechanics*. **11**, 339-369.
- Gersting, J.M.Jr. and D.F. Jankowski (1972). Numerical methods for Orr-Sommerfeld problems. *International Journal of numerical methods in Engineering*. **4**, 195-206.
- Goldstein, S. (1931). On the stability of superposed streams of fluids of different densities. *Proceedings of the Royal Society of London, A* **132**, 524-548.
- Gossard, E.E., D.R. Jensen and J.H. Richter (1971). An analytical study of tropospheric structure as seen by high-resolution radar. *Journal of the Atmospheric Sciences*. **28**, 794-807.
- Gossard, E.E. (1974). Dynamic stability of an isentropic shear layer in a statically stable medium. *Journal of the Atmospheric Sciences*. **31**, 483-492.
- Gotoh, K. (1971). Hydromagnetic instability of a free shear layer at small magnetic Reynolds number. *Journal of Fluid Mechanics*. **49**, 21-31.
- Grubert, J.P. (1980). Experiments on arrested saline wedge. *Journal of the Hydraulics Division, Proceedings of the American Society of Civil Engineers*. **106**, 945-960.
- Hayakawa, N. and T.E. Unny (1974). Viscous stability of parallel streams of superposed fluids. *The Physics of Fluids*. **17**, 879-882.

- Hazel, P. (1972). Numerical studies of the stability of inviscid stratified shear flows. *Journal of Fluid Mechanics*, **51**, 39-61.
- Helmholtz, H.von. (1868). Uber discontinuierliche Flussigkeitsbewegungen. *Monats. Konigl. Preuss. Akad. Wiss. Berlin*. **23**, 215-228. also *Wissenschaftliche Abhandlungen* (1882 J.A. Barth ed.), Leipzig, Vol. I, 146-157.: Translated into English by F. Guthrie as 'On discontinuous movements of fluids', *The London, Edinburge, and Dublin Philosophical Magazine and Journal of Science*. **36**, 337-346.
- Hino, M. and N.G. Hung (1982). The stability and interfacial waves of viscous-diffusive stratified two-layer flows. *Proceedings of the 26th Japanese Conference on Hydraulics*. 513-519. (in Japanese)
- Hino, M., K. Nadaoka and N.G. Hung (1984). Turbulent interfacial structure of two-layered stratified flows. 'Turbulence and Chaotic Phenomena in Fluids'. (T. Tatsumi Ed.) *IUTAM*, 489-494.
- Holmboe, J. (1962). On the behavior of symmetric waves in stratified shear layers. *Geofysiske Publikasjoner*. **24**, 67-113.
- Howard, L.N. and A. Maslowe (1973). Stability of stratified shear flows. *Boundary Layer Meteorology*. **4**, 511-523.
- Ippen, A.T. (1966). 'Estuary and Coastline Hydrodynamics'. McGraw Hill.
- Kaneko, Y. (1966). An example of the interfacial drag coefficient of two-layered flow. *Proceedings of 16th Japanese Conference on Coastal Engineering*. 263-267. (in Japanese).
- Kaplan, R.E. (1964). The stability of laminar incompressible boundary layers in the presence of compliant boundaries. *Aeroelastic and Structures Research Laboratory. Report No. ASRLTR 166-1 M.I.T.*
- Kelvin, L. (1871). Hydrokinetic solutions and observations. *The London, Edinburge, and Dublin Philosophical Magazine and Journal of Science*. **42**, 362-377.
- Keulegan, G. (1966). The mechanism of an arrested saline wedge. 'Estuary and Coastline Hydrodynamics'. Ch.11. A.T. Ippen Ed., McGraw Hill. 546-574.
- Koop, C.G. and F.K. Browand (1979). Instability and turbulence in a stratified fluid with shear. *Journal of Fluid Mechanics*, **93**, 135-159.

- Koppel, D. (1964). On the stability of flow of a thermally stratified fluid under the action of gravity. *Journal of Mathematical Physics*. **5**, 963-982.
- Lalas, D.P. and F. Einaudi (1976). On the characteristics of gravity waves generated by atmospheric shear layers. *Journal of the Atmospheric Sciences*. **33**, 1248-1259.
- Lalas, D.P., F. Einaudi and D. Fua (1976). The destabilizing effect of the ground on Kelvin-Helmholtz waves in the atmosphere. *Journal of the Atmospheric Sciences*. **33**, 59-69.
- Lawrence, G.A., F.K. Browand and L.G. Redkopp (1991). The stability of a sheared density interface. *The Physics of Fluids*. Oct. Vol.3(10) (in press)
- LeBlond, P.H. and L.A. Mysak (1978). 'Waves in the Ocean'. Elsevier Scientific Publishing.
- Lee, F.A. (1974). Hydrodynamical stability of salt wedge. *Journal of the Hydraulics Division, Proceedings of the American Society of Civil Engineers*. **100**, 17-24.
- Lessen, M. (1950). On stability of free laminar boundary layer between parallel streams, *NASA Report 979*, 571-573.
- Lindzen, R.S. (1976). Stability of Helmholtz velocity profile in a continuously stratified, infinite Boussinesq fluid: Application to clear air turbulence. *Journal of the Atmospheric Sciences*. **31**, 1507-1514.
- Lindzen, R.S. and J. Rosenthal (1976). On the instability of Helmholtz velocity profiles in stably stratified fluids when a lower boundary is present. *Journal of Geophysical Researches*. **81**, 1561-1571.
- Maslowe, S.A. and J.M. Thompson (1971). Stability of a stratified free shear layer. *The Physics of Fluids*. **14**, 453-458.
- Maxworthy, T. and F.K. Browand (1975). Experiments in stratified flows; Oceanographic application. *Annual Review of Fluid Mechanics*, **7**, 273-305.
- Metcalf, R.W., S.A. Orszag, M.E. Brachet, S. Menon and J.J. Riley (1987). Secondary instability of a temporally growing mixing layer. *Journal of Fluid Mechanics*. **184**, 207-243.

- Miller, J.R. and K.S. Gage (1972). Prandtl number dependence of the stability of a stratified free shear layer. *The Physics of Fluids*. **15**, 723-725.
- Nishida, S. and S. Yoshida (1984). Stability of a two-layer shear flow. *Proceedings of the 32nd Japan National Congress for Applied Mechanics*. University of Tokyo Press. **32**, 35-45.
- Nishida, S. and S. Yoshida (1987). Stability and eigenfunctions of disturbances in stratified two-layer shear flows. *Proceedings of Third International Symposium on Stratified Flows*.
- Nishida, S. and S. Yoshida (1990). Influence of the density and velocity profiles on calculated instability characteristics in an inviscid two-layer shear flow. *Journal of Hydrosience and Hydraulic Engineering*. **7**, 61-68.
- Officer, C.B. (1976). 'Physical Oceanography of Estuaries (and Associated Coastal Waters)', John Wiley & Sons Inc.
- Pedersen F.B. (1972). Gradually varying two-layer stratified flow. *Journal of the Hydraulics Division, Proceedings of the American Society of Civil Engineerings*. **98**, 257-268.
- Riethmuller, M.L. (1981). 'Laser Velocimetry', Von Karman Institute Lecture Series **1981-3**. Rhode Saint Genese Belgium.
- Sargent, F.E. and G.H. Jirka (1987). Experiments on saline wedge, *Journal of Hydraulic Engineering*. **113**(10), 1307-1324.
- Schijf, J.B. and J.C. Schonfeld (1953). The motion of salt and fresh water. *Proceedings Minesota International Hydraulics Convention, Joint Meeting of International Association for Hydraulic Research and Hydraulics Division of American Society of Civil Engineers*, 321-333.
- Squire, H.B. (1933). On the stability of three-dimensional disturbances of viscous flow between parallel walls. *Proceedings of the Royal Society of London, A* **142**, 621-628.
- Smyth, W.D. and W.R. Peltier (1989). The transition between Kelvin-Helmholtz and Holmboe instability; An investigation of the overreflection hypothesis. *Journal of the Atmospheric Sciences*. **46**(24), 3698-3720.
- Smyth, W.D. and W.R. Peltier (1990). Three-dimensional primary instabilities of a stratified, dissipative,

- parallel flow. *Geophysical and Astrophysical Fluid Dynamics*. **52**, 249-261.
- Tashiro, Y., S. Yoshida and M. Yoneya (1983). *Proceedings of the 27th Japanese Conference on Hydraulics*. 523-530 (in Japanese)
- Taylor, G.I. (1931). Effect of variation in density on the stability of superposed streams of fluids. *Proceedings of the Royal Society of London, A* **132**, 499-523.
- Thorpe, S.A. (1973). Turbulence in stratified fluids; A review of laboratory experiments. *Boundary Layer Meteorology*. **5**, 95-119.
- Tsubaki, T., M. Hamamura and M. Hashimoto (1969). On the statistical properties of internal waves formed at the interface of arrested saline wedges. *Proceedings of 13th Congress of IAHR*. **17**, 63-74.
- Woods, J.D. (1968). Wave-induced shear instability in the summer thermocline. *Journal of Fluid Mechanics*. **32**, 791-800.
- Yonemitsu, N. (1986). Hydrodynamic stability of the salt wedge and interfacial waves. *M.Sc. Thesis, Department of Applied Physics, University of Hokkaido, Japan*. (in Japanese)
- Yoshida, S. and M. Kashiwada (1988). Linear solution and experimental value of interfacial wave velocity in a two-layer flow. *Proceedings of the 32nd Japanese Conference on Hydraulics*. 173-177 (in Japanese)

**APPENDIX A: RELATIONSHIP BETWEEN REYNOLDS STRESS AND
PHASE CHANGE OF PERTURBATION VELOCITY \tilde{w} .**

in section 2.3, it was seen that the phase change of perturbation velocity \tilde{w} (i.e. $d\theta/dz$) is strongly related to the flow stability. In fact, the phase change $d\theta/dz$ represents the direction of the energy transfer between the mean flow and turbulence which is the same as Reynolds stress. In this appendix, it will be proven that $d\theta/dz$ and Reynolds stress are identical in the piece-wise linear velocity profile cases.

Let us consider the phase change of the perturbation velocity \tilde{w} , which is

$$\theta = \tan^{-1} \frac{\tilde{w}_I}{\tilde{w}_R} = \tan^{-1} \frac{\hat{w}_I}{\hat{w}_R} , \quad (\text{A.1})$$

where

$$\tilde{w} = \tilde{w}_R + i\tilde{w}_I \quad \text{and} \quad \hat{w} = \hat{w}_R + i\hat{w}_I .$$

Since the piece-wise linear velocity profile was employed in section 2, it can be seen that only $|z| < 1.0$ region contributes to the energy supply for the turbulence (see Figures 2. to 2.). Thus, $|z| < 1.0$ region will be investigated in the following part of this appendix.

The general form of the governing equation for this region may be written as,

$$\hat{w} = A \exp(\alpha z) + B \exp(-\alpha z) , \quad (\text{A.2})$$

where A and B are complex numbers and may be written as

$$A = A_R + iA_I \quad \text{and} \quad B = B_R + iB_I .$$

From equation (2.2.) the Reynolds stress is

$$\tau = \frac{i}{2\alpha} \exp(2\omega_i t) \operatorname{Im} \left(\hat{w}^* \frac{d\hat{w}}{dz} \right) . \quad (\text{A.3})$$

If the flow is unstable for $\alpha > 0.0$ cases, then

$$\tau > 0 ,$$

and

$$\exp(2\omega_i t) > 0 .$$

Therefore, the following relation has to be satisfied.

$$\operatorname{Im} \left(\hat{w}^* \frac{d\hat{w}}{dz} \right) > 0 . \quad (\text{A.4})$$

Substituting (A.), then

$$\begin{aligned} & \operatorname{Im} \left(\hat{w}^* \frac{d\hat{w}}{dz} \right) , \\ & = \operatorname{Im} \left(\alpha (A^* \exp(\alpha z) + B^* \exp(-\alpha z)) (A \exp(\alpha z) - B \exp(-\alpha z)) \right) , \\ & = \operatorname{Im} \left(\alpha (|A|^2 \exp(2\alpha z) - |B|^2 \exp(-2\alpha z)) + \alpha A B^* - \alpha A^* B \right) , \\ & = \operatorname{Im} \left(\alpha (A B^*) - \alpha (A B^*)^* \right) , \\ & = \operatorname{Im} \left(2i\alpha \operatorname{Im} (A B^*) \right) , \\ & = 2\alpha \operatorname{Im} (A B^*) , \\ & > 0 . \end{aligned} \quad (\text{A.5})$$

Therefore, the condition for instability becomes

$$\operatorname{Im} (A B^*) > 0 . \quad (\text{A.6})$$

However, from (A.), we know

$$A = A_R + iA_I \quad \text{and} \quad B^* = B_R - iB_I ,$$

then

$$\text{Im} (AB^*) = A_i B_{iR} - A_i B_{iI} > 0 \quad . \quad (\text{A.7})$$

Thus the condition may be written as

$$A_i B_{iR} > A_i B_{iI} \quad . \quad (\text{A.8})$$

Analysis of the perturbation quantity profiles showed that if $d\theta/dz > 0$ was satisfied, then $C_i > 0$ was found. It implies that some relationship between $d\theta/dz$ and Reynolds stress τ exists. Let us consider the condition for $d\theta/dz$ in the followings. From (A.1),

$$\theta = \tan^{-1} \frac{\widehat{w}_i}{\widehat{w}_R} \quad ,$$

then

$$\begin{aligned} \frac{d\theta}{dz} &= \frac{1}{1 + \left(\frac{\widehat{w}_i}{\widehat{w}_R}\right)^2} \cdot \frac{d}{dz} \left(\frac{\widehat{w}_i}{\widehat{w}_R}\right) \quad , \\ &= \frac{\widehat{w}_R \frac{d\widehat{w}_i}{dz} - \widehat{w}_i \frac{d\widehat{w}_R}{dz}}{|\widehat{w}|^2} > 0 \quad . \end{aligned} \quad (\text{A.9})$$

Thus, the condition may be written as

$$\widehat{w}_R \frac{d\widehat{w}_i}{dz} > \widehat{w}_i \frac{d\widehat{w}_R}{dz} \quad , \quad (\text{A.10})$$

but

$$\widehat{w} = A \exp(\alpha z) + B \exp(-\alpha z) \quad .$$

Then the relationship (A.) may be rewritten as

$$\alpha (A_R \exp(\alpha z) + B_R \exp(-\alpha z)) (A_I \exp(\alpha z) - B_I \exp(-\alpha z)) > \alpha (A_I \exp(\alpha z) + B_I \exp(-\alpha z)) (A_R \exp(\alpha z) - B_R \exp(-\alpha z)) , \quad (A.11)$$

then

$$-A_R B_I + A_I B_R > -A_I B_R + A_R B_I . \quad (A.12)$$

Therefore

$$A_I B_R > A_R B_I . \quad (A.13)$$

This condition is exactly the same expression as (A.8) which implies that $\tau > 0$ and $C_i > 0$. Hence it may be concluded that

$$\frac{d\theta}{dz} > 0 \quad \leftrightarrow \quad \tau > 0 \text{ and } C_i > 0 . \quad (A.14) .$$

APPENDIX B: COMPUTER PROGRAMS

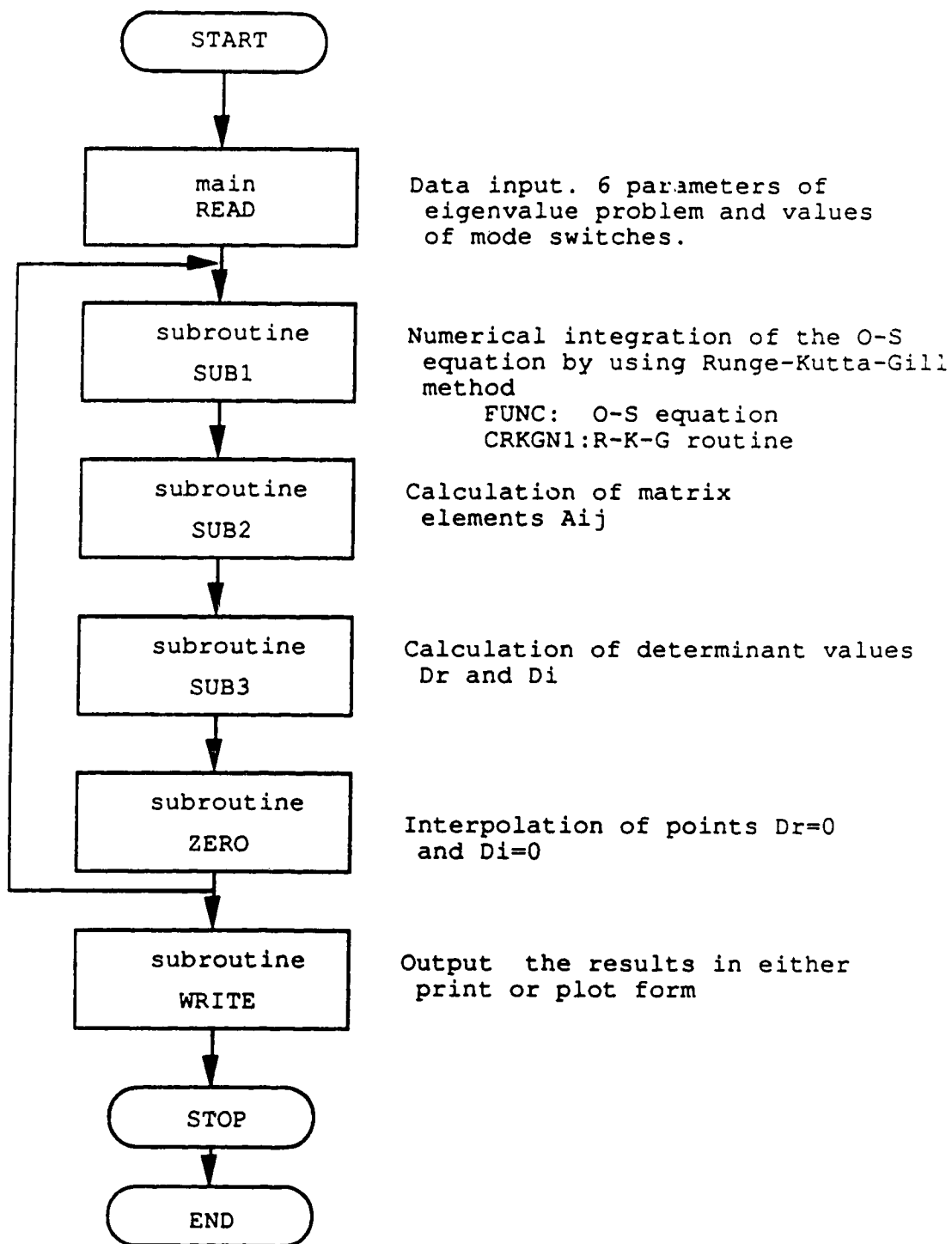
In this section, the computer programs which were used in part three are presented. Flow charts are attached in front of each program and the symbols utilized in the programs are defined as follows.

<Symbols in the programs>

A	Eigen matrix A_{ij}
C, CR, CI	Complex phase velocity c and its real and imaginary part
ENE	Turbulent kinetic energy
ETA, ABSETA, ARGETA	Interfacial displacement η and its amplitude and phase
F, DF, D2F, D3F	The stream function $\hat{\phi}_i$ and their derivatives
FIN	Solution Φ_{i1}
FVI	Solution Φ_{i2}
GAMMA	Relative density γ
GR	Growth rate of perturbation = αc_i
ND(1), ND(2)	Step intervals of modification of solutions
NX(1), NX(2)	Number of integration steps in upper and lower layer
RE(1), RE(2)	Reynolds numbers of upper and lower layer
RI	Richardson number

S	Non-dimensional interfacial tension
TAU	Reynolds stress averaged over wave length
UO, ABSUO, ARGUO	Perturbation velocity \tilde{u} and its amplitude and phase
V(1), V(2)	Characteristic velocities for the mean velocity profile (i.e. $U_0 = V(i) \tanh(z)$)
VO, ABSVO, ARGVO	Perturbation velocity \tilde{w} and its amplitude
W, DW, D2W, D3W	Solution vector at $z=0$ and its derivatives
WN	Wave number α
ZR(1), ZR(2)	Upper and lower boundary values of integration i.e. $-ZR(2) \leq Z \leq ZR(1)$

These programs are designed to calculate the eigenvalues for the bounded (THIC.FOR) case and the displaced velocity profile case (SHIFT.FOR). They have two modes of calculation. In mode 1, the wave number α is fixed and points are plotted where the determinant $D_R=0$ and $D_I=0$ on C_R-C_I plane. In mode 2, C_I is fixed and points are plotted on $\alpha-C_R$ plane. The programs "THIC.FOR" and "SHIFT.FOR" are exactly the same except for the velocity profile which is calculated in the complex function "FUNC". Thus, only the flow chart and program for "THIC.FOR" are presented here.



```

C*****
C          PROGRAM THIC.FORT2 (DOUBLE PRECISION)
C*****
      IMPLICIT REAL*8 (A-H,O-Z)
      COMPLEX*16 C,W,DW,D2W,D3W,A,DET1,DET2

      COMMON /BL1/ V,WN,C,RE /BL2/ GAMMA,RI,S /BL5/
      |          ZR,NX,ND,NPLOT
      |          /BL40/ WNS,WNE,CRS,CRE,CIS,CIE,ITAG
      DIMENSION V(2),RE(2),ZR(2),NX(2),ND(2),
      |          W(2,2),DW(2,2),D2W(2,2),D3W(2,2),A(4,4),
      |          DETR(21,21,21),DETI(21,21,21),
      |          AWN(21),ACR(21),ACI(21)

      READ(5,100) WNS,WNE,NWN,
      |          CRS,CRE,NCR,
      |          CIS,CIE,NCI,
      |          V(1),RE(1),ZR(1),NX(1),ND(1),
      |          V(2),RE(2),ZR(2),NX(2),ND(2),
      |          GAMMA,RI,S,
      |          NN,NPLOT,ITAG
      NTOTAL=(NWN+1)*(NCR+1)*(NCI+1)
      IF (ITAG .EQ. 1) GOTO 111
      WRITE(6,200) V(1),RE(1),ZR(1),NX(1),ND(1),
      |          V(2),RE(2),ZR(2),NX(2),ND(2),
      |          GAMMA,RI,S,NTOTAL
      WRITE(6,300)
111 DO 10 N1=1,NWN+1
      IF (NWN .EQ. 0) GOTO 1
      WN=WNS+(WNE-WNS)*DFLOAT(N1-1)/DFLOAT(NWN)
      GOTO 2
      1 WN=WNS
      2 CONTINUE
      AWN(N1)=WN
      IF (ITAG .EQ. 1) GOTO 112
      WRITE(6,400)
112 DO 10 N2=1,NCR+1
      IF (NCR .EQ. 0) GOTO 3
      CR=CRS+(CRE-CRS)*DFLOAT(N2-1)/DFLOAT(NCR)
      GOTO 4
      3 CR=CRS
      4 CONTINUE
      ACR(N2)=CR
      DO 10 N3=1,NCI+1
      IF (NCI .EQ. 0) GOTO 5
      CI=CIS+(CIE-CIS)*DFLOAT(N3-1)/DFLOAT(NCI)
      GOTO 6
      5 CI=CIS
      6 CONTINUE
      ACI(N3)=CI
      C=CR+(0.0D0,1.0D0)*CI
      GR=WN*CI

```



```

IF (CDABS(C) .EQ. 0.0D0) GOTO 7

CALL SUB1(ZR,NX,ND,W,DW,D2W,D3W)
CALL SUB2(W,DW,D2W,D3W,A)
CALL SUB3(A,DET1,ADET1,DET2,ADET2,AGAP,NSTOP)

IF (ITAG .EQ. 1) GOTO 113
WRITE(6,500) WN,CR,CI,GR,DET1,ADET1,DET2,ADET2,AGAP,
! NSTOP
113 GOTO 8
7 CONTINUE
IF (ITAG .EQ. 1) GOTO 8
WRITE(6,600) WN,CR,CI,GR
8 CONTINUE
IF (NN .NE. 0 .AND. NN .NE. 1) GOTO 10
IF (NN .EQ. 1) GOTO 9
DEIR(N3,N2,N1)=DIMAG((0.0D0,1.0D0)*DET1)
DETI(N3,N2,N1)=DIMAG(DET1)
GOTO 10
9 CONTINUE
DETR(N1,N2,N3)=DIMAG((0.0D0,1.0D0)*DET1)
DETI(N1,N2,N3)=DIMAG(DET1)
10 CONTINUE

IF (NN .NE. 0 .AND. NN .NE. 1) GOTO 30
IF (NN .EQ. 1) GOTO 20
CALL ZERO(NN,DETR,DETI,ACI,ACR,AWN,NCI+1,NCR+1,NWN+1)
GOTO 30
20 CONTINUE
CALL ZERO(NN,DETR,DETI,AWN,ACR,ACI,NWN+1,NCR+1,NCI+1)
30 CONTINUE

100 FORMAT(3(2F10.4,I5/),2(2F10.4,F5.1,2I5/),3F10.4/,3I5)
200 FORMAT(1H1//,11X,'U1=',F6.3,'DTANH(Y)',10X,'RE(1)=',
| F6.1,10X,'ZR(1)=',F5.1,5X,'NX(1)=',I4,5X,
| 'ND(1)=',I4//,11X,'U2=',F6.3,'DTANH(Y)',10X,
| 'RE(2)=',F6.1,10X,'ZR(2)=',F5.1,5X,'NX(2)=',
| I4,5X,'ND(2)=',I4//,11X,'GAMMA=',F6.3,10X,'RI=',
| F6.2,10X,'S=',F7.2,10X,'NTOTAL=',I4//)
300 FORMAT(1H ,8X,'(WN,CR,CI,GR)',11X,
| 'NORMALIZED DETERMINANT DET1',4X,'|DET1|',5X,
| 'ORIGINAL DETERMINANT DET2',5X,'|DET2|',4X,
| 'ELEMENT GAP',2X,'NS'//)
400 FORMAT(1H )
500 FORMAT(1H , '( ',F6.3,', ',F6.3,', ',F6.3,', ',F7.4,') ',3X,
| '( ',E11.4,', ',E11.4,') ',2X,E11.4,3X,'( ',E11.4,
| ', ',E11.4,') ',2X,E11.4,3X,E9.2,2X,I2)
600 FORMAT(1H , '( ',F6.3,', ',F6.3,', ',F6.3,', ',F7.4,') ',3X,
| '( * * * ) ',2X,' * ',3X,
| ' * ',2X,' * ')

STOP
END

```

```

C*****
SUBROUTINE SUB1 (ZR, NX, ND, W, DW, D2W, D3W)
C*****

  IMPLICIT REAL*8 (A-H, O-Z)
  COMPLEX*16    C, P1, P2, FUNC, F0, G, FVI, FIN,
  |             W, DW, D2W, D3W,
  |             COEF1, COEF2, COEF

  COMMON /BL1/ V, WN, C, RE /BL3/ N
  DIMENSION V(2), RE(2), ZR(2), NX(2), ND(2), F0(4), G(4, 13),
  |         FVI(4, 601), FIN(4, 601),
  |         W(2, 2), DW(2, 2), D2W(2, 2), D3W(2, 2)
  EXTERNAL FUNC

  DO 10 N=1, 2
    SIGN=(-1.0D0)**N
    Z0=-DABS(ZR(N))*SIGN
    LX=NX(N)
    LD=ND(N)
    H=-Z0/DFLOAT(LX-1)
    P1=SIGN*CDSQRT(WN*WN-2.0D0*V(N)*DTANH(Z0)*(1.0D0-
  |   DTANH(Z0)*DTANH(Z0))/(V(N)*DTANH(Z0)-C))
    P2=SIGN*CDSQRT(WN*WN+(0.0D0, 1.0D0)*WN*RE(N)*(V(N)
  |   *DTANH(Z0)-C))
    IF (V(N) .EQ. 0.0D0) GOTO 100
  C   F0(1)=CDEXP(P2*Z0)
    F0(1)=0.0D0
  C   F0(2)=P2*CDEXP(P2*Z0)
    F0(2)=0.0D0
  C   F0(3)=P2*P2*CDEXP(P2*Z0)
    F0(3)=0.0D0
  C   F0(4)=P2*P2*P2*CDEXP(P2*Z0)
    F0(4)=1.0D0
    CALL CRKGN1(FUNC, Z0, F0, 4, H, C, FVI, LX, 4)
    W(N, 2)=FVI(1, LX)
    DW(N, 2)=FVI(2, LX)
    D2W(N, 2)=FVI(3, LX)
    D3W(N, 2)=FVI(4, LX)

  C   F0(1)=CDEXP(P1*Z0)
    F0(1)=0.0D0
  C   F0(2)=P1*CDEXP(P1*Z0)
    F0(2)=0.0D0
  C   F0(3)=P1*P1*CDEXP(P1*Z0)
    F0(3)=1.0D0
  C   F0(4)=P1*P1*P1*CDEXP(P1*Z0)
    F0(4)=0.0D0
    MX=LD+1
    IF (MX .GE. LX) GOTO 30
    DO 20 I=LD+1, LX-1, LD
      M=I
      CALL CRKGN1(FUNC, Z0, F0, 4, H, G, FIN, MX, 4)

```

```

      Z0=Z0+DFLOAT(LD)*H
      P1=SIGN*CDSQRT(WN*WN-2.0D0*V(N)*DTANH(Z0))*(1.0D0-
|      DTANH(Z0)*DTANH(Z0))/(V(N)*DTANH(Z0)-C)
      P2=SIGN*CDSQRT(WN*WN+(0.0D0,1.0D0)*WN*RE(N))*(V(N)
|      *DTANH(Z0)-C)
C      COEF1=FIN(4,MX)+P2*FIN(3,MX)-P1*P1*FIN(2,MX)-P1*P1*P2*
C      |      FIN(1,MX)
      COEF1=FIN(1,MX)*DCONJG(FVI(1,M))+FIN(2,MX)
|      *DCONJG(FVI(2,M))+FIN(3,MX)*DCONJG(FVI(3,M))
|      +FIN(4,MX)*DCONJG(FVI(4,M))
C      COEF2=FVI(4,M)+P2*FVI(3,M)-P1*P1*FVI(2,M)-P1*P1*P2*
C      |      FVI(1,M)
      COEF2=FVI(1,M)*DCONJG(FVI(1,M))+FVI(2,M)
|      *DCONJG(FVI(2,M))+FVI(3,M)*DCONJG(FVI(3,M))
|      +FVI(4,M)*DCONJG(FVI(4,M))
      COEF=COEF1/COEF2
      F0(1)=FIN(1,MX)-COEF*FVI(1,M)
      F0(2)=FIN(2,MX)-COEF*FVI(2,M)
      F0(3)=FIN(3,MX)-COEF*FVI(3,M)
      F0(4)=FIN(4,MX)-COEF*FVI(4,M)
20  CONTINUE
      MX=LX-M+1
      GOTO 40
30  MX=LX
40  CALL CRKGN1(FUNC,Z0,F0,4,H,G,FIN,MX,4)
      W(N,1)=FIN(1,MX)
      DW(N,1)=FIN(2,MX)
      D2W(N,1)=FIN(3,MX)
      D3W(N,1)=FIN(4,MX)
      GOTO 10

100 W(N,2)=1.0D0
      DW(N,2)=P2
      D2W(N,2)=P2*P2
      D3W(N,2)=P2*P2*P2
      W(N,1)=1.0D0
      DW(N,1)=P1
      D2W(N,1)=P1*P1
      D3W(N,1)=P1*P1*P1

10  CONTINUE

      RETURN
      END

```

```

C*****
      COMPLEX FUNCTION FUNC(K,Z,F)
C*****

      IMPLICIT REAL*8(A-H,O-Z)
      COMPLEX*16  C,F

```

```

COMMON /BL1/ V,WN,C,RE /BL3/ N
DIMENSION F(4),V(2),RE(2)

GOTO (1,2,3,4),K
1 FUNC=F(2)
GOTO 10
2 FUNC=F(3)
GOTO 10
3 FUNC=F(4)
GOTO 10
4 FUNC=(2.0D0*WN*WN+(0.0D0,1.0D0)*WN*RE(N)
| *(V(N)*DTANH(Z)-C))*F(3)-(WN**4+(0.0D0,1.0D0)
| *WN*RE(N)*(WN*WN*(V(N)*DTANH(Z)-C)-2.0D0*V(N)
| *DTANH(Z)*(1.0D0-DTANH(Z)*DTANH(Z))))*F(1)
10 RETURN
END

```

```

C*****
SUBROUTINE CRKGN1(FUNC,X0,Y0,N,H,F,Y4,NX,NR)
C N-TH ORDER DIFERENTIALL EQUATION (RUNGE-KUTTA-GILL)
C*****

```

```

IMPLICIT REAL*8(A-H,O-Z)
COMPLEX*16 FUNC,Y0,F,Y4

DIMENSION Y0(N),Y4(NR,NX),F(NR,13)

IF(N.LE.0.OR.N.GT.NR)GOTO 80
CR2I=1.0D0-DSQRT(0.5D0)
DO 10 K=1,N
F(K,1)=0.0D0
Y4(K,1)=Y0(K)
10 F(K,2)=Y0(K)
I=1
20 X=X0+(DFLOAT(I-1))*H
DO 30 K=1,N
F(K,3)=H*FUNC(K,X,F(1,2))
F(K,4)=0.5D0*F(K,3)-F(K,1)
F(K,5)=F(K,2)+F(K,4)
30 F(K,6)=F(K,1)+3.0D0*F(K,4)-0.5D0*F(K,3)
DO 40 K=1,N
F(K,7)=H*FUNC(K,X+0.5D0*H,F(1,5))
F(K,8)=CR2I*(F(K,7)-F(K,6))
F(K,9)=F(K,5)+F(K,8)
40 F(K,10)=F(K,6)+3.0D0*F(K,4)-CR2I*F(K,7)
DO 50 K=1,N
F(K,11)=H*FUNC(K,X+0.5D0*H,F(1,8))
F(K,12)=(2.0D0-CR2I)*(F(K,11)-F(K,10))
F(K,13)=F(K,9)+F(K,12)
50 F(K,12)=F(K,9)+3.0D0*F(K,4)-(2.0D0-CR2I)*F(K,11)
DO 60 K=1,N
F(K,13)=H*FUNC(K,X+H,F(1,11))
60

```

```

      F(K,4)=(F(K,13)-2.0D0*F(K,12))/6.0D0
      F(K,2)=F(K,11)+F(K,4)
      Y4(K,I+1)=F(K,2)
60   F(K,1)=F(K,12)+3.0D0*F(K,4)-0.5D0*F(K,13)
      I=I+1
      IF (NX-I)70,70,20
80   WRITE(6,100) N,NR
100  FORMAT('0(SUBR.CRKGN1) N=',I3,', NR=',I3,
|         ', N SHOULD BE A POSITIVE INTEGER LESS THAN
|         OR EQUAL TO NR.  RETURNED WITH NO CALCULATION.'
|         //)
70   RETURN
      END

```

```

C*****
      SUBROUTINE SUB2(W,DW,D2W,D3W,A)
C*****

      IMPLICIT REAL*8(A-H,O-Z)
      COMPLEX*16   C,A10,A20,B11,B21,B10,B20,
|                C12,C22,C10,C20,
|                D13,D23,D11,D21,D10,D20,
|                A,W,DW,D2W,D3W

      COMMON      /BL1/ V,WN,C,RE /BL2/ GAMMA,RI,S
      DIMENSION  V(2),RE(2),A(4,4),W(2,2),DW(2,2),
|                D2W(2,2),D3W(2,2)

      A10=1.0D0
      A20=1.0D0
      B11=-C
      B21=-C
      B10=-V(1)
      B20=-V(2)
      C12=-C*GAMMA*RE(2)
      C22=-C*RE(1)
      C10=-WN*WN*C*GAMMA*RE(2)
      C20=-WN*WN*C*RE(1)
      D13=- (0.0D0,1.0D0) *C*GAMMA*RE(2)/WN
      D23=- (0.0D0,1.0D0) *C*RE(1)/WN
      D11=C*GAMMA*(C*RE(1)*RE(2)+(0.0D0,3.0D0)*WN*RE(2))
      D21=C*(C*RE(1)*RE(2)+(0.0D0,3.0D0)*WN*RE(1))
      D10=(C*GAMMA*V(1)+RI)*RE(1)*RE(2)
      D20=(C*V(2)-WN*WN*S)*RE(1)*RE(2)
      A(1,1)=A10*W(1,1)
      A(1,2)=A10*W(1,2)
      A(1,3)=-A20*W(2,1)
      A(1,4)=-A20*W(2,2)
      A(2,1)=B11*DW(1,1)+B10*W(1,1)
      A(2,2)=B11*DW(1,2)+B10*W(1,2)
      A(2,3)=-B21*DW(2,1)-B20*W(2,1)
      A(2,4)=-B21*DW(2,2)-B20*W(2,2)

```

```

A(3,1)=C12*D2W(1,1)+C10*W(1,1)
A(3,2)=C12*D2W(1,2)+C10*W(1,2)
A(3,3)=-C22*D2W(2,1)-C20*W(2,1)
A(3,4)=-C22*D2W(2,2)-C20*W(2,2)
A(4,1)=D13*D3W(1,1)+D11*DW(1,1)+D10*W(1,1)
A(4,2)=D13*D3W(1,2)+D11*DW(1,2)+D10*W(1,2)
A(4,3)=-D23*D3W(2,1)-D21*DW(2,1)-D20*W(2,1)
A(4,4)=-D23*D3W(2,2)-D21*DW(2,2)-D20*W(2,2)

```

```

RETURN
END

```

```

C*****
SUBROUTINE SUB3(A,DET1,ADET1,DET2,ADET2,AGAP,NSTOP)
C*****

IMPLICIT REAL*8(A-H,O-Z)
COMPLEX*16 A,DET1,DET2,WA,B

DIMENSION A(4,4),AMXJ(4),AMXI(4),AMNJ(4),WA(24),WK(4),
| B(4)

DO 10 J=1,4
AMXJ(J)=DMAX1(CDABS(A(1,J)),CDABS(A(2,J)),
| CDABS(A(3,J)),CDABS(A(4,J)))
AMNJ(J)=DMIN1(CDABS(A(1,J)),CDABS(A(2,J)),
| CDABS(A(3,J)),CDABS(A(4,J)))
DO 20 II=1,4
A(II,J)=A(II,J)/AMXJ(J)
20 CONTINUE
10 CONTINUE
DO 30 I=1,4
AMXI(I)=DMAX1(CDABS(A(I,1)),CDABS(A(I,2)),
| CDABS(A(I,3)),CDABS(A(I,4)))
DO 40 JJ=1,4
A(I,JJ)=A(I,JJ)/AMXI(I)
40 CONTINUE
30 CONTINUE

C DO 554 IJ=1,4
C B(IJ)=(1.0D0,0.0D0)
C 554 CONTINUE
C IAA=4
C IBB=4
C NNN=4
C IMM=1
C IJOB=1
C
C CALL LEQ2C(A,NNN,IAA,B,IMM,IBB,IJOB,WA,WK,NSTOP)
C
C DET1=(1.0D0,0.0D0)
C DO 555 JI=1,NNN

```

```

C      IPVT=WK(JI)
C      IF (IPVT .NE. JI) DET1=-DET1
CC     INDX=JI+(JI-1)*NNN
C      DET1=DET1*WA(INDX)
C 555 CONTINUE

```

```

      DET1=A(1,1)*(A(2,2)*A(3,3)*A(4,4)+A(2,3)*A(3,4)*A(4,2)
|      +A(2,4)*A(3,2)*A(4,3)-A(2,4)*A(3,3)*A(4,3)
|      -A(2,3)*A(3,2)*A(4,4)-A(2,2)*A(3,4)*A(4,3))
|      -A(2,1)*(A(1,2)*A(3,3)*A(4,4)+A(1,3)*A(3,4)
|      *A(4,2)
|      +A(1,4)*A(3,2)*A(4,3)-A(1,4)*A(3,3)*A(4,2)
|      -A(1,3)*A(3,2)*A(4,4)-A(1,2)*A(3,4)*A(4,3))
|      +A(3,1)*(A(1,2)*A(2,3)*A(4,4)+A(1,3)*A(2,4)
|      *A(4,2)
|      +A(1,4)*A(2,2)*A(4,3)-A(1,4)*A(2,3)*A(4,2)
|      -A(1,3)*A(2,2)*A(4,4)-A(1,2)*A(2,4)*A(4,3))
|      -A(4,1)*(A(1,2)*A(2,3)*A(3,4)+A(1,3)*A(2,4)
|      *A(3,2)
|      +A(1,4)*A(2,2)*A(3,3)-A(1,4)*A(2,3)*A(3,2)
|      -A(1,2)*A(2,4)*A(3,3)-A(1,3)*A(2,2)*A(3,4))

```

```

      ADET1=CDABS(DET1)
      DET2=AMXJ(1)*AMXJ(2)*AMXJ(3)*AMXJ(4)*
|      AMXI(1)*AMXI(2)*AMXI(3)*AMXI(4)*DET1
      ADET2=CDABS(DET2)
      AMX=DMAX1(AMXJ(1),AMXJ(2),AMXJ(3),AMXJ(4))
      AMN=DMIN1(AMNJ(1),AMNJ(2),AMNJ(3),AMNJ(4))
      AGAP=AMX/AMN
      RETURN
      END

```

```

C*****
C      SUBROUTINE ZERO(NN,FR,FI,X1,X2,X3,M1,M2,M3)
C*****

```

```

      IMPLICIT REAL*8(A-H,O-Z)
      COMMON /BL4/ X10R,X20R,X30R,X10I,X20I,X30I,
|      SGR,SGI,J,K,L,M
      DIMENSION FR(21,21,21),FI(21,21,21),X1(21),X2(21),
|      X3(21),X10R(2,21,450),X20R(2,21,450),
|      X30R(2,21,450),X10I(2,21,450),X20I(2,21,450),
|      X30I(2,21,450),SGR(2,21,450),SGI(2,21,450),
|      J(21),K(21),L(21),M(21)

```

```

      DO 10 I1=1,M1
      JJ=0
      KK=0
      LL=0
      MM=0
      IF (M3 .LE. 1) GOTO 26

```

```

DO 20 I2=1,M2
DO 20 I3=1,M3-1
IF (FR(I1,I2,I3)*FR(I1,I2,I3+1)) 12,12,11
12 JJ=JJ+1
IF (FR(I1,I2,I3) .NE. 0.0D0 .AND.
| FR(I1,I2,I3+1) .NE. 0.0D0) GOTO 8
GRD=0.0D0
X3OR(1,I1,JJ)=0.5D0*(X3(I3+1)+X3(I3))
GOTO 9
8 GRD=(X3(I3+1)-X3(I3))/(FR(I1,I2,I3+1)-FR(I1,I2,I3))
X3OR(1,I1,JJ)=X3(I3)-GRD*FR(I1,I2,I3)
9 X1OR(1,I1,JJ)=X1(I1)
X2OR(1,I1,JJ)=X2(I2)
IF (GRD) 13,14,15
13 SGR(1,I1,JJ)=-1.0D0
GOTO 11
14 SGR(1,I1,JJ)=0.0D0
GOTO 11
15 SGR(1,I1,JJ)=1.0D0
11 CONTINUE

IF (FI(I1,I2,I3)*FI(I1,I2,I3+1)) 22,22,21
22 KK=KK+1
IF (FI(I1,I2,I3) .NE. 0.0D0 .AND.
| FI(I1,I2,I3+1) .NE. 0.0D0) GOTO 18
GRD=0.0D0
X3OI(1,I1,KK)=0.5D0*(X3(I3+1)+X3(I3))
GOTO 19
18 GRD=(X3(I3+1)-X3(I3))/(FI(I1,I2,I3+1)-FI(I1,I2,I3))
X3OI(1,I1,KK)=X3(I3)-GRD*FI(I1,I2,I3)
19 X1OI(1,I1,KK)=X1(I1)
X2OI(1,I1,KK)=X2(I2)
IF (GRD) 23,24,25
23 SGI(1,I1,KK)=-1.0D0
GOTO 21
24 SGI(1,I1,KK)=0.0D0
GOTO 21
25 SGI(1,I1,KK)=1.0D0
21 CONTINUE
20 CONTINUE

26 IF (M2 .LE. 1) GOTO 10
DO 30 I3=1,M3
DO 30 I2=1,M2-1
IF (FR(I1,I2,I3)*FR(I1,I2+1,I3)) 32,32,31
32 LL=LL+1
IF (FR(I1,I2,I3) .NE. 0.0D0 .AND.
| FR(I1,I2+1,I3) .NE. 0.0D0) GOTO 28
GRD=0.0D0
X2OR(2,I1,LL)=0.5D0*(X2(I2+1)+X2(I2))
GOTO 29
28 GRD=(X2(I2+1)-X2(I2))/(FR(I1,I2+1,I3)-FR(I1,I2,I3))
X2OR(2,I1,LL)=X2(I2)-GRD*FR(I1,I2,I3)
29 X1OR(2,I1,LL)=X1(I1)

```



```

      X30R(2,I1,LL)=X3(I3)
      IF (GRD) 33,34,35
33  SGR(2,I1,LL)=-1.0D0
      GOTO 31
34  SGR(2,I1,LL)=0.0D0
      GOTO 31
35  SGR(2,I1,LL)=1.0D0
31  CONTINUE

      IF (FI(I1,I2,I3)*FI(I1,I2+1,I3)) 42,42,41
42  MM=MM+1
      IF (FI(I1,I2,I3) .NE. 0.0D0 .AND.
      |      FI(I1,I2+1,I3) .NE. 0.0D0) GOTO 38
      GRD=0.0D0
      X20I(2,I1,MM)=0.5D0*(X2(I2+1)+X2(I2))
      GOTO 39
38  GRD=(X2(I2+1)-X2(I2))/(FI(I1,I2+1,I3)-FI(I1,I2,I3))
      X20I(2,I1,MM)=X2(I2)-GRD*FI(I1,I2,I3)
39  X10I(2,I1,MM)=X1(I1)
      X30I(2,I1,MM)=X3(I3)
      IF (GRD) 43,44,45
43  SGI(2,I1,MM)=-1.0D0
      GOTO 41
44  SGI(2,I1,MM)=0.0D0
      GOTO 41
45  SGI(2,I1,MM)=1.0D0
41  CONTINUE
30  CONTINUE

      J(I1)=JJ
      K(I1)=KK
      L(I1)=LL
      M(I1)=MM
10  CONTINUE

      CALL WRITE(NN,M1)

      RETURN
      END

```

```

C*****
      SUBROUTINE WRITE(NN,M1)
C*****

      IMPLICIT REAL*8(A-H,O-Z)
      COMPLEX*16 C

      COMMON      /BL4/ X10R,X20R,X30R,X10I,X20I,X30I,
      |              SGR,SGI,J,K,L,M
      |              /BL40/ WNS,WNE,CRS,CRE,CIS,CIE,ITAG
      |              /BL1/ V,WN,C,RE /BL2/ GAMMA,RI,S
      |              /BL5/ ZR,NX,ND,NPLOT

```

```

DIMENSION X10R(2,21,450),X20R(2,21,450),X30R(2,21,450),
|         X10I(2,21,450),X20I(2,21,450),X30I(2,21,450),
|         SGR(2,21,450),SGI(2,21,450),RE(2),
|         J(21),K(21),L(21),M(21),ZR(2),NX(2),ND(2)

```

```

IF (ITAG .EQ. 1) GOTO 135
DO 50 JJ=1,M1

```

```

WRITE(6,100)
DO 60 II=1,2
GOTO (61,62),II
61 JL=J(JJ)
GOTO 63
62 JL=L(JJ)
63 CONTINUE
IF (JL .EQ. 0) GOTO 64
IF (NN .EQ. 1) GOTO 65
WRITE(6,200) (X30R(II,JJ,KK),X20R(II,JJ,KK),
|             X10R(II,JJ,KK),SGR(II,JJ,KK),KK=1,JL)
GOTO 66
65 WRITE(6,200) (X10R(II,JJ,KK),X20R(II,JJ,KK),
|             X30R(II,JJ,KK),SGR(II,JJ,KK),KK=1,JL)
GOTO 66
64 WRITE(6,300)
66 WRITE(6,400)
60 CONTINUE

```

```

WRITE(6,500)
DO 80 II=1,2
GOTO (81,82),II
81 KM=K(JJ)
GOTO 83
82 KM=M(JJ)
83 CONTINUE
IF (KM .EQ. 0) GOTO 84
IF (NN .EQ. 1) GOTO 85
WRITE(6,200) (X30I(II,JJ,KK),X20I(II,JJ,KK),
|             X10I(II,JJ,KK),SGI(II,JJ,KK),KK=1,KM)
GOTO 86
85 WRITE(6,200) (X10I(II,JJ,KK),X20I(II,JJ,KK),
|             X30I(II,JJ,KK),SGI(II,JJ,KK),KK=1,KM)
GOTO 86
84 WRITE(6,300)
86 WRITE(6,400)
80 CONTINUE

```

```

50 CONTINUE

```

C+++++++ TAG FILE GENERATOR ++++++

```

135 IF (ITAG .EQ. 0) GOTO 111
DO 150 JJ=1,M1

```

```

WRITE(6,101)
IF (NN .EQ. 1) GOTO 112
WRITE(6,103)
WRITE(6,104) WNS,WNE,CRS,CRE
WRITE(6,105) ZR(2),RE(1),RI,CIS
WRITE(6,107)
GOTO 113
112 WRITE(6,102)
WRITE(6,104) CIS,CIE,CRS,CRE
WRITE(6,106) ZR(2),RE(1),RI,WNS
WRITE(6,107)
113 DO 160 II=1,2
GOTO (161,162), II
161 JL=J(JJ)
GOTO 163
162 JL=L(JJ)
163 CONTINUE
IF (JL .EQ. 0) GOTO 160
IF (NN .EQ. 1) GOTO 165
WRITE(6,201) (X30R(II, JJ, KK), X20R(II, JJ, KK),
| KK=1, JL)
GOTO 160
165 WRITE(6,201) (X30R(II, JJ, KK), X20R(II, JJ, KK),
| KK=1, JL)
160 CONTINUE

WRITE(6,501)
DO 180 II=1,2
GOTO (181,182), II
181 KM=K(JJ)
GOTO 183
182 KM=M(JJ)
183 CONTINUE
IF (KM .EQ. 0) GOTO 180
IF (NN .EQ. 1) GOTO 185
WRITE(6,201) (X30I(II, JJ, KK), X20I(II, JJ, KK),
| KK=1, KM)
GOTO 180
185 WRITE(6,201) (X30I(II, JJ, KK), X20I(II, JJ, KK),
| KK=1, KM)
180 CONTINUE

150 CONTINUE
WRITE(6,601)
C+++++
100 FORMAT(1H ///,10X, 'ZERO-POINT OF REAL PART OF
| DETERMINANT DET1'//,1H ,20X, '( WN , CR , CI
| )',5X, 'SIGN OF GRADINT',/)
200 FORMAT(1H ,21X,F6.3,1X,F6.3,1X,F6.3,14X,F4.1)
300 FORMAT(1H ,25X, 'NO ZERO-POINT')
400 FORMAT(1H )
500 FORMAT(1H //,10X, 'ZERO-POINT OF IMAGINARY PART OF
| DETERMINANT DET1'//,1H ,20X, '( WN , CR , CI

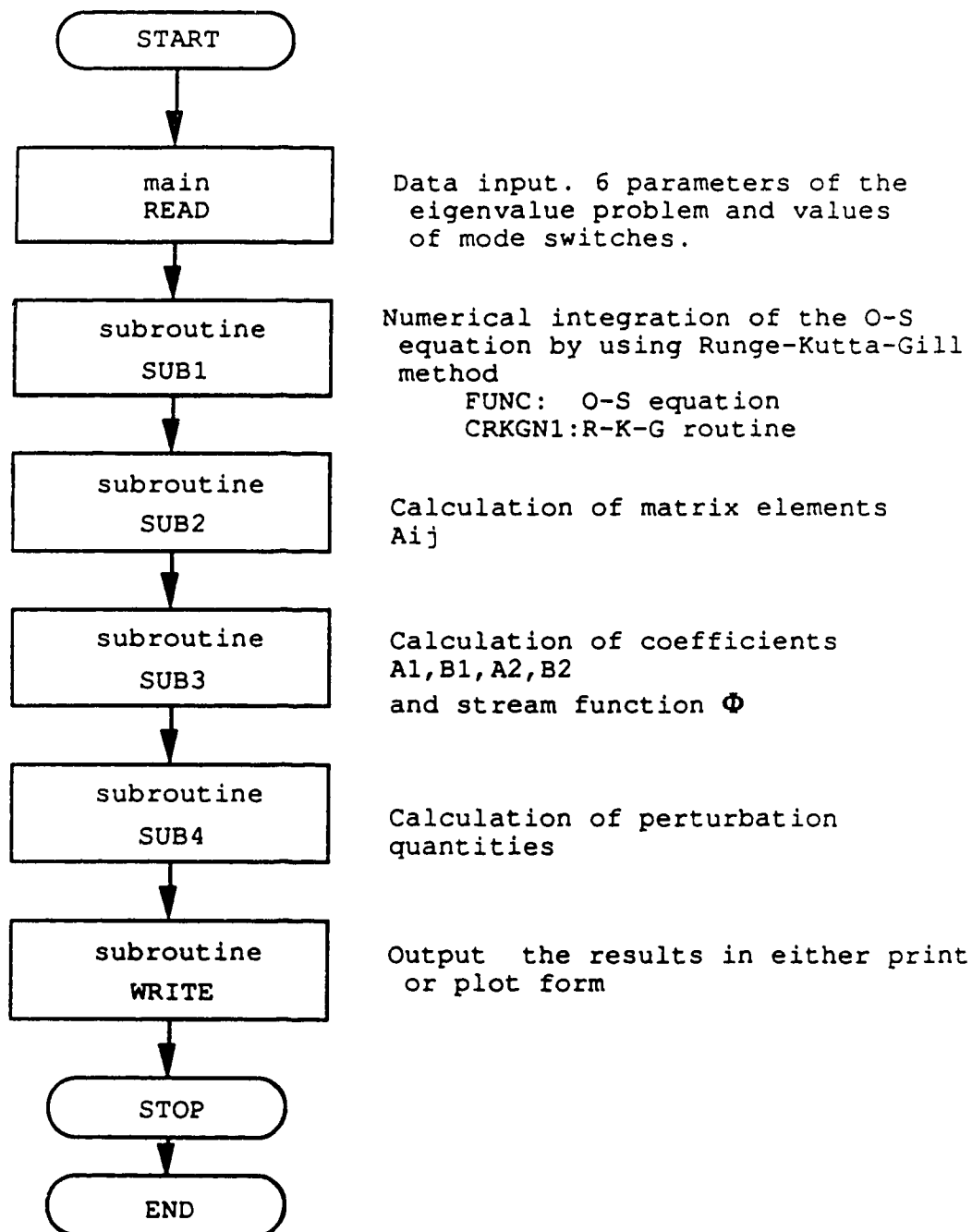
```

```

|          )',5X,'SIGN OF GRADIENT',/)
101 FORMAT(6X,'GEN A PLOT.',/,6X,
|      'LEGEND OFF.',/,6X,
|      'X PAGE IS 11.',/,6X,'Y PAGE IS 8.5.')
102 FORMAT(6X,'X LABEL IS "CI".',/,6X,'Y LABEL IS "CR".')
103 FORMAT(6X,'X LABEL IS "WN".',/,6X,'Y LABEL IS "CR".')
104 FORMAT(6X,'X LENGTH=9.0,AXIS ORIGIN 1.0.',/,6X,
|      'Y LENGTH=6.5,AXIS ORIGIN 1.0.',/,6X,
|      'X MIN ',F10.4,',MAX ',F10.4,',',/,6X,
|      'Y MIN ',F10.4,',MAX ',F10.4,',')
105 FORMAT(6X,'TITLE "WALL EFFECT THICKNESS=',F4.2,' RE=',
|      F5.1,' RI=',F5.3,' CI=',F5.3,',")
106 FORMAT(6X,'TITLE "WALL EFFECT THICNESS=',F4.2,' RE=',
|      F5.1,' RI=',F5.3,' WN=',F5.3,',")
107 FORMAT(6X,'FRAME.',/,6X,'INPUT DATA.',/,6X,
|      "REAL PART")
201 FORMAT(3X,F8.5,',',3X,F8.5)
501 FORMAT(6X,"IMAGINARY PART")
601 FORMAT(6X,'END OF DATA.',/,6X,
|      'CURVE 1 SYMBOL COUNT 1,SCATTERED.',/,6X,
|      'CURVE 2 SYMBOL COUNT 2,SCATTERED.',/,6X,
|      'LEGEND UNITS PLOT%.',/,6X,
|      'LEGEND X ORIGIN 70.',/,6X,
|      'LEGEND Y ORIGIN 10.',/,6X,
|      'LEGEND HEIGHT 0.10.',/,6X,
|      'LEGEND FRAME 1.',/,6X,'SEND.',/,6X,
|      'QUIT.')
```

111 RETURN
END

The program "THIC10.FOR" is designed to calculate the stream function and other perturbation quantities based upon the eigenvalues which are obtained from previous programs. Its flow chart and program are as follows.



```

C*****
C      STABILITY OF A TWO-LAYER SHEAR FLOW
C      --- CALCULATION OF EIGENFUNCTION --- <THIC10.FOR2>
C      DOUBLE PRECISION TYPE
C*****
      IMPLICIT REAL*8 (A-H, O-Z)
      COMPLEX*16 C, W, DW, D2W, D3W, A, DET1, DET2, AA, Q, V0, DV0, D2V0,
      | D3V0
      COMMON /BL1/ V, WN, C, RE /BL2/ GAMMA, RI, S
      DIMENSION V(2), RE(2), ZR(2), NX(2), ND(2), Z(2, 601),
      | W(2, 2), DW(2, 2), D2W(2, 2), D3W(2, 2), A(4, 4), Q(3),
      | V0(2, 601), DV0(2, 601), D2V0(2, 601), D3V0(2, 601),
      | ABSV0(2, 601), ARGV0(2, 601), ABSU0(2, 601),
      | ARGU0(2, 601), ABSETA(2, 601), ARGETA(2, 601),
      | TAU(2, 601), ENE(2, 601)

      READ(5, 100) WN, CR, CI,
      | V(1), RE(1), ZR(1), NX(1), ND(1),
      | V(2), RE(2), ZR(2), NX(2), ND(2),
      ! GAMMA, RI, S, RT,
      ! ICONT, IVO
      IF (ICONT .EQ. 1) GOTO 10
      WRITE(6, 200) V(1), RE(1), ZR(1), NX(1), ND(1),
      | V(2), RE(2), ZR(2), NX(2), ND(2),
      | GAMMA, RI, S
      WRITE(6, 300)

10 C=CR+(0.0D0, 1.0D0)*CI
      GR=WN*CI
      IF (CDABS(C) .EQ. 0.0D0) GOTO 1

      CALL SUB1(ZR, NX, ND, Z, W, DW, D2W, D3W)
      CALL SUB2(W, DW, D2W, D3W, A)
      CALL SUB3(NX, A, DET1, ADET1, DET2, ADET2, AGAP, NS1,
      | AA, Q, NS2, V0, DV0, D2V0, D3V0)
      CALL SUB4(NX, Z, V0, DV0, ABSV0, ARGV0,
      | ABSU0, ARGU0, ABSETA, ARGETA, TAU, ENE)

      IF (ICONT .EQ. 1) GOTO 20
      WRITE(6, 400) WN, CR, CI, GR, DET1, ADET1, DET2, ADET2, AGAP, NS1
      WRITE(6, 500)
      WRITE(6, 600) AA, Q(1), Q(2), Q(3), NS2

      CALL WRITE(NX, Z, V0, DV0, D2V0, D3V0, ABSV0, ARGV0,
      | ABSU0, ARGU0, ABSETA, ARGETA, TAU, ENE)

20 CALL STFUNC(NX, Z, V0, RT, ICONT, IVO, ZR)
      CALL VOPLO(Z, NX, V0, IVO)

      GOTO 2
1 CONTINUE
      IF (ICONT .EQ. 1) GOTO 2
      WRITE(6, 700) WN, CR, CI, GR

```

2 CONTINUE

```

100 FORMAT(3F10.4/,2(2F10.4,F5.1,2I5/),4F10.4,/,2I5)
200 FORMAT(1H1//,11X,'U1=',F6.3,'DTANH(Y)',10X,'RE(1)=' ,
|       F6.1,10X,'ZR(1)=' ,F5.1,5X,'NX(1)=' ,I4,5X,
|       'ND(1)=' ,I4//,11X,'U2=' ,F6.3,'DTANH(Y)',10X,
|       'RE(2)=' ,F6.1,10X,'ZR(2)=' ,F5.1,5X,'NX(2)=' ,
|       I4,5X,'ND(2)=' ,I4//,11X,'GAMMA=' ,F6.3,10X,'RI=' ,
|       F6.2,10X,'S=' ,F7.2//)
300 FORMAT(1H ,8X,'(WN,CR,CI,GR)',11X,
|       'NORMALIZED DETERMINANT DET1',4X,'|DET1|',5X,
|       'ORIGINAL DETERMINANT DET2',5X,'|DET2|',4X,
|       'ELEMENT GAP',2X,'NS'//)
400 FORMAT(1H ,',',F6.3,',',F6.3,',',F6.3,',',F7.4,')',3X,
|       '(',E11.4,',',E11.4,')',2X,E11.4,3X,'(',E11.4,
|       ',',E11.4,')',2X,E11.4,3X,E9.2,2X,I2)
500 FORMAT(1H //,25X,'AA',24X,'Q(1)',23X,'Q(2)',23X,
|       'Q(3)',18X,'NS2'//)
600 FORMAT(1H ,13X,'(',E11.4,',',E11.4,')',2X,'(',E11.4,
|       ',',E11.4,')',2X,'(',E11.4,',',E11.4,')',2X,'(',
|       E11.4,',',E11.4,')',8X,I2)
700 FORMAT(1H ,',',F6.3,',',F6.3,',',F6.3,',',F7.4,')',3X,
|       '(', * , * )',2X,' * ',3X,
|       '(', * , * )',2X,' * ',3X,
|       ' * ',2X,' * ')

```

STOP
END

```

C*****
SUBROUTINE SUB1(ZR,NX,ND,Z,W,DW,D2W,D3W)
C*****

IMPLICIT REAL*8(A-H,O-Z)
COMPLEX*16 C,P1,P2,FUNC,F0,G,FVI,FIN,W,DW,D2W,D3W,
| COEF1,COEF2,COEF,F,DF,D2F,D3F
COMMON /BL1/ V,WN,C,RE /BL3/ N /BL6/ F,DF,D2F,D3F,
| COEF
DIMENSION V(2),RE(2),ZR(2),NX(2),ND(2),Z(2,601),F0(4),
| G(4,13),FVI(4,601),FIN(4,601),W(2,2),DW(2,2),
| D2W(2,2),D3W(2,2),F(2,2,601),DF(2,2,601),
| D2F(2,2,601),D3F(2,2,601),COEF(2,601)
EXTERNAL FUNC

DO 10 N=1,2
SIGN=(-1.0D0)**N
Z0=-DABS(ZR(N))*SIGN
LX=NX(N)
LD=ND(N)
H=-Z0/DFLOAT(LX-1)
DO 50 J=1,LX
Z(N,J)=Z0+H*(J-1)
50 CONTINUE

```

```

P1=SIGN*CDSQRT(WN*WN-2.0D0*V(N)
| *DTANH(ZO)*(1.0D0-DTANH(ZO)*
| DTANH(ZO))/(V(N)*DTANH(ZO)-C)
P2=SIGN*CDSQRT(WN*WN+(0.0D0,1.0D0)
| *WN*RE(N)*(V(N)*DTANH(ZO)-C)
IF (V(N) .EQ. 0.0D0) GOTO 100
C F0(1)=CDEXP(P2*ZO)
F0(1)=0.0D0
C F0(2)=P2*CDEXP(P2*ZO)
F0(2)=0.0D0
C F0(3)=P2*P2*CDEXP(P2*ZO)
F0(3)=0.0D0
C F0(4)=P2*P2*P2*CDEXP(P2*ZO)
F0(4)=1.0D0
CALL CRKGN1(FUNC,ZO,F0,4,H,G,FVI,LX,4)
DO 200 J1=1,LX
F(N,2,J1)=FVI(1,J1)
DF(N,2,J1)=FVI(2,J1)
D2F(N,2,J1)=FVI(3,J1)
D3F(N,2,J1)=FVI(4,J1)
COEF(N,J1)=0.0D0
200 CONTINUE
W(N,2)=FVI(1,LX)
DW(N,2)=FVI(2,LX)
D2W(N,2)=FVI(3,LX)
D3W(N,2)=FVI(4,LX)

C F0(1)=CDEXP(P1*ZO)
F0(1)=0.0D0
C F0(2)=P1*CDEXP(P1*ZO)
F0(2)=0.0D0
C F0(3)=P1*P1*CDEXP(P1*ZO)
F0(3)=1.0D0
C F0(4)=P1*P1*P1*CDEXP(P1*ZO)
F0(4)=0.0D0
MX=LD+1
M=1
IF (MX .GE. LX) GOTO 30
DO 20 I=LD+1,LX-1,LD
M=I
CALL CRKGN1(FUNC,ZO,F0,4,H,G,FIN,MX,4)
K1=1
DO 300 J2=M-LD,M
F(N,1,J2)=FIN(1,K1)
DF(N,1,J2)=FIN(2,K1)
D2F(N,1,J2)=FIN(3,K1)
D3F(N,1,J2)=FIN(4,K1)
K1=K1+1
300 CONTINUE
ZO=ZO+DFLOAT(LD)*H
P1=SIGN*CDSQRT(WN*WN
| -2.0D0*V(N)*DTANH(ZO)*(1.0D0-DTANH(ZO)*
| DTANH(ZO))/(V(N)*DTANH(ZO)-C)
P2=SIGN*CDSQRT(WN*WN+(0.0D0,1.0D0)

```



```

      *WN*RE(N)*(V(N)*DTANH(Z0)-C)
C   COEF1=FIN(4,MX)+P2*FIN(3,MX)-P1*P1*FIN(2,MX)-P1*P1*P2*
C   |   FIN(1,MX)
      COEF1=FIN(1,MX)*DCONJG(FVI(1,M))+FIN(2,MX)
      |   *DCONJG(FVI(2,M))+FIN(3,MX)*DCONJG(FVI(3,M))
      |   +FIN(4,MX)*DCONJG(FVI(4,M))
      COEF2=FVI(1,M)*DCONJG(FVI(1,M))+FVI(2,M)
      |   *DCONJG(FVI(2,M))+FVI(3,M)*DCONJG(FVI(3,M))
      |   +FVI(4,M)*DCONJG(FVI(4,M))
C   COEF2=FVI(4,M)+P2*FVI(3,M)-P1*P1*FVI(2,M)-P1*P1*P2*
C   |   FVI(1,M)
      COEF(N,M)=COEF1/COEF2
      F0(1)=FIN(1,MX)-COEF(N,M)*FVI(1,M)
      F0(2)=FIN(2,MX)-COEF(N,M)*FVI(2,M)
      F0(3)=FIN(3,MX)-COEF(N,M)*FVI(3,M)
      F0(4)=FIN(4,MX)-COEF(N,M)*FVI(4,M)
20  CONTINUE
      MX=LX-M+1
      GOTO 40
30  MX=LX
40  CALL CRKGN1(FUNC,Z0,F0,4,H,G,FIN,MX,4)
      K2=1
      DO 400 J3=M,LX
      F(N,1,J3)=FIN(1,K2)
      DF(N,1,J3)=FIN(2,K2)
      D2F(N,1,J3)=FIN(3,K2)
      D3F(N,1,J3)=FIN(4,K2)
      K2=K2+1
400  CONTINUE
      W(N,1)=FIN(1,MX)
      DW(N,1)=FIN(2,MX)
      D2W(N,1)=FIN(3,MX)
      D3W(N,1)=FIN(4,MX)
      GOTO 10

100  CONTINUE
      DO 500 J4=1,LX
      F(N,2,J4)=CDEXP(P2*Z(N,J4))
      DF(N,2,J4)=P2*CDEXP(P2*Z(N,J4))
      D2F(N,2,J4)=P2*P2*CDEXP(P2*Z(N,J4))
      D3F(N,2,J4)=P2*P2*P2*CDEXP(P2*Z(N,J4))
      F(N,1,J4)=CDEXP(P1*Z(N,J4))
      DF(N,1,J4)=P1*CDEXP(P1*Z(N,J4))
      D2F(N,1,J4)=P1*P1*CDEXP(P1*Z(N,J4))
      D3F(N,1,J4)=P1*P1*P1*CDEXP(P1*Z(N,J4))
      COEF(N,J4)=0.0D0
500  CONTINUE
      W(N,2)=F(N,2,LX)
      DW(M,2)=DF(N,2,LX)
      D2W(N,2)=D2F(N,2,LX)
      D3W(N,2)=D3F(N,2,LX)
      W(N,1)=F(N,1,LX)
      DW(N,1)=DF(N,1,LX)
      D2W(N,1)=D2F(N,1,LX)

```

```

D3W(N,1)=D3F(N,1,LX)
10 CONTINUE
RETURN
END

```

```

C*****
COMPLEX FUNCTION FUNC(K,Z,F)
C*****

```

```

IMPLICIT REAL*8(A-H,O-Z)
COMPLEX*16 C,F
COMMON /BL1/ V,WN,C,RE /BL3/ N
DIMENSION F(4),V(2),RE(2)

GOTO (1,2,3,4),K
1 FUNC=F(2)
GOTO 10
2 FUNC=F(3)
GOTO 10
3 FUNC=F(4)
GOTO 10
4 FUNC=(2.0D0*WN*WN+(0.0D0,1.0D0)
| *WN*RE(N)*(V(N)*DTANH(Z)-C))*F(3)
| -(WN**4+(0.0D0,1.0D0)*WN*RE(N)
| *(WN*WN*(V(N)*DTANH(Z)-C)
| -2.0D0*V(N)*DTANH(Z)
| *(1.0D0-DTANH(Z)*DTANH(Z)))*F(1)
10 RETURN
END

```

```

C*****
*
SUBROUTINE CRKGN1(FUNC,X0,Y0,N,H,F,Y4,NX,NR)
C N-TH ORDER DIFERENTIALL EQUATION (RUNGE-KUTTA-GILL)
C*****
*

```

```

IMPLICIT REAL*8(A-H,O-Z)
COMPLEX*16 FUNC,Y0,F,Y4
DIMENSION Y0(N),Y4(NR,NX),F(NR,13)

IF(N.LE.0.OR.N.GT.NR)GOTO 80
CR2I=1.0D0-DSQRT(0.5D0)
DO 10 K=1,N
F(K,1)=0.0D0
Y4(K,1)=Y0(K)
10 F(K,2)=Y0(K)
I=1
20 X=X0+(DFLOAT(I-1))*H

```

```

DO 30 K=1,N
F(K,3)=H*FUNC(K,X,F(1,2))
F(K,4)=0.5D0*F(K,3)-F(K,1)
F(K,5)=F(K,2)+F(K,4)
30 F(K,6)=F(K,1)+3.0D0*F(K,4)-0.5D0*F(K,3)
DO 40 K=1,N
F(K,7)=H*FUNC(K,X+0.5D0*H,F(1,5))
F(K,4)=CR2I*(F(K,7)-F(K,6))
F(K,8)=F(K,5)+F(K,4)
40 F(K,9)=F(K,6)+3.0D0*F(K,4)-CR2I*F(K,7)
DO 50 K=1,N
F(K,10)=H*FUNC(K,X+0.5D0*H,F(1,8))
F(K,4)=(2.0D0-CR2I)*(F(K,10)-F(K,9))
F(K,11)=F(K,8)+F(K,4)
50 F(K,12)=F(K,9)+3.0D0*F(K,4)-(2.0D0-CR2I)*F(K,10)
DO 60 K=1,N
F(K,13)=H*FUNC(K,X+H,F(1,11))
F(K,4)=(F(K,13)-2.0D0*F(K,12))/6.0D0
F(K,2)=F(K,11)+F(K,4)
Y4(K,I+1)=F(K,2)
60 F(K,1)=F(K,12)+3.0D0*F(K,4)-0.5D0*F(K,13)
I=I+1
IF (NX-I) 70,70,20
80 WRITE(6,100) N,NR
100 FORMAT('0(SUBR.CRKGN1) N=',I3,', NR=',I3,
|
|      ', N SHOULD BE A POSITIVE INTEGER LESS THAN
|      OR EQUAL TO NR. RETURNED WITH NO CALCULATION.'
|      //)
70 RETURN
END

```

```

C*****
SUBROUTINE SUB2(W,DW,D2W,D3W,A)
C*****

```

```

IMPLICIT REAL*8(A-H,O-Z)
COMPLEX*16 C,A10,A20,B11,B21,B10,B20,C12,C22,C10,C20,
| D13,D23,D11,D21,D10,D20,A,W,DW,D2W,D3W
COMMON /BL1/ V,WN,C,RE /BL2/ GAMMA,RI,S
DIMENSION V(2),RE(2),A(4,4),W(2,2),DW(2,2),
| D2W(2,2),D3W(2,2)

```

```

A10=1.0D0
A20=1.0D0
B11=-C
B21=-C
B10=-V(1)
B20=-V(2)
C12=-C*GAMMA*RE(2)
C22=-C*RE(1)
C10=-WN*WN*C*GAMMA*RE(2)
C20=-WN*WN*C*RE(1)

```

```

D13=- (0.0D0,1.0D0)*C*GAMMA*RE(2)/WN
D23=- (0.0D0,1.0D0)*C*RE(1)/WN
D11=C*GAMMA*(C*RE(1)*RE(2)+(0.0D0,3.0D0)*WN*RE(2))
D21=C*(C*RE(1)*RE(2)+(0.0D0,3.0D0)*WN*RE(1))
D10=(C*GAMMA*V(1)+RI)*RE(1)*RE(2)
D20=(C*V(2)-WN*WN*S)*RE(1)*RE(2)
A(1,1)=A10*W(1,1)
A(1,2)=A10*W(1,2)
A(1,3)=-A20*W(2,1)
A(1,4)=-A20*W(2,2)
A(2,1)=B11*DW(1,1)+B10*W(1,1)
A(2,2)=B11*DW(1,2)+B10*W(1,2)
A(2,3)=-B21*DW(2,1)-B20*W(2,1)
A(2,4)=-B21*DW(2,2)-B20*W(2,2)
A(3,1)=C12*D2W(1,1)+C10*W(1,1)
A(3,2)=C12*D2W(1,2)+C10*W(1,2)
A(3,3)=-C22*D2W(2,1)-C20*W(2,1)
A(3,4)=-C22*D2W(2,2)-C20*W(2,2)
A(4,1)=D13*D3W(1,1)+D11*DW(1,1)+D10*W(1,1)
A(4,2)=D13*D3W(1,2)+D11*DW(1,2)+D10*W(1,2)
A(4,3)=-D23*D3W(2,1)-D21*DW(2,1)-D20*W(2,1)
A(4,4)=-D23*D3W(2,2)-D21*DW(2,2)-D20*W(2,2)

C      DO 10 I=1,2
C      DO 20 J=1,2
C      WRITE(6,100) I,J,D3W(I,J)
C 100  FORMAT(2X,2(I5,2X),' ',E20.10,' ',E20.10,' ')
C 20  CONTINUE
C 10  CONTINUE

      RETURN
      END

C*****
      SUBROUTINE SUB3(NX,A,DET1,ADET1,DET2,ADET2,AGAP,NS1,
|          AA,Q,NS2,V0,DV0,D2V0,D3V0)
C*****

      IMPLICIT REAL*8(A-H,O-Z)
      COMPLEX*16  F,DF,D2F,D3F,COEF,A,AA,P,Q,DET1,DET2,WW1,
|          WW2,VMAX,SHIFT,V0,DV0,D2V0,D3V0,A11,A12,
|          A21,A22,BBB,TDET,TP,TQ
      COMMON /BL6/ F,DF,D2F,D3F,COEF
      DIMENSION NX(2),F(2,2,601),DF(2,2,601),D2F(2,2,601),
|          D3F(2,2,601),A(4,4),P(3,3),Q(3),WW1(24),
|          IP1(4),WW2(15),IP2(3),V0(2,601),DV0(2,601),
|          D2V0(2,601),D3V0(2,601),AMXJ(4),AMNJ(4),
|          AMXI(4),COEF(2,601),A11(601),A12(601),
|          A21(601),A22(601),BBB(4),TP(3,3),TQ(3)

      AA=(1.0D0,0.0D0)
      DO 100 I=1,3

```

```

      Q(I)=-A(I,1)*AA
      DO 200 J=1,3
      P(I,J)=A(I,J+1)
200 CONTINUE
100 CONTINUE

C      EPS=1.0D0D-14
C      CALL DCLNLU(P,3,3,Q,EPS,WW2,IP2,NS2)
C      DO 102 I1=1,3
C      WRITE(6,103) (I1,J,P(I1,J),J=1,3)
C      WRITE(6,104) Q(I1)
C 103 FORMAT(2(I5,2X),4X,'(',E12.6,',',E12.6,')')
C 104 FORMAT(10X,'Q=',',',E12.6,',',E12.6,')')
C 102 CONTINUE

      TDET=P(1,1)*P(2,2)*P(3,3)+P(1,2)*P(2,3)*P(3,1)
      !      +P(1,3)*P(2,1)*P(3,2)-P(1,3)*P(2,2)*P(3,1)
      !      -P(1,1)*P(2,3)*P(3,2)-P(1,2)*P(2,1)*P(3,3)
      IF (TDET .EQ. (0.0D0,0.0D0)) THEN
      WRITE(6,105)
105 FORMAT(20X,'MATRIX IS SINGULAR')
      STOP
      END IF

      TP(1,1)= (P(2,2)*P(3,3)-P(2,3)*P(3,2))/TDET
      TP(1,2)=- (P(1,2)*P(3,3)-P(1,3)*P(3,2))/TDET
      TP(1,3)= (P(1,2)*P(2,3)-P(1,3)*P(2,2))/TDET
      TP(2,1)=- (P(2,1)*P(3,3)-P(2,3)*P(3,1))/TDET
      TP(2,2)= (P(1,1)*P(3,3)-P(1,3)*P(3,1))/TDET
      TP(2,3)=- (P(1,1)*P(2,3)-P(1,3)*P(2,1))/TDET
      TP(3,1)= (P(2,1)*P(3,2)-P(2,2)*P(3,1))/TDET
      TP(3,2)=- (P(1,1)*P(3,2)-P(1,2)*P(3,1))/TDET
      TP(3,3)= (P(1,1)*P(2,2)-P(1,2)*P(2,1))/TDET

      TQ(1)=TP(1,1)*Q(1)+TP(1,2)*Q(2)+TP(1,3)*Q(3)
      TQ(2)=TP(2,1)*Q(1)+TP(2,2)*Q(2)+TP(2,3)*Q(3)
      TQ(3)=TP(3,1)*Q(1)+TP(3,2)*Q(2)+TP(3,3)*Q(3)

      Q(1)=TQ(1)
      Q(2)=TQ(2)
      Q(3)=TQ(3)

C      CALL LEQ2C(P,3,3,Q,1,3,0,WW2,IP2,NS2)

C      WRITE(6,111) Q(1),Q(2),Q(3)
C 111 FORMAT(2X,'NO1',3(2X,'(',E12.6,',',E12.6,')'))

      A11(NX(1))=AA
      A12(NX(1))=Q(1)
      A21(NX(2))=Q(2)
      A22(NX(2))=Q(3)

      DO 50 L1=NX(1)-1,1,-1

```

```

A11(L1)=A11(L1+1)
A12(L1)=A12(L1+1)-COEF(1,L1+1)*A11(L1+1)
50 CONTINUE
DO 60 L2=NX(2)-1,1,-1
A21(L2)=A21(L2+1)
A22(L2)=A22(L2+1)-COEF(2,L2+1)*A21(L2+1)
60 CONTINUE

VMAX=(0.0D0,0.0D0)
DO 300 K1=1,NX(1)
V0(1,K1)=A11(K1)*F(1,1,K1)+A12(K1)*F(1,2,K1)
DV0(1,K1)=A11(K1)*DF(1,1,K1)+A12(K1)*DF(1,2,K1)
D2V0(1,K1)=A11(K1)*D2F(1,1,K1)+A12(K1)*D2F(1,2,K1)
D3V0(1,K1)=A11(K1)*D3F(1,1,K1)+A12(K1)*D3F(1,2,K1)
IF (CDABS(V0(1,K1)) .GT. CDABS(VMAX)) VMAX=V0(1,K1)

300 CONTINUE
DO 400 K2=1,NX(2)
V0(2,K2)=A21(K2)*F(2,1,K2)+A22(K2)*F(2,2,K2)
DV0(2,K2)=A21(K2)*DF(2,1,K2)+A22(K2)*DF(2,2,K2)
D2V0(2,K2)=A21(K2)*D2F(2,1,K2)+A22(K2)*D2F(2,2,K2)
D3V0(2,K2)=A21(K2)*D3F(2,1,K2)+A22(K2)*D3F(2,2,K2)
IF (CDABS(V0(2,K2)) .GT. CDABS(VMAX)) VMAX=V0(2,K2)
400 CONTINUE

FAI=-3.141592D0*0.5D0

C WRITE(6,411) V0(1,1)
C 411 FORMAT(2X,'V0=', '( ',E12.6,' ',', ',E12.6,' ') ')

C SHIFT=DCONJG(V0(1,1)/VMAX)/CDABS(V0(1,1)/VMAX)*
C | CDEXP((0.0D0,1.0D0)*FAI)

C SHIFT=CDEXP((0.0D0,1.0D0)*FAI)

SHIFT=DCONJG(V0(2,2)/VMAX)/CDABS(V0(2,2)/VMAX)*
| CDEXP((0.0D0,1.0D0)*FAI)

DO 500 K3=1,NX(1)
V0(1,K3)=V0(1,K3)/VMAX*SHIFT
DV0(1,K3)=DV0(1,K3)/VMAX*SHIFT
D2V0(1,K3)=D2V0(1,K3)/VMAX*SHIFT
D3V0(1,K3)=D3V0(1,K3)/VMAX*SHIFT
500 CONTINUE
DO 600 K4=1,NX(2)
V0(2,K4)=V0(2,K4)/VMAX*SHIFT
DV0(2,K4)=DV0(2,K4)/VMAX*SHIFT
D2V0(2,K4)=D2V0(2,K4)/VMAX*SHIFT
D3V0(2,K4)=D3V0(2,K4)/VMAX*SHIFT
600 CONTINUE

DO 10 J=1,4
AMXJ(J)=DMAX1(CDABS(A(1,J)),CDABS(A(2,J))),

```

```

|           CDABS ( A ( 3 , J ) ) , CDABS ( A ( 4 , J ) ) )
AMNJ ( J ) = DMIN1 ( CDABS ( A ( 1 , J ) ) , CDABS ( A ( 2 , J ) ) ,
|           CDABS ( A ( 3 , J ) ) , CDABS ( A ( 4 , J ) ) )
DO 20 II=1,4
A ( II , J ) = A ( II , J ) / AMXJ ( J )
20 CONTINUE
10 CONTINUE
DO 30 I=1,4
AMXI ( I ) = DMAX1 ( CDABS ( A ( I , 1 ) ) , CDABS ( A ( I , 2 ) ) ,
|           CDABS ( A ( I , 3 ) ) , CDABS ( A ( I , 4 ) ) )
DO 40 JJ=1,4
A ( I , JJ ) = A ( I , JJ ) / AMXI ( I )
40 CONTINUE
30 CONTINUE

C      CALL DCINV ( A , 4 , 0 , 4 , 4 , 0 . 0 D 0 , DET1 , WW1 , IP1 , NS1 )
C
C      DO 556 IJ=1,4
C      BBB ( IJ ) = ( 1 . 0 D 0 , 0 . 0 D 0 )
C 556 CONTINUE
C
C      CALL LEQ2C ( A , 4 , 4 , BBB , 1 , 4 , 1 , WW1 , IP1 , NS1 )
C
C      WRITE ( 6 , 112 )
C 112 FORMAT ( 2X , 'NO2' )

      DET1 = A ( 1 , 1 ) * ( A ( 2 , 2 ) * A ( 3 , 3 ) * A ( 4 , 4 ) + A ( 2 , 3 ) * A ( 3 , 4 ) * A ( 4 , 2 )
|           + A ( 2 , 4 ) * A ( 3 , 2 ) * A ( 4 , 3 ) - A ( 2 , 4 ) * A ( 3 , 3 ) * A ( 4 , 3 )
|           - A ( 2 , 3 ) * A ( 3 , 2 ) * A ( 4 , 4 ) - A ( 2 , 2 ) * A ( 3 , 4 ) * A ( 4 , 3 ) )
|
|           -
A ( 2 , 1 ) * ( A ( 1 , 2 ) * A ( 3 , 3 ) * A ( 4 , 4 ) + A ( 1 , 3 ) * A ( 3 , 4 ) * A ( 4 , 2 )
|           + A ( 1 , 4 ) * A ( 3 , 2 ) * A ( 4 , 3 ) - A ( 1 , 4 ) * A ( 3 , 3 ) * A ( 4 , 2 )
|           - A ( 1 , 3 ) * A ( 3 , 2 ) * A ( 4 , 4 ) - A ( 1 , 2 ) * A ( 3 , 4 ) * A ( 4 , 3 ) )
|
|           +
+A ( 3 , 1 ) * ( A ( 1 , 2 ) * A ( 2 , 3 ) * A ( 4 , 4 ) + A ( 1 , 3 ) * A ( 2 , 4 ) * A ( 4 , 2 )
|           + A ( 1 , 4 ) * A ( 2 , 2 ) * A ( 4 , 3 ) - A ( 1 , 4 ) * A ( 2 , 3 ) * A ( 4 , 2 )
|           - A ( 1 , 3 ) * A ( 2 , 2 ) * A ( 4 , 4 ) - A ( 1 , 2 ) * A ( 2 , 4 ) * A ( 4 , 3 ) )
|
|           -
A ( 4 , 1 ) * ( A ( 1 , 2 ) * A ( 2 , 3 ) * A ( 3 , 4 ) + A ( 1 , 3 ) * A ( 2 , 4 ) * A ( 3 , 2 )
|           + A ( 1 , 4 ) * A ( 2 , 2 ) * A ( 3 , 3 ) - A ( 1 , 4 ) * A ( 2 , 3 ) * A ( 3 , 2 )
|           - A ( 1 , 2 ) * A ( 2 , 4 ) * A ( 3 , 3 ) - A ( 1 , 3 ) * A ( 2 , 2 ) * A ( 3 , 4 ) )

C      DET1 = ( 1 . 0 D 0 , 0 . 0 D 0 )
C      DO 555 JI=1,4
C      IPVT = IP1 ( JI )
C      IF ( IPVT .NE. JI ) DET1 = -DET1
C      INDX = JI + ( JI - 1 ) * 4
C      DET1 = DET1 * WW1 ( INDX )
C 555 CONTINUE

      ADET1 = CDABS ( DET1 )
      DET2 = AMXJ ( 1 ) * AMXJ ( 2 ) * AMXJ ( 3 ) * AMXJ ( 4 ) *
|           AMXI ( 1 ) * AMXI ( 2 ) * AMXI ( 3 ) * AMXI ( 4 ) * DET1
      ADET2 = CDABS ( DET2 )

```

```

AMX=DMAX1 (AMXJ (1) , AMXJ (2) , AMXJ (3) , AMXJ (4) )
AMN=DMIN1 (AMNJ (1) , AMNJ (2) , AMNJ (3) , AMNJ (4) )
AGAP=AMX/AMN
RETURN
END

```

```

C*****
SUBROUTINE SUB4 (NX, Z, V0, DVO, ABSV0, ARGV0,
| ABSU0, ARGU0, ABSETA, ARGETA, TAU, ENE)
C*****

```

```

IMPLICIT REAL*8 (A-H, O-Z)
COMPLEX*16 C, V0, DVO, U0, ETA
COMMON /BL1/ V, WN, C, RE
DIMENSION V (2) , RE (2) , NX (2) , Z (2, 601) , V0 (2, 601) ,
| DVO (2, 601) , U0 (2, 601) , ETA (2, 601) , TAU (2, 601) ,
| ENE (2, 601) , ABSV0 (2, 601) , ARGV0 (2, 601) ,
| ABSU0 (2, 601) , ARGU0 (2, 601) , ABSETA (2, 601) ,
| ARGETA (2, 601)

```

```
DO 10 N=1,2
```

```

ABSV0 (N, 1) =0.0D0
ARGV0 (N, 1) =0.0D0
ABSU0 (N, 1) =0.0D0
ARGU0 (N, 1) =0.0D0
ABSETA (N, 1) =0.0D0
ARGETA (N, 1) =0.0D0
TAU (N, 1) =0.0D0
ENE (N, 1) =0.0D0

```

```

DO 20 I=2, NX (N)
U0 (N, I) =(0.0D0, 1.0D0) *DVO (N, I) /WN
ETA (N, I) =V0 (N, I) / ((0.0D0, 1.0D0) *WN* (DTANH (Z (N, I) ) -C) )
ABSV0 (N, I) =CDABS (V0 (N, I) )
ARGV0 (N, I) =DATAN2 (DIMAG (V0 (N, I) ) , DREAL (V0 (N, I) ) )
| *180.0D0/3.141592D0
ABSU0 (N, I) =CDABS (U0 (N, I) )
ARGU0 (N, I) =DATAN2 (DIMAG (U0 (N, I) ) , DREAL (U0 (N, I) ) )
| *180.0D0/3.141592D0
ABSETA (N, I) =CDABS (ETA (N, I) )
ARGETA (N, I) =DATAN2 (DIMAG (ETA (N, I) ) , DREAL (ETA (N, I) ) ) *
| 180.0D0/3.141592D0
TAU (N, I) =-ABSU0 (N, I) *ABSV0 (N, I) *COS (ARGV0 (N, I)
| -ARGV0 (N, I) ) /2.0D0
ENE (N, I) =(ABSU0 (N, I) **2+ABSV0 (N, I) **2) /2.0D0

```

```

20 CONTINUE
10 CONTINUE

```

```

RETURN
END

```



```

C*****
  SUBROUTINE WRITE(NX,Z,VO,DVO,D2VO,D3VO,ABSV0,ARGV0,
|              ABSU0,ARGU0,ABSETA,ARGETA,TAU,ENE)
C*****

  IMPLICIT REAL*8(A-H,O-Z)
  COMPLEX*16   VO,DVO,D2VO,D3VO
  DIMENSION NX(2),Z(2,601),
|            VO(2,601),DVO(2,601),D2VO(2,601),D3VO(2,601),
|            ABSV0(2,601),ARGV0(2,601),ABSU0(2,601),
|            ARGU0(2,601),ABSETA(2,601),ARGETA(2,601),
|            TAU(2,601),ENE(2,601)

  WRITE(6,100)
  WRITE(6,200) (Z(1,I),VO(1,I),DVO(1,I),D2VO(1,I),
|              D3VO(1,I),I=1,NX(1),2)
  WRITE(6,200) (Z(2,J),VO(2,J),DVO(2,J),D2VO(2,J),
|              D3VO(2,J),J=NX(2),1,-2)
  WRITE(6,300)
  WRITE(6,400)
  WRITE(6,500) (Z(1,I),ABSV0(1,I),ARGV0(1,I),
|              ABSU0(1,I),ARGU0(1,I),
|              ABSETA(1,I),ARGETA(1,I),TAU(1,I),ENE(1,I),
|              I=1,NX(1),2)
  WRITE(6,500) (Z(2,J),ABSV0(2,J),ARGV0(2,J),
|              ABSU0(2,J),ARGU0(2,J),
|              ABSETA(2,J),ARGETA(2,J),TAU(2,J),ENE(2,J),
|              J=NX(2),1,-2)

100 FORMAT(1H //,8X,'Z',16X,'VO',23X,'DVO/DZ',20X,
|         'D2VO/DZ2',19X,'D3VO/DZ3'/)
200 FORMAT(1H ,5X,F6.3,2X,'(',E11.4,',',E11.4,')',2X,
|         '(',E11.4,',',E11.4,')',2X,'(',E11.4,',',
|         E11.4,')',2X,'(',E11.4,',',E11.4,')')
300 FORMAT(1H //,8X,'Z',16X,'VO',25X,'U0',25X,'ETA',18X,
|         'TAU',12X,'ENE')
400 FORMAT(1H ,17X,'DABS(V0) ARG(V0)',10X,'DABS(U0)
|         ARG(U0)',10X,'DABS(ETA) ARG(ETA)')
500 FORMAT(1H ,5X,F6.3,2X,'(',E11.4,',',E11.4,')',2X,'(,
|         E11.4,',',E11.4,')',2X,'(',E11.4,',',E11.4,
|         ')',3X,E11.4,4X,E11.4)

  RETURN
  END

```

```

C*****
  SUBROUTINE STFUNC(NX,Z,VO,RT,ICONT,IVO,ZR)
C*****

  IMPLICIT REAL*8(A-H,O-Z)

```

```

COMPLEX*16  C,VO
COMMON  /EL1/ V,WN,C,RE /BLP/ AMP /BLV/ VP,VA
DIMENSION NX(2),Z(2,601),VO(2,601),F(2,601),VP(2,601),
|          VA(2,601),AMP(21,41),ZR(2),V(2),RE(2)

```

```

CR=DREAL(C)

```

```

C----- BACKGROUND STREAM FUNCTION -----
DZ1=Z(1,1)-Z(1,2)
DZ2=Z(2,2)-Z(2,1)
DO 10 I0=1,601
F(1,I0)=0.0D0
F(2,I0)=0.0D0
10 CONTINUE
DO 20 I1=NX(1)-1,1,-1
F(1,I1)=F(1,I1+1)
|          +((DTANH(Z(1,I1))+DTANH(Z(1,I1+1)))/2-CR)*DZ1
20 CONTINUE
DO 30 I2=NX(2)-1,1,-1
F(2,I2)=F(2,I2+1)
|          -((DTANH(Z(2,I2))+DTANH(Z(2,I2+1)))/2-CR)*DZ2
30 CONTINUE

```

```

C-----
C----- MESH GENERATOR -----

```

```

C      TZ=ZR(1)+ZR(2)
      TZ=3.0D0+ZR(2)
      DTZ=TZ/40.0D0
      IZ1=INT(DTZ/DZ1)
      IZ2=INT(DTZ/DZ2)
      IMZ2=IZ2*INT(NX(2)/IZ2)+1
      IMZ1=NX(1)-INT((DTZ-(NX(2)-IMZ2)*DZ2)/DZ1)
      ISZ1=IMZ1-IZ1*(41-(INT(NX(2)/IZ2)+1)-1)
      IF (ISZ1 .LT. 1) THEN
      ISZ1=1
      END IF

```

```

C-----
      VMAX=0.0D0
      VP(1,1)=0.0D0
      VA(1,1)=0.0D0
      DO 40 J1=2,NX(1)
      VP(1,J1)=CDABS(VO(1,J1))
      SA1=DIMAG(VO(1,J1))/VP(1,J1)
      VA(1,J1)=-DASIN(SA1)-(3.141592/2.0D0)
      IF (VP(1,J1) .GT. VMAX) THEN
      VMAX=VP(1,J1)
      ELSE
      VMAX=VMAX
      END IF
40 CONTINUE

      VP(2,1)=0.0D0

```

```

      VA(2,1)=0.0D0
      DO 50 J2=2,NX(2)
      VP(2,J2)=CDABS(V0(2,J2))
      SA2=DIMAG(V0(2,J2))/VP(2,J2)
      VA(2,J2)=-DASIN(SA2)-(3.141592/2.0D0)
      IF (VP(2,J2) .GT. VMAX) THEN
      VMAX=VP(2,J2)
      ELSE
      VMAX=VMAX
      END IF
50 CONTINUE

```

```

      DO 60 K1=1,NX(1)
      VP(1,K1)=VP(1,K1)/VMAX
60 CONTINUE

```

```

      DO 70 K2=1,NX(2)
      VP(2,K2)=VP(2,K2)/VMAX
70 CONTINUE

```

C----- COMBINING -----

```

      DO 80 I=1,81
      PN=(I-1)*(3.141592/20.0D0)
      II=0
      DO 90 J1=ISZ1,IMZ1,IZ1
      II=II+1
      AMP(I,II)=F(1,J1)+RT*VP(1,J1)*COS(VA(1,J1)+PN)
90 CONTINUE
      DO 110 J2=IMZ2,1,-IZ2
      II=II+1
      AMP(I,II)=F(2,J2)+RT*VP(2,J2)*COS(VA(2,J2)+PN)
110 CONTINUE
80 CONTINUE

```

C----- FIND AMOUNT OF SHIFTING -----

```

      AMIN=10.0D0
      DO 200 I3=1,81
      DO 210 J3=1,41
      IF (AMP(I3,J3) .LT. AMIN) THEN
      AMIN=AMP(I3,J3)
      END IF
210 CONTINUE
200 CONTINUE

```

C----- SHIFTING ACCORDING TO AMIN -----

```

      DO 300 I4=1,81
      DO 310 J4=1,41
      AMP(I4,J4)=AMP(I4,J4)-AMIN
310 CONTINUE
300 CONTINUE

```

C----- CREAT OUTPUT FILE -----

```

      DO 500 I=1,81
      IF (IVO .EQ. 1) GOTO 120

```

```

WRITE(6,100) AMP(I, 1),AMP(I, 2),AMP(I, 3),AMP(I, 4),
|           AMP(I, 5),AMP(I, 6),AMP(I, 7),AMP(I, 8),
|           AMP(I, 9),AMP(I,10),AMP(I,11),AMP(I,12),
|           AMP(I,13),AMP(I,14),AMP(I,15),AMP(I,16),
|           AMP(I,17),AMP(I,18),AMP(I,19),AMP(I,20),
|           AMP(I,21),AMP(I,22),AMP(I,23),AMP(I,24),
|           AMP(I,25),AMP(I,26),AMP(I,27),AMP(I,28),
|           AMP(I,29),AMP(I,30),AMP(I,31),AMP(I,32),
|           AMP(I,33),AMP(I,34),AMP(I,35),AMP(I,36),
|           AMP(I,37),AMP(I,38),AMP(I,39),AMP(I,40),
|           AMP(I,41)
100 FORMAT(41(1X,F6.3))
500 CONTINUE

120 RETURN
END

```

```

C*****
C      SUBROUTINE VOPLO(Z,NX,VO,IVO)
C      TAG GENERATOR.
C*****

      IMPLICIT REAL*8(A-H,O-Z)
      COMPLEX*16   VO
      COMMON /BLV/ VP,VA
      DIMENSION Z(2,601),NX(2),VO(2,601),VP(2,601),VA(2,601)

      IF (IVO .EQ. 0) RETURN
      WRITE(6,100)
      WRITE(6,200)
      WRITE(6,300)
      WRITE(6,400)

      DO 10 I1=1,NX(1)
      WRITE(6,500) VP(1,I1),Z(1,I1)
10 CONTINUE
      DO 15 I2=NX(2),1,-1
      WRITE(6,500) VP(2,I2),Z(2,I2)
15 CONTINUE

      WRITE(6,600)

      DO 20 J1=1,NX(1)
      WRITE(6,500) VA(1,J1),Z(1,J1)
20 CONTINUE
      DO 25 J2=NX(2),1,-1
      WRITE(6,500) VA(2,J2),Z(2,J2)
25 CONTINUE

      WRITE(6,700)

```

```

100 FORMAT(6X, 'GEN A PLOT.',/, 6X,
|         'LEGEND OFF.',/, 6X,
|         'X PAGE IS 11.',/, 6X, 'Y PAGE IS 8.5.',/
|         6X, 'X LABEL IS "V0" ',/, 6X, 'Y LABEL IS "Z" .')
200 FORMAT(6X, 'X LENGTH=9.0, AXIS ORIGIN 1.0D0.',/, 6X,
|         'Y LENGTH=6.5, AXIS ORIGIN 1.0D0.',/, 6X,
|         'X MIN -3.0D0 ',',', 'MAX 3.0D0 ',',',',/, 6X,
|         'Y MIN -3.0D0 ',',', 'MAX 3.0D0 ',',',')
300 FORMAT(6X, 'TITLE "V0 DISTRIBUTIONS" .')
400 FORMAT(6X, 'FRAME.',/, 6X, 'INPUT DATA.',/, 6X,
|         '"ABS V0"')
500 FORMAT(3X, F10.5, ', ', 3X, F10.5)
600 FORMAT(6X, '"PHASE V0"')
700 FORMAT(6X, 'END OF DATA.',/, 6X,
|         'CURVE 1 SYMBOL COUNT 1, SCATTERED.',/, 6X,
|         'CURVE 2 SYMBOL COUNT 2, SCATTERED.',/, 6X,
|         'LEGEND UNITS PLOT%.',/, 6X,
|         'LEGEND X ORIGIN 70.',/, 6X,
|         'LEGEND Y ORIGIN 10.',/, 6X,
|         'LEGEND HEIGHT 0.10.',/, 6X,
|         'LEGEND FRAME 1.',/, 6X, 'SEND.',/, 6X,
|         'QUIT.')
```

RETURN
END

APPENDIX C: DETERMINATION OF WAVE LENGTH λ AND PHASE VELOCITY C_R

In section 4.2.3, it was mentioned that two sets of independent wave sensors located along the longitudinal axis of the flume, gave enough information to evaluate the interfacial wave length λ and its phase velocity C_R . In this appendix, the process used to determine these properties is shown by way of example output data.

Let us consider a the typical output example which is shown in Figure C.1. From the FFT output (b), we can obtain the dominant frequency of the wave f_d which can be confirmed by comparison with the raw data (a) (in this example, $f_d = 1.52$ Hz). Output (c) shows the result of a cross correlation between two sensors located 10cm apart longitudinally, which indicates the maximum correlation time t_d . Care must be taken when using this time scale since there are several identical peaks in the output produced by the wave phenomena, since the waves are basically periodic. Therefore, some information is required to distinguish between the correlation time and others.

In this thesis, the additional information was provided using a stop watch and physical observation; a technique which supplied reasonable range for the time scale. Using this process, the maximum correlation time in this particular example was found to be $t_d=3.13$ sec. Since we already know

the distance between the two wave sensors, the phase velocity of the interfacial wave can be calculated as follows;

$$C_R = 10 \text{ (cm)} / t_d = 10 \text{ (cm)} / 3.13 \text{ (sec)} = 3.20 \text{ (cm/sec)}.$$

Since the dominant frequency f_d was obtained from (b), the wave length λ is calculated as,

$$\lambda = C_R / F_d = 3.20 \text{ (cm/sec)} / 1.52 \text{ (Hz)} = 2.10 \text{ (cm)}. \quad .$$

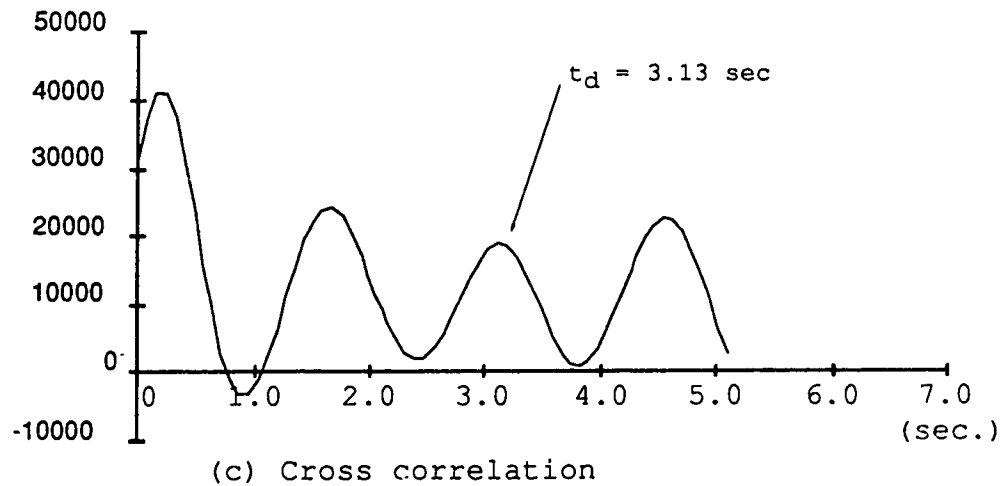
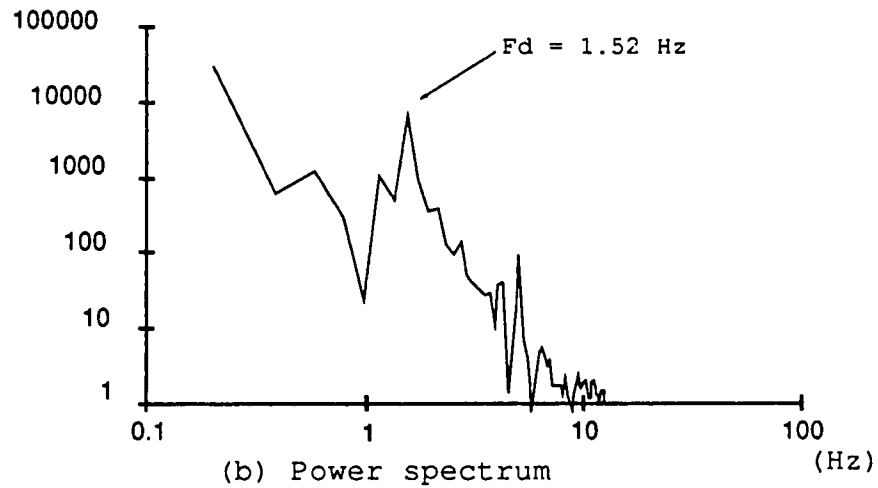
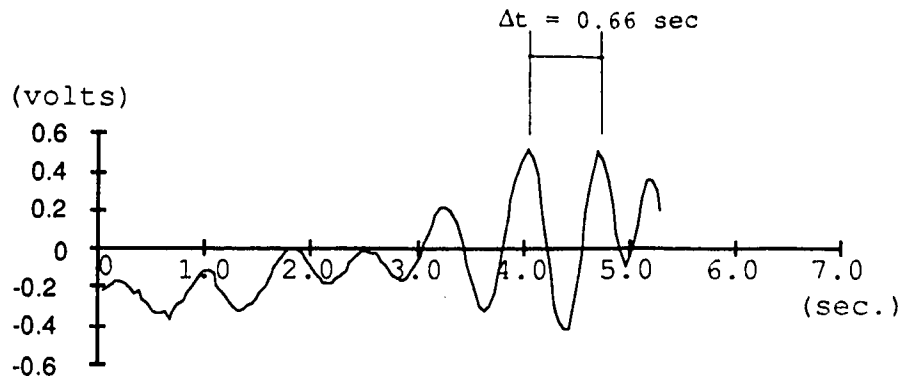


Figure C.1. Wave detector output and processed data example. (90.6.9(1) case. $\lambda^* = 2.10 \text{ cm}$, $C_R^* = 3.20 \text{ cm/sec.}$)